Three-Body Reaction Dynamics
in cold Atom-Ion Experiments

Dissertation

zur Erlangung des akademischen Grades
Doktor der Naturwissenschaften (Dr. rer. nat.)

eingereicht an der
Fakultät für Naturwissenschaften
der
Universität Ulm

von
Artjom Krükow
aus
Gurjew

Betreuer der Dissertation: Johannes Hecker Denschlag

2016

Die in dieser Dissertation beschriebenen Arbeiten wurden durchgeführt an der

Universität Ulm

Institut für Quantenmaterie

Albert-Einstein-Allee 45

D-89069 Ulm

Abstract

Over the recent years a new research field emerged that combines technologies for cooling and trapping of *neutral* atoms and *charged* ions in one experimental apparatus. These atom-ion hybrid traps enable the investigation of atom-ion interactions at unprecedentedly low collision energies targeting the ultracold s-wave regime.

In this thesis I report on experiments performed in an hybrid atom-ion apparatus combining single Ba^+ or Rb^+ ions with ultracold neutral Rb atoms. The main focus of this work is studying the emerging three-body reaction dynamics in a cold charged gas.

First, I will present measurements investigating cold reactions in the hetero-nuclear Ba^+-Rb system. So far, most theoretical and experimental studies have been dealing with reactions between two particles. However, we find that three-body reactions already dominate over two-body ones at atomic densities down to 10^{-11} cm^{-3} once collision energies are in the low mK regime. We then investigate the energy scaling of inelastic ternary collisions between an ion and two atoms. A power-law scaling of the three-body rate coefficient is predicted by theory. We find agreement with the experiment if we include the ion's kinetic energy distribution that we access numerically.

The next study elaborates on the very first observation of ternary reactions in a hybrid cold atom-ion setup. For this we immerse a single Rb^+ ion into ultracold Rb atoms with sufficiently reduced excess micromotion. Occurring reactions are signaled by the creation of highly energetic Rb^+ ions.

I will also showcase novel techniques to investigate the atom and the ion system by using the respective other one which were developed by us over the course of the last years.

In order to reduce the total ion kinetic energy in a Paul trap one has to compensate the ion's excess micromotion. This is routinely being done by analyzing the ion's fluorescence. By observing collision energy dependent elastic atom-ion collisions in an ultracold atom cloud we directly infer the ion's micromotion energy. This way we can perform atom-ion experiments with optically dark Rb^+ ions and good excess micromotion.

Without the need of visible laser light for micromotion compensation we are able to investigate the evolution of quasi-static stray electric fields in a Paul trap over a period of several months.

The last study I will present is targeted at neutral Rb only. There, we spectroscopically access the molecular state distribution of Rb_2 molecules formed in neutral three-body recombination by state-selective ionization of these molecules. Trapping and subsequent detection of these ions is being done with our Paul trap, which has the role of a very sensitive single ion detector in these measurements.

Zusammenfassung

In den letzten Jahren hat sich ein neues Forschungsgebiet aufgetan, welches Technologien zum Kühlen und Speichern von *neutralen* Atomen und *geladenen* Ionen in einer experimentellen Apparatur vereint. Diese Atom-Ionen Hybridfallen ermöglichen die Erforschung von Atom-Ion Wechselwirkungen bei unerreicht niedrigen Kollisionsenergien, mit dem Ziel das ultrakalte s-Wellenregime zu erreichen.

In dieser Dissertation berichte ich über Experimente in einer hybriden Atom-Ion Apparatur, welche einzelne Ba^+ oder Rb^+ Ionen mit ultrakalten Rb Atomen vereint. Der Schwerpunkt dieser Arbeit liegt auf der entstehenden Dreikörperreaktionsdynamik in einem kalten geladenen Gas.

Zunächst stelle ich Messungen vor, die kalte Reaktionen im heteronuklearen Ba^+-Rb System untersuchen. Bisher behandelten die meisten theoretischen und experimentellen Arbeiten nur Reaktionen zwischen je einem Ion und Atom. Wir beobachten jedoch dass Dreikörperreaktionen bereits bei moderaten Atomdichten von $n \approx 10^{11}$ cm^{-3} über Zweikörperreaktionen dominieren sobald die Kollisionsenergien im niedrigen mK Regime sind. Daraufhin untersuchen wir die Energieskalierung von inelastischen Ternärreaktionen zwischen einem Ion und zwei Atomen. Die Theorie sagt dafür ein Exponentialgesetzt voraus, welches wir in unseren Experimenten wiederfinden. Dafür müssen wir aber die Energieverteilung des Ions berücksichtigen, auf die nummerisch zugegriffen wird. Die nächste Studie legt die erste Beobachtung von Dreikörperreaktionen in kalten Atom-Ion Experimenten dar. Dabei werden Reaktionen von einem Rb^+ mit zwei Rb Atomen durch das Entstehen von hoch energetischen Rb^+ Ionen signalisiert.

Ich werde auch von uns entwickelte neuartige Methoden vorstellen bei denen das Atom- oder das Ionsystem untersucht wird mithilfe des jeweils Anderen. Unter Verwendung des energieabhängigen elastischen Streuquerschnittes kompensieren wir die Excess Mikrobewegung indem wir kollisionsbedingte Atomverluste minimieren. Dieser neue Ansatz basiert vollständig auf gemessenen Signalen der Atomwolke und benötigt keine Ionenfluoreszenz zur Mikrobewegungskompensation.

Mithilfe von optisch dunklem Rb^+ beobachten wir eine eine Langzeitdrift von elektrischen Streufeldern welche zur Excess Mikrobewegung führen. Verschiedene Streufeldquellen werden identifiziert, da diese zu unterschiedliche Zeitskalen und Richtungen der Drift führen.

Die letzte Studie die ich vorstellen werde behandelt die Populationsverteilung von Rb_2 Produkten der Dreikörperrekombination in neutralem Rb. Wir führen eine resonanzverstärkte multiphoton Ionisationsspektroskopie an neu gebildeten Rb_2 Molekülen durch, mit anschließender Detektion der Molekularionen in unserer Paulfalle.

Contents

4   Single Ion as a Three-Body Reaction Center in an Ultracold Atomic Gas   **47**

5   Minimization of ion micromotion using ultracold atomic probes   **61**

6   Long-term drifts of stray electric fields in a Paul trap   **73**

Chapter 1

Introduction

Investigating and understanding the fundamental interaction between particles has always been a driving force in scientific advance. With sufficient knowledge of the underlying mechanisms one can tailor techniques to directly control this interaction down to the single particle level, allowing experimental access to new phenomena and enabling the design of complex physical systems of interest. Examples of these achievements can be found in recent scientific history within the success stories of laser-cooled charged and neutral atoms, resulting in four physics Nobel prizes (1989, 1997, 2001 and 2012).

Confining charged particles with electric and magnetic fields dates back to the 1950s. With the advent of laser cooling some 20 years later, the preparation of single trapped ions became a reality [Neu80, Win81] paving the road for complex experiments. By today, ions are routinely cooled to the quantum mechanical ground state of their confinement [Mon95] in laboratories all around the world. Even multi-qubit quantum computation with trapped ions has been demonstrated (e.g., Ref. [Mon16]), making these systems *the* classic example of fully controllable quantum systems. Trapping of neutral atoms has always been a more involved topic as applicable external forces are weaker compared to the electric force on charged particles resulting in shallow traps. Laser cooling techniques were crucial in reducing the kinetic energies sufficiently and finally allowed for accumulation of cold atoms in a magnetic [Mig85], optical [Chu86] or magneto-optical traps [Raa87]. This starting point enabled the development of evaporative cooling techniques and ultimately made Bose-Einstein condensation in dilute atomic gases a reality [And95, Dav95]. Starting with direct tunability of the inter-particle interaction via Feshbach resonances [Ino98] tremendous progress has been made over the course of the following years. Today, ultracold quantum gases allow preparation and readout at the single atom level (e.g., Ref. [Wei10]) making them the leading platform to study the dynamics of many-body quantum systems.

The overall progress of laser-cooling, trapping and manipulating both ultracold neutral atoms and charged ions has enabled excellent experimental control of internal and external degrees of freedom on the single particle and multi-particle level. In the beginning of the 21st century proposals were brought up to investigate combined ultracold atom-ion systems as the similarity in technology and utilized techniques offered very good starting conditions for experiments. Investigation of cold chemistry in charged gases at very low collision energies was but one of the topics of interest [Côt00a, Smi03, Mak03]. Reaching these collision energies was apparently straight forward as ultracold atoms should sympathetically cool ions via elastic collisions [Mak03, Kry11]. Using already established tools from ultracold atoms and single ion experiments one could investigate atom-ion physics in regimes that weren't accessible before.

The new research field was also driven by the promise of having a different inter-particle interaction compared to what has been utilized so far with neutrals or ions only. With an underlying strong and long-range polarization potential between an atom and an ion proposals were brought up to use hybrid atom-ion systems as a testbed to study strongly correlated many-body effects [Côt02, Mas05, Goo10, Cas11] or for quantum information and simulation purposes [Doe10, Bis13]. A quantum mechanical theory of ultracold atom-ion collisions was developed, predicting Feshbach resonances [Côt00b, Idz07, Idz09, Gao10, Idz11]. These theoretical insights encouraged ongoing experimental work towards ultracold atom-ion systems. Feshbach resonances would allow a direct tunability of the inter-particle interaction, as soon as low enough collision energies have been realized experimentally.

Several hybrid atom-ion experiments were set up in the mean time and the first ones were in operation by the end of the first decade of the new millennium. Elastic collision dynamics was among the first things to be under investigation [Gri09, Zip10b, Sch10a, Haz13]. Sympathetic cooling of atomic [Zip11b, Här12, Rav12] and molecular [Rel13] ions via elastic collisions with ultracold atoms was demonstrated. Inelastic two-body collisions in form of charge transfer and molecule formation for various species combinations (see e.g. [Rel11, Hal12, Smi13, Haz15]) as well as inelastic spin changing collisions [Rat13] were explored. The observation of a rich reaction dynamics governed by state dependent inelastic channels [Hal11, Rat12, Sul12, Hal13] marked the first step towards reaction control by external fields.

The combination of neutral and charged particles trapped in one experimental setup also introduced new tools to investigate properties of each system by using the other one. Owing to the good confinement in a Paul trap, single ions were used to locally probe the density of the atomic gas [Sch10a]. Vice versa, the ultracold atomic temperatures allowed for a very sensitive calorimeter when evaluating the kinetic energy of a single ion

[Zip11b, Här13b]. For a detailed achievement overview of the young field of cold atom-ion physics I recommend to take a look at three recent review articles [Här14a, Wil15, Sia14].

This thesis contains a compilation of experiments performed over the last years, studying elastic and inelastic collision dynamics of a single ion (Ba^+ or Rb^+) immersed in an ultracold Rb atom cloud.

First, I will present experiments investigating cold reactions in the hetero-nuclear Ba^+-Rb system. Understanding available inelastic collision channels is crucial for future prospects of ultracold atom-ion experiments. Potentially unwanted reactions will naturally limit viable experimental times and hence pose restrictions on accessible interaction regimes. Most theoretical and experimental studies have been dealing with two-body reactions so far. This approach is given by the fact that many atom-ion experiments operate magneto-optical traps (MOT) which can only prepare relatively low atomic densities compared to magnetic or dipole traps and make many-body channels seem unlikely. However, we find that three-body reactions already dominate over two-body ones at atomic densities down to 10^{-11} cm^{-3} [Krü16a] once collision energies are in the low mK regime. Then we investigate the energy scaling of inelastic ternary collisions between an ion and two atoms. A power-law scaling of the three-body rate coefficient is predicted by theory. We find agreement with the experiment if we include the ion's kinetic energy distribution that we access numerically [Krü16b].

The next study elaborates on the very first observation of ternary reactions in a hybrid cold atom-ion setup. Immersing a single Rb^+ ion into ultracold Rb atoms with sufficiently reduced excess micromotion we observe three-body atom-atom-ion recombination. These reactions are signaled by the creation of highly energetic Rb^+ ions during the atom-ion interaction [Här12].

I will also showcase novel techniques to investigate the atom and the ion system by using the respective other one which were developed by us over the course of the last years.

In order to reduce the total ion kinetic energy in a Paul trap one has to compensate the ion's excess micromotion. This is routinely being done by analyzing the ion's fluorescence. By observing collision energy dependent elastic atom-ion collisions in an ultracold atom cloud we directly infer the ion's micromotion energy.This way we can perform atom-ion experiments with optically dark Rb^+ ions and good excess micromotion [Här13b].

Without the need of visible laser light for micromotion compensation we are able to investigate the evolution of quasi-static stray electric fields in a Paul trap over a period of several months [Här14b].

The last study I will present is targeted at neutral Rb only. There, we spectroscopically

access the molecular state distribution of Rb$_2$ molecules formed in neutral three-body recombination by state-selective ionization of these molecules. Trapping and subsequent detection of these ions is being done with our Paul trap, which has the role of a very sensitive single ion detector in these measurements[Här13c].

The remainder of the introduction is meant to provide some basics about this young research field of (ultra-)cold atom-ion physics. The polarization potential between an atom and an ion is presented first. Next, a recipe on how to realize hybrid atom-ion experiments is sketched, including the so-far encountered obstacles concerning ultracold collision energies. Then I will give a schematic overview of the hybrid atom-ion trap in Ulm. At the end, an outline of the thesis is given accompanied by a list of publications that resulted from this work and my .

1.1 The polarization potential

The electric field of a charge gives rise to the strong and long-range r^{-1} Coulomb potential, characterizing the repulsive interaction between ions with the same charge. The interaction between polarizable neutral atoms is governed by induced dipole moments which result in a short-range r^{-6} and (mostly) attractive Van-der Waals potential. The particles' internal spin structure is only notable if they can approach each other close enough for their spins to interact. With different range characteristics of the two potentials spin orientations become irrelevant for interacting ions but detrimental when neutral atoms collide. The atom-ion polarization potential represents an intermediate case allowing for both long-range interactions and an internal spin state dependency.

Having atom and ion separated by a distance r, the ion's electric field $E(r) = \frac{e}{4\pi\epsilon_0 r^2}$, with the elementary charge e and the vacuum permittivity ϵ_0, induces a dipole $p(r) = 4\pi\epsilon_0\alpha E(r)$ given by the atoms polarizability α. This induced dipole within the ion's electric field leads to the polarization potential

$$V(r) = -\frac{1}{2}p(r)E(r) = -\frac{1}{2}\frac{C_4}{r^4},$$

with the coefficient $C_4 = \frac{\alpha e^2}{4\pi\epsilon_0}$.

For the description of a collision process in a radial symmetric potential it is convenient to employ to spherical coordinates in the center-of-mass reference frame. In addition to the interaction potential a centrifugal energy appears, introducing an effective radial potential which depends on the angular momentum. Considering quantum mechanical scattering,

this angular momentum is quantized, giving rise to specific potentials for each angular momentum quantum number l. This approach is known as the partial wave expansion, allowing the total collision cross section to be separated into the independent contributions of each partial wave with its angular momentum l. By equating the interaction potential $\frac{C_4}{2r^4}$ with the centrifugal energy $\frac{\hbar^2}{2\mu r^2}$ one defines a length scale $R^* = \sqrt{\frac{\mu C_4}{\hbar^2}}$ and the associated energy $E^* = \frac{\hbar^2}{2\mu R^{*2}}$ which are characteristic for the interaction potential. E^* is related to the lowest centrifugal barrier, implying that at a collision energy on the order of E^* all partial waves but the $l = 0$ wave , the s-wave, are reflected off their respective centrifugal barrier. In other words, the s-wave completely defines the collision process making a quantum mechanical treatment essential. The *ultracold* regime directly refers to s-wave collisions. With increasing number of contributing partial waves the collision can then again be described classically. In general low collision energies combined with a low reduced mass and short-range interactions push towards the ultracold regime.

For our system of interest Ba$^+$-Rb, $E^* = 52$nK, while for neutral Rb-Rb $E^*_{\mathrm{RbRb}} = 292\mu$K. Consequently, multiple partial waves can be relevant for Ba$^+$-Rb at collision energies where neutral Rb-Rb is already in the s-wave regime. This makes atom-ion collisions somewhat peculiar as a classical description can be fully sufficient despite having collision energies in the low mK range. Looking at the typical length scales, being $R^* = 295$ nm and $R^*_{\mathrm{RbRb}} \sim 4$ nm, one can see a difference by almost 2 orders of magnitude. This comparison suggests that atom-ion systems can be used as a promising testbed for strongly correlated many-body physics as the underlying long-range potential favors many-body interactions naturally. This characteristic feature of ultracold atom-ion systems combined with the already demonstrated superb experimental control of the individual sub-systems resulted in several proposals:

- ultracold charge transport was investigated in [Côt00a] showing a sharp increase charge mobility at ultracold temperatures. The increase was attributed to a charge hopping mechanism which induces an insulator-conductor transition in the ultracold charged gas.

- mesoscopic molecular ions were predicted in [Côt02] where hundreds of atoms would be trapped in the long-range polarization potential of a single ion. Multiple atoms from a BEC would inelastically collide with the ion and in the limit of nK collision energies preferably populate the most weakly bound states. .

- polaron type physics was proposed where a charged impurity in an ultracold gas modifies the surrounding atom density [Mas05, Goo10]. Furthermore, reaching the

strong-coupling regime which is required for so-called Fröhlich polaron seemed feasible with an ionic impurity due to the underlying long-range interaction potential [Cas11]

- Feshbach resonances in atom-ion systems were theoretically examined in Ref. [Idz09] and [Idz11]. This work covered the atom-ion interaction tunability via an external magnetic field in s-wave collisions known from ultracold *neutral* gases

- quantum information processing [Doe10] and simulation [Bis13] proposals were brought up where the long-range polarization potential in combination with separately controllable confinement allows to engineer the desired quantum system.

1.2   Realizing (ultra-)cold atom-ion experiments

About a dozen laboratories world wide are performing cold atom-ion experiments and a few more are being set-up. In contrast with previous experiments with beam/target or drift tube both neutral and charged particles are trapped at the same time, promising very low collision energies. Basically all cold atom-ion experiments start with laser cooled atoms, most also use laser cooled ions. A large group of laser cool-able species are represented by alkali-earth and alkali-metal elements. Commonly, the former is chosen for neutral atoms and the latter for charged ions due to the simple hydrogen-like electronic configuration with a single valence electron. These first two groups of the periodic table alone allow for a plethora of species atom-ion combinations that can be experimentally investigated.

For our experiments a combination of ^{138}Ba$^+$ and ^{87}Rb was chosen. This system allows for many elastic collisions before an inelastic collision takes place due to a strong suppression of charge transfer (see section 1.2.3). Looking at the proposals mentioned in the last section gaining experimental access to the regime of ultracold atom-ion collisions seems like a very promising short-term goal. The term "ultracold" typically defines a range of energies where collisions can be described quantum mechanically and more specifically by a single partial wave, the s-wave. Several groups, including ours, are working towards atom-ion s-wave collisions which so far have not been demonstrated yet. The required low collision energy, due to the small characteristic energy E^*, is just one of the reasons why this turned out to be non-trivial. Several obstacles have been identified by now that have to be overcome, which I will describe in this section after sketching how to realize a hybrid atom-ion experiment.

1.2.1   Hybrid atom-ion trapping

There is a multitude of different trap types being used as workhorses in both communities of ultracold neutral atoms and charged ions. The associated technology is well known by now and can in principle be directly employed for atom-ion experiments. The only remaining challenge when designing a hybrid atom-ion trap, is the spacial combination of the atom and the ion trap, allowing for overlapping trap volumes of both traps. In the following, i will briefly describe different viable atom and ion trapping methods. This list is by no means complete as it only mirrors the so far utilized traps in atom-ion experiments.

Atom traps
Currently, three distinct types of atom traps are in use. Next to their respective up- and downsides they vary in their achievable atomic densities and temperatures, mostly set by the experimentally applicable cooling mechanisms in these traps.

- A magneto-optical trap (MOT) induces atom confinement through a position dependent photon scattering force, introduced by a quadrupolar magnetic field and 3 orthogonal pairs of counter-propagating laser cooling beams. Given the continuous scattering of photons a standard MOT is inherently limited to Doppler temperatures. Even though sub-doppler cooling techniques are available and readily being used, the resulting atom temperatures and densities are in general not sufficient to produce degenerate quantum gases. Hence, typical ultracold atom experiments use a MOT as an initial stage to trap and cool atoms before transferring the sample into a different trap for additional cooling. So far, many atom-ion experiments do not aim for ultracold degenerate gases, allowing them to omit the additional complexity and work with a MOT only.

- Magnetic traps utilize a low field seeking Zeeman sub-level and a quadrupole magnetic field created by a coil pair in anti-Helmholtz configuration. By adding an extra coil, the Ioffe coil, this trap is then extended to a quadrupole-Ioffe configuration (QUIC) [Ess98]. This eliminates the zero field crossing of the pure quadrupole field, which leads to Majorana losses when approaching low temperatures. Creation of degenerate gases is then routinely done via forced RF evaporative cooling down to the nK regime. Another noteworthy advantage over a MOT is that the confinement is conservative and the trapped atoms are in their electronic ground state only as no photon are being scattered. However it is non-trivial to combine the three magnetic coils with the electrodes needed for a Paul trap. So far only one atom-ion experiment

(Köhl group [Zip11a]) has used a magnetic QUIC trap to store ultracold atoms.

- A dipole trap relies on the AC-stark shift induced by far-off resonant laser [Gri00]. The resulting potential is conservative, however photon heating is present due to off-resonant scattering. This heating can be lowered sufficiently by increasing the detuning and total power at the same time. The simplest configurations use a single focused laser beam making this approach dramatically more flexible than magnetic traps. Evaporative cooling down to nK temperatures is also feasible in this trap type making dipole traps a popular choice to prepare degenerate gases. Due to the general versatility it integrates very well with a Paul trap as it only requires optical access.

Ion traps

The history of ion trapping is exceeds that for neutral trapping by several decades. Today, single ion trapping is done routinely in many laboratories around the world. Out of the two main trap types only the Paul trap is being used for atom-ion experiments. The Penning trap does not seem appealing mainly because of the huge magnetic fields that are required for stable ion trapping. Generating these field strengths requires a trap design that usually limits optical access heavily and therefore the compatibility with atom dipole traps. Laser cooling of ions in Penning traps is also non-trivial due to the involved motional modes [Tho00]. Additional considerations have to be made when trying to introduce ultracold atoms into the enormous magnetic fields of a Penning trap.

Paul traps, on the other hand, introduce barely any effects [Sch11] on the neutral atoms as they work with electric fields only. The needed electrodes can be designed to support very generous optical access to the trapping region, required for ion cooling and detection. The working principle relies on an electric quadrupole field oscillating at radio frequencies (RF) because static electrical fields cannot create a local potential minimum and satisfy the Laplace equation at the same time. A very common design is the linear Paul trap with 2 dimensional RF confinement and DC confinement along the third dimension. Figure 1.1 depicts the Paul trap used in our experiment in Ulm and shows all electrodes, which create the trapping fields as well as additional so-called compensation electrodes, which are used to create static offset fields. I will refrain from a detailed derivation of the trapping mechanism of a Paul trap, as it can be found in many text books (see e.g. [Lei03]) and the reader is most likely familiar with it already. In first order, the resulting ion trajectory can be decomposed into a slow harmonic oscillation within the so-called pseudo-potential, modified with a fast micromotion, which follows the local RF field at the position of the
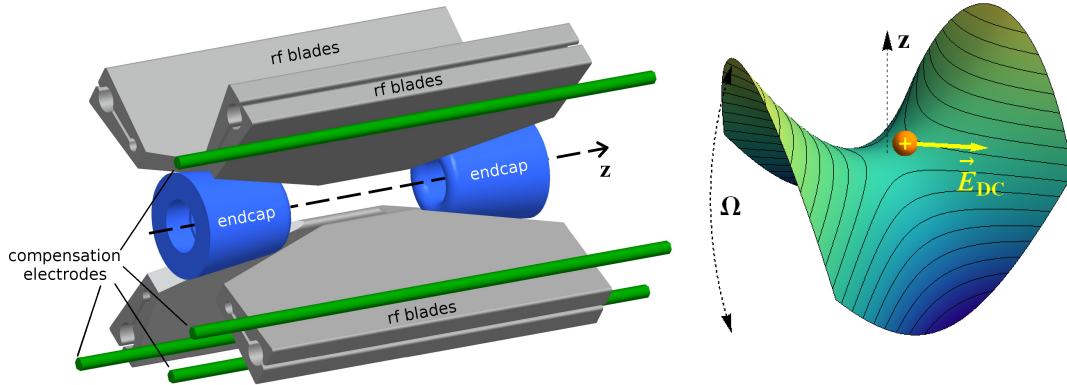
Figure 1.1: Left: Linear Paul trap used in our atom-ion apparatus in Ulm. Two dimensional confinement in the radial plane is created by applying an sinusoidal voltage at a frequency Ω to the RF blades with a phase shift of π between neighboring blades. Static voltages are applied to the endcaps and provide axial confinement in the third dimension. Two pairs of compensation electrodes can be used to create additional static or oscillating electric forces in the radial plane. **Right**: The resulting radial quadrupole potential oscillates at a frequency Ω and gives rise to a trapped ion trajectory (upper trajectory Fig. 1.2). The RF node can be found along the z-axis of a linear Paul trap. Electrical stray fields $\vec{E}_{DC}$ shift the trap center away from the RF node, inducing excess micromotion (lower trajectory Fig. 1.2).

ion (upper trajectory in Fig. 1.2).
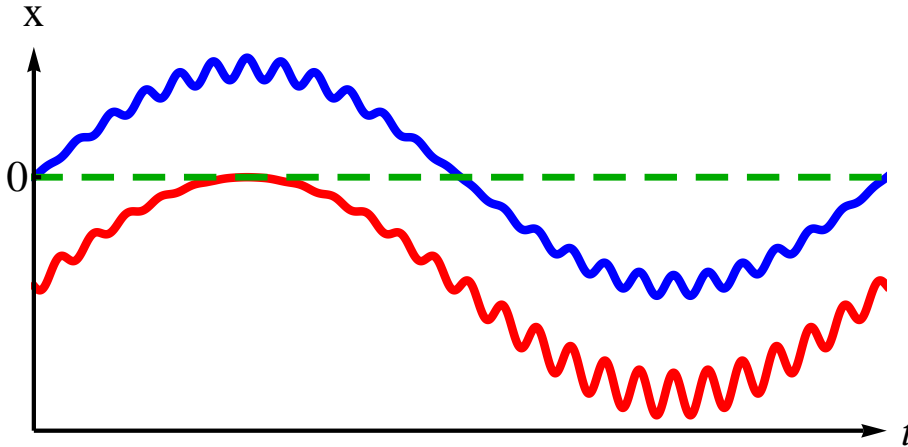
Figure 1.2: Upper trajectory: The ion trajectory can be decomposed in a slow harmonic oscillation modified with a fast micromotion. The micromotion is proportional to the local RF field amplitude, which increases linearly with distance from the RF node. **Lower trajectory**: Additional static electrical fields create a constant force, shifting the trap center away from the RF field node, inducing excess micromotion.

A very important aspect is that the dynamic nature of a Paul trap does not create a conservative potential. The resulting driven micromotion modes are inherently coupled to an additional energy reservoir given by the RF fields. This does not have to be a

problem because this driven motion is coherent and not thermal. Also, for a single ion in a perfect Paul trap, there is no coupling between the secular modes of the harmonic pseudo potential and the micromotion modes. This allows laser cooling of the secular modes down to Doppler temperatures in a Paul trap. Even cooling to the quantum mechanical ground state of the harmonic pseudo-potential is possible without being directly affected by the micromotion heating. This situation changes drastically if motional modes are coupled, as is the case in atom-ion collisions.

Micromotion cannot be cooled directly due to its driven nature. Its amplitude can however be minimized as it is directly proportional to the local RF electric field amplitude. Using on a quadrupolar RF field means that only the saddle point in the center supports zero RF amplitude, which then increases linearly with the distance from the center. Direct cooling of the secular motion reduces the ion orbit and hence possible micromotion. In real world Paul traps unwanted static stray electrical fields $\vec{E}_{DC}$ can apply additional forces on the ion and shift the center-of-mass of the secular motion out of saddle point (right panel in Fig. 1.1 and lower trajectory in Fig. 1.2), inducing the so-called excess micromotion. This can only be compensated by applying external electric field fields which aim to cancel the stray fields [Ber98].

1.2.2 Sympathetic cooling

Sympathetic cooling in principle only requires a buffer gas acting as a refrigerator. Using a refrigerator for cooling can not only be conceptually simpler compared to more complex laser cooling techniques, like the mentioned ground-state cooling but also applicable to a wider range of species. This is because laser cooling is limited to particles where closed cycling transitions are available. The concept of sympathetic cooling on the other hand is applicable even without exact knowledge of available internal states. The momentum transfer in elastic collisions between cold buffer gas atoms and the hot target, in our case a single ion, facilitate a redistribution of kinetic energy until a equilibrium temperature is reached. The only requirement is that many elastic collisions can take place before an inelastic collision occurs. Inelastic collisions can introduce heating via the released energy when internal states of the particles are changed, i.e. spin flips, and even change the species in a chemical reaction. Charge transfer of the type $A^+ + B \rightarrow A + B^+$ or molecular formation $A^+ + B \rightarrow AB^+$ have been the most investigated inelastic processes in cold atom-ion systems so far. Historically, chemically inert buffer gases, like noble gases, are used for sympathetic cooling in order to suppress inelastic collisions. A classic example is Helium buffer gas cooling down to the K range which can be extended down to tens of

mK in a helium dilution cryostat. Using noble gases for experiments in the emerging cold atom-ion field however is not a viable option yet as the achievable temperatures cannot compete with ultracold atoms. Ultracold atomic gases constitute the perfect buffer gas in terms of temperature as they can be in the low nK regime. They are however far from perfect regarding reactivity as one typically works with alkali atoms. Therefore, careful choice of the atom and ion species is necessary as sympathetic cooling might only be viable if inelastic collisions or reactions occur very infrequently.

The simplicity of sympathetic cooling can however be perturbed by additional complications which arise due to the utilized trapping techniques. The non-conservative ion trapping in a Paul trap introduces driven micromotion modes which depict an energy reservoir that is accessible through elastic collisions.

Micromotion and elastic collisions

Thermalization of a single ion in contact with an ultracold atomic bath would be the desired scenario to reach ultracold collision energies. This however does not occur in current generation hybrid atom-ion experiments. The sole reason for this phenomenon is the dynamic ion trapping in a Paul trap. The driven micromotion, can transfer energy into the secular motion via elastic atom-ion collisions. This can be understood as a phase jump of the ion's secular oscillation, depending not only on the momentum exchange between atom and ion but also on the exact phase of the micromotion at the time of the atom-ion collision. An increase or decrease of the secular oscillation amplitude is possible in such a scenario (see Fig. 1.3). The non-conservative trapping potential in combination with collisions can effectively introduces additional energy into the system also known as micromotion heating. Here, the resulting equilibrium energies can be far beyond the temperatures of the ultracold atomic gas used for sympathetic cooling.

This micromotion heating above the buffer gas temperature was known back to early experiments aiming at sympathetic cooling of ions [Maj68]. Further investigations of this process involved numeric simulations of the atom-ion collision dynamics in a Paul trap with two important results [DeV09]. First, the micromotion heating was recovered in simulations in form of the resulting ion kinetic energy distribution. Instead of a Maxwell-Boltzmann distribution a Tsallis distribution would arise, featuring a power law E_{ion}^{α} tail towards high ion energies. High ion energies and therefore orbits were probable, resulting in ion loss in experiments. Second, the exponent α was depending mostly on the ratio $\frac{m_a}{m_i}$, with the atom mass m_a and the ion mass m_i, as this determines how drastic the ion's momentum change can be in a single collision. In the limit $\frac{m_a}{m_i} << 1$ of light atoms
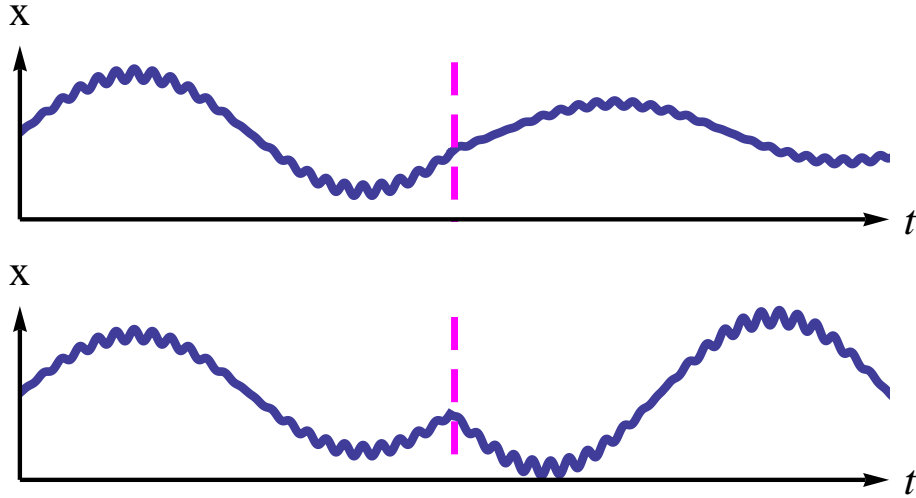
Figure 1.3: One dimensional ion trajectory in a Paul trap over time, colliding with an atom
at rest (dashed line). The elastic collision will transfer momentum from the ion
onto the atom, reducing the ion's instant velocity. As the micromotion is driven,
its micromotion velocity will be reinstated after the collision, effectively coupling
the secular oscillation with the micromotion. This way, the final ion velocity is not
only determined by momentum transfer during the collision. Depending on the exact
micromotion phase at the time of the collision the secular energy can be decreased
(upper panel) or increased (lower panel).

and heavy ions one would recover a Maxwell-Boltzmann distribution. As the ratio $\frac{m_a}{m_i}$
approaches 1 the energy distributions would form power law tails towards high energies.
Finally, the energy distributions would diverge above $\frac{m_a}{m_i} \approx 1.55$, creating time-dependent
energy distributions, hence, runaway micromotion heating in experiments. Further theo-
retical studies of this phenomenon have been undertaken over the course of the last years
incorporating excess micromotion [Zip11b], extending to higher $\frac{m_a}{m_i}$ ratios [Höl16], analyt-
ical derivations of the power law behavior [Che14] and even proposed fundamental limits
of sympathetic cooling in a Paul trap [Cet12, Kry15].

In the parameter range of our experiment an equilibrium energy distribution is reached
which currently is mainly defined by ion's excess micromotion. In order to reduce atom-ion
collision energies, we have to lower the excess micromotion energy by compensating stray
electric fields through applied voltages on the compensation electrodes. Once the excess
micromotion is minimized we can increase it in a controlled way allowing us to tune the
collision energy in the experiment. This way we can determine the energy dependence of
cross sections of different processes that are of interest.

Having reduced the excess micromotion far enough other energy sources can come into play.
At some point the atomic gas temperature will set a bound, but even before that predicted

fundamental limits should become important. In the absence of any static electric fields, hence no displacement of the ion from the RF node, the atom-ion interaction potential itself can displace the ion during a collision, allowing work to be done on the particles by the oscillating RF field. The quantum mechanical calculation of this effect predicts steady state energies of the ion corresponding to the sum of the trapping frequencies of the Paul trap [Kry15]. For typical trap frequencies in our setup: $\sum \omega_i \approx 2\pi \times 200\,\mathrm{kHz}$ which equals energies of $\sim 10\,\mu\mathrm{K} \times k_\mathrm{B}$. As the s-wave barrier depends on the reduced atom-ion mass, this energy can be sufficiently low for species combinations like Yb^+-Li. For our species combination, Ba^+-Rb, a fundamental limit would imply that switching to another ion trapping technique is required in order to reach s-wave collision energies. A possibly viable option might be ion trapping in an optical dipole trap, which is a new research field on its own as the first demonstration was only a few years ago [Sch10b].

1.2.3 Inelastic processes

A thorough investigation of available inelastic processes in cold atom-ion collisions is vital for the future development of the whole field. The example of sympathetic cooling already showcases this as it can only be feasible (including down to s-wave collision energies) if inelastic processes do not occur frequently. Looking at a broader context, this applies to any kind of atom-ion interaction that is mediated by elastic collisions. This is evident when looking at many-body proposals like the mesoscopic molecular ion [Côt02] or polaron formation [Cas11]. It is highly improbable that the formed many-body state will be the absolute ground state of the combined system as only the long range interaction is being considered in the proposals. Any kind of transition to a lower lying state would release energy, potentially destroying the many-body system. This implies that the time scales of the available inelastic channels would set a natural time limit for experiments with these systems.

Two-body inelastic collisions

In general, a collision is termed inelastic when not only momentum is being exchanged but also a change of the internal states of the particles occurs. A prominent example, known from ultracold atoms, are spin flips or in general, hyperfine transitions. If spin exchange during a collision between the particles is possible, i.e. the spin configuration is not stretched, the associated energy can be accessed, providing a loss and/or heating mechanism. This process can also occur in cold atom-ion collisions and has been investigated with $^{174}\mathrm{Yb}^+$-$^{87}\mathrm{Rb}$ [Rat13].
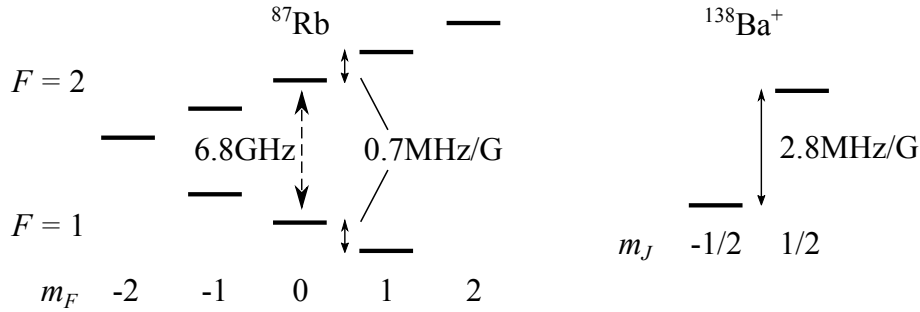
Figure 1.4: Illustrated are the ground states of ^{87}Rb and ^{138}Ba$^+$. This includes the Hyperfine structure for ^{87}Rb and the Zeeman-splittings of both systems. Spin exchange collisions between the two systems can potentially release energy. Preparing spin stretched configurations could suppress this process if no spin relaxation occurs. Preparation in the lowest available states of both systems should in principle negate this type of inelastic collisions.

The relevant level structure of our ^{138}Ba$^+$-^{87}Rb system is equivalent to ^{174}Yb$^+$-^{87}Rb(see Fig. 1.4), suggesting that the observed spin exchange and relaxation should occur here as well. Preparation of ^{87}Rb atoms in the $F = 2$ hyperfine state allows for collisional transitions to the lower lying $F = 1$ state, which can release $h \times 6.8\,\text{GHz} \cong k_\text{B} \times 325\,\text{mK}$ of energy. Even when working with the $F = 1$ manifold one has to carefully chose the m_F Zeeman substates. As a magnetic bias field of a few Gauss is basically always present in experiments, inducing a Zeeman-splitting of $0.7\,\text{MHz/G}$ on the m_F states. For a typical offset field of $\sim 2\,\text{G}$ and spin polarized ^{87}Rb atoms in $F = 1\ m_F = -1$ (a magnetic trappable state) this corresponds to $h \times 2.8\,\text{MHz} \cong k_\text{B} \times 130\,\mu\text{K}$ of energy that can potentially being accessed via collisions with the ion. The same line of arguments applies to the state preparation of the ion where the Zeeman-splitting of the two ground states comes into play. Negating this type of inelastic collisions is feasible by preparing both systems in their respective absolute lowest energy hyperfine and/or Zeeman state.

Chemical reactions however can still occur because the combined atom-ion system does not have to be in it's electronic ground state even if both systems on their own are in their respective ground states. The Ba$^+$-Rb system is an example of this behavior. Here, the initially prepared Ba$^+$-Rb is energetically roughly $\sim 1\text{eV}$ above the electronic configuration of an ionized Rb$^+$ and a neutral Ba [Hal13] (see Fig. 1.5). Charge transfer and molecule formation are a consequence if the system can transition between these two electronic configurations. In this specific system the transition is only possible via the emission of a photon, as in radiative charge transfer, which reduces the associated probability for these processes and allows for $\sim 10^5$ elastic collisions before one charge transfer collision occurs [Kry11].
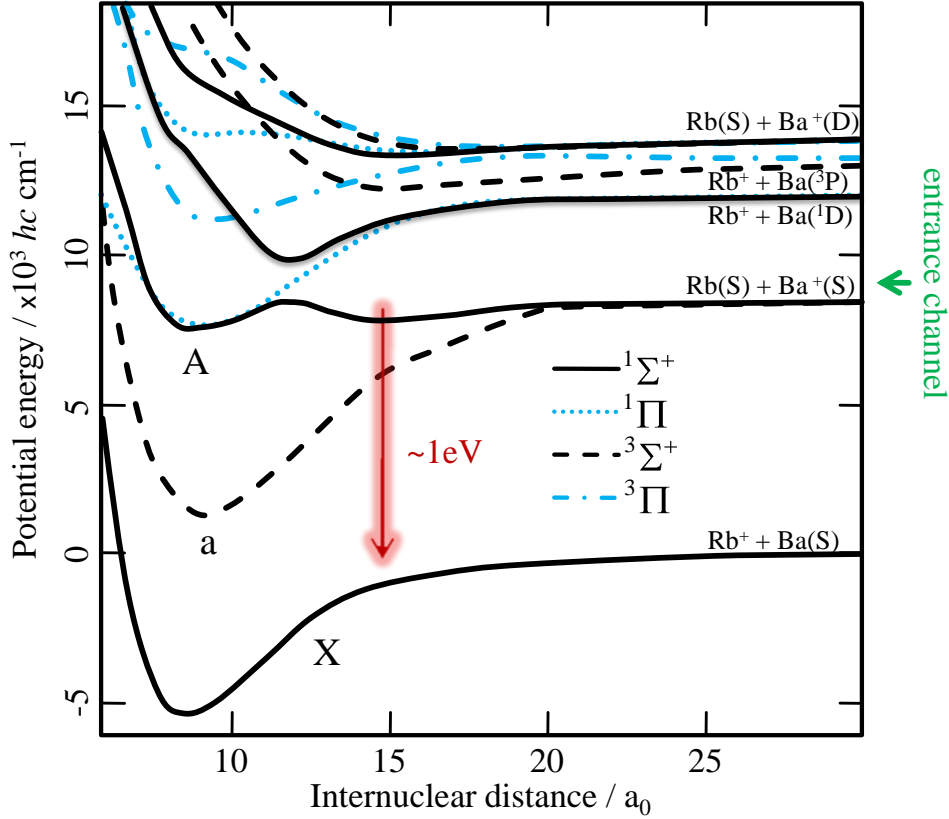
Figure 1.5: Molecular potential curves for the Ba^+-Rb system showing the collisional entrance channel (green arrow) together with the lower lying ground state and multiple excited states. Transitions to the lower potential, asymptotically connected to the electronic configuration Ba-Rb^+, is only possible via a photon emission. The plethora of low lying upper potentials can become relevant for light-assisted collisions. Here, only the lowest asymptotes are shown. Even long-wavelength infrared dipole traps at 1064 nm or 1550 nm could in principle become relevant as they can connect the entrance channel to the upper repulsive potential curves. Potentials taken from [Hal13].

The details of possible charge transfer reactions will depend on the specific species combination. For example, mixtures like Ca^+ + Rb also feature non-radiative charge transfer as non-adiabatic crossings of the molecular potential curves exist, allowing to transition from the entrance channel to an energetically lower lying electronic configuration of Ca + Rb^+ during a collision [Hal11]. Avoiding charge transfer all together is possible by choosing a system where the entrance channel also represents the electronic ground state of the combined system. This is the case in a homo-nuclear atom-ion mixture like Yb^+-Yb, Rb^+-Rb, Sr^+-Sr or Ca^+-Ca. Hetero-nuclear combinations which satisfy this condition also exist, with Ba^+-Li being the only alkali atom alkali-metal ion mixture. A recent study proposed the use of Chromium atoms in combination with $Ca^+/Sr^+/Ba^+/Yb^+$ ions to eliminate charge transfer [Tom15].

Considering that inelastic atom-ion collisions are a research field of their own, many experimental and theoretical studies have been focusing on this topic. The insights have proven to be valuable to understand and suppress inelastic channels for future experiments. However, most of this research was aimed at processes based on two-body collisions, motivated by the typically low densities used in atom-ion experiments so far. Three-body inelastic collisions are known from ultracold atoms, especially towards Bose-Einstein condensation at high densities. Hence, in ultracold atom-ion systems, it is reasonable to expect ternary collisions as well with increasing atomic densities.

Many-body inelastic collisions

One of the fundamental reasons to be interested in cold atom-ion systems is the underlying r^{-4} polarization potential, which promises to be strong and long-range compared to the r^{-6} Van-der-Waals interaction in neutral atoms. The strong interaction favors many-body phenomena, making experimental and theoretical investigation of atom-ion systems attractive. But a many-body system inherently introduces bound states at lower energies, potentially allowing for new inelastic processes. Here, a prime example is three-body recombination which describes molecule formation in a ternary collision. Binary collisions on their own cannot facilitate molecule formation as a single product particle would violate the laws of energy and momentum conservation. This restriction is lifted only in the presence of a third particle, be it an extra atom or photon. Three-body recombination itself is known from ultracold neutrals [Esr99] as well as from plasmas and charged gases in general, including species relevant for interstellar chemistry (e.g. [Krs03] or [Pla12]). However, the first observation of three-body reactions in the new field of cold atom-ion experiments were reported only very recently (see chapter 2, 3 and 4). Even though three-body recombination can be considered as an undesired inelastic process, as it was the case in the initial attempts to Bose-Einstein condense spin-polarized hydrogen [Sil92], it signals the onset of many-body interactions, which is one of the goals in present day cold atom-ion experiments.

Light assisted processes

The presence of light during atom-ion collisions has to be considered as well when designing experiments. This goes beyond the obvious problems when working with a constantly laser cooled atom-ion system, that utilizes a MOT and/or a Coulomb crystal. In both these cases, near-resonant cooling light has to be present during the experiments. This allows for photo-association and collisions in excited states which introduces vastly different reaction dynamics [Hal11].

But even off-resonant light can potentially influence the collision dynamics. Laser light that is off-resonant for both species on their own, might still drive transitions to excited potential curves of the combined system. A typical scenario is the use of an optical dipole trap at 1064 nm or 1550 nm to store the ultracold atoms. Similar to the necessity of constant laser cooling in a MOT this light is needed for trapping and is therefore always present. Looking at the Ba^+-Rb system, there are several low lying asymptotes above the entrance channel, which could possibly be accessed with infrared photons (Fig. 1.5). Here the use of 1064 nm light has not turned out to be problematic so far, but its role should be considered as soon as many-body collisions come into play. The resulting excited potential energy surfaces of Ba^+-N Rb ($N \geq 2$) might in principle support transitions with 1064 nm photons.

Things get even more involved if one thinks of using light at smaller wavelengths, i.e. for ion dipole trapping. The demonstrated ion dipole traps have relied on UV (280 nm for Mg^+ [Sch10b]) and visible (532 nm for Ba^+ [Hub14, Lam16]) laser light for trapping. This photon energy will very likely be able to photo-excite a colliding atom-ion pair due to the densely packed excited molecular potentials one can expect with increasing energy.

1.3 The atom-ion trap in Ulm

Our experimental setup in Ulm is one of the first two hybrid atom-ion traps that can prepare degenerate atomic samples. Being in operation since 2009 a thorough description of the machine and operation principle already exist [Sch12, Sch11, Här13a]. Hence, I will limit myself only on briefly describing the core of the whole lab, the vacuum system that contains the hybrid atom-ion trap (see Fig. 1.6).

The vacuum system consists of three connected chambers named after their respective roles (lower left in Fig. 1.6). Rb atoms are trapped in a MOT loaded from background vapor then magnetically transported into a chamber with a low enough pressure for evaporative cooling down to Bose-Einstein condensation. After an optical transport into the center of the Paul trap, Rb atoms are loaded in a crossed dipole trap (upper right in Fig. 1.6). The Paul trap can store single ions, for our current experiments both Ba^+ and Rb^+ ions are used routinely. During the final preparation stage we overlap the two trap centers and immerse the ion into a cloud of ultracold atoms (lower right in Fig. 1.6).

During my time in the lab most changes on the hardware were devoted to optimizing the short and long term stability of the neutral atom production cycle. Ensuring stable operation conditions not only reduce shot-to-shot atom number fluctuations but also
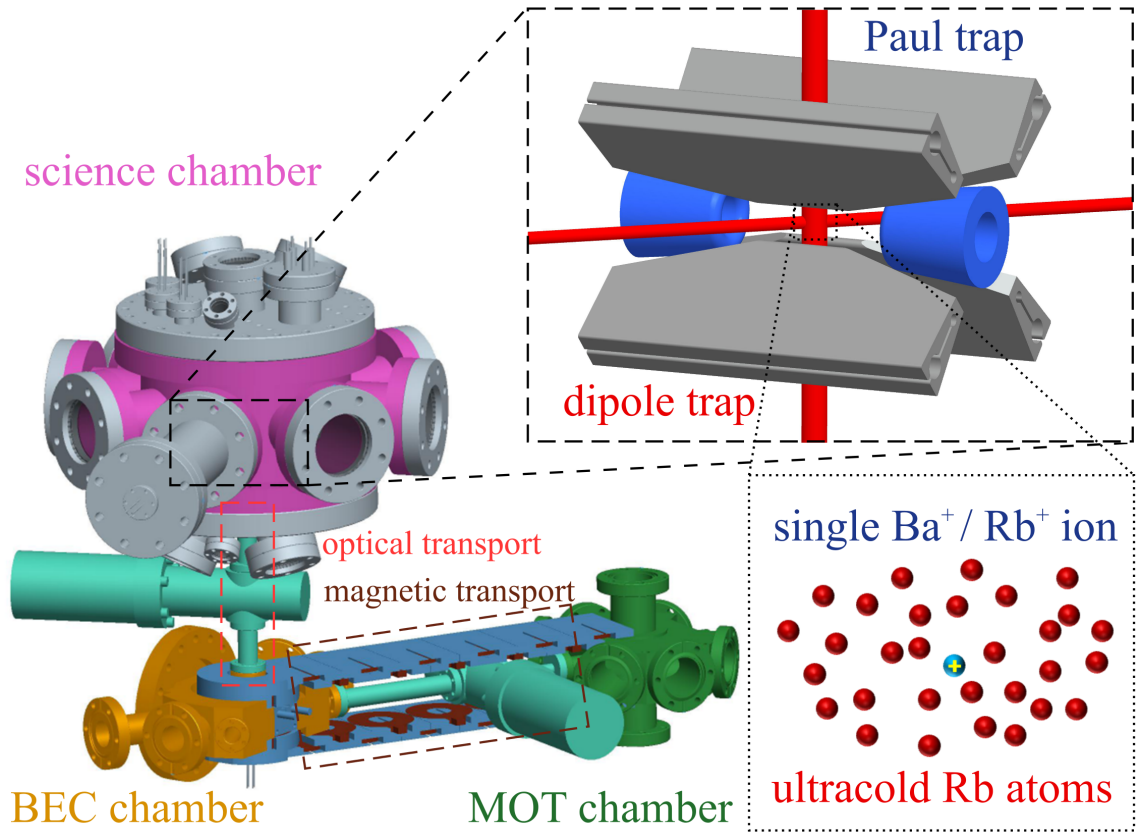
Figure 1.6: Lower Left The vacuum system consisting of a MOT, BEC and science chamber together with the magnetic and optical transport sections for the Rb atoms. **Upper right** The heart of the experimental setup, the combined atom-ion trap. Two laser beams at 1064 nm form a crossed dipole trap within the trapping volume of a linear Paul trap. **Lower right** Spatially overlapping trap centers allow the immersion of single ions (typically Ba^+ or Rb^+) into ultracold Rb atom clouds.

dramatically reduces the required maintenance down time. The undertaken efforts are self-evident and only require lab time to implement solutions for reoccurring problems. An important example is the need for regular alignment of beams that are directly pointed at the atoms/ions. One solution is simply to switch from free space to fiber delivery of the laser light and to reduce the remaining beam path towards the atoms/ions as much as possible. In combination with the beam paths upgrades with stable low drift opto-mechanics and laboratory temperature stability improvements to $\pm 0.1\,\mathrm{K}$ we could achieve completely maintenance free operation of the whole setup for multiple weeks at a time.

One noteworthy upgrade was switching from a magnetic QUIC trap to a mixed magnetic and optical dipole trap for the initial evaporative cooling [Lin09]. The stability of our QUIC trap is in general excellent, but only if it is being cycled constantly. This cycling has to be interrupted every now and then when we need to prepare the ion system, i.e. reloading a new Ba^+ after a reaction. Irregular spaced atom production cycles however

introduce a changing thermal load on the coils and create significant drifts in the final trap geometry. Especially at low temperatures, when aiming for BEC production, huge atom number fluctuations are the consequence. The atom number stability in the mixed magnetic and optical trap however does not have to suffer from irregular cycling. After an initial evaporation in the magnetic quadrupole trap the trapping potential is solely dictated by the dipole trap which can provide excellent atom number stability if set up correctly.

A great deal of PhD student hours were spent on upgrading the experiment control software. Many new features were added with the implementation of a closed loop controlled experimental sequence. Measured signals, usually taken by the cameras responsible for atom or ion imaging, could now directly set the parameters for the next sequence. In combination with a black box optimization algorithm [Aud09, Le 11] we could increase atom number efficiencies in a multi-dimensional parameter space without the necessity of scanning every parameter by hand. Closed loop optimization is in particular helpful with non-trivial problems like defining a transport function for the magnetic and optical transport stages of our atom preparation procedure. Many small improvements over the course of the last years amount to a reduction of the cycle time for atom preparation from the initial $\sim 40\,\text{s}$ to $\sim 8\,\text{s}$, boosting the data taking rate considerably.

Yet, the ion side of our setup profited the most from the software upgrades, making fully automated handling of single Ba^+ ions possible. When studying atom-ion reactions with a single ion the observable of interest is mostly the loss of the initially prepared ion. With the ionization of a single Ba^+ being probabilistic one requires some form of back action for a deterministic preparation. In case of ion loss the current control software automatically prepares a new single Ba^+ with ionization and subsequent compensation of excess micromotion.

1.4   Outline of the thesis

This thesis is structured as follows:

Chapter 2 focuses on reactive collisions in the hetero nuclear system of Ba^+-Rb. We find both two-body charge transfer and three-body recombination to be responsible for chemical reactions. A surprising result is that ternary reactions dominate over binary ones at already moderate atomic densities and mK collision energies.

Chapter 3 studies the energy scaling of three-body recombination in the Ba^+-Rb-Rb system at mK collision energies. An energy dependent rate coefficient is measured and compared to a theoretical prediction of a power law scaling. Agreement is found when we assume that at least two different micromotion induced energy scales determine the ion energy distribution. In addition, classical trajectory calculations of the three-body problem predict the median binding energy of the formed molecules to scale with the collision energy.

Chapter 4 demonstrates three-body recombination of a single trapped Rb^+ ion with two neutral Rb atoms. The three-body reaction is identified through the resulting atom number statics, as the effective atom-ion interaction stops once large amounts of energy are released through the reaction. The three-body rate coefficient is found to be three orders of magnitude higher compared to neutral Rb recombination.

Chapter 5 presents a novel technique to minimize excess micromotion in a hybrid atom-ion trap. As opposed to established methods, no ion fluorescence is required here. Instead, the atomic cloud is used to directly infer the ion's excess micromotion energy. This method allows us to perform atom-ion experiments with optically dark Rb^+ ions and good excess micromotion compensation.

Chapter 6 investigates on the evolution of quasi-static stray electrical field in a Paul trap over a period of several months. Different sources are identified for the field drifts as they induce different time-scales and directions.

Chapter 7 reports on the first measurements of the population distribution of Rb_2 products after three-body recombination of neutral Rb. Newly formed Rb_2 are resonantly ionized in a multi-photon process and are confined in our Paul trap. This approach demonstrates how a Paul can be used as a very sensitive ion detector, allowing precision molecular spectroscopy in extremely dilute gases.

Individual contributions to this thesis

Parts of this cumulative thesis originated in co-authorship with other scientists. This refers to chapters 2,3,4,5,6 and 7 which are congruent with the corresponding publications.

- chapter 2 and 3: I was crucially involved in conceiving the measurement protocol as well as data acquisition in close cooperation with the second author Amir Mohammadi and the third author Arne Härter. I conducted major parts of the data analysis and was responsible for writing the manuscript.

- chapter 5 and 6: I was substantially involved in conceiving the measurement protocol as well as data acquisition in close cooperation with the first author Arne Härter and the third author Andreas Brunner. I conducted parts of the data analysis and assisted with writing the manuscript. The first author Arne Härter has already presented the data in his thesis "Two-Body and Three-Body Dynamics in Atom-Ion Experiments".

- chapter 4 and 7: I was substantially involved in conceiving the measurement protocol as well as data acquisition in close cooperation with the first author Arne Härter. I conducted parts of the data analysis and assisted with writing the manuscript. The first author Arne Härter has already presented a reprint of the published manuscript in his thesis "Two-Body and Three-Body Dynamics in Atom-Ion Experiments".

1.5   Publications

The following articles (in chronological order) were published during the course of this thesis:

- A. Härter, A. Krükow, A. Brunner, W. Schnitzler, S. Schmid, and J. Hecker Denschlag,
  "Single Ion as a Three-Body Reaction Center in an Ultracold Atomic Gas",
  Physical Review Letters **109**, 123201 (2012)
  (congruent with chapter 4)

- A. Härter, A. Krükow, M. Deiß, B. Drews, E. Tiemann and J. Hecker Denschlag,
  "Shedding Light on Three-Body Recombination in an Ultracold Atomic Gas",
  Nature Physics **9**, 512-517 (2013)
  (congruent with chapter 7)

- A. Härter, A. Krükow, A. Brunner and J. Hecker Denschlag,
  "Minimization of ion micromotion using ultracold atomic probes",
  Applied Physics Letters **102**, 221115 (2013)
  (congruent with chapter 5)

- A. Härter, A. Krükow, A. Brunner and J. Hecker Denschlag,
  "Long-term drifts of stray electric fields in a Paul trap",
  Applied Physics B **114**, 275-281 (2014)
  (congruent with chapter 6)

- A. Krükow, A. Mohammadi, A. Härter and J. Hecker Denschlag,
  "Energy Scaling of Cold Atom-atom-ion Three-body Recombination",
  Physical Review Letters **116**, 193201 (2016)
  (congruent with chapter 3)

- A. Krükow, A. Mohammadi, A. Härter and J. Hecker Denschlag,
  "Reactive Two-body and Three-body Collisions of Ba^+ in an Ultracold Rb Gas",
  Physical Review A **94**, 030701 (R) (2016)
  (congruent with chapter 2)

Chapter 2

Reactive two-body and three-body collisions of Ba$^+$ in ultracold Rb

Physical Review A **94**, 030701 (R) (2016)
Rapid Communication

Artjom Krükow, Amir Mohammadi, Arne Härter and Johannes Hecker Denschlag

Institut für Quantenmaterie und Center for Integrated Quantum Science and Technology IQST, Universität Ulm, 89069 Ulm, Germany

We analyze reactive collisions of a single Ba$^+$ ion in contact with an ultracold gas of Rb atoms at low three-body collision energies of $2.2(9)$ mK$\times k_{\mathrm{B}}$. Mapping out the Ba$^+$ loss rate dependence on the Rb atom density we can discern two-body reactive collisions from three-body ones and determine both rate coefficients which are $k_2 = 3.1(6)(6) \times 10^{-13}$cm^{3}s^{-1} and $k_3 = 1.04(4)(45) \times 10^{-24}$cm^{6}s^{-1}, respectively (statistical and systematic errors in parentheses). Thus, the measured ternary recombination dominates over binary reactions even at moderate atom densities of $n \approx 10^{12}$ cm^{-3}. The results for Ba$^+$ and Rb are representative for a wide range of cold ion-atom systems and can serve as guidance for the future development of the field of hybrid atom-ion research.

2.1   Introduction

Cold atom-ion physics in hybrid traps is a young, developing field [Här14a, Sia14, Wil15], which builds on the relatively long-range r^{-4} polarization potential between an atom and an ion. In general, this potential promises large cross sections and therefore strong interactions between particles. As a consequence, a number of interesting research proposals have been brought forward ranging from sympathetic cooling down to ultracold temperatures [Kry11], to studying the physics of strongly correlated many-body systems, e.g., ultracold charge transport [Côt00a], novel many-body bound states [Côt02] and strong-coupling polarons [Cas11], quantum information processing [Doe10], and quantum simulation [Bis13]. Most of these ideas rely on interactions mediated by elastic atom-ion collisions, while inelastic collisions and chemical reactions are undesired as they represent a time limit for the suggested experiments. Therefore it is important to identify and investigate possible reactions and to eventually gain control over them. Inelastic processes can be divided up into classes such as two-body or three-body collisions. In general, binary collisions are dominant at low enough atomic densities, while ternary collisions will eventually take over with increasing density. This knowledge has been extensively applied in the field of ultracold neutral atoms by typically working with low enough atomic densities (e.g. smaller than about 10^{14}cm^{-3} for ^{87}Rb) in order to keep three-body losses negligible [Ket99]. Considering the low-density limit, theoretical predictions for cold hybrid atom-ion systems have been focusing on binary inelastic/reactive atom-ion collisions (e.g. [Côt00b, SJ15]) which were discussed as the limiting factors for proposed atom-ion experiments [Mak03, Kry11, Sul12, Tom15]. Along the same lines, measurements on atom-ion reactions in the low mK regime were, until recently, unanimously interpreted in terms of pure two-body decay [Gri09, Zip10a, Sch10a, Hal11, Smi13, Haz15].

In this Rapid Communication we show, however, that in general the decay analysis requires the simultaneous consideration of both two- and three-body reactions. Our measurements reveal that at mK temperatures inelastic three-body collisions of the ion can dominate over its two-body reactions, even at moderate atomic densities down to $3 \times 10^{11} \mathrm{cm}^{-3}$. Indeed, the main focus of this work lies on how to clearly distinguish two-body from three-body processes and extract the corresponding rate coefficients. One could in principle argue that in order to study only two-body reactions the atomic density simply needs to be lowered sufficiently. This is, however, not practical in standard set-ups with magnetic or dipole traps because the resulting reaction rate can be so small that the ion lifetime exceeds the atomic cloud lifetime. Alternatively, one could consider working with a magneto-optical trap (MOT) which allows for both, low densities and long lifetimes due to continuous loading. However, in a MOT the reaction rate measurements of the ground-state atoms are swamped beneath a background of reactions of electronically excited atoms occurring at much higher rates.

For our investigations we use a heteronuclear combination of $\mathrm{Ba}^+ + \mathrm{Rb}$, where both two-body and three-body collisions lead to reactions and hence to ion loss in the experiment. This complements a recent experiment of ours with homonuclear $\mathrm{Rb}^+ + \mathrm{Rb} + \mathrm{Rb}$ [Här12] for which reactive and inelastic two-body collisions are either forbidden or irrelevant. Furthermore, we note that in parallel to the work discussed here, we have studied the energy scaling of atom-ion three-body recombination [Krü16b].

We measure the density dependence of the reaction rate $\Gamma = k_2 n + k_3 n^2$ and extract the binary and ternary loss rate coefficients k_2 and k_3. Here, n is the peak atom density at the cloud center where the ion is located. For the analysis the evolution of $n(t)$ needs to be included, as the atom cloud is decaying during the time t due to elastic atom-ion collisions. We experimentally determine $n(t)$ by excluding experimental runs where the ion has undergone a reaction during the interaction time t in order to avoid systematic errors introduced by reactive collisions.

2.2   Experimental setup

The experiments are performed in a hybrid apparatus that has already been described in detail elsewhere [Sch12]. We prepare a single $^{138}\mathrm{Ba}^+$ in a linear Paul trap and bring it into contact with an ultracold cloud of spin-polarized $^{87}\mathrm{Rb}$ ($F = 1, m_F = -1$). The atoms are prepared at a separate location from which they are transported to the Paul trap and loaded into a far off-resonant crossed optical dipole trap. During the final preparation

stage for the atoms, the cloud and the ion are separated by about 100 μm along the Paul trap axis to avoid unwanted atom-ion interactions. By ramping one endcap voltage of the linear Paul trap to its final value, we shift the ion into the center of the atom cloud within 10 ms and start the atom-ion interaction. We use thermal atom clouds consisting of typically $N \approx 40 - 135 \times 10^3$ atoms at temperatures of $T \approx 330$ nK with peak densities between $n \approx 6$ and 84×10^{11} cm^{-3}. The Ba$^+$ ion is confined in a linear Paul trap which is operated at a frequency of 4.21 MHz with radial and axial trapping frequencies of $(\omega_r; \omega_a) = 2\pi \times (59.5; 38.4)$ kHz. Single ^{138}Ba$^+$ ions are loaded by isotope selective, resonant two-photon ionization. Using standard laser cooling techniques these are cooled to Doppler temperatures of ≈ 0.5 mK. Before immersing the Ba$^+$ into the atomic bath we switch off the laser cooling, which guarantees that the ion is in the electronic ground state during the atom-ion interaction. The average kinetic energy $\overline{E}_{\text{kin}}$ of the ion is determined by the interplay of elastic collisions and the driven micromotion [Ber98, DeV09, Zip10a, Cet12, Kry15]. $\overline{E}_{\text{kin}}$ is adjusted by tuning the excess micromotion of the ion and sets the average three-body collision energy $\overline{E}_{\text{col}}$, through the relation $\overline{E}_{\text{col}} \approx 0.55 \, \overline{E}_{\text{kin}}$ [Krü16b]. For the experiments discussed in the following we work either at an energy of $\overline{E}_{\text{kin}} \approx 4$ or of 70 mK$\times k_{\text{B}}$.

2.3 Measuring and modeling the time dependent ion loss rate

We start our investigations by measuring the lifetime of a single Ba$^+$ in contact with a thermal cloud of Rb atoms. For this, we immerse the ion ($\overline{E}_{kin} \approx 67$ mK$\times k_{\text{B}}$) into the atom cloud (density $n \approx 16 \times 10^{11}$ cm^{-3}) for various periods of time t. After the interaction, we check if the Ba$^+$ is still present by switching on the laser cooling for 100 ms and collecting its fluorescence on a EMCCD camera. If no Ba$^+$ is detected, we conclude that a reaction must have taken place. If we apply additional laser cooling with a red detuning of 2 GHz for several seconds, typically 50% of the initially undetected Ba$^+$ ions can be recovered. These ions have gained high kinetic energies in a chemical reaction, which will be discussed later. Figure 2.1 shows the measured probability p to detect the Ba$^+$ ion as a function of the interaction time t (please note the time scale change after 0.8 s). We model the decay using the rate equation $\dot{p} = -\Gamma(t) \cdot p$, with the loss rate $\Gamma(t) = k_2 \cdot n(t) + k_3 \cdot n(t)^2$, where $n(t)$ is the time-dependent atom density at the location
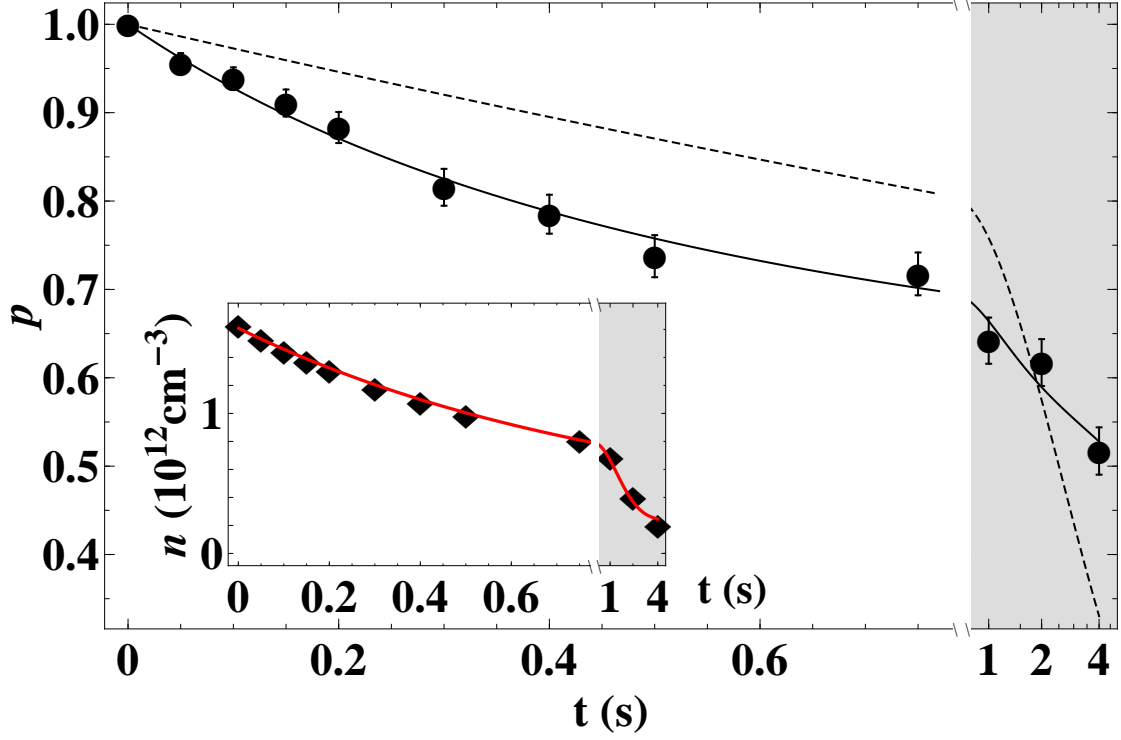
Figure 2.1: Probability p to detect the Ba$^+$ ion after the interaction time t with a Rb atom cloud at an average ion kinetic energy of $\overline{E}_{\text{kin}} \approx 67 \, \text{mK} \times k_{\text{B}}$. One data point is the average of the binary result over roughly 330 single-ion experiments. A fit (solid line) taking into account the decay of the atom density during the interaction reproduces this behavior while a simple exponential fit (dashed line) does not. The inset shows the corresponding atom density evolution, which is well described by an exponential decay with an offset (solid line). Note the time-scale change at 0.8 s, as indicated by the shaded background. All error bars represent the 1σ statistical uncertainty of the measurements.

of the ion. Integrating the equation yields

$$p(t) = \exp(-\int_0^t \Gamma(t')dt'). \tag{2.1}$$

A constant density $n(t)$ would lead to an exponential decay, $p(t) = \exp(-\Gamma t)$, which does not describe the observed loss very well (Fig. 2.1, dashed line). As the inset of Fig. 2.1 shows, the density decreases during the interaction time. This is because elastic atom-ion collisions either remove atoms from the shallow atom trap or heat up the atomic ensemble. If we take into account the decay of $n(t)$, a fit of Eq (2.1) (solid line) describes the data very well.

2.4   Accessing the atom density evolution

In other words, for a proper description of the ion loss Γ and to determine the rate constants k_2 and k_3, the evolution of the density $n(t)$ has to be accurately determined. This, however, is somewhat involved and will be discussed in the following.

To determine $n(t)$, we measure the remaining atom number N and temperature T of the cloud via absorption imaging after 15 ms time of flight. Figure 2.2(a) shows histograms of the atom number distributions for various interaction times t. Initially the distribution is Gaussian. As time goes on, elastic atom-ion collisions shift this distribution towards lower atom numbers. In addition, a broad tail develops. This tail can be explained as a consequence of reactive atom-ion collisions that release substantial amounts of energy which eject the product ion out of the atom cloud onto a large orbit trajectory in the Paul trap. This is consistent with the recovery of hot Ba$^+$ ions when additional far red-detuned laser cooling is applied, as mentioned in the previous paragraph. Although two-body and three-body reactions at mK temperatures are predicted to dominantly produce translationally cold molecular BaRb$^+$ ions [Hal13, PR15], additional kinetic energy can be released in fast secondary processes such as photo dissociation or collisional relaxation. Once the ion is on the large orbit, the atom-ion collision rate is significantly reduced, essentially stopping the continuous atom loss [Här12]. From Fig. 2.2(a) we find that the counts in the tail almost exclusively correspond to experimental runs where a reaction with Ba$^+$ occurred (green color), whereas the counts in the Gaussian dominantly correspond to runs without reactions (blue color).

For our analysis we only consider system trajectories without reactions, making sure that the ion has been constantly exposed to the central density $n(t)$. The average atom number N and temperature T of these post selected trajectories are plotted in Fig. 2.2(b). We then calculate the peak atom density (shown in Fig. 2.1 inset) $n = (\frac{m}{2\pi k_{\mathrm{B}}})^{3/2} \cdot \frac{\omega_x \omega_y \omega_z N}{T^{3/2}}$, with the mass m, using separately measured trap frequencies $(\omega_x, \omega_y, \omega_z)$ of the atom dipole trap. From these sampling points we extract the time-dependent density $n(t)$.
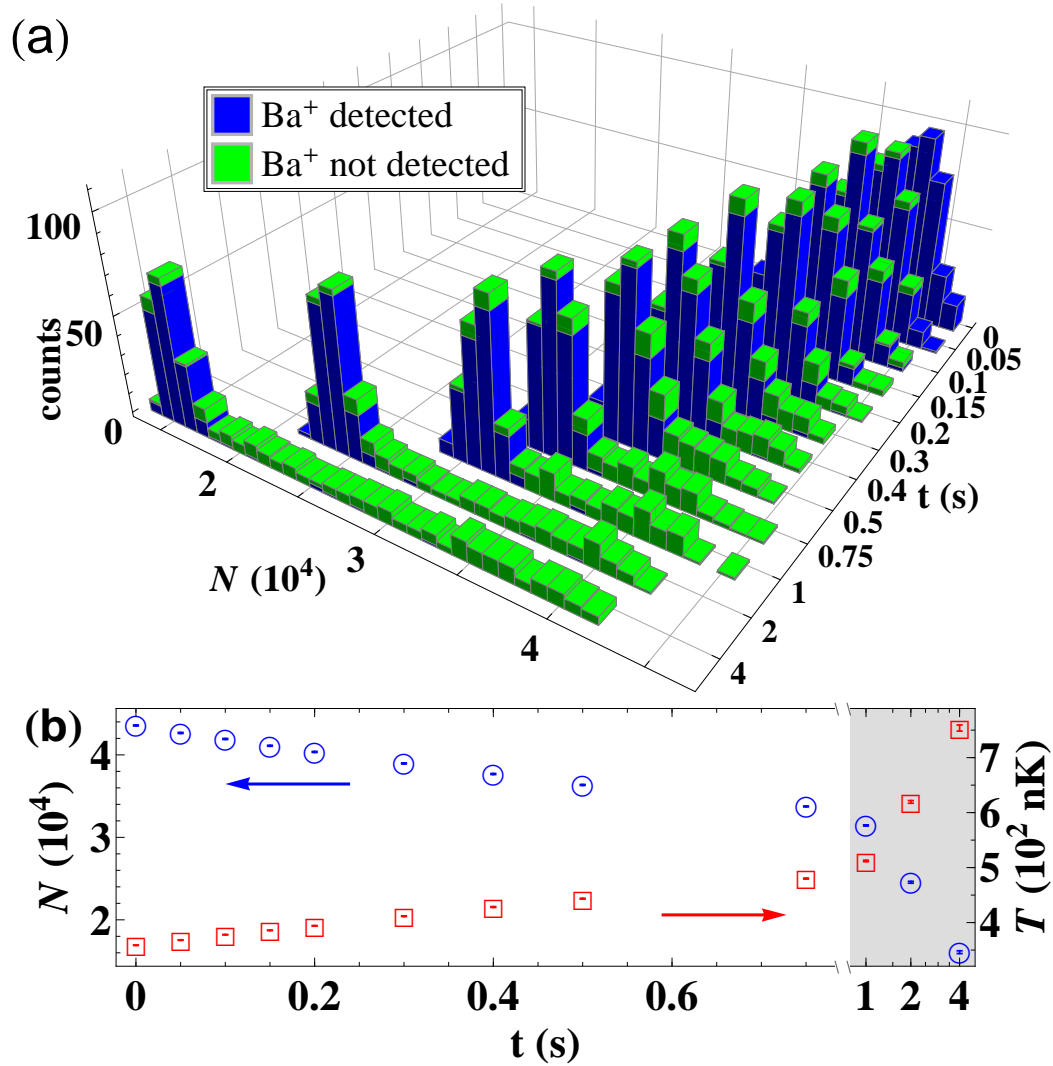
Figure 2.2: (a) Histogram of the atom numbers N belonging to the measurement in Fig. 2.1. A Gaussian atom number distribution develops a broad tail with increasing interaction times. Experimental runs where the Ba^+ ion was detected (not detected) after the interaction are marked in blue (green), respectively. Atom numbers within the tail (Gaussian peak) of the distribution correspond to runs with (without) a reactive collision, respectively. (b) Average atom number N (circles) and temperature T (squares) over all runs without reactions, corresponding to the blue colored counts in (a).

2.5   Extracting the binary and ternary reaction rate constants

We are now ready to quantitatively analyze the reaction rate and to extract binary and ternary reaction rate constants. In order to obtain a high accuracy (and as a check for consistency) we perform Ba$^+$ lifetime measurements at 10 different initial peak densities [Fig. 2.3(a)]. Atom clouds with different densities are prepared by varying the trap frequencies and the atom number but keeping the atom temperature T at a constant value of $T \approx 330$ nK. This temperature was chosen in order to be sufficiently above the critical temperature T_c for Bose-Einstein condensation and to have negligible losses due to evaporative cooling. The trap depths are between 5 to 10 μK$\times k_B$ resulting in trap frequencies of $(\omega_x, \omega_y, \omega_z) \approx 2\pi \times (16$ to 27; 97 to 151; 107 to 161) Hz. The mean ion kinetic energy is 4.0 (1.6) mK $\times k_B$, as determined in [Krü16b]. The densities between $n \approx 6$ and 22×10^{11} cm^{-3} are prepared with $N \approx 40 \times 10^3$ atoms, while densities between $n \approx 24$ and 84×10^{11} cm^{-3} are prepared with $N \approx 135 \times 10^3$ atoms.

In a first simple analysis we do not include the density evolution and fit exponential decays (dashed lines) to each data set in Fig. 2.3(a). The resulting loss rates Γ are then plotted as a function of their respective initial atom densities $n(t = 0)$ in Fig. 2.3(b). By fitting $\Gamma = k_2 \cdot n + k_3 \cdot n^2$ (blue dashed line) we obtain a quasi pure quadratic density dependence, where $k_3 = 1.03(2)(45) \times 10^{-24}$cm^{6}s^{-1} and k_2 is consistent with zero. For comparison, if we try to describe the data only by two-body reactions, $\Gamma \propto n$, no agreement is found (red dashed line).

Now, we perform a more rigorous analysis, where we account for the density decay during the interaction time, which can be as much as 20 % for the experimental runs in Fig. 2.3. This will enable us to also extract a reliable k_2 rate constant from the data. With the previously described method we determine $n(t)$ for each Ba$^+$ lifetime curve. We then fit Eq. (2.1) to all of the 10 measured decays in Fig. 2.3(a) (solid lines) simultaneously, with only two free fit parameters, the binary and ternary rate coefficients k_2 and k_3, which amount to $k_2 = 3.1(6)(6) \times 10^{-13}$cm^{3}s^{-1} and $k_3 = 1.04(4)(45) \times 10^{-24}$cm^{6}s^{-1}. The first parentheses denotes the 1 σ statistical uncertainty of the fitted values. The second one gives the 1 σ systematic error due to the atom density uncertainty of 20 %, which translates linearly into k_2 and quadratically to k_3.

Notably, both approaches yield the same k_3 within their uncertainties, but only the latter provides a non zero k_2, which emphasizes the necessity to include the atom cloud decay. We plot $\Gamma = k_2 \cdot n + k_3 \cdot n^2$, using the extracted k_2 and k_3 coefficients in Fig. 2.3(b) (green

curve). Even at low densities $n < 10^{12} \mathrm{cm}^{-3}$ the green curve deviates only slightly from the pure three-body loss (blue dashed line), highlighting the small contribution of binary reactions to the total ion loss.
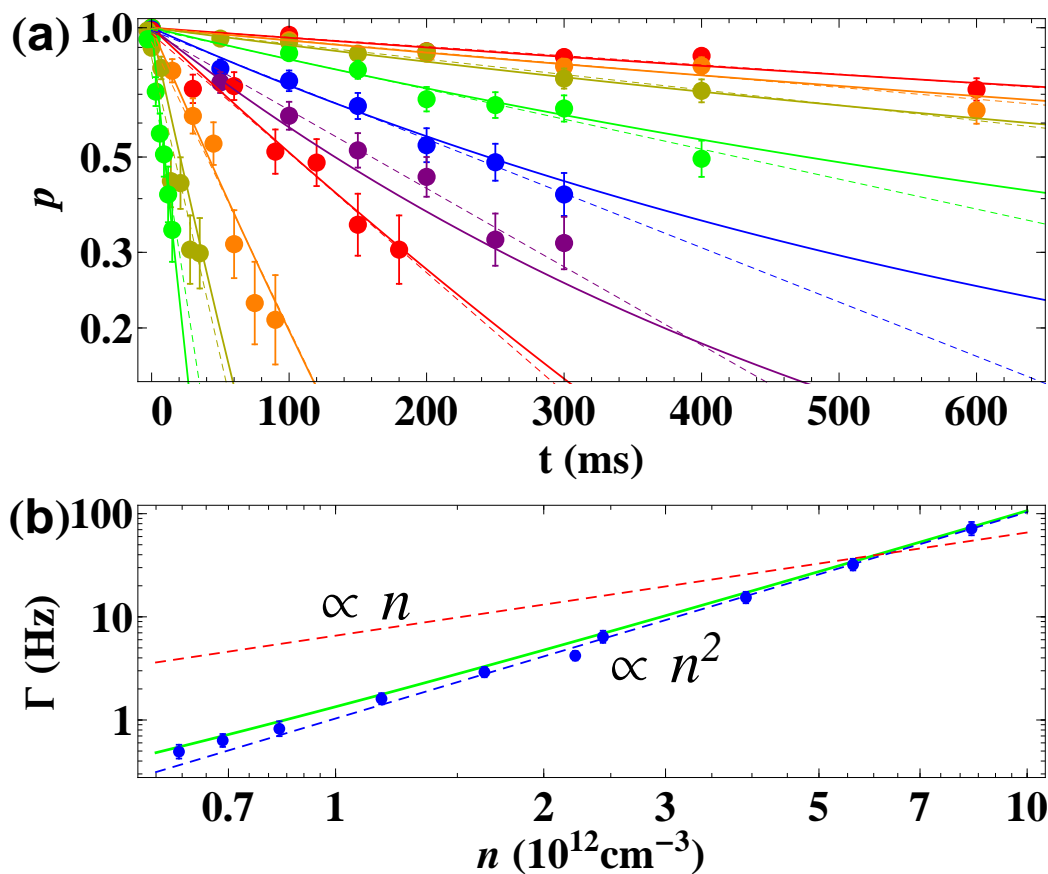

Figure 2.3: (color online) (a) Logarithmic plot of p as a function of the interaction time t for 10 different initial atom peak densities. Each data point corresponds to an average of roughly 100 single ion experiments. The dashed curves are simple exponential fits, while the solid curves originate from a simultaneous fit of Eq. 2.1 to the full data set with two free parameters, the two-body rate coefficient k_2 and the three-body rate coefficient k_3 (see text for details). (b) Double-logarithmic plot of the Ba$^+$ loss rates Γ extracted from an exponential fit to each individual data set in (a) over the respective initial peak densities (solid circles). A fit of the form $\Gamma = k_2 \cdot n + k_3 \cdot n^2$ to the loss rates yields a pure quadratic density dependence (blue dashed curve). For comparison, this function was also plotted using k_2 and k_3 from (a) (green curve). A pure linear dependence ($\Gamma \propto n$) does not describe the data (red dashed curve).

2.6   Comparison to previous results

We now compare the obtained rate coefficients to the results of other groups in the field. Our extracted two-body charge-transfer rate coefficient k_2 for the Ba^+ + Rb system is compatible with a MOT measurement from Ref. [Hal13] where an upper bound of $k_2 < 5 \times 10^{-13}\,\mathrm{cm^3 s^{-1}}$ is given for ground state charge-transfer. An *ab-initio* calculation within [Hal13] predicts $k_2 \approx 1 \times 10^{-14}\,\mathrm{cm^3 s^{-1}}$ which is a factor of 30 smaller compared to our present k_2. A possible explanation for this large discrepancy is an additional two-body loss channel that might appear in our experiment. Indeed, calculated Ba^+ + Rb molecular potential energy curves (see, e.g., Ref. [Hal13]) indicate that the 1064 nm dipole laser can near-resonantly photo-excite a colliding atom-ion pair to a repulsive molecular potential energy curve. For the potential curves that correlate with ionized Rb^+ and electronically excited neutral Ba, this process is experimentally indistinguishable from charge transfer.

We note that the three-body rate coefficient k_3, determined in this work for Ba^+ + Rb + Rb is of similar magnitude as the one for Rb^+ + Rb + Rb [Här12], which is only by a factor of 3 smaller. This can be understood as a consequence of the same long-range atom-ion interaction potential of both systems, as it only depends on the polarizability of the Rb atom. Indeed, a theoretical classical trajectory study predicted very similar three-body cross sections for Ba^+ and Rb^+ [PR15]. Furthermore, since in cold reactive ternary collisions typically large, weakly bound molecules should be formed [Krü16b], the short-range details of the molecular interaction potential do not contribute. This suggests a universal behavior of cold atom-atom-ion three-body recombination, leading to similar reaction-rate coefficients for a variety of hybrid atom-ion systems.

2.7   Conclusion

In conclusion, we have studied reactive collisions of a cold, single Ba^+ ion in contact with an ultracold cloud of Rb atoms. Mapping out the Ba^+ loss dependence on the Rb atom density enabled us to extract both the binary (k_2) and ternary (k_3) reaction-rate coefficients at $mK \times k_B$ ion energies. The Ba^+ + Rb + Rb three-body rate coefficient k_3 is comparatively large, about four orders of magnitude larger than the one for ultracold neutral Rb + Rb + Rb collisions [Esr99]. Moreover, it dominates over the two-body loss down to comparatively low densities of $k_2/k_3 \approx 3 \times 10^{11} \mathrm{cm^{-3}}$. If working with degenerate quantum gases such as Bose-Einstein condensates with typical densities around $10^{14}\,\mathrm{cm^{-3}}$, three-body recombination will occur on the sub-ms time scale, limiting the time for atom-

ion experiments. As shown in parallel work of ours [Krü16b], this time scale gets even shorter when lowering the collision energy E_{col}, as k_3 scales as $k_3 \propto E_{\mathrm{col}}^{-3/4}$. In view of the number of proposed experiments where reactive collisions are unwanted, we expect a future demand for schemes to suppress three-body reactions besides the existing ones for two-body reactions [Tom15].

Chapter 3

Energy Scaling of Cold Atom-atom-ion Three-body Recombination

Artjom Krükow, Amir Mohammadi, Arne Härter and Johannes Hecker Denschlag

Institut für Quantenmaterie und Center for Integrated Quantum Science and Technology IQST, Universität Ulm, 89069 Ulm, Germany

Jesús Pérez-Ríos and Chris H. Greene

Department of Physics and Astronomy, Purdue University, West Lafayette, Indiana 47907, USA

We study three-body recombination of Ba^+ + Rb + Rb in the mK regime where a single $^{138}Ba^+$ ion in a Paul trap is immersed into a cloud of ultracold ^{87}Rb atoms. We measure the energy dependence of the three-body rate coefficient k_3 and compare the results to the theoretical prediction, $k_3 \propto E_{col}^{-3/4}$ where E_{col} is the collision energy. We find agreement if we assume that the nonthermal ion energy distribution is determined by at least two different micromotion induced energy scales. Furthermore, using classical trajectory calculations we predict how the median binding energy of the formed molecules scales with the collision energy. Our studies give new insights into the kinetics of an ion immersed in an ultracold atom cloud and yield important prospects for atom-ion experiments targeting the s-wave regime.

3.1   Introduction

When three atoms collide, a diatomic molecule can form in a three-body recombination (TBR) process. In cold neutral atomic gases, TBR was investigated for spin-polarized hydrogen as well as alkalis (see e.g. [Hes83, Bur97, Esr99]). In the context of Bose-Einstein condensation, TBR plays a crucial role as a main loss mechanism. By now, the scaling of TBR as a function of collision energy and scattering lengths in *neutral* ultracold gases has been investigated in detail [D'I05]. When considering TBR in atom-ion systems, one can expect three-body interactions to be more pronounced due to the underlying longer-range r^{-4} polarization potential. Energy scaling of TBR in charged gases was studied at temperatures down to a few K, especially for hydrogen and helium due to their relevance in plasmas and astrophysics (e.g. [Krs03, Pla12]). Depending on the studied temperature range a variety of power laws was found but not a common threshold law. The recent development of novel hybrid traps for both laser cooled atoms and ions has opened the possibility to investigate cold atom-ion interactions and chemical reactions in the mK regime and below. First experiments in such setups studied elastic and reactive two-body collisions (e.g. [Gri09, Zip10b, Sch10a, Hal11, Sul12, Rav12, Siv12, Haz13]). In accordance with the well-known Langevin theory, the corresponding reactive rates were measured to be independent of the collision energy [Zip10b, Hal11]. Very recently we predicted a theoretical threshold law on the scaling properties for cold atom-atom-ion three-body collisions [PR15]. Understanding the scaling of reaction rates with quantities such as the collision energy is crucial for fundamentally understanding TBR and for the prospects of the experimental realization of ultracold s-wave atom-ion collisions. Furthermore, as we will show here, studying TBR allows for insights into the kinetics of an ion immersed

in a cloud of atoms. Experimentally, TBR in the mK regime was recently observed for
$Rb^+ + Rb + Rb$ [Här12] and $Ba^+ + Rb + Rb$ [Krü16a]. In the Ba^+ experiments TBR
was already dominating over two-body reactions even for moderate atomic densities of
$10^{12}\,\mathrm{cm}^{-3}$.

This Letter reports on the combined theoretical and experimental investigation of the
energy scaling of three-body atom-atom-ion collisions in the mK regime. We measure the
TBR rate coefficient $\overline{k}_3$ of Ba^+ in an ultracold Rb cloud as a function of the mean collision
energy of the ion, $\overline{E}_{\mathrm{col}}$, which we control via the excess micromotion (eMM) of the Paul
trap. $\overline{k}_3$ is formally distinguished from k_3 which is the TBR rate coefficient for a precise
collision energy E_{col} in the center-of-mass frame. By averaging k_3 over the ion energy
distribution $\overline{k}_3$ is obtained. We calculate k_3 using classical trajectory calculations (CTC)
[PR14, PR15] and derive its energy scaling, $k_3 \propto E_{\mathrm{col}}^{-3/4}$. Agreement is found between
theory and experiment if we assume that the energy distribution of the ion depends on
multiple energy scales due to various sources of excess micromotion. Besides the prediction
of k_3, the CTC calculations also provide the binding energy distribution of the formed
molecules and the scaling properties of these distributions when the collision energy is
varied.

3.2 Experimental Setup

The experiments are performed in a hybrid apparatus that has already been described in
detail elsewhere [Sch12]. After loading a single $^{138}Ba^+$ ion by isotope selective, resonant
two-photon ionization it is stored in a linear Paul trap driven at a frequency of 4.21 MHz
with radial and axial trapping frequencies of $(\omega_r; \omega_a) = 2\pi \times (59.5; 38.4)\,\mathrm{kHz}$, respectively.
There, it is laser cooled to Doppler temperatures of ≈ 0.5 mK. In order to perform our
experiments in the electronic ground state, we switch off the cooling and repumper light,
before immersing the ion into the ultracold atomic cloud.

Once in the cloud, there is a complicated interplay of elastic two-body atom-ion collisions
and the driven micromotion of the Paul trap. This interplay leads to a non-Maxwell-
Boltzmann distribution of the ion's kinetic energy E_{kin} [DeV09, Zip10b, Cet12, Kry15]
with an equilibration time on the ms time scale [1]. The average kinetic energy $\overline{E}_{\mathrm{kin}}$ of
the ion in the atom cloud is then determined by the available energy sources for the ion,
such as the eMM energy [Zip10b]. In our experiment we can adjust $\overline{E}_{\mathrm{kin}}$ by controlling

---

[1] The equilibration time can be estimated from the Langevin collision rate which at our given density is
about $4\,\mathrm{ms}^{-1}$.

one part of the eMM energy, E_{fMM}, which is set via static electric fields. Concretely, we can write $\overline{E}_{\text{kin}} = c_{dyn}(E_{\text{fMM}} + E_{\text{min}})$, where the offset energy E_{min} contains all other energy contributions, *e.g.* phase micromotion (ϕMM) [Ber98] or residual collisional effects [Cet12, Kry15]. The proportionality factor $c_{dyn} \approx 5.0$, which depends on the atom-ion mass ratio and the trap parameters, is extracted from a MC calculation similar to [Zip11b]. We can tune E_{fMM} accurately between $5\mu\text{K}\times k_{\text{B}}$ and $100\text{mK}\times k_{\text{B}}$. E_{min}, on the other hand, is not known precisely. From independent measurements and MC calculations based on the scaling of elastic atom-ion collisions, we estimate E_{min} to be in the range between 200 and 800 $\mu\text{K}\times k_{\text{B}}$.

The cloud consists of $N \approx 1.2 \times 10^5$ ^{87}Rb atoms at a temperature of $T_{\text{at}} \approx 700$ nK with a peak density of $n \approx 19 \times 10^{11}$ cm^{-3}. It is cigar shaped with a radial and axial size of roughly 10 μm and 50 μm, respectively. The atoms are spin polarized ($F = 1, m_F = -1$) and confined in a far off-resonant crossed optical dipole trap at a wavelength of 1064 nm with a trap depth of $\approx 10\mu\text{K}\times k_{\text{B}}$. We shift the ion into the cloud over a distance of $120\,\mu$m within 2 ms by changing the endcap voltage of the linear ion trap. After an interaction time of $\tau = 300$ ms, during which the Ba$^+$ ion is typically lost with a probability of up to 65 %, we separate the two traps again and detect whether the Ba$^+$ ion is still present. For this, we shine a laser cooling beam focused to a waist of 20 μm through the Paul trap center and collect the possible fluorescence on a EMCCD camera for 100 ms. If no Ba$^+$ is detected, we conclude that a reaction must have taken place during τ [2].

3.3   Energy dependent reactions

Repeating the single ion experiment roughly 170 times we extract the probability p that Ba$^+$ is still present. For the given experimental settings the ion loss is well described by an exponential decay of the form $p = \exp(-\Gamma\tau)$. This can be seen in the inset of Fig. 3.1, where we plot p as a function of interaction time τ measured at $E_{\text{fMM}} \approx 8\,\mu$K. Figure 3.1 plots the loss rate Γ as a function of E_{fMM}. A Ba$^+$ ion in our experiment is lost either by a two-body charge transfer or by a three-body event [Krü16a]. The corresponding loss rate Γ of the ion is $\Gamma = -nk_2 - n^2\overline{k}_3$. The charge transfer rate coefficient k_2 has been previously measured for Ba$^+$ + Rb, $k_2 = 3.1(6)(6) \times 10^{-13}$cm^3/s (statistical and systematic errors in parentheses) [Krü16a] (see also [Sch10a, Hal13]), and contributes less than $1\,\text{s}^{-1}$ to

---

[2]   We note that our detection scheme cannot detect a reaction if the final product (e.g. after a secondary process) is again a cold Ba$^+$ ion. From parallel experiments where we investigate the reaction products, however, we have no evidence for such a reaction outcome. In fact, our present work shows good agreement between theory and experiment if we assume that a reaction channel producing cold Ba$^+$ ions is negligible.
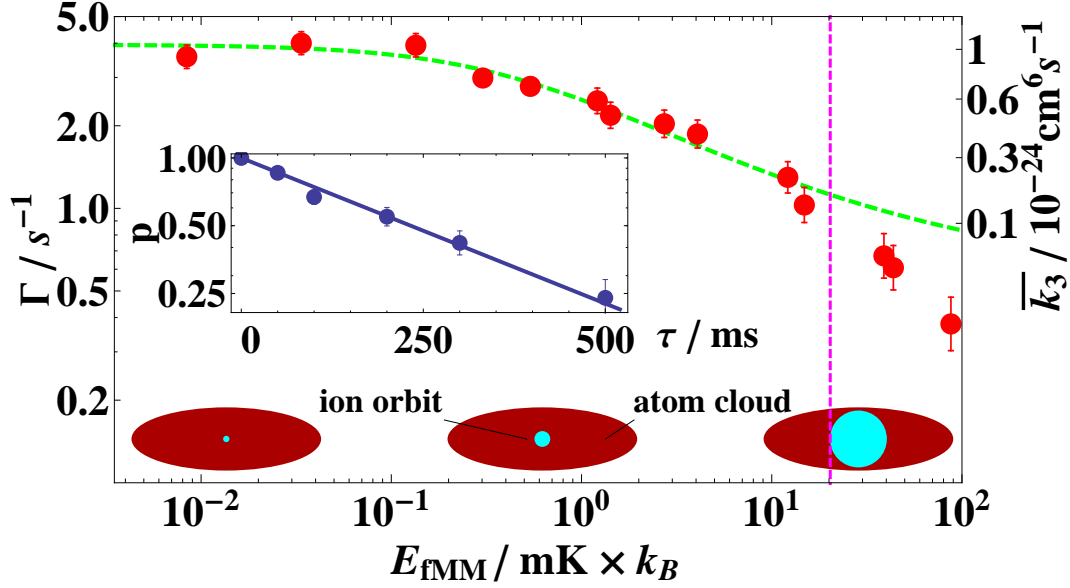
Figure 3.1: Double-logarithmic plot of the measured loss rate Γ for Ba$^+$ as a function of the tuned eMM energy E_{fMM}. Red circles are the experimental data; the curve represents a fit of Eq. (1) (see text for details). The corresponding values of $\bar{k}_3$ are indicated on the right-hand side. The inset is the Logarithmic plot of the decay curve of the Ba$^+$ ion. p is the probability to recover Ba$^+$ after interacting with Rb. The straight line is an exponential fit to the data. The sketch shows the ion orbit in the atom cloud. With increasing ion energy its orbit becomes comparable to the atom cloud size.

the loss rate Γ for the given atomic density. Also, it has been verified that k_2 is energy independent [Gri09, Zip10b, Hal11], consistent with Langevin theory. By subtracting this constant k_2 loss from Γ and dividing by the (constant) density n^2 we obtain $\bar{k}_3$ (see Figs. 1 and 3b). Clearly, $\bar{k}_3$ is energy dependent. As we discuss later, we expect a scaling of k_3 with a power law, $k_3 \propto E_{\text{col}}^{\alpha}$. Neglecting the atom motion due to ultracold temperatures we can express E_{col} in terms of the ion kinetic energy E_{kin}, $E_{\text{col}} = (1 - \frac{m_{\text{Ba}}}{m_{\text{Ba}} + 2m_{\text{Rb}}})E_{\text{kin}}$. We attempt to describe the scaling of the measured $\bar{k}_3$ with a power law $\bar{k}_3 \propto \overline{E}_{\text{kin}}^{\alpha}$ by fitting the expression

$$\bar{k}_3 = \bar{k}_{3,\text{min}}\left[(E_{\text{fMM}} + E_{\text{min}})/E_{\text{min}}\right]^{\alpha} \tag{3.1}$$

to the data. Here, E_{min} and α are free parameters. The constant $\bar{k}_{3,\text{min}} = 1.04(4)(45) \times 10^{-24}\text{cm}^6/\text{s}$ is $\bar{k}_3$ at $E_{\text{fMM}} = 0$ and was determined in a parallel study [Krü16a]. For the fit we discard data points above $E_{\text{fMM}} > 20\,\text{mK} \times k_{\text{B}}$, as for such energies, the ion is not localized well enough in the center of the cloud. It probes areas of the atomic cloud at lower densities, hence decreasing the observed loss rate (see sketch in Fig. 1). The fit yields $\alpha = -0.46(9)$ and $E_{\text{min}} = 410(180)\,\mu\text{K} \times k_{\text{B}}$ (green dashed line in Fig. 3.1), with the errors denoting a 1σ statistical uncertainty of the fitted values. Interestingly, in our

previous study of TBR of $Rb^+ + Rb + Rb$ [Här12] we observed a similar scaling exponent of $\alpha = -0.43$.

3.4   Theoretical approach

We now turn to investigate the scaling of TBR theoretically with a CTC formalism. A classical treatment of the collision dynamics is appropriate, since the experiments described here in general involve much higher energies than the threshold energy of $\sim 50\,\mathrm{nK} \times k_\mathrm{B}$ for entering the s-wave regime of Ba^+-Rb. We have adapted a recently developed method for the calculation of three-body recombination cross sections based on classical trajectories [PR14, PR15] for the study of atom-atom-ion recombination. The method employed relies on mapping the three-body problem into a six-dimensional configuration space, described in hyperspherical coordinates, after separating out the center-of-mass motion [PR14]. Since the kinetic energy of the ion is typically several orders of magnitude higher than the temperature of the ultracold neutral atoms we fix one of the hyperangles associated to the ratio of the atom-ion versus the atom-atom initial momentum, guaranteeing that in the center-of-mass coordinate system 95 % of the collision energy E_col is along the direction of the ion. In the classical trajectory calculations only Rb-Rb collisions in triplet states are considered and spin flip transitions are neglected. For the Rb-Rb pair interaction we employ the $a^3\Sigma_u^+$ potential of Strauss *et al.* [Str10]. On the other hand, the Ba^+-Rb interaction potential is taken to be $-C_4(1 - (r_m/r)^4/2)/r^4$, where $C_4 = 160$ a.u. denotes the experimental long-range value of the interaction and r_m represents the position of the minimum of the potential, taken from Ref. [Kry11].

The TBR rate for $Ba^+ + Rb + Rb$ has been computed by running 10^5 trajectories per collision energy. We checked that during the simulation the total energy and angular momentum are conserved up to the fifth decimal place. Details about the numerical method employed to solve Hamilton's equations of motion, in conjunction with the sampling of the initial conditions, can be found in [PR14]. Figure 3.2a shows a three-body trajectory that results in a recombination event with a collision energy of $100\,\mu\mathrm{K} \times k_\mathrm{B}$. This particular trajectory leads to large size ($\sim 800\,\mathrm{a}_0$), very weakly-bound molecular ion. Counting the fraction of trajectories that lead to molecule formation we can extract the TBR rate coefficient k_3 for $Ba^+ + Rb + Rb$. Figure 3.2b plots k_3 as a function of collision energy E_col. We compare these CTC calculations (diamonds) with an analytically derived scaling law [PR15] where $k_3 \propto E_\mathrm{col}^{-3/4}$ (dashed line in Fig. 3.2b and find very good agreement.
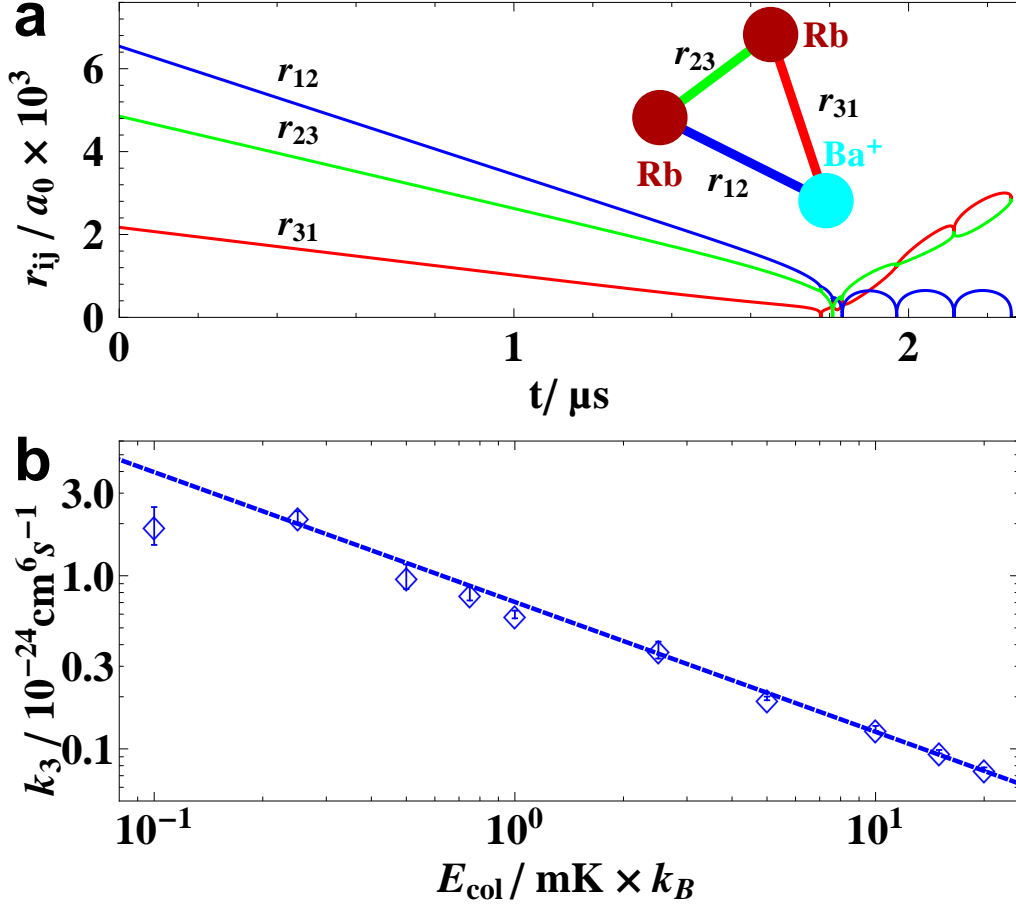
Figure 3.2: (a) A typical trajectory at a collision energy of $100\,\mu\mathrm{K}\times k_\mathrm{B}$ associated with the three-body collision $\mathrm{Ba^+ + Rb + Rb}$ that leads to the formation of $\mathrm{BaRb^+}$. We show the distances r_{ij} between the particles as indicated in the sketch. (b) Double log plot of k_3 obtained with CTC for $\mathrm{Ba^+ + Rb + Rb}$ as a function of the collision energy E_col (circles). The straight line shows the analytically predicted power law dependence $k_3 \propto E_\mathrm{col}^{-3/4}$.

3.5   Comparing experiment to theory

Strikingly, the theory prediction of $\alpha = -0.75$ does not seem to agree well with the experimentally observed value of $\alpha = -0.46(9)$ from the fit of Eq. (3.1) to our data. We explain this discrepancy as follows. In contrast to the theoretical approach where k_3 is determined for a precisely defined collision energy E_col, in the experiments we observe $\overline{k}_3$, an average over a distribution $P(E_\mathrm{col}, \{E_i^S\})$ of collision energies, calculated as

$$\overline{k}_3(\{E_i^S\}) = \int k_3(E_\mathrm{col})\, P(E_\mathrm{col}, \{E_i^S\})\, dE_\mathrm{col}. \tag{3.2}$$

Here, $\{E_i^S\}$ is a list of the relevant energy scales that determine the distribution, such as the experimentally tuned E_{fMM} or $E_{\phi\text{MM}}$. We extract these distributions with a MC calculation based on [Zip11b]. If only a single scale E_1^S is present, the energy distributions can be expressed as functions of the ratio E_{col}/E_1^S,

$$P(E_{\text{col}}, E_1^S)dE_{\text{col}} = \tilde{P}(E_{\text{col}}/E_1^S)dE_{\text{col}}/E_1^S. \tag{3.3}$$

Figure 3.3a shows three calculated distributions each with its own scale E_1^S. The distributions $P(E_{\text{col}}, E_{\text{fMM}})$ for $E_{\text{fMM}} = 1\,\text{mK}$ (green) and $20\,\text{mK}$ (red) have the exact same shape, a consequence of Eq. (3.3). The third distribution $P(E_{\text{col}}, E_{\phi\text{MM}} = 1\,\text{mK})$ (blue), generated with a phase micromotion has a somewhat different shape. Using Eq. (3.2) one can show which distributions which satisfy Eq. (3.3) translate the power law $k_3 \propto E_{\text{col}}^{-3/4}$ into $\overline{k}_3 \propto (E_1^S)^{-3/4}$. In our experiment, however, where at least two energy scales, E_{fMM} and E_{min} occur, this translation of the scaling breaks down and Eq. (3.1) cannot be used in the data analysis anymore. Instead, we calculate $\overline{k}_3$ with Eq. (3.2) to directly compare theory and experiment. The choice and magnitude of E_{min} is the only free model parameter. Here, we assume that E_{min} is entirely determined by phase micromotion, $E_{\text{min}} = E_{\phi\text{MM}}$. The phase micromotion is chosen to be shared equally between both pairs of opposing radio frequency (rf) driven electrodes [Ber98]. Figure 3.3b shows the experimental $\overline{k}_3$ (full circles), together with the calculation (blue solid line) with $E_{\phi\text{MM}} = 790\,\mu\text{K}$[3]. The shape of the theory curve describes the experimental data quite well, apart from an overall factor of about 1.1 (see blue and red solid lines). In general, the overall magnitude and energy dependence of $\overline{k}_3$ is reproduced by the presented *ab initio* CTC treatment down to the mK Regime, which is remarkable as E_{min} is the only free parameter.

3.6   Binding energy distribution

We now turn to briefly discuss the molecular products after TBR. In a previous study of TBR for He, it was suggested that the binding energy of the products is correlated with the collision energy [PR14]. We find again the same behavior for TBR of an ion with two atoms. Figure 3.4a shows two logarithmically binned histograms of molecular binding energies after TBR. The maximum of each histogram can be considered the typical binding energy and is shown in Fig. 3.4b as a function of the collision energy E_{col}. A fit to a power-law dependence gives $E_{\text{binding}} \sim E_{\text{col}}^{0.88\pm0.02}$ for the energy range investigated

---

[3] Such a phase micromotion can be caused by a relative length difference of $\Delta l/l \approx 10^{-3}$ between the cables supplying opposing rf electrodes, which is well within the tolerances of our setup.
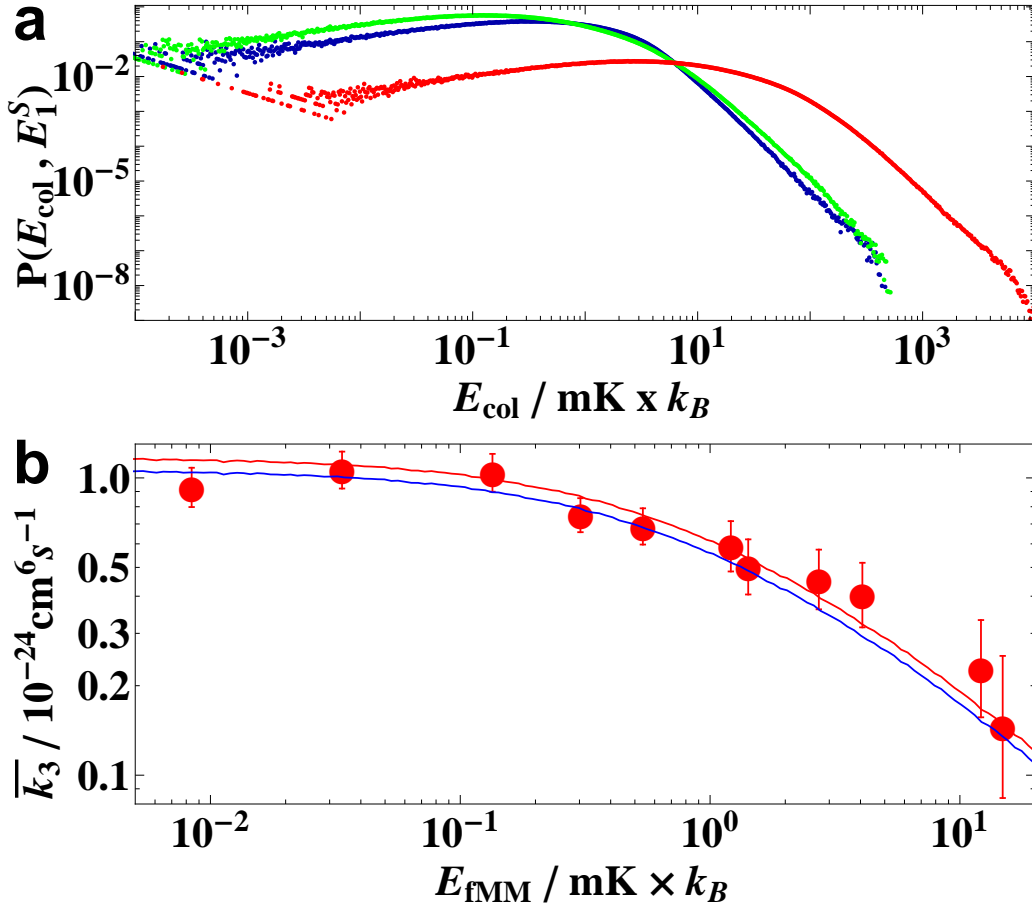
Figure 3.3: (a) Calculated ion energy distributions $P(E_{col}, E_1^S)$ each with a single energy scale E_1^S. An energy of $E_1^S = E_{fMM} = 1$ mK (20 mK) was used for the green (red) distribution. Choosing $E_1^S = E_{\phi MM} = 1$ mK produces the blue distribution, which has a different shape compared to both previous distributions. (b) Comparison of the experimental (full circles) $\overline{k}_3$ data as a function of E_{fMM} with the full calculation (blue line). The red line is the same calculation but multiplied by 1.1.

here. Thus our calculations suggest that the formation of deeply bound molecules after TBR should be highly improbable at low collision energies.

The present CTC results also suggest that BaRb$^+$ should be the dominant product state of the three-body recombination in the collision energy range considered here. Indeed, we have observed the formation of BaRb$^+$ ions in our experiment. However, collisional or light induced secondary processes lead to short lifetimes. A detailed study of the initial TBR products and involved secondary reactions is currently in progress and needs to be discussed elsewhere.
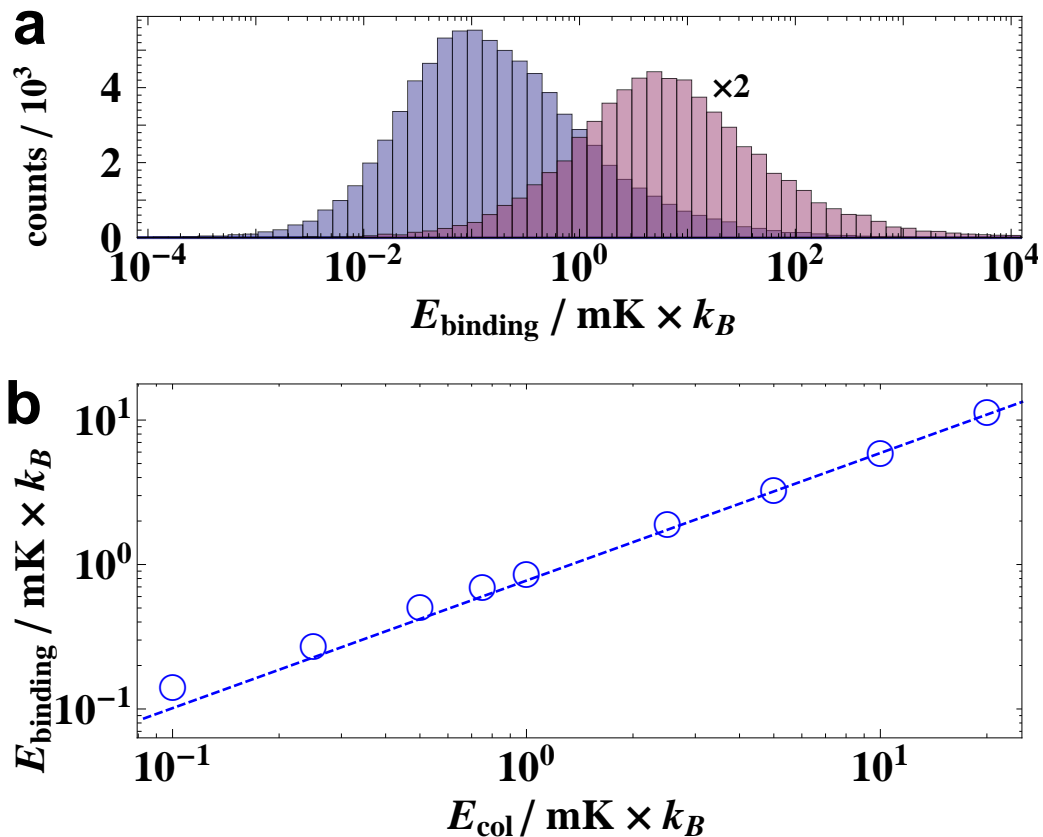
Figure 3.4: (a) Logarithmically binned histogram of the binding energies at collision energies of 100 μK$\times k_B$ (blue) and 10 mK$\times k_B$ (red). The second histogram is magnified by a factor of two. (b) Double-logarithmic plot of the typical binding energy of the formed molecule as a function of the collision energy. The dashed line represents a power law fit.

3.7   Conclusion

In conclusion, we have investigated the energy scaling of three-body recombination in an atom-ion system down to mK energies. Single Ba$^+$ ions in contact with ultracold Rb atoms have been used to measure the TBR rate coefficient $\overline{k}_3$. Utilizing classical trajectory calculations, we numerically accessed the TBR rate coefficient k_3 for the Ba$^+$ + Rb + Rb system for various collision energies. We find a power law scaling of the form $k_3(E_{\mathrm{col}}) \propto E_{\mathrm{col}}^{\alpha}$ with an exponent $\alpha = -3/4$. Our experimental and theoretical studies indicate that the presence of several energy scales gives rise to energy distributions of the immersed ion that impede a direct application of scaling laws to the measured data. The obtained energy scaling provides an important insight for prospects of atom-ion experiments in the ultracold regime, as the already strong TBR rate observed here will increase by another three orders of magnitude once the s-wave regime at 50 nK is reached.

Chapter 4

Single Ion as a Three-Body Reaction Center in an Ultracold Atomic Gas

Arne Härter, Artjom Krükow, Andreas Brunner, Wolfgang Schnitzler, Stefan Schmid, and Johannes Hecker Denschlag

Institut für Quantenmaterie und Center for Integrated Quantum Science and Technology IQST, Universität Ulm, 89069 Ulm, Germany

We report on three-body recombination of a single trapped Rb^+ ion and two neutral Rb atoms in an ultracold atom cloud. We observe that the corresponding rate coefficient K_3 depends on collision energy and is about a factor of 1000 larger than for three colliding neutral Rb atoms. In the three-body recombination process large energies up to several $0.1\,eV$ are released leading to an ejection of the ion from the atom cloud. It is sympathetically recooled back into the cloud via elastic binary collisions with cold atoms. Further, we find that the final ionic product of the three-body processes is again an atomic Rb^+ ion suggesting that the ion merely acts as a catalyzer, possibly in the formation of deeply bound Rb_2 molecules.

4.1   Introduction

Early on in the quest for ultracold quantum gases three-body recombination played a crucial role as a limiting factor for Bose-Einstein condensation. It was first investigated in spin-polarized hydrogen [Hes83] and somewhat later for alkali atoms [Esr99, Bur97]. Recently, three-body recombination was investigated with single atom resolution [Spe12]. Combining ultracold atoms with cold trapped ions is an emerging field where large scattering cross sections naturally come into play due to the comparatively long range $1/r^4$ polarization interaction potential. Two-body collisions between atoms and ions in the low energy regime have been recently studied [Côt00b, Gri09, Zip10b, Sch10a, Hal11, Rel11, Rav12]. In this letter, we report on three-body collisions involving two ultracold ^{87}Rb atoms and a $^{87}Rb^+$ ion at mK temperatures. The ion in our experiment can be regarded as a reaction center, facilitating molecule formation through its large interaction radius.

For the work presented here, it is essential that we work with ions and atoms of the same species. This renders charge transfer reactions irrelevant, which otherwise would strongly constrain our measurements. As Rb^+ is not amenable to laser-cooling and cannot be imaged, we detect the ion and investigate its dynamics in an indirect way, i.e. through its action on the atom cloud. In our experiments, we place a single ion into the center of an atomic sample resulting in a continuous loss of atoms due to elastic atom-ion collisions. This behavior is interrupted when a highly energetic three-body process ejects the ion from the atom cloud. By examining the statistics of ion-induced atom loss in hundreds of repetitions of the experiment, we can investigate a number of important details of the three-body process, such as its quadratic density-dependence, the energy that it releases, its rate coefficient K_3, the dependence of K_3 on collisional energy, and its reaction products. Furthermore, our measurements also demonstrate sympathetic cooling of an ion

from eV energies down to about $1\,\mathrm{mK}$ using an ultracold buffer gas.

4.2   Experimental Setup

The atom-ion collision experiments are conducted in a hybrid apparatus (for details see [Sch12]) where a single $^{87}\mathrm{Rb}^+$ ion, trapped in a linear Paul trap, is brought in contact with an ultracold cloud of spin polarized $^{87}\mathrm{Rb}$ atoms ($F = 1, m_F = -1$). The atom cloud is previously prepared at a separate location from where it is transported to the Paul trap and loaded into a far off-resonant crossed optical dipole trap. The dipole trap is at first spatially separated from the trapped ion by about $50\,\mu\mathrm{m}$. To start the atom-ion collision experiments it is then centered on the ion with $\mu\mathrm{m}$ precision within a few $100\,\mathrm{ms}$. At this point the atom cloud consists of $N_\mathrm{at} \approx 4.0 \times 10^4$ atoms at a temperature of $T_\mathrm{at} \approx 1.2\,\mu\mathrm{K}$ and a peak density $n_\mathrm{at} \approx 1.1 \times 10^{12}\,\mathrm{cm}^{-3}$. At trapping frequencies of $(190, 198, 55)\,\mathrm{Hz}$ this results in a cigar shaped cloud with radial and axial extensions of about $10\,\mu\mathrm{m}$ and $35\,\mu\mathrm{m}$, respectively.

The single Rb^+ ion is confined in a Paul trap driven at a frequency of $4.17\,\mathrm{MHz}$ resulting in radial and axial trapping frequencies of $350\,\mathrm{kHz}$ and $72\,\mathrm{kHz}$, respectively. As the trap is about $4\,\mathrm{eV}$ deep, the ion typically remains trapped for thousands of experimental cycles. It is initially produced by photoionization of an atom from a cold Rb cloud in the Paul trap [Här13c]. Typical kinetic energies E_ion of the ion after sympathetic cooling in the atom cloud are about a few $\mathrm{mK}\cdot k_\mathrm{B}$. This energy scale is mainly set by two quantities: (1) The excess micromotion (eMM) [Ber98] in the Paul trap whose main part we can control by compensating stray electric fields [Här13b]. (2) Heating effects induced by the interplay of micromotion and elastic collisions [DeV09, Zip10a, Cet12].

4.3   Evidence for Atom-Ion Three-Body Interaction

As described in Ref. [Sch10a], an ion immersed in an ultracold atom cloud leads to atom loss by expelling atoms from the shallow optical trap ($\approx 10\,\mu\mathrm{K} \cdot k_\mathrm{B}$ trap depth) via elastic collisions. The radio frequency (rf) driven micromotion is a constant source of energy which drives these loss-afflicting collisions. Figure 4.1(a) shows such a decay of an atom cloud at relatively low densities ($\approx 10^{11}\,\mathrm{cm}^{-3}$) and relatively high ion energies [1] ($\approx 35\,\mathrm{mK} \cdot k_\mathrm{B}$). Plotted is the number of remaining atoms after an atom-ion interaction

---

[1]   Due to the non-thermal energy distribution of the immersed ion [Cet12, Zip11b] we use the median as an energy measure.
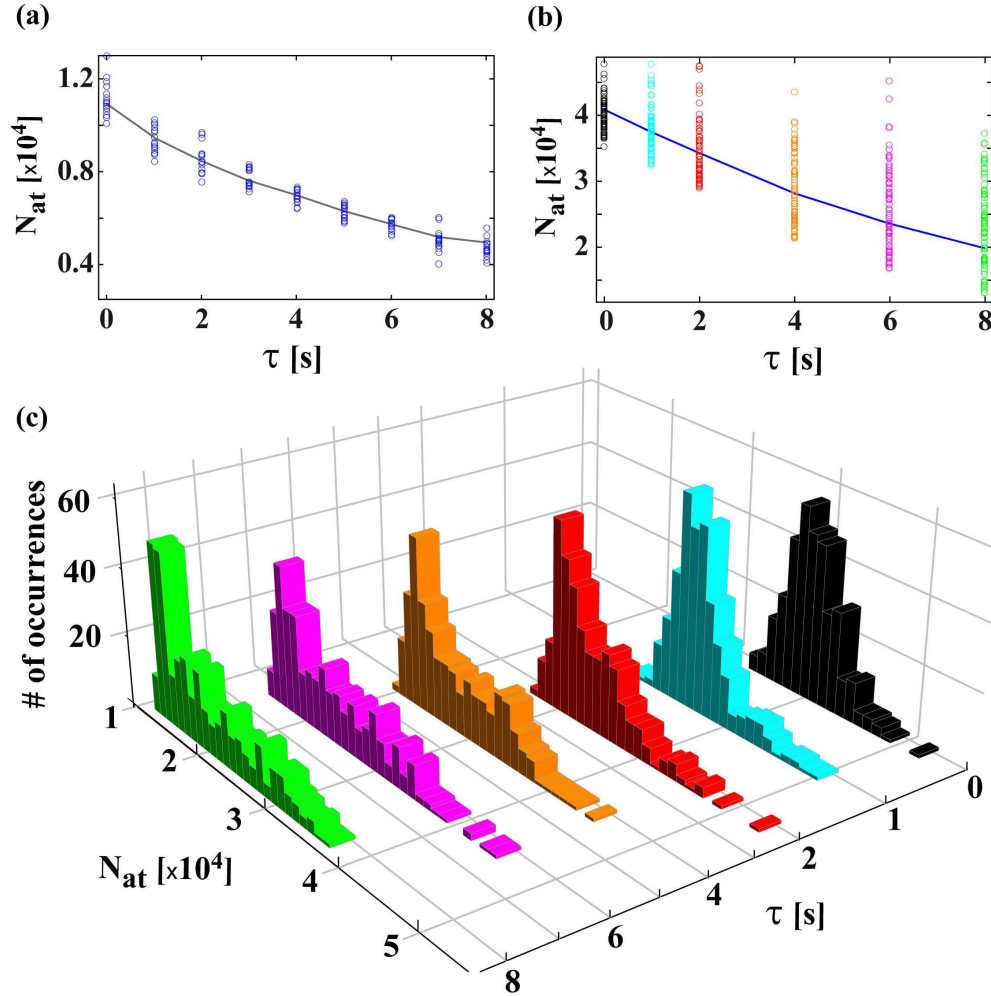
Figure 4.1: Decay of the atom cloud under influence of a single trapped ion. (a) Remaining atom numbers after interaction time τ for an ion with $E_{\rm ion} \approx 35$ mK·$k_{\rm B}$ and $n_{\rm at} \approx 10^{11}$ cm^{-3}. The solid line indicates the decay of the mean atom number. (b) Same as (a) but $E_{\rm ion} \approx 0.5$ mK·$k_{\rm B}$ and $n_{\rm at} \approx 1.1 \times 10^{12}$ cm^{-3}. (c) Histograms containing the data shown in (b).

time τ. Each data point corresponds to a single measurement. Overall, the plot shows a relatively smooth decay of the atom cloud with a relative scatter of the atom number of less than 10%. This changes drastically when we carry out the experiments at low ion energies (≈ 0.5 mK·k_B) and larger densities ($\approx 10^{12}$ cm^{-3}) (Fig. 4.1(b)). Here, the scatter dramatically increases with τ and is on the order of the number of lost atoms. In Fig. 4.1(c) histograms are shown which contain the data of Fig. 4.1(b). With increasing time τ the initial Gaussian distribution develops a striking tail towards large atom numbers. At the tips of the tails we find cases where even after interaction times of several seconds barely any atoms have been lost, a signature of missing atom-ion interaction. Apparently, sporadically the ion is ejected from the atom cloud and promoted onto a large orbit for a period of time during which atom-ion collisions are negligible (Fig. 4.2(a)). In principle, this is reminiscent of the energy distributions with high energy tails that have recently been predicted for trapped ions immersed in a buffer gas [DeV09, Zip10a]. However, it turns out that such an explanation is inconsistent with our observations on the grounds of energetics and scaling. Rather, we find that it is a three-body recombination process involving the ion and two neutrals that ejects the ion from the cloud. Due to the large trap depth the ion is not lost in such an event, but it is recooled back into the cloud through binary collisions after some time.

Figure 4.2(b) illustrates in a simple picture how the decay of the atom number over time can follow different paths. The solid trace T_1 shows the case when only binary atom-ion collisions occur. Such traces result in the narrow Gaussian peak of the atom number distribution shown on the right of Fig. 4.2(b). Traces T_2 and T_3 exhibit three-body collisions at points E_2 and E_3. At point R_2 the ion reenters the atom cloud after an interruption time t_{out}. Rare three-body events and long times t_{out} result in a long tail of the distribution. We can reproduce the histograms in Fig. 4.1 with a simple Monte Carlo type simulation (for details see supplemental material). We assume an initial Gaussian distribution of the atom number which then decays exponentially with the binary atom-ion collision rate $K_2 n_{at}$. Here, K_2 is a rate constant given by the product of the elastic cross section and the ion velocity. A three-body event, occurring at a rate $K_3 n_{at}^2$, interrupts this decay for a period t_{out}. As the ion can only be recooled by the atomic sample, we assume the rate for reentry of the ion into the atom cloud to be proportional to the number of atoms $1/\langle t_{out}\rangle = N_{at}/c_{out}$ with c_{out} being a constant that depends on the trap parameters. Figure 4.2(b) (right) shows exemplarily that the model can describe well the histograms in Fig. 1. In the following we continue the analysis by studying $P_{threebody}$ which is the probability that at least one three-body process takes place within time τ. For each τ we determine $P_{threebody}$ from our histograms. $P_{threebody}$ is the count number of the tail of
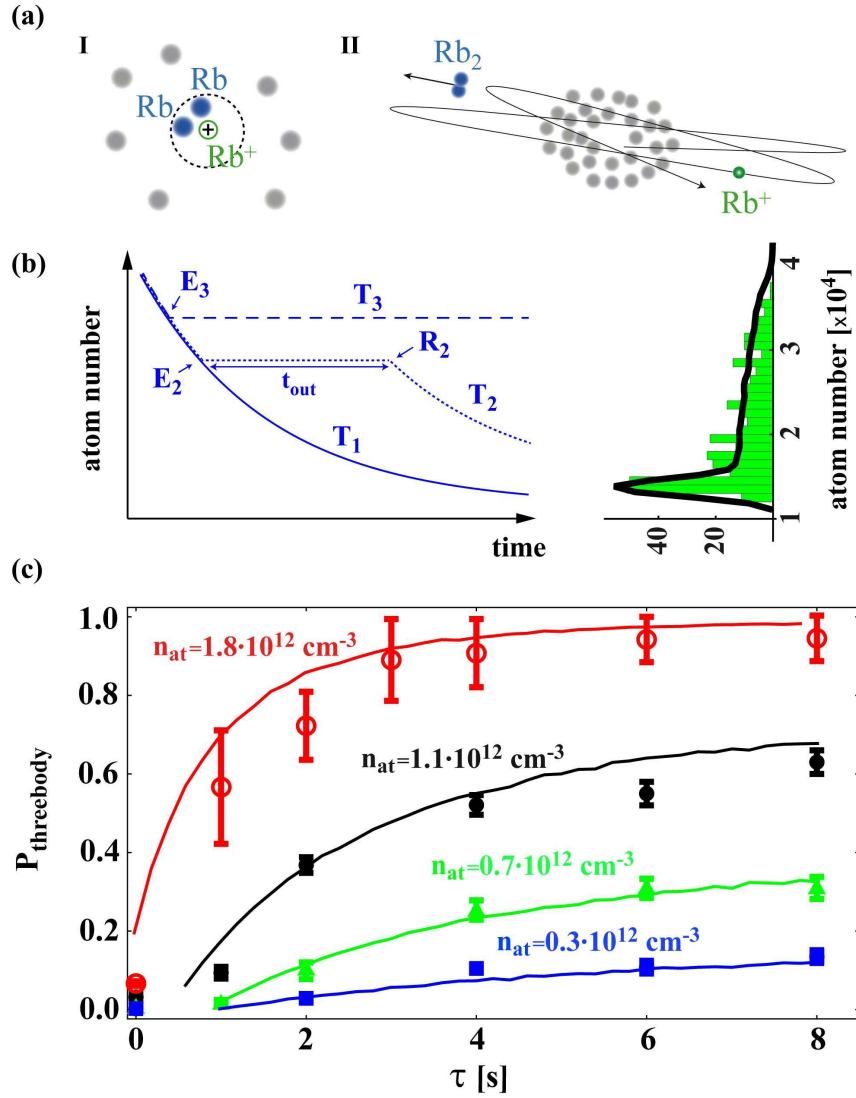
Figure 4.2: (a) Illustration of an atom-atom-ion collision. (I) Two atoms simultaneously enter the interaction radius of the ion and a three-body process takes place. (II) The three-body reaction ejects the ion onto a trajectory much larger than the atom cloud. (b) Illustration of our simple model. *Left:* Various possible time traces for the atom number. If only binary atom-ion collision occur the atomic sample decays exponentially (Trace T_1). Three-body events (E_2, E_3) interrupt the atom loss until the atom is recooled and reenters the sample at point R_2 (Traces T_2 and T_3). *Right:* Atom number histogram from Fig. 4.1(c) ($\tau = 8\,\mathrm{s}$) and the corresponding simulation result (solid black line). (c) Plot of the probability $P_{\mathrm{threebody}}$ for initial atomic densities $(1.8, 1.1, 0.7, 0.3) \times 10^{12}\mathrm{cm}^{-3}$ and atom numbers $(6.5, 4.0, 2.8, 1.6) \times 10^4$, respectively. The solid lines are results of the numerical simulation.

a histogram divided by the histogram's total count number (for details see supplemental material). Fig. 4.2(c) shows these data for four atomic densities, including the data in Fig. 4.1(c). All four data sets have in common that the number of three-body events first rapidly increases and subsequently levels off. The levelling off is mainly due to the fact that the probability for a three-body reaction is strongly density-dependent. Surprisingly, in the beginning of the interaction ($\tau \lesssim 1\,\mathrm{s}$) only very few three-body events are detected for the lower density samples. We explain this delay by an initial phase of sympathetic cooling of the Rb^+ ion which experiences significant heating during the preparation (e.g. rf evaporative cooling) of the atom cloud. From numerical calculations similar to [Zip10a] we estimate that recooling times of about $1\,\mathrm{s}$ in atom clouds with $n_\mathrm{at} \approx 10^{12}\,\mathrm{cm}^{-3}$ correspond roughly to ion kinetic energies of a few $100\,\mathrm{K}\cdot k_\mathrm{B}$. The ion will typically undergo several thousand binary collisions with cold atoms until it is sympathetically recooled to $\mathrm{mK}\cdot k_\mathrm{B}$ energies. We are able to describe all four data sets in Fig. 4.2(c) consistently with our simple Monte Carlo model (continuous lines) [2]. From a fit to the data sets we obtain rate coefficients $K_2 = 5.0(5) \times 10^{-9}\ \mathrm{cm}^3/\mathrm{s}$ and $K_3 = 3.3(3) \times 10^{-25}\ \mathrm{cm}^6/\mathrm{s}$ and the reentry parameter $c_\mathrm{out} \approx 1.7 \times 10^5\,\mathrm{s}$. The errors given exclude systematic uncertainties in the atomic density. We note that the value for our atom-atom-ion K_3 rate coefficient is more than three orders of magnitude larger than the three-body coefficient for three colliding neutral $^{87}\mathrm{Rb}$ atoms [Esr99]. The value of K_2 roughly agrees with previously obtained results [Zip10b, Sch10a]. For the typical atom numbers used here the obtained value of c_out results in several seconds of negligible atom-ion interaction following each ejection of the ion.

In order to challenge our analysis we have attempted to model the events that send the ion into orbit as two-body processes. The corresponding linear density dependence of the event rate yields inconsistent fit results such that we can exclude two-body interactions as an explanation for our data (for details see supplemental material). As a cautionary note, we point out that three-body recombination processes to weakly-bound molecular states with binding energies $\lesssim 10\,\mathrm{meV}$ are not detected in our experiments as the ion will not leave the atom cloud. Thus, the true three-body coefficient may even be significantly larger.

---

[2] The initial cool-down time is accounted for by adjusting the starting time for each data set.

4.4   Direct Measurement of the Energy released in the Recombination Events

In a further experiment, we quantify the kinetic energy gained by the ion in a three-body event. The idea is to lower the depth of the ion trap such that an ion with an energy of a few 0.1 eV escapes while a cold ion remains trapped. The experiment is performed as follows. We prepare a first atom cloud which we bring to interaction with an ion for 4 s. Similar to the previously described experiments, we measure the ion-induced atom loss from which we judge whether or not the ion has participated in a three-body event. Directly afterwards, the ion trap depth is reduced to one of 5 values U_{red} by lowering one of the endcap voltages of the Paul trap within 300 ms. The voltage is held at this value for 200 ms and ramped back up within 200 ms. Subsequently, we probe the ion's presence in the trap via the loss it inflicts on a second atom cloud. This cloud is prepared within 40 s and contains about 5×10^4 atoms. Figure 4.3(a) shows the remaining atom number of the atom cloud after 6 s of interaction time [3]. An atom number $\lesssim 1 \times 10^4$ indicates the presence of an ion while a number around 4.5×10^4 shows its absence. The clear splitting of the two groups of data allows for ion detection with an efficiency close to unity. Figure 4.3(a) contains two different plot symbols, distinguishing two classes of ions. Black squares correspond to ions that have participated in a three-body event within the first atom cloud while grey circles correspond to ions where only binary collisions were detected. We now analyze the data points of Fig. 4.3(a) by calculating the probability for ion loss P_{loss} for each trap depth (P_{loss} = Number of lost ions / Number of trials). The result is shown in Fig. 4.3(b). As expected, ions that were previously involved in a three-body recombination process can in general escape from deeper traps than ions only involved in binary interactions. To obtain a more quantitative measure of the ion energy we fit broadened step functions of the form $1/\{1 + \exp[(U_{\mathrm{red}} - U_{\mathrm{loss}})/d]\}$ to the data. The width of the steps d is on the order of 0.15 eV. From the energy offset between the two fit curves we estimate the gained energy $\Delta U_{\mathrm{loss}} \approx 0.4$ eV. We note that for trap depths $U_{\mathrm{red}} \lesssim 0.25$ eV the probability of loss is high in general. This suggests that the stability of our trap is compromised at shallow trap settings. In fact, lowering the voltage of only one of the two endcaps renders the trap quite asymmetric. This degrades the ideal quadrupole field configuration and thus the stability of the ion trap. As a consequence the accuracy with which we can determine the energy released in the three-body process is limited. Still, we find a clear splitting between the step functions of 0.4 eV in Fig. 4.3(b). Thus, a

---

[3]   We deliberately apply an offset electric field of about 6 V/m to increase the eMM energy. In this way, we make three-body reactions unlikely and induce a rapid loss of atoms through binary atom-ion collisions.
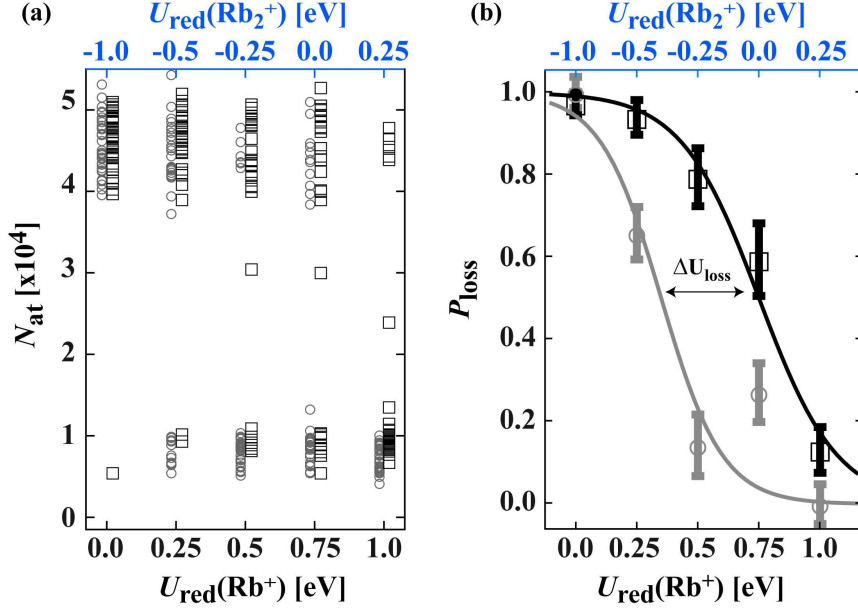
Figure 4.3: (a) Probing the ion's presence using an atom cloud. A low (high) remaining atom number N_{at} signals the presence (absence) of an ion. For better visibility, we have slightly offset in energy the black squares corresponding to ions that have participated in a three-body process from the grey circles corresponding to ions where purely binary collisions were detected. (b) Ion loss probability P_{loss} calculated from the data in (a). The continuous lines are fits to the data using a broadened step function. The trap depths U_{red} are determined for our Paul trap geometry using methods detailed in [Sin10] for both Rb^+ (bottom abscissa scale) and Rb_2^+ (top). A trap with negative trap depth value is non-trapping.

resolution of the measurement on the order of 0.1 eV seems plausible.

Mainly two recombination processes come into consideration. In a reaction of the type $Rb + Rb + Rb^+ \rightarrow Rb_2 + Rb^+$ the formation of a neutral molecule is catalyzed by the ion which carries away 2/3 of the energy released. If deeply bound Rb_2 molecules are produced, binding energies of up to ~ 0.5 eV are released, in agreement with the measurement. A second possible recombination process, $Rb + Rb + Rb^+ \rightarrow Rb_2^+ + Rb$, produces a molecular ion and a neutral atom. However, as indicated in figure 3, the molecular ion, due to its higher mass, experiences a significantly shallower trap than the atomic ion and would immediately be lost for our parameter range. We thus infer that the ion at hand is Rb^+. However, we cannot completely exclude the formation of an intermediate molecular ionic state which may subsequently dissociate.

4.5 Measurement of the Energy Dependence of the Three-Body Coefficient

In a third type of measurement we study the dependence of the three-body coefficient on the ion kinetic energy which we can tune by controlling the ion micromotion. For this we apply a static electric field ϵ perpendicular to the axis of the Paul trap and let the ion interact for $\tau = 8\,\mathrm{s}$ with an atom cloud with $n_{\mathrm{at}} \approx 1.0 \times 10^{12}\,\mathrm{cm}^{-3}$. We find $P_{\mathrm{threebody}}$ to increase roughly by a factor of 5 when reducing ϵ from $3.25\,\mathrm{V/m}$ to $0\,\mathrm{V/m}$ (Fig. 4.4(a)).
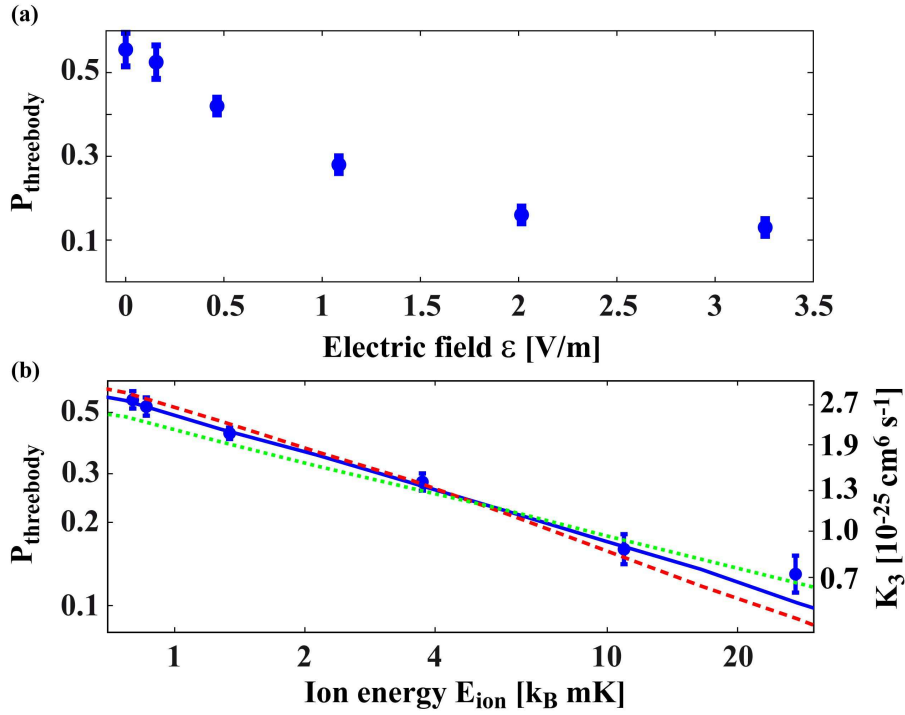

Figure 4.4: (a) $P_{\mathrm{threebody}}$ as a function of the external electric field. (b) Double-logarithmic plot of $P_{\mathrm{threebody}}$ as a function of the ion energy E_{ion}. A scale for the three-body coefficients K_3 as derived from the simulation is also given (see text for details).

In order to express the electric field values in terms of kinetic energy we make use of the relation $E_{\mathrm{eMM}} = c_{\mathrm{trap}} \cdot \epsilon^2 + E_{\mathrm{res}}$ with c_{trap} being a constant that depends on the trap configuration and the ion mass [Ber98]. E_{res} stands for residual uncompensated micromotion energy. The ion energy can be expressed as $E_{\mathrm{ion}} = c_{\mathrm{dyn}} \cdot E_{\mathrm{eMM}}$. c_{dyn} is a constant which depends on the atom-ion mass ratio and the spatial extension of the atom cloud and for our experiments can be estimated to be about 2 [Zip10a]. We attempt to describe our data with a power-law dependence of the form $K_3 \propto E_{\mathrm{ion}}^{\alpha}$ within our simulation. Good agreement with the data is achieved for $\alpha = -0.43$, $E_{\mathrm{res}} = 370\,\mu\mathrm{K}$ $\cdot k_{\mathrm{B}}$ and a maximal value for K_3 of $2.75 \times 10^{-25}\,\mathrm{cm}^6/\mathrm{s}$ (solid trace in Fig. 4.4(b)). For

comparison, curves for exponents $\alpha = -0.5$ and $\alpha = -0.33$ (dashed and dotted traces, respectively) are shown as well. A residual energy $E_\text{res} = 370 \, \mu\text{K} \cdot k_\text{B}$ is a reasonable value for our current setup and in agreement with other measurements of ours [Krü16b].

4.6 Conclusion

In conclusion, we have studied three-body recombination involving a single trapped ion and two of its parent atoms at collision energies approaching the sub-mK regime. With a relatively simple model we can understand the two- and three-body collision dynamics and extract corresponding rate coefficients. We observe an increase of the three-body rate coefficient with decreasing collision energy, a behavior that can be expected to become crucial for future experiments targeting even lower temperatures. After a three-body event, ion energies on the order of 0.4 eV were measured, indicating that deeply bound molecules have been created. Since we have not observed Rb_2^+ ions, the formation of Rb_2 seems probable. The ion would then act as an atomic size catalyzer at mK temperatures.

4.7 Supplemental Material

1. Method to determine $P_\text{threebody}$

$P_\text{threebody}$ is the probability for at least one three-body process to happen within time τ. We describe here in more detail how we extract $P_\text{threebody}$ from an atom number histogram. Fig. 4.5 shows such a histogram which consists of two components: a Gaussian distribution on the left hand side and a tail on the right hand side. We assume that only counts outside the Gaussian (i.e. within the tail) correspond to experimental runs with atom-atom-ion three-body events. Then,

$$P_\text{threebody} = \frac{\text{Sum of all counts in the tail}}{\text{Total number of counts of histogram}} .$$

A Gaussian fit to the peak on the left hand side of the histogram separates the tail from
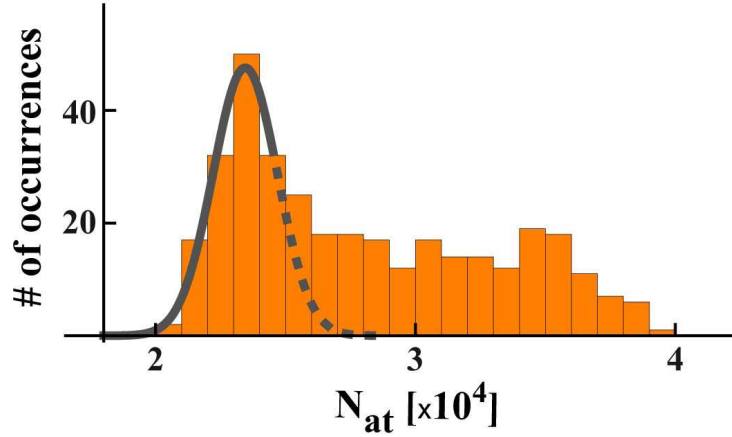
Figure 4.5: Illustration of the fit method used to determine $P_{\text{threebody}}$. The histogram shown is taken from Fig. 1 of the main text ($\tau = 4\,\text{s}$).

the Gaussian distribution. For the fit we use the data points roughly up to the top of the peak of the distribution (solid line in the figure). In addition, we estimate the uncertainty of $P_{\text{threebody}}$. For this, we vary the number of columns used for the fit and record the corresponding fluctuations of the fit results.

2. Description of the numerical simulation

Based on Monte Carlo techniques, we have implemented a simple numerical simulation of the atom-ion interactions. The simulation takes into account the binary atom-ion collisions leading to atom loss, recooling of the ion and the three-body events which eject the ion from the atom cloud.

Initially the ion is positioned at the center of the atom cloud. Time advances in small steps Δt. The evolution of atom number N_{at} and density n_{at} (for the time being) follows

$$N_{\text{at}}(t + \Delta t) = N_{\text{at}}(t) - K_2 n_{\text{at}}(t)\Delta t$$

and

$$n_{\text{at}}(t + \Delta t) = n_{\text{at}}(t)\frac{N_{\text{at}}(t + \Delta t)}{N_{\text{at}}(t)}\ .$$

Thus, in our simple model two-body collisions lead to an exponential decay of the atom number, which is a sufficiently good approximation of the observed behavior. We neglect ion-induced temperature changes of the atom cloud which would lead to corrections of the density evolution.
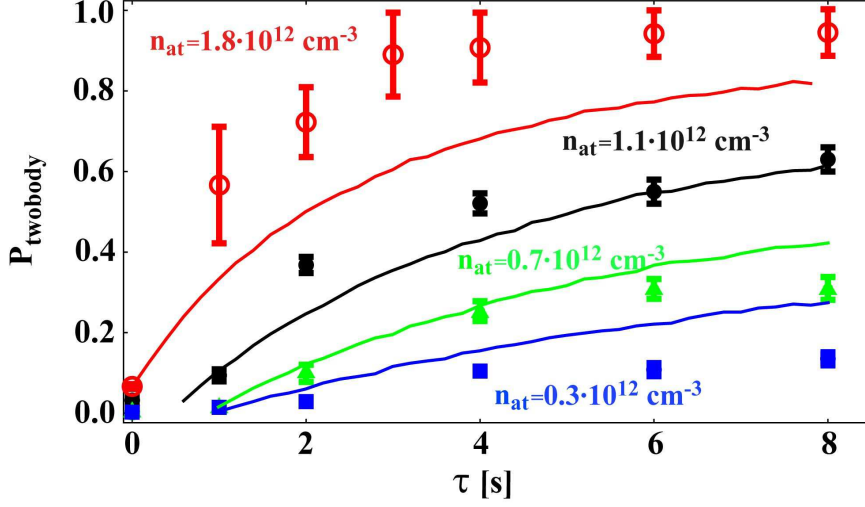
Figure 4.6: Data points from Fig. 2c of the main text and results of simulations of the ion ejection as two-body events.

The possibility of a three-body event is included in the simulation in a probabilistic way. We compute

$$\wp_{\text{threebody}} = K_3 n_{\text{at}}(t)^2 \Delta t$$

which is the probability that within the time step Δt a three-body event will take place. If the three-body event does happen, the simulation stops the evolution of N_{at} and n_{at} until a reentry of the ion into the atom cloud takes place. The probability for the reentry within a time step Δt is

$$\wp_{\text{reentry}} = \frac{N_{\text{at}}(t)}{c_{\text{out}}} \Delta t.$$

The simulation runs until the total interaction time τ is reached. By performing many runs of the simulation we arrive at the atom number distribution in figure 2b and the averaged values for $P_{\text{threebody}}$ in figures 2c and 4 of the main text.

3. Modelling of the ion ejections as two-body events

An important test of our interpretation of the experimental data is the comparison with a model that does not contain three-body collisions. Instead, events sending the ion onto large orbits are also modelled as two-body processes. We can adapt our simulation of the previous section by simply replacing the probability density $\wp_{\text{threebody}}$ by $\wp_{\text{twobody}}^*$ where

$$\wp_{\text{twobody}}^* = K_2^* n_{\text{at}}(t) \Delta t . \tag{4.1}$$

Fig. 4.6 shows the simulation results using a best fit value of $K_2^* = 2.0 \times 10^{-13}$ cm^3/s.

While a data set for a single density can still be described reasonably well, this clearly does not work for all four sets with a single K_2^* rate constant. Thus we exclude two-body interactions as the cause of the ion-ejection.

Notes

- References referring to unpublished work in the original publication have been replaced with [Här13c, Här13b, Krü16b] in this reprint.

- The more recent results with Ba^+ in [Krü16b] predict the dominant formation of weakly-bound molecular ions in three-body-recombination based on classical trajectory calculations. This statement is compatible with this publications' observation of highly energetic Rb^+ as the sole product, if fast secondary reactions dissociate the primary product Rb_2^+. Collisional or light induced processes can fulfill this role and provide the kinetic energies we observed in the experiments. Ongoing measurements with Ba^+ indicate that newly formed $BaRb^+$ molecules are indeed photo-excited by the 1064 nm dipole trap laser. This possible secondary process however was not yet investigated with the Rb^+-Rb system.

Chapter 5

Minimization of ion micromotion using ultracold atomic probes

Arne Härter, Artjom Krükow, Andreas Brunner and Johannes Hecker Denschlag

Institut für Quantenmaterie und Center for Integrated Quantum Science and Technology IQST, Universität Ulm, 89069 Ulm, Germany

---

A reprint of the original publication can be found in the appendix at the end of the thesis

We report on a sensitive method to minimize excess micromotion of an ion in a Paul trap. The ion is placed in an ultracold cloud of neutral Rb atoms in which ionic micromotion induces atomic losses and heating. Micromotion is minimized by applying static electric offset fields such that both loss and heating are minimized. We achieve a compensation on the level of the most precise compensation methods to date. In contrast to these methods, our scheme is applicable even for ions that cannot be optically probed. Furthermore, it avoids the formation of temporary patch charges which are a main issue for the long-term stability of micromotion minimization.

5.1   Introduction

In the last decades there has been tremendous progress in experiments with ions confined in Paul traps. Single or well-defined numbers of ions have been prepared and manipulated on the quantum level [Lei03, Bla08, Häf08, Bla12]. Laser cooling and manipulation of these strongly isolated quantum objects can then be used for precision spectroscopy, quantum simulation and quantum computation. For such experiments, control over the ionic excess micromotion is a pre-condition. Furthermore, a young line of research investigates cold collisions between trapped ions and ultracold neutral atomic gases [Gri09, Zip10b, Sch10a, Hal11, Rel11, Rav12]. Here, excess micromotion sets the dominant energy scale and it needs to be compensated with high precision to reduce the atom-ion collision energies to the mK regime and beyond.

Micromotion is a driven oscillatory motion of the ions in the radio frequency (rf) field of the Paul trap. Ideally, the ion is trapped at a node of the rf field, where micromotion is minimal. However, possible stray electric fields displace the ion from this location and into trap regions with increased rf fields. These in turn increase the micromotion amplitudes by inducing the so-called excess micromotion. This micromotion contribution thus needs to be minimized by compensating the stray electric fields. To date, a number of methods have been devised to accurately compensate excess micromotion, all of which employ resonant scattering of light off the ion. Such methods employ, e.g., motional side-band spectroscopy [Ber98, Raa00, Chu13], photon correlation measurements [Ber98, Pyk13], precise position detection of the ion while changing the rf confinement [Ber98], or detection of ionic motional excitation when resonantly modulating the ion trap potential [Nar11, Tan12]. For the ionic species typically used in these experiments, resonant light at wavelengths below 500 nm is needed. This is known to produce unstable patch charges on dielectric surfaces making frequent readjustments of the compensation voltages necessary.

Also, the laser-based compensation methods fail when working with "dark" ions, such as Rb^+, where optical transitions are not accessible.

Here, we present a compensation method where ion micromotion is probed by immersing a single ion into an ultracold ^{87}Rb atom cloud. The ion collides with the atoms at typical rates of several kHz. Since the atomic temperatures T_{at} in our experiments are on the order of $1\,\mu K$, the dominant energy scale for these collisions is set by the ion micromotion which typically is orders of magnitude larger. Through the collisions, energy is transferred from the ion to the atoms [Zip10b, Sch10a, Zip11b]. If the transferred energy is larger than the atom trap depth, the colliding atom will be lost. Otherwise, the atom remains trapped and eventually rethermalizes with the rest of the cloud leading to an increase of the atomic temperature. After several seconds of immersion and typically many thousand collisions we detect both the number of remaining atoms and the final atomic temperature by standard absorption imaging techniques. In an iterative process, we minimize the loss and heating of the atom cloud by applying electric compensation fields, thus minimizing excess micromotion.

5.2   Experimental Setup

The experiments are performed with ^{87}Rb$^+$ ions confined in a linear Paul trap of which the design is discussed in detail in reference[Sch12]. The effective radial distance from the trap center to the four rf electrodes is $R' = 2.6\,mm$ and the trap is driven at a frequency of $\Omega = 2\pi \times 4.17\,MHz$ and an amplitude of $V_0 = 500\,V$. The endcap electrodes are supplied with static voltages of about $8\,V$. This configuration results in trapping frequencies of $(\omega_r, \omega_z) = 2\pi \times (350, 51)\,kHz$. To compensate radial ion micromotion, we apply electric offset fields perpendicular to the trap axis by using two pairs of compensation electrodes. We begin our investigations by immersing the ion into the center of a comparatively dilute atom cloud which is held in a far-detuned optical dipole trap [Sch10a]. At atomic trap frequencies of $(136, 141, 40)\,Hz$, initial atom number $N_{at} = 1.1 \times 10^4$ and temperature $T_{at} = 1.1\,\mu K$, the initial atomic peak density is $n_{at} = 1 \times 10^{11}\,cm^{-3}$. The atom clouds are reproduced within an experimental cycle time of about $30\,s$ with fluctuations in atom number of less than $5\,\%$, even for thousands of experimental cycles.

Figure 5.1(a) shows both decay and heating of the atom cloud as a function of the interaction time τ when exposed to a single ion. This measurement was performed for two micromotion settings as determined by the radial electric offset field ε_r. For a small offset field ($\varepsilon_r < 0.1\,V/m$, blue data points), atom loss and heating are suppressed as compared
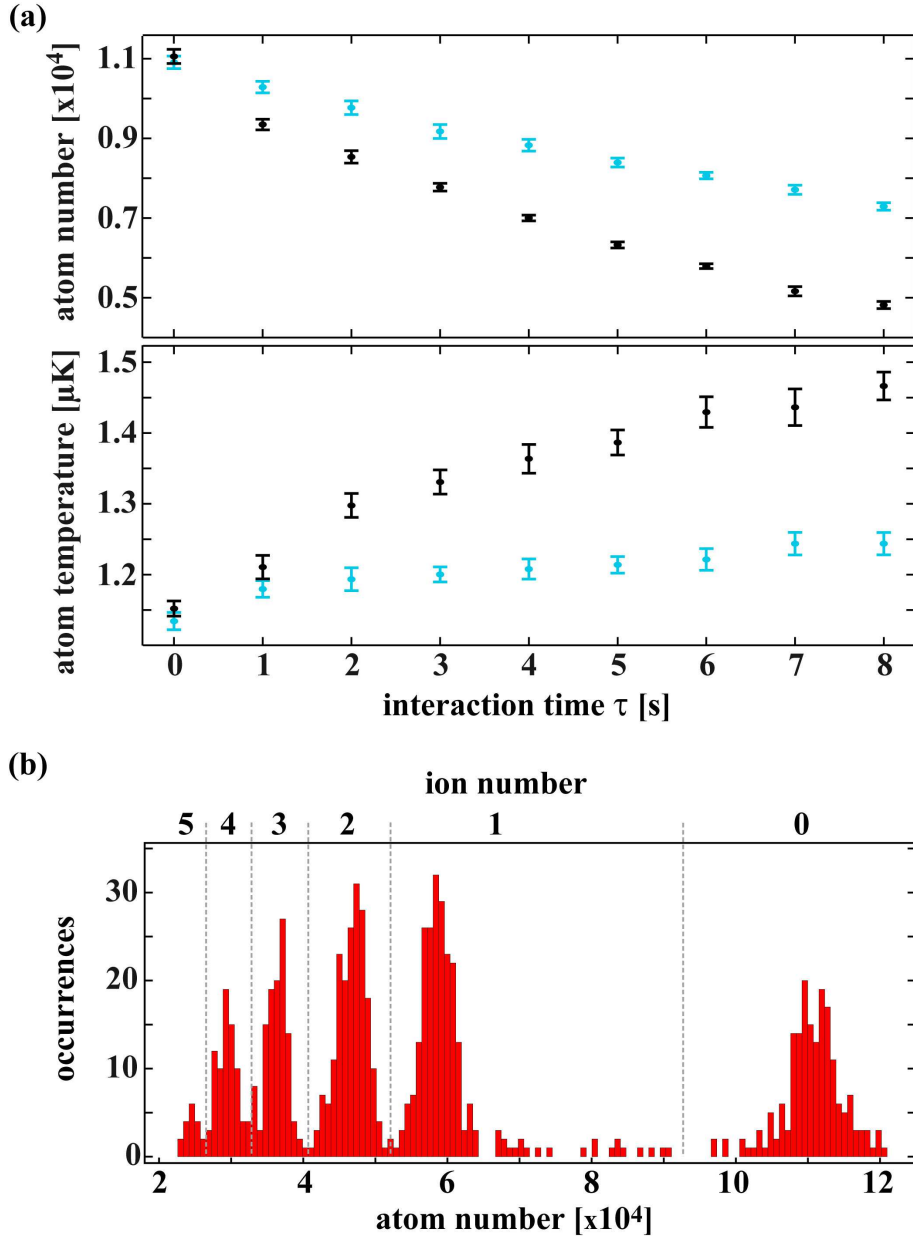
(a)

(b)

Figure 5.1: Atomic signals after atom-ion interaction. (a) Evolution of atom numbers (upper panel) and atomic temperatures (lower panel) during interaction with a single ion. The measurement was performed both for $\varepsilon_r < 0.1$ V/m (blue data points) and for $\varepsilon_r = 4$ V/m (black data points). (b) Histogram of remaining atom numbers after exposing about 1000 atom clouds for 2 s to a variable number of trapped ions. The peak structure of the histogram indicates that the atom number decreases in nearly discrete steps with an increasing number of ions in the trap (indicated on the top axis). This result is used to determine an unknown number of ions in the trap by measuring the losses that the ions inflict on a cold atom cloud.

to a field of $\varepsilon_r = 4\,\text{V/m}$ (black data points). In addition to the electric fields, also the number of trapped ions obviously strongly affects the losses and heating of the atom cloud. As we want to carry out all our minimization experiments with a single ion, we have developed a way to determine the ion number in the cloud by simply looking at atomic losses. Fig. 5.1(b) shows a histogram of about 1000 atom loss experiments where atomic clouds $(N_{\text{at}} = 1.1 \times 10^5,\ n_{\text{at}} = 3 \times 10^{12}\,\text{cm}^{-3})$ were exposed to a variable number of trapped Rb^+ ions for $2\,\text{s}$ at electric fields of several V/m. The well separated peaks of the distribution of the histogram reflect the number of trapped ions, as indicated in the graph. As an example, an atom number around 6×10^4 indicates the presence of a single trapped ion. We then use such a single ion for the investigations of ion micromotion.

5.3   Radial excess micromotion compensation

We now perform a first micromotion compensation measurement for which we immerse the single ion for a fixed interaction time $\tau = 8\,\text{s}$ into the dilute atom cloud $(N_{\text{at}} = 1.1 \times 10^4$, $n_{\text{at}} = 1 \times 10^{11}\,\text{cm}^{-3})$. We vary the radial electric fields between $\varepsilon_r = \pm 5$ V/m and measure the final atom numbers and temperatures (Fig. 5.2). At each electric field setting we perform about 15 individual measurements which are shown as the scattered grey points in the figure. Each data point was measured with a freshly prepared atom cloud. While most of these points lie within a relatively small range of scatter, there are some extreme outliers with almost no atom loss or heating effect (best seen in Fig. 5.2(a)). These extreme events occur predominantly when ion micromotion is well compensated and are explained by three-body recombination processes between the ion and two neutral atoms, as described in detail in ref. [Här12]. Briefly, the energy released upon recombination ejects the ion from the atom cloud so that atom-ion collisions temporarily stop and no more losses occur. In the measurement shown in Fig. 5.2, the atomic density is low enough that three-body recombination processes are quite rare.

At this point of our investigations, we want to suppress their influence on the data. To do this, we first determine the mean atom number and temperature at each interaction time from all data points at this field setting. Then, we ignore those data points which lie outside a 2σ environment around these mean values and average over the remaining measurement outcomes. In this way, the influence of the extreme events is filtered out to a large part and the mean values given in Fig. 5.2 contain almost exclusively two-body atom-ion collisions.
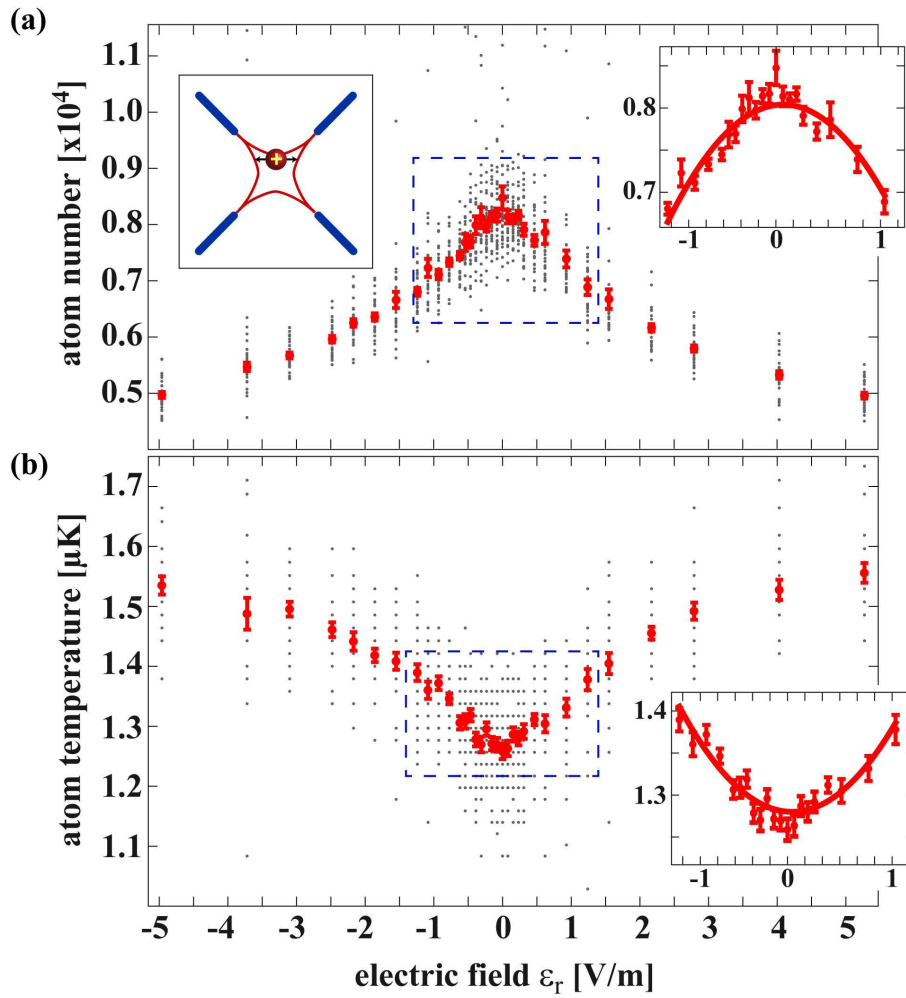
Figure 5.2: Micromotion compensation using a dilute atom cloud. *Insets:* Parabolas are fitted locally to the atom number maximum and the temperature minimum. This allows for electric field compensation down to $\Delta\varepsilon_r < 0.05\,\mathrm{V/m}$.
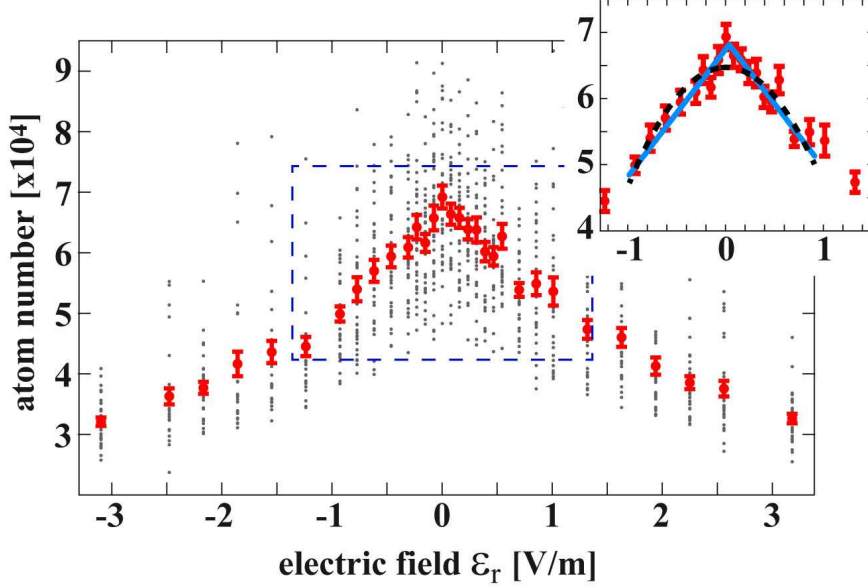
Figure 5.3: Same as Fig. 5.2 but using an atomic sample at a density of $n_{at} \approx 1.5 \times 10^{12}$ cm^{-3}. The additional effects of three-body atom-ion recombination increase the electric field sensitivity and allow for field compensation down to $\Delta\varepsilon_r < 0.02$ V/m.

Figure 5.2 shows a monotonic dependence on the electric field strength $|\varepsilon_r|$, both in the atom numbers and the atomic temperatures. Atom losses and heating are minimal for a vanishing offset field. Furthermore, as one might expect, the data is symmetric with respect to the sign of the electric field. Scans of this type can be used to minimize electric fields with a sensitivity given by how precisely we can determine the center of the peak (dip). Fitting a parabola to the data (see insets in Fig. 5.2) allows us to extract the optimal electric field setting to within $\Delta\varepsilon_r < 0.05$ V/m. A corresponding parameter of crucial importance in cold atom-ion interactions is the average micromotion energy [Ber98]

$$E_r = \frac{m_{ion}}{16}(q_r r\,\Omega)^2\,, \tag{5.1}$$

where m_{ion} is the ionic mass, $q_r = 2eV_0/(m_{ion}R'^2\Omega^2) \approx 0.24$ and $r = e\varepsilon_r/(m_{ion}\omega_r^2)$ is the displacement of the ion from the rf node. Using equation (5.1) we derive a residual radial micromotion energy of $E_r = k_B \times 3.2\mu$K from our uncertainty in the electric offset field ε_r.

It turns out that we can increase the sensitivity by carrying out the measurement using a larger and denser atom cloud ($N_{at} = 9 \times 10^4$, $n_{at} = 1.5 \times 10^{12}$ cm^{-3}). The increase in density by more than an order of magnitude compared to the previous measurement strongly increases the three-body atom-ion recombination rate. This can be seen when

comparing the data scatter in Figs. 5.3 and 5.2(a). Especially for small electric fields ε_r the scatter in Fig. 5.3 is large, indicating that nearly every atom-ion interaction period includes at least one three-body event. Thus, it does not make sense to sort out data with three-body events. We simply take the mean of all data points. Oddly, this changes the form of the data curve (as compared to Fig. 5.2(a)) which is now cusp-shaped. The cusp can be explained by two facts: 1) Three body-recombination events in general lead to an increase in the final atom number, as an ejected ion does not kick out atoms. 2) The probability for three-body events increases strongly with decreasing micromotion. As seen in the inset of Fig. 5.3(a), a parabola is not the ideal fit to the cusp. A cusp function such as $c_1|\varepsilon_r - c_2| + c_3$, where $c_{1,2,3}$ are fit parameters, does much better. We obtain an uncertainty of $\Delta\varepsilon_r < 0.02\,\mathrm{V/m}$ which corresponds to a micromotion energy $E_r = k_\mathrm{B} \times 0.6\,\mu\mathrm{K}$.

5.4   Axial excess micromotion compensation

The data shown in Figs. 5.1-5.3 are obtained by varying electric offset fields in the vertical direction, perpendicular to the trap axis. Measurements in the horizontal direction are performed in a similar way with similar results. In a symmetrically driven linear Paul trap, ideally, there is no micromotion along the trap axis. We drive our trap in an asymmetric way where two of the four rf electrodes are grounded. This leads to non-vanishing rf fields (and micromotion) everywhere along the trap axis except in the central point (see schematic in Fig. 5.4), analogous to the radial directions. Although these axial rf fields are significantly weaker than the corresponding radial ones, they still result in large micromotion energies if the ion is strongly shifted from the trap center. Due to the small axial trapping frequency of about $50\,\mathrm{kHz}$, ions in our trap are highly susceptible to electric stray fields in axial direction. We adjust the axial offset electric fields by changing the voltage on one of the endcap electrodes. Figure 5.4 shows a scan over several V/m which moves the ion through the entire atom cloud. The inner parabolically shaped parts of the data around $\varepsilon_r = 0$ are similar to the curves in Figs. 5.2 and 5.3. The outer wings, however, mainly reflect the decrease of the density at the edge of the atom cloud. Here, the ion probes the Gaussian density distribution of the atoms (as discussed in ref. [Sch10a]). Again, fitting a parabola to the central region of Fig. 5.4 we obtain an electric field uncertainty of $\Delta\varepsilon_z < 0.06\,\mathrm{V/m}$ which corresponds to a positional accuracy of $\Delta z < 0.7\,\mu\mathrm{m}$ and a residual axial micromotion energy $E_\mathrm{z} = k_\mathrm{B} \cdot 21\,\mu\mathrm{K}$ [1]. Thus, the micromotion energy is significantly larger than for the radial directions. Stronger axial confinement of the ion

---

[1] To calculate E_z we use equation 5.1 and replace q_r and r by q_z and z. In our trap $q_z \approx 0.04 \cdot q_r \approx 0.01$.
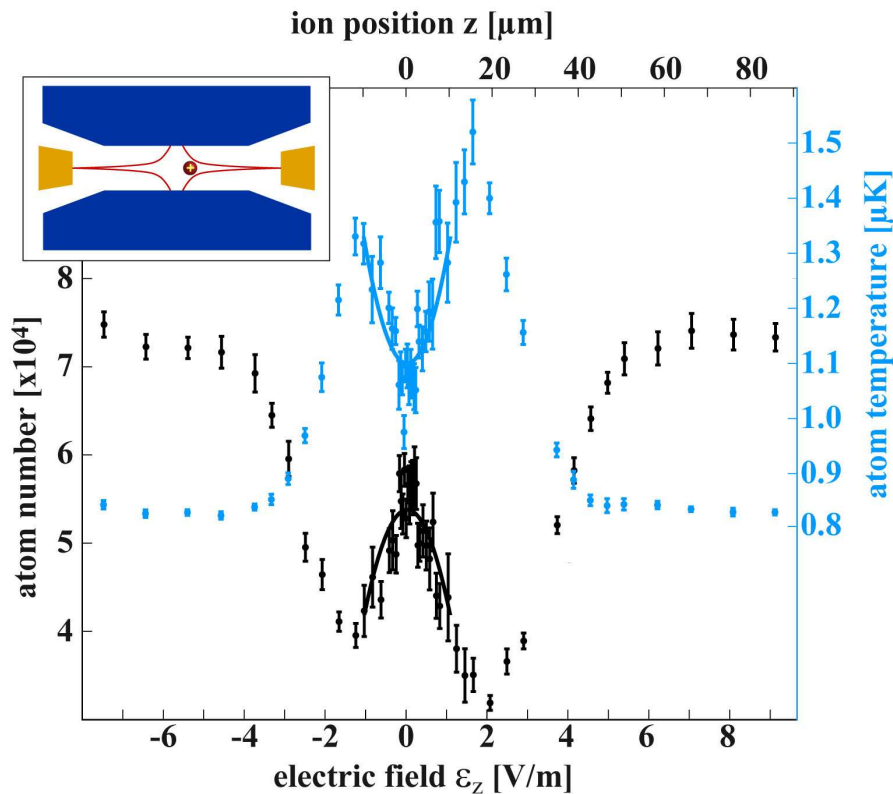
Figure 5.4: Influence of axial ion micromotion on atom number and atom temperature. By scanning the electric field ε_z, the ion is moved across the atom cloud. Losses and heating are a convolution of both micromotion and atomic density. The parabolic fits allow us to determine the electric field uncertainty to $\Delta\varepsilon_z < 0.06\,\text{V/m}$ and the position of the rf frequency node to within $\Delta z \approx 0.7\,\mu\text{m}$.

would increase the achievable positional accuracy of this measurement and thereby reduce the corresponding micromotion energy.

5.5 Comparison with established compensation methods

The micromotion minimization scheme using atomic probes works in all three spatial dimensions. This is a great advantage as it relaxes the experimental complexity, e.g. in terms of optical access to the trap center. Practically, however, a good compensation in one direction requires an iterative process of compensating all three dimensions. Only then can the micromotion energy of the ion be significantly reduced. Indeed, the data shown in this work were acquired after micromotion in the remaining two dimensions had already been minimized.

Table 5.1: Comparison of commonly used figures of merit to quantify ion micromotion. Residual electric fields $\varepsilon_{r,z}$ and corresponding micromotion amplitudes $u_{r,z}$ and energies $E_{r,z}$ are given along with the trap drive frequency and the secular frequencies. The first seven rows show values extracted from information of the given references. The last row gives the values obtained in this work.

Ion species	$\dfrac{\Delta\varepsilon_r}{\text{V/m}}$	$\dfrac{u_r}{\text{nm}}$	$\dfrac{E_r}{\mu\text{K}\,k_\text{B}}$	$\dfrac{\Delta\varepsilon_z}{\text{V/m}}$	$\dfrac{u_z}{\text{nm}}$	$\dfrac{E_z}{\mu\text{K}\,k_\text{B}}$	$\dfrac{\Omega/2\pi}{\text{MHz}}$	$\dfrac{\omega_r/2\pi}{\text{MHz}}$	$\dfrac{\omega_z/2\pi}{\text{MHz}}$
^{138}Ba$^{+\ \text{a}}$	1.8	7	230	-	-	-	5.3	1.2	0.4
^{172}Yb$^{+\ \text{b}}$	0.9	1.1	175	0.3	0.2	5.4	25.7	0.48	0.12
^{40}Ca$^{+\ \text{c}}$	0.4/2.5	6/40	380/17000	-	-	-	15	1.2/1.4	0.4
^{27}Al$^{+\ \text{d}}$	7	2.5	710	-	-	-	59	6	3
^{88}Sr$^{+\ \text{e}}$	1.0	0.8	33	-	-	-	22	3.6	3.1
^{40}Ca$^{+\ \text{f}}$	0.4	0.4	4.8	-	-	-	23.5	3.4	1.2
^{25}Mg$^{+\ \text{g}}$	-	-	-	-	0.2	0.75	25	4.5	2
^{87}Rb^{+}	0.02	0.5	0.5	0.06	3.4	21	4.17	0.35	0.05

[a] [Chu13]   [b] [Pyk13]   [c] [Nar11]   [d] [Cho10]   [e] [Ake12]   [f] [Chw09]   [g] [Hem11]

To verify that the atom-based micromotion compensation yields the same optimal electric field settings as established optical methods, we perform measurements on a single ^{138}Ba^{+} ion with no atom cloud being present. We laser cool the ion and detect its fluorescence on a charge-coupled device camera. We use two micromotion minimization methods: 1) minimizing position changes of the ion when changing the trap frequency of the Paul trap [Ber98]. 2) minimizing motional excitation of the ion while modulating the rf with the trap frequency [Nar11, Tan12]. With these methods we are able to compensate radial electric fields to about $0.1\,\text{V/m}$ and to position the ion axially to better than $1\,\mu\text{m}$ (corresponding to $\Delta\varepsilon_z \approx 0.09\,\text{V/m}$).

In order to benchmark our minimization method, we compare its accuracy to the ones of various optical methods, as reported in the literature. Table 5.1 lists the field uncertainties $\Delta\varepsilon_{r,z}$, the motional micromotion amplitudes $u_{r,z}$, and the micromotion kinetic energies $E_{r,z}$ for a variety of species and ion traps. Care has to be taken when directly comparing the results, as the set-ups, trap frequencies and rf-drive frequencies differ substantially. Nevertheless, the table shows that atom-based micromotion compensation is as precise as the reported values achieved with optical methods.

5.6   Conclusion

In conclusion, we have presented a method to compensate ion excess micromotion in a Paul trap. The trapped ion is immersed into an atomic cloud. Micromotion is detected

in terms of atomic loss and heating of the cloud as induced by two-body and three-body collisions between ion and atoms. Our minimization results are as precise as reported values for fluorescence-based detection methods. While our minimization method is certainly somewhat slower than most optical ones, it works in all three dimensions while requiring optical access from only a single direction. Besides compensation of excess micromotion due to stray electric fields, as demonstrated here, it should also work to reduce excess micromotion due to phase differences of opposing rf electrodes of the Paul trap. The method can be used for all ionic species, including "dark" ions without accessible optical transitions, as long as collisions with the atomic gas are mainly elastic. Finally, as it does not involve optical ion detection, creation of patch charges is avoided. Hence, long-term stability of the compensation settings is achieved, which is a prerequisite for precision compensation of micromotion.

Chapter 6

Long-term drifts of stray electric fields in a Paul trap

Arne Härter, Artjom Krükow, Andreas Brunner and Johannes Hecker Denschlag

Institut für Quantenmaterie und Center for Integrated Quantum Science and Technology IQST, Universität Ulm, 89069 Ulm, Germany

We investigate the evolution of quasi-static stray electric fields in a linear Paul trap over a period of several months. Depending on how these electric fields are initially induced, we observe very different time scales for the field drifts. Photo-induced electric fields decay on time scales of days. We interpret this as photo-electrically generated charges on insulating materials which decay via discharge currents. In contrast, stray fields due to the exposure of the ion trap to a beam of Ba atoms mainly exhibit slow dynamics on the order of months. We explain this observation as a consequence of a coating of the trap electrodes by the atomic beam. This may lead to contact potentials which can slowly drift over time due to atomic diffusion and chemical processes on the surface. In order not to perturb the field evolutions, we suppress the generation of additional charges and atomic coatings in the Paul trap during the measurements. For this, we shield the ion trap from ambient light and only allow the use of near-infrared lasers. Furthermore, we minimize the flux of atoms into the ion trap chamber. Long-term operation of our shielded trap led us to a regime of very low residual electric field drifts of less than $0.03\,\text{V/m}$ per day.

6.1   Introduction

Paul traps have become essential tools in widely different fields of research ranging from quantum information [Lei03, Bla08, Häf08] and quantum simulation [Bla12] to precision metrology [Ros08] and cold collisions between ions and neutrals [Sch10a, Zip10b, Gri09, Rel11, Rav12, Hal11]. The further development of all these lines of research hinges on continuing improvements of the Paul trap architectures and on a better understanding of the current experimental issues.

Ideally, a single ion in a Paul trap is only subjected to the electric fields generated by the voltages applied to the trap electrodes. However, even small spatial variations of the electrode surface potential (i.e. patch potentials) in the vicinity of the trap center create stray electric fields which significantly perturb this ideal configuration. This leads to undesired experimental complications. Quasi-static stray fields lead to positional shifts of the trapped ion [Har10, Wan11a, Dan11, Yu91, DeV02, Nar11, All12, Deb08] and thus to excess micromotion [Ber98]. Rapidly fluctuating stray fields lead to ion heating [Yu91, DeV02, Nar11, All12, Tur00, Des06, Lab08, All11, Hit12].

For the following discussion, we will formally group patch potentials into two categories. Patch potentials of category 1 can decay via electronic discharge currents, similar to a capacitor that is shorted with a resistor. Thus, their evolution is in general governed by the motion of electrons. For example, the photoelectric effect can generate charges on the

dielectric surfaces of the Paul trap. These surfaces could be the trap mounts but also insulating oxide layers on the trap electrodes. The photoelectric effect typically appears with light at wavelengths below about 500 nm. As most of the trapped ion species require light at such "blue" wavelengths for laser cooling and interrogation, light-induced patch charges will continuously be created while the experiments are carried out. In addition, patch potentials of category 1 can also be generated in other ways such as the direct deposition of electrons and ions on dielectric surfaces (see e.g. [Dan11]).

Patch potentials of category 2 are stable as long as the surface atoms do not move. They are due to a spatial variation of the material's work function which depends on its composition, its crystal orientation and its surface adsorbates [Ros92, Cam92]. Surface adsorbates can be elements or compounds which are physically or chemically bound onto the surface. Crystal orientation comes into play for neighboring grains in a polycrystalline structure. A change in composition comes about e.g. when two different metals are brought into contact. This gives rise to the contact potential, i.e. the difference of the work functions of the two metals. Ion traps are often loaded from atomic beams which are directed towards the trap center. If the atomic beam hits the Paul trap electrodes, atoms are deposited on the electrode surface, potentially forming contact potentials. Furthermore, as previously mentioned, the formation and deposition of chemical compounds on the trap surface can also create electric stray fields.

Patch potentials of both categories have been observed to cause deteriorations of Paul traps leading to strong ion heating effects [Yu91, DeV02, Nar11, Tur00, Des06, Lab08, All11, Hit12]. However, the influence and evolution of the patch potentials of category 2 was often masked by the presence of photo-induced patch potentials.

Here, we study the long-term dynamics of quasi-static electric fields in a Paul trap in an environment where we systematically suppress both continuous surface contamination and continuous photo-induced patch charge build-up. We observe smooth drifts of the quasi-static electric stray fields on various time scales from days to months. We interpret these different time scales as indications of different physical and chemical processes that take place. For example, electric fields induced by the exposure of the trap to laser light typically decay within a few days. Fields induced by creating an atomic beam using a barium oven show slower dynamics on the order of months. After longer time periods without surface contamination and photo-induced charging, the stray electric fields settle smoothly towards a stable value with very small residual drifts as low as 0.03 V/m per day.

In our setup, we achieve the suppression of surface contamination and photo-induced patch charges as follows. We create and probe ions (Rb^+) in a linear Paul trap by using only near-

infrared light sources ($\lambda = 780\,\mathrm{nm}$ and $1064\,\mathrm{nm}$) and small clouds of $\approx 10^5$ ultracold Rb atoms, which have previously been optically transported into the chamber citeHaerter2013. Thus, the net flux of atoms into the chamber is negligible. We measure the electric stray fields by applying compensating electric fields until the excess micromotion of the ion is minimized [Här13b].

6.2 Experimental setup and methods

The design of our linear Paul trap is shown in Fig. 6.1. The effective distance from the trap center to each of the four radiofrequency (rf) electrodes is $2.6\,\mathrm{mm}$, while the distance to the endcap electrodes measures $7\,\mathrm{mm}$. To create radial confinement, a voltage driven at a frequency of $4.17\,\mathrm{MHz}$ with an amplitude of $500\,\mathrm{V}$ is applied to two of the rf electrodes while the other two are held at ground potential. Axial confinement is generated by applying static voltages of about $8\,\mathrm{V}$ to the two endcap electrodes. Under these experimental conditions, a $^{87}\mathrm{Rb}^+$ ion is confined at radial trapping frequencies of about $350\,\mathrm{kHz}$ and an axial trapping frequency of about $50\,\mathrm{kHz}$. The total depth of the trap is on the order of $4\,\mathrm{eV}$ and allows for ion storage times of many days, even without any type of cooling. The Paul trap is part of a hybrid atom-ion trap setup that brings the trapped ion into contact with an ultracold cloud of atoms [Sch12]. Ensembles of $^{87}\mathrm{Rb}$ atoms are prepared in a separate vacuum chamber and transported into the Paul trap using a long-distance optical transport line. They are then loaded into a crossed dipole trap where further evaporative cooling down to typical temperatures of $700\,\mathrm{nK}$ is performed. The atom numbers typically range between 10^5 and 10^6 atoms. Both the optical transport and the crossed dipole trap are implemented using several W of laser power at a wavelength of $1064\,\mathrm{nm}$. To perform absorption imaging of the atoms, resonant laser light at $780\,\mathrm{nm}$ is used. After this destructive imaging process, a new atom cloud is prepared within $30\,\mathrm{s}$ for the next measurement. To load an ion, a Rb atom cloud with a density of several $10^{13}\,\mathrm{cm}^{-3}$ is prepared and positioned at the center of the Paul trap. Three-body recombination processes in the atom cloud produce Rb_2 molecules which are subsequently ionized by a REMPI process using photons from the dipole trap laser [Här13c]. Subsequently, the molecular Rb_2^+ ions quickly dissociate via collisions with neutral atoms and finally yield Rb^+ ions.

To detect the number of trapped Rb^+ ions and measure their micromotion, we employ a sensitive probing scheme using ultracold atomic clouds [Här13b]. For this, we immerse the ions into clouds consisting of about 10^5 atoms at densities around $10^{12}\,\mathrm{cm}^{-3}$. After a
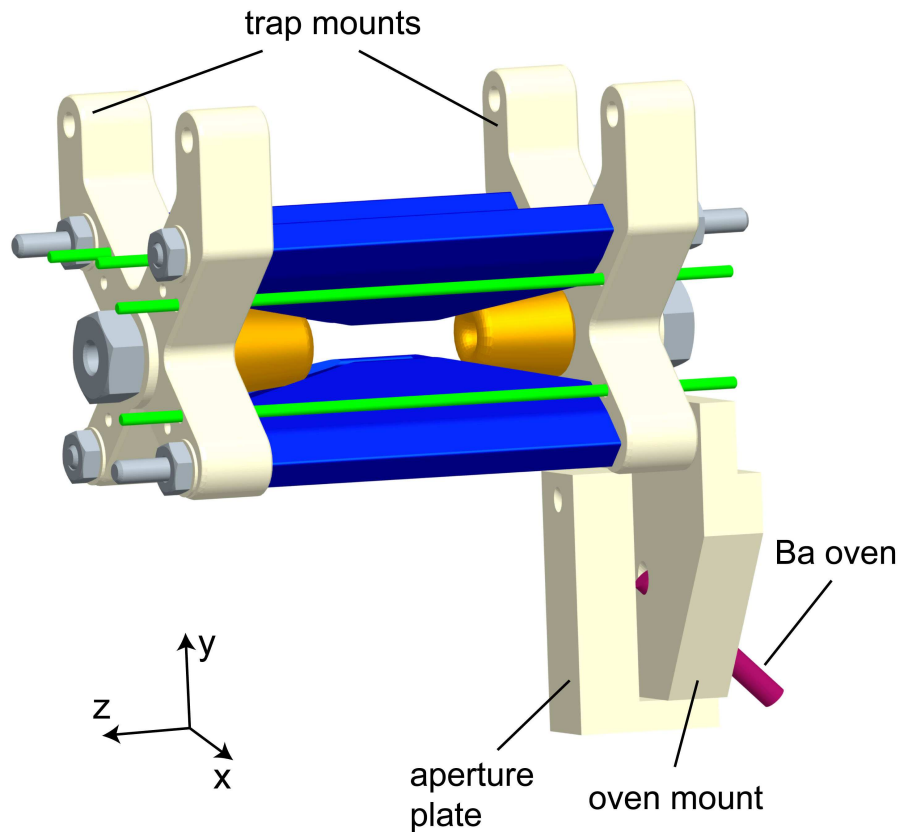
Figure 6.1: Paul trap with mounts. The trap consists of four rf electrodes (blue), two endcap
electrodes (yellow) and two pairs of compensation electrodes (green). The mounts for
the trap and the barium oven are made of MACOR. The aperture plate was installed
to reduce the amount of barium deposited on the trap electrodes.

few seconds of interaction time, we detect the final atom number and atom temperature
which depend on the number of ions and their micromotion. This enables us to reliably
work with a single ion and, by minimizing its excess micromotion with the help of electric
compensation fields, to measure the stray electric fields acting on the ion [Ber98, Här13b].
Due to the production time required for the atom clouds, an electric field measurement
requires about an hour of measurement time, resulting in a limited temporal resolution.
The measurement precision is high and typically ranges around $0.1\,\mathrm{V/m}$ for the results
presented here.

6.3   Time evolution of electrical stray fields

6.3.1   Wavelength dependence

As a first step we investigate the susceptibility of our trap setup with respect to laser light at various wavelengths which are available in our laboratory (Fig. 6.2). For these and the following measurements, each laser beam propagates through the center of the ion trap in horizontal direction at an angle of $45\,°$ with respect to the trap axis. In particular, the laser beam and its specular reflection from the vacuum windows do not directly impinge on any trap electrode or trap mount. Only some stray scattered light from the windows illuminates the trap parts diffusely and quite evenly. Both the trap electrodes and the trap mounts can be "charged up" via the photoelectric effect. The trap mounts and the mounts for the barium oven are made of machinable glass-ceramic (MACOR), which is very susceptible for accumulating charges. Charges can also accumulate on the trap electrode surfaces as these often feature undesired insulating coatings such as oxide layers. As expected, for wavelengths below 500 nm we find a sharp increase in light-induced build-up of electric fields (see Fig. 6.2). For 780 nm or the even longer wavelength of 1064 nm, we did not detect any measurable light-induced electric fields.
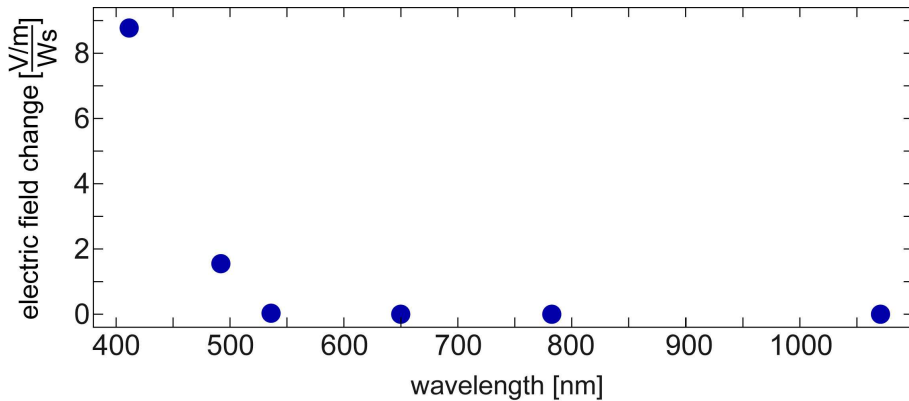

Figure 6.2: Changes of the vertical stray electric field normalized to laser power and exposure time. The field changes were observed to be linear in both laser power and exposure time. At wavelengths below 500 nm, light-induced electric fields sharply increase.

In general, we find the photo-induced stray electric fields to be pointing mostly in vertical ($+y$-axis) and axial ($+z$-axis) direction. There might be a number of reasons how this asymmetry in the direction of the electric stray field comes about. One reason could be that the laser light illuminates the trap setup asymmetrically. However, we can exclude this possibility as the field direction is quite insensitive to changes in the propagation direction of the laser light, in particular when it is flipped by 90° in the horizontal plane. Another

possible explanation for the asymmetry could be the presence, e.g. of a single dust particle on the trap electrodes, which is something we cannot rule out. An obvious asymmetry, however, is already inherent in our Paul trap setup due to the location of the mount and aperture plate of the barium oven (see Fig. 6.1, lower right). Indeed, we estimate that these two parts (which are made of MACOR) can lead to significant electric stray fields at the location of the ion. For one, they can potentially be charged to voltages of up to 500 V, as determined by the amplitude of the rf trap drive. (The rf fields prevent the patch potentials from saturating at a low voltage, the value of which would be normally set by the difference of the work function and the photon energy.) Secondly, our trap geometry is relatively open such that external electric fields can penetrate quite well to the position of the ion. We cannot deterministically charge the aperture plate or the oven mount to a certain voltage in order to test their effect on the electric field at the position of the ion. However, we can apply voltages to the Ba oven itself which should create electric fields of similar magnitude and orientation. We find that a voltage of 1 V on the oven indeed results in a dominant electric field contribution of $+0.1\,\mathrm{V/m}$ in y-direction. The other two field components are each about a factor of 6 smaller ($-0.016\,\mathrm{V/m}$ in x-direction and $+0.016\,\mathrm{V/m}$ in z-direction). These values set a lower bound to the expected fields originating from a charged aperture plate which is located closer to the ion than the oven.

6.3.2 Long-term drift

Next, we start a long-term experiment where we monitor the evolution of all three spatial components of the stray electric field over a time span of about four months (Fig. 6.3). Before the start of these measurements, the ion trap was operated with $\mathrm{Ba^+}$ ions so that both the barium oven and the necessary lasers were frequently used. Consequently, there is a substantial stray electric field to begin with. During the measurements (except for two short occasions) the whole experimental setup is almost entirely shielded from ambient light by means of light-tight protective covers to avoid any patch charge build-up. All three electric field components (in x, y, z direction) show a more or less monotonic decay and converge towards long-term limits which are each set to $\Delta\varepsilon = 0$ in the plot. The solid lines in Fig. 6.3 are double-exponential fits of the form

$$\varepsilon(t) = \Delta\varepsilon_1 \exp(-t/\tau_1) + \Delta\varepsilon_2 \exp(-t/\tau_2),$$

where $\Delta\varepsilon_{1,2}$ are the electric field shifts and $\tau_{1,2}$ are the time constants of the exponential decay curves. For the two radial directions (x- and y-directions) we find relatively rapid
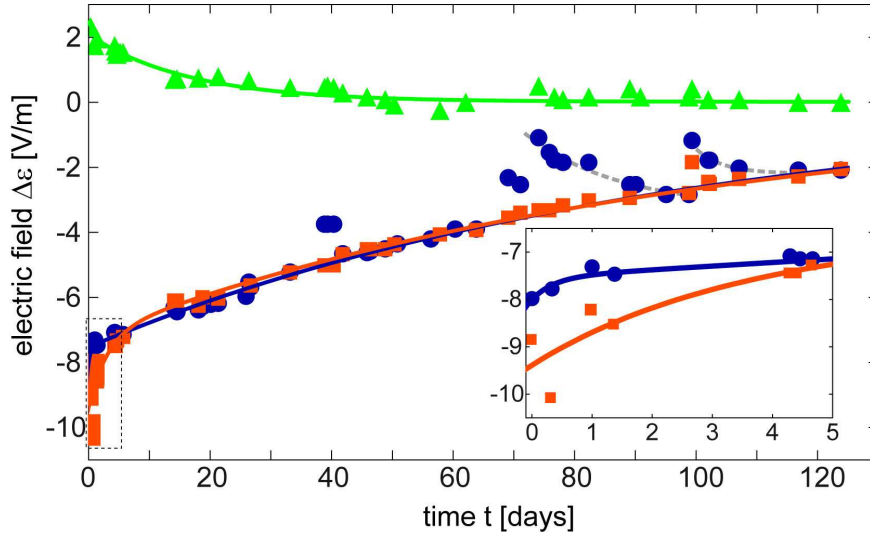
Figure 6.3: Long-term drift of the horizontal (x-direction, orange squares), vertical (y-direction, blue circles) and axial (z-direction, green triangles) electric fields. Except for two occasions ($t \approx 70$ days and $t \approx 100$ days), the trap was isolated from any light below a wavelength of 780 nm. Solid lines are double-exponential fits with long-term time constants on the order of three months. Offsets of the electric fields are chosen such that $\Delta\varepsilon$ converges towards 0 in the long-term limit. *Inset*: Zoom into the initial field evolution with time constants of 0.3 and 2.7 days (cf. table 6.1).

initial decays with time constants $\tau_1 = 0.3 - 2.7$ days (see inset of Fig. 6.3) and subsequent slow decays with $\tau_2 \approx 90$ days. In axial direction the time constants are 0.6 and 18 days. For all three directions the slow decays are dominant as they account for roughly 80-95 % of the electric field shifts (see table 1).

On two occasions ($t \approx 70$ days and $t \approx 100$ days), the light-tight protective covers around the experimental setup had to be removed for several hours so that the Paul trap was subjected (quite uniformly) to ambient white light from the fluorescent ceiling lights. As a consequence, the electric field in vertical (y) direction shows a sharp increase and then decays back towards its long-term behavior within several days. We investigate this effect in detail below.

After about 100 days, the daily drift of the vertical field was below 0.03 V/m yielding extremely stable experimental conditions. In addition, this slow drift allows for a precise prediction of the expected electric fields at a given time so that the field compensation can be adjusted without requiring additional measurements.

6.3.3   Light-induced stray field dynamics

After the time period shown in Fig. 6.3, we make use of the low stray field drift to selectively test the dynamics of photo-induced patch charges. For this measurement we shine through the chamber about 2.5 mW of laser power at a wavelength of 413 nm (3 eV) for 4 minutes. The direction of the laser beam and the conditions with respect to trap illumination are the same as for the measurements in Fig. 6.2, as discussed in the beginning of section 6.3.1. The strongest effect is again observed in the vertical electric field component which increases by about 6 V/m. The axial field component increases by 1.5 V/m, the horizontal component by 0.6 V/m. The laser was then switched off and the decay of the vertical field component was monitored over 5 days (Fig. 6.4). The data is fit by a double-exponential curve with an initial decay on a timescale $\tau_1 = 1.2$ days and a slow decay with $\tau_2 = 11$ days. This slow decay accounts for about 80 % of the field shift. The observed initial increase and subsequent decay of the electric field are in rough agreement with the behavior seen in Fig. 6.3 after the Paul trap had been subjected to ambient light. Thus, our data in Figs. 6.3 and 6.4 clearly indicate that photo-induced electric fields decay on typical timescales of a few days.
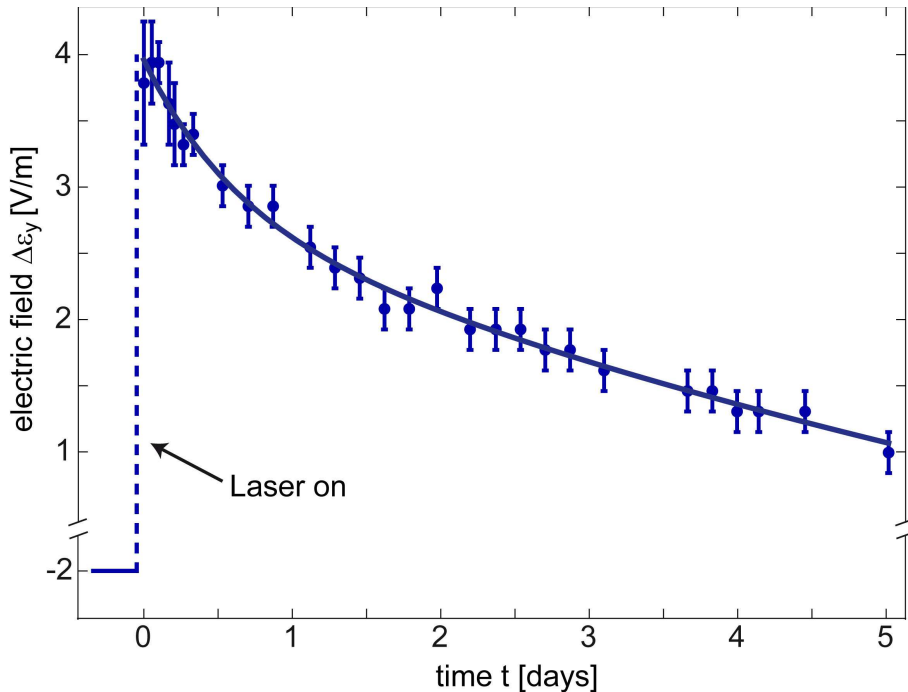

Figure 6.4: Vertical electric field shift induced by subjecting the Paul trap to light at 413 nm. The subsequent relaxation is fit by a double-exponential function with a dominant slow decay accounting for 80% of the field shift. The corresponding time constant is $\tau_2 = 11$ days.

We explain the evolution of the photo-induced stray fields as follows: Initially, the photo-electric effect generates charges on electrically isolated surfaces resulting in electric stray potentials. Over time these potentials discharge by the finite resistivity of the material. In case of a charging of the aperture plate or the oven mount we can estimate a timescale for the discharge. At room temperature, MACOR has a specific volume resistivity of about $10^{17}\,\Omega\times$cm. The typical resistance of a cm-sized component then is on the order of $10^{17}\,\Omega$. The electric capacitance of a cm^2-sized plate is about $4\epsilon_0$ cm, with ϵ_0 denoting the vacuum permittivity. Thus, the decay constant is on the order of 10 hours, which roughly agrees with our observed time scales. We note that the resistivity of MACOR is strongly temperature dependent. We do not have a precise knowledge of the temperature of the mount but from our estimate it is clear that time scales for the discharging of the MACOR parts should not be much longer than a few days. The fact that we observe not only a single timescale for the field decay indicates that there is more than one contribution to the stray fields. A charged up MACOR part might exhibit a different discharge behavior than a dust particle or an isolated patch on the electrode surface. In any case, the data in Fig. 6.4 and especially in Fig. 6.3 (at $t \approx 70$ and $t \approx 100$ days) clearly indicate that photo-induced fields always decay on a timescale faster than two weeks. The question is then how the very slow drift taking place over about 90 days can be explained (see Fig. 6.3). Our observations suggest that the electric fields linked to this slow decay have a different origin than the photoelectric effect.

We conjecture that the slow drifts originate from the dynamics of potentials of category 2, e.g. contact potentials. These potentials may change due to slow chemical reactions in the ultrahigh vacuum environment or by diffusion and migration processes on the electrode surface. It is known that barium reacts and forms compounds with O_2, N_2, CO_2 and H_2O. It also acts as a getter material, inclosing non-reactive gases. Thus, the mobility of Ba on a surface is sizeable. (Interestingly, the work function of barium is known to remain quite constant ($\approx 2.5\,$eV) even when contaminated with other substances.) Diffusion or migration of barium on the electrode surface can coat certain compound layers and set other ones free – thus giving rise to slowly changing contact potentials. At room temperature the vapor pressure of barium is very low. Even at 200°C it only reaches $10^{-12}\,$mbar. This suggests that barium coatings have a long lifetime at ambient temperatures.

Previous studies have investigated the influence of barium contaminations on Paul trap electrodes made of Be-Cu [DeV02]. Long time scales for the quasi-static electric stray field drifts on the order of months were found, similar to our time constant for the slow drift ($\tau_2 = 90$ days) in Fig. 6.3. Furthermore, it was found in [Yu91] that baking out a Paul trap with tungsten electrodes that had been coated with Ba significantly changed electric

stray fields.

6.3.4 Influence of the Barium oven

In order to test our conjecture, we now investigate the influence of the barium oven (while keeping any light below a wavelength of 780 nm blocked off). Immediately after the measurements of Fig. 6.4 are completed, the oven is heated to a temperature of more than 600 °C for 10 minutes inducing a drop of the vertical electric field component by about 7.5 V/m (Fig. 6.5). The horizontal and axial fields each drop by about 2 V/m (not shown).

Table 6.1: Overview of the observed drift time constants and the corresponding electric field shifts. Oven-induced and light-induced effects give rise to drifts with opposite signs.

direction	cause	τ_1 [days]	$\Delta\varepsilon_1$[V/m]	τ_2 [days]	$\Delta\varepsilon_2$[V/m]
vertical (Fig. 6.3)	blue light + oven	0.3±0.4	-0.4±0.2	90±10	-7.4±0.4
horizontal (Fig. 6.3)	blue light + oven	2.7±0.8	-2.1±0.3	94±21	-7.3±0.7
axial (Fig. 6.3)	blue light + oven	0.6±0.8	0.4±0.2	18±3	1.9±0.1
vertical (Fig. 6.4)	blue light	1.2±0.1	1.2±0.1	11±0.3	4.9±0.1

This electric field drop may be partially explained by a rapid discharging of left-over light-induced charges on the oven mount caused by the heat dissipated by the oven. The conductivity of MACOR increases by more than ten orders of magnitude when heated from room temperature to several 100 °C. It can thus be expected that any left-over charges in the vicinity of the oven will be efficiently removed at such high temperatures. However, the electric field $\Delta\varepsilon$ drops much further than the initial value of -2 V/m in Fig. 6.4, namely down to -6.5 V/m. This additional negative electric field drop cannot be explained by the discharge of the charges that were previously produced photoelectrically. One possible explanation for this field contribution is the effect of contact potentials on the trap electrodes. Despite the collimation of the atomic beam through the aperture plate, a fraction of the atoms emerging from the barium oven reaches the rf electrodes close to the trap center. Such a coating of the electrodes might immediately change the distribution of the contact potentials in close vicinity to the ion. These potentials can be on the order of a few V, as determined by the difference in work function of the metals involved. In our setup there is a clear asymmetry on how the Ba oven may coat the trap electrodes with Ba atoms. The two lower rf electrodes will each be coated only on one side, whereas the two upper electrodes will probably be coated over the full tip. It is then to be expected that contact potentials of the upper electrodes dominate over the potentials of the lower
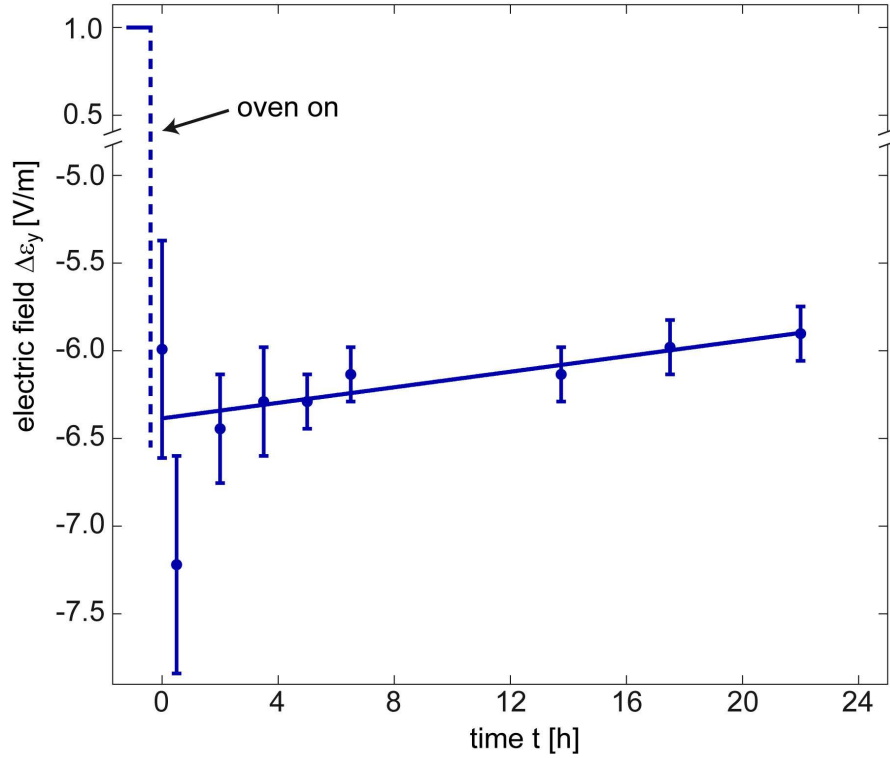
Figure 6.5: Vertical electric field shift induced by heating the barium oven for 10 minutes. During the oven heating time the field dropped by about 7.5 V/m. After the oven was turned off, the field shows a drift towards higher values. The straight solid line is a guide to the eye.

ones. As the work function of Ba is lower than that of stainless steel, an electric field component should build up which points towards the negative y-axis. This is indeed what we observe. Furthermore, there is also an asymmetry in z-direction, as the atomic beam from the oven passes at an angle of about 45° through the blades (see Fig. 6.1). This may give rise to an electric stray field component in z-direction.

Fig. 6.5 shows that after the oven is turned off, the vertical electric field component increases by about 0.5 V/m per day. Such a behavior agrees with the observations at the beginning of the long-term measurements shown in the inset of Fig. 6.3. This again supports our interpretation that the 90-day long drift behavior of the electric field in Fig. 6.3 is a result of initially coating the trap electrodes and mounts with Ba which afterward migrates and undergoes chemical reactions on the surface.

6.4   Conclusion

In conclusion, we have investigated the long-term drifts of quasi-static electric stray fields in a linear Paul trap. We find drifts on time scales ranging from about half a day to three months. We suggest that these different time scales reflect different physical or chemical processes. Light-induced electric fields decay on relatively short time scales on the order of a few days. This is most probably due to charges located on insulating material which slowly discharge via the high electric resistance. In contrast, electric fields which are induced by turning on the Ba oven exhibit long-term drifts on time scales of up to 90 days. Guided by analysis, our interpretation is that the oven coats the trap electrodes or mounts. As a consequence, contact potentials appear which give rise to the electric fields. These fields show long-term drifts possibly due to slow migration or reaction processes taking place on the electrode surface.

Patch potentials have been identified as the common source of both quasi-static and fluctuating electric fields. The time scales for the drifts and fluctuations of these fields is reflected by the dynamics taking place on different length scales of the patches. It has been found that atomic contamination of Paul traps lead to both quasi-static and rapidly fluctuating patch fields [Dan11, Nar11, DeV02]. Our findings on the evolution and the origins of quasi-static charges may thus provide new insights into mechanisms connected to rapidly fluctuating charges such as anomalous heating effects. The results presented here are a first investigation with our setup in the direction of surface dynamics of patch potentials. In the future the experiments can easily be refined to obtain more detailed information and to test hypotheses. For example, by locally applying laser fields on trap mounts and electrodes (either to heat them up or to produce photo-induced patch charges in a controlled way), we should be able to spatially probe surface properties. Another result of our work is that by systematically avoiding the creation of electric patch potentials we are able to get into a regime of very small and predictable electric stray field drifts as low as $0.03\,\mathrm{V/m}$ per day. Such stability of the trap conditions may prove valuable for the future development of precision ion trap experiments.

Chapter 7

Population distribution of product states following three-body recombination in an ultracold atomic gas

Arne Härter, Artjom Krükow, Markus Deiß, Björn Drews and
Johannes Hecker Denschlag

Institut für Quantenmaterie und Center for Integrated Quantum Science and Technology
IQ^{ST}, Universität Ulm, 89069 Ulm, Germany

Eberhard Tiemann

Institut für Quantenoptik, Leibniz Universität Hannover, 30167 Hannover, Germany

---

A reprint of the original publication can be found in the appendix at the end of the thesis

Three-body recombination is a collision between three atoms where two atoms combine to form a molecule and the third atom carries away part of the released reaction energy. Here, we experimentally determine for the first time a population distribution of molecular reaction products after three-body recombination for non-resonant particle interactions. The key to our measurements is a novel sensitive detection scheme which combines photoionization of the molecules with subsequent ion trapping. Using an ultracold ^{87}Rb gas at very low kinetic energy below $h \times 20\,\mathrm{kHz}$, we find a broad population of final states with binding energies of up to $h \times 750\,\mathrm{GHz}$. This is in contrast with previous experiments, performed in resonant interaction regimes, that found dominant population of only the most weakly bound molecular state or the occurrence of Efimov resonances. This work may contribute to the development ofan in-depth model that can qualitatively and quantitatively predict the reaction products of three-body recombination.

7.1   Introduction

While cold collisions of two atoms are well understood, the addition of a third collision partner markedly complicates the interaction dynamics. In the context of Bose-Einstein condensation in atomic gases, three-body recombination plays a crucial role[Hes83, Bur97, Söd99, Esr99] and it constitutes a current frontier of few-body physics[Sun09, Wan11b, Gue12]. Until now, recombination events were mainly investigated by measuring atom loss rates. Discussions of the final states populated in the recombination process were restricted to the special case of resonant interactions[Fed96, Bed00] and culminated in the observations of Efimov resonances[Efi70, Bra01, Kra06] and of molecules in the most weakly bound states [Web03, Joc03]. However, in the more general case of non-resonant interaction, that is, a modulus of the scattering length smaller or comparable to the van der Waals radius, the recombination products might depend on details of the interaction potential. In fact, ongoing theoretical studies using simplified models indicate that recombination does not necessarily always favor the most weakly bound state [d'I13](see also [Sim06]). In general, recombination processes are of fundamental interest in various physical systems[Bat62, Hes83, Flo07]. The control and tunability of ultracold atomic systems provide an experimental testbed for a detailed understanding of the nature of these processes.

Here, we demonstrate the probing of molecules with binding energies up to $h \times 750\,\mathrm{GHz}$ (where h is Planck's constant) generated through three-body recombination of ultracold
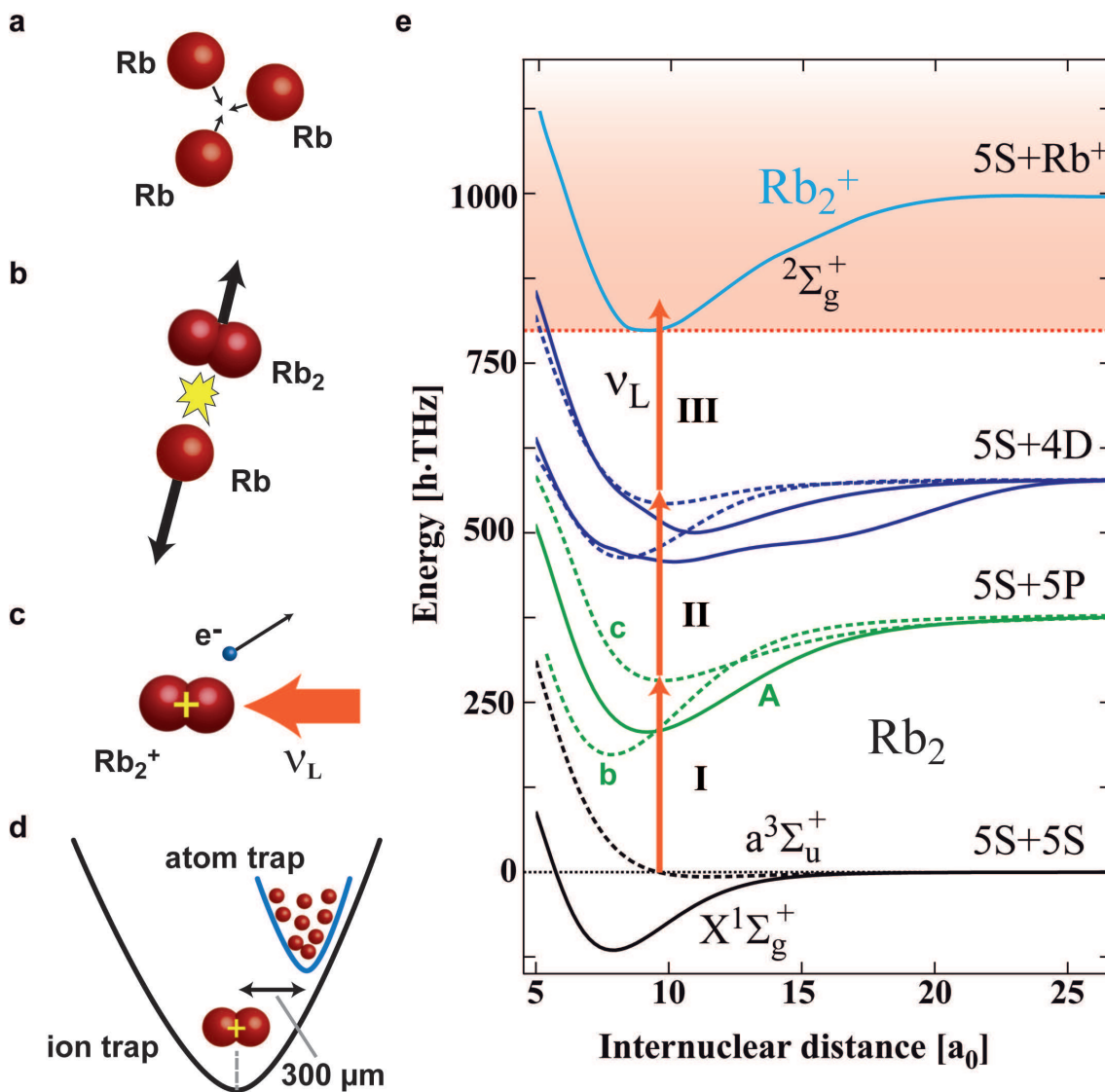
Figure 7.1: Illustration of recombination and ionization in the atom-ion trap. a,b, A three-body collision in the ultracold gas of ^{87}Rb atoms (**a**) leads to a recombination event in which a Rb_2 molecule is formed with high kinetic energy (**b**). **c**, While the atom is lost from the trap, the molecule can be photoionized in a REMPI process and trapped in the Paul trap. **d**, The relative positions of the atom and ion trap centers are shifted by about 300 μm to avoid atom-ion collisions. **e**, Potential energy curves of the Rb_2 and Rb_2^+ molecule adapted from refs [Loz06, Aym03]. The curves A, b, c, are $A^1\Sigma_u^+$, $b^3\Pi_u$, $c^3\Sigma_u^+$. The internuclear distance is given in units of Bohr radii a_0. A REMPI path with three photons is shown. It can create Rb_2^+ ions in vibrational states up to $v \approx 17$.

thermal ^{87}Rb atoms. We produce the atomic sample in an optical dipole trap located within a linear Paul trap. The recombination and detection process is illustrated in Fig. 7.1a-d. Following a recombination event, the created Rb$_2$ molecule can undergo resonance-enhanced multi-photon ionization (REMPI) by absorbing photons from the dipole trap laser at a wavelength around 1064.5 nm. The ion is then captured in the Paul trap and detected essentially background-free with very high sensitivity on the single particle level. Figure 7.1e shows a simplified scheme of the Rb$_2$ and Rb$_2^+$ potential energy curves. From weakly-bound molecular states, three photons suffice to reach the molecular ionization threshold. An additional photon may dissociate the molecular ion. By scanning the frequency of the dipole trap laser by more than 60 GHz we obtained a high resolution spectrum featuring more than 100 resonance peaks. This dense and complex spectrum contains information which vibrational, rotational and hyperfine levels of the Rb$_2$ molecule are populated. We present an analysis of these data and make a first assignment of the most prominent resonances. This assignment indicates that in the recombination events a broad range of levels is populated in terms of vibrational, rotational, electronic and nuclear spin quantum numbers.

7.2   Experimental scheme

Our experimental scheme to detect cold molecules makes use of the generally excellent detection efficiencies attainable for trapped ions. It is related to proven techniques where cold molecules in magneto-optical traps were photoionized from the singlet and triplet ground states[Fio98, Gab00, Loz06, Hua06, Sal08, Sul11] (see also ref[Mud09]). Our method is unique as it introduces the usage of a hybrid atom-ion trap which significantly improves the detection sensitivity. We perform the following experimental sequence. A thermal atomic sample typically containing $N_{at} \approx 5 \times 10^5$ spin-polarized ^{87}Rb atoms in the $|F = 1, m_F = -1\rangle$ hyperfine state is prepared in a crossed optical dipole trap at a magnetic field of about 5 G. The trap is positioned onto the nodal line of the radiofrequency field of a linear Paul trap. Along the axis of the Paul trap the centers of the atom and ion trap are separated by about 300 μm to avoid unwanted atom-ion collisions (Fig. 7.1d). At atomic temperatures of about 700 nK and peak densities $n_0 \approx 5 \times 10^{13}\,\mathrm{cm}^{-3}$ the total three-body recombination rate in the gas is $\Gamma_{rec} = L_3 n_0^2 N_{at}/3^{5/2} \approx 10\,\mathrm{kHz}$. Here, the three-body loss rate coefficient L_3 was taken from ref[Söd99]. At the rate Γ_{rec}, pairs of Rb$_2$ molecules and Rb atoms are formed as final products of the reactions. Both atom and molecule would generally be lost from the shallow neutral particle trap due to the comparatively

large kinetic energy they gain in the recombination event (in our case typically on the order of a few K k_B where k_B is the Boltzmann constant). The molecule, however, can be state-selectively ionized in a REMPI process driven by the dipole trap laser. All of these molecular ions remain trapped in the deep Paul trap and are detected with single particle sensitivity (Methods). In each experimental run, we hold the atomic sample for a time $\tau \approx 10\,\mathrm{s}$. After this time we measure the number of produced ions in the trap from which we derive (after averaging over tens of runs) the ion production rate Γ_{ion} normalized to a cloud atom number of 10^6 atoms.

As a consistency check of our assumption that Rb_2 molecules are ionized in the REMPI process, we verify the production of Rb_2^+ molecules. For this, we perform ion mass spectrometry in the Paul trap (Methods). We detect primarily molecular Rb_2^+ ions, a good fraction of atomic Rb^+ ions but no Rb_3^+ ions. Our experiments show that Rb^+ ions are produced in light-assisted collisions of Rb_2^+ ions with Rb atoms on timescales below a few milliseconds. Details of this dissociation mechanism are currently under investigation and will be discussed elsewhere.

7.3   Dependence of the ion production rate

7.3.1   Density dependence

Two pathways for the production of our neutral Rb_2 molecules come immediately to mind. One pathway is far-off-resonant photoassociation of two colliding Rb atoms (here with a detuning of about $500\,\mathrm{GHz} \times h$). This pathway can be ruled out using several arguments, the background of which will be discussed in more depth later. For one, we observe molecules with a parity that is incompatible with photoassociation of totally spin polarized ensembles. Furthermore, we observe a dependence of the ion production rate on light intensity that is too weak to explain photoassociation.

The second pathway is three-body recombination of Rb atoms. Indeed, by investigating the dependence of the ion production rate Γ_{ion} (which is normalized to a cloud atom number of 10^6 atoms) on atomic density, we find the expected quadratic dependence (Fig. 7.2). For this measurement the density was adjusted by varying the cloud atom number while keeping the light intensity of the dipole trap constant.
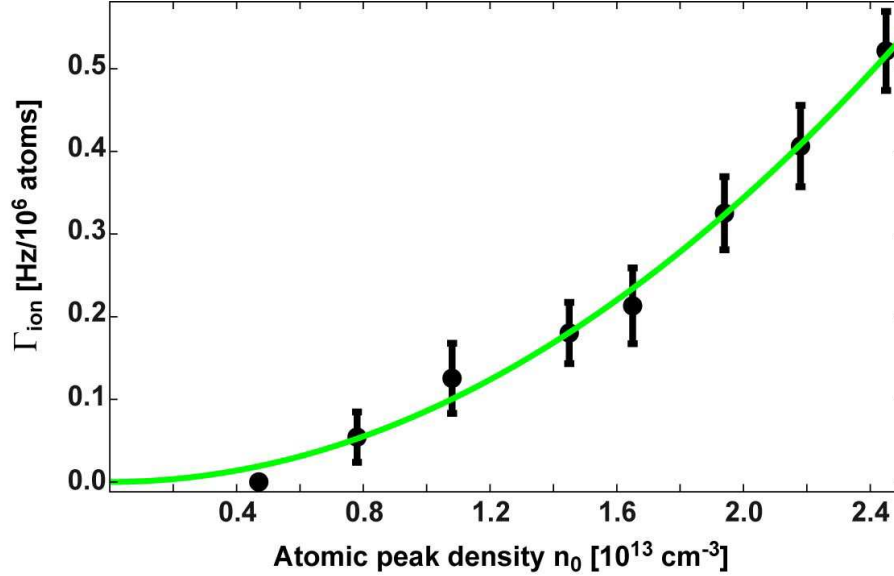
Figure 7.2: Dependence of the ion production rate $\Gamma_{\mathbf{ion}}$ on atomic density. Γ_{ion} is normalized to a cloud atom number of 10^6 atoms. The data are well described by a quadratic fit (solid green line). They were taken at a constant dipole trap laser intensity $I_{\mathrm{L}} = 36\,\mathrm{kW/cm^2}$ and a laser frequency of $\nu_{\mathrm{L}} = 281630$ GHz. The error bars indicate statistical uncertainties and represent one standard deviation from the mean.

7.3.2 Laser frequency dependence - REMPI spectrum

Next, we investigate the dependence of the ion production rate on the wavelength of the narrow-linewidth dipole trap laser (Methods). We scan the wavelength over a range of about 0.3 nm around 1064.5 nm, corresponding to a frequency range of about 60 GHz. Typical frequency step sizes are 50 MHz or 100 MHz. We obtain a rich spectrum of resonance lines which is shown in Fig. 7.3a. The quantity $\bar{\Gamma}_{\mathrm{ion}}$ denotes the ion production rate normalized to the atom number of the cloud and to the square of the atomic peak density. We find strongly varying resonance strengths and at first sight fairly irregular frequency spacings. In the following we will argue that most resonance lines can be attributed to respective well-defined molecular levels (resolving vibrational, rotational and often even hyperfine structure) that have been populated in the recombination process. These levels are located in the triplet or singlet ground state, $a^3\Sigma_u^+$ and $X^1\Sigma_g^+$, respectively. The relatively dense distribution of these lines reflects that a fairly broad range of states is populated. A direct assignment of the observed resonances is challenging, as it hinges on the precise knowledge of the level structure of all the relevant ground and excited states. In the following we will access and understand the data step by step.
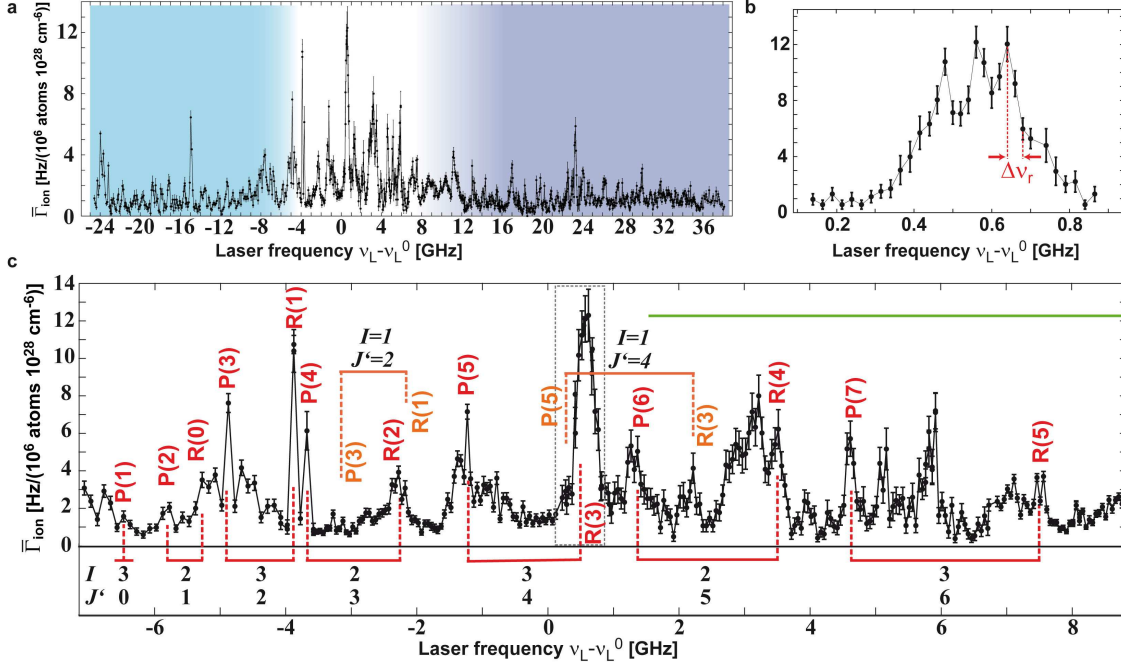
Figure 7.3: REMPI spectrum. a, A scan of the dipole trap laser frequency ν_L over more than 60 GHz around an offset frequency $\nu_L^0 = 281.610$ THz shows a multitude of resonance lines. Each data point is the result of 30 to 60 repetitions of the experiment with ion detection on the single particle level. The total spectrum was obtained over a time span of 2 months. Checks of the long-term consistency of resonance positions and strengths were performed. Spectral regions dominated by transitions to $c^3\Sigma_g^+$ are indicated by the shaded areas in dark and light blue (0_g^- and 1_g component, respectively). **b**, High-resolution scan of the strong resonance at $\nu_L - \nu_L^0 \approx 0.5$ GHz. **c**, Central spectral region with assigned P/R branches of the transition $X^1\Sigma_g^+(v = 115) \rightarrow A^1\Sigma_u^+(v' = 66)$. The corresponding quantum numbers I and J' are given. P(J) marks the transition $J \rightarrow J - 1$, R(J) the transition $J \rightarrow J + 1$. These lines can be grouped into pairs sharing the same J' of the excited state and I quantum number. The region where also transitions to $b^3\Pi_u$ appear is marked by a green horizontal bar. The error bars indicate statistical uncertainties and represent one standard deviation from the mean.

One feature of the spectrum that stands out is the narrow linewidth of many lines. For example, Fig. 7.3b shows a resonance of which the substructures have typical half-widths $\Delta\nu_r \approx 50$ MHz. This allows us to roughly estimate the maximal binding energy of the molecules involved. As the velocity of the colliding ultracold atoms is extremely low, the kinetics of the recombination products is dominated by the released molecular binding energy E_b. Owing to energy and momentum conservation the molecules will be expelled from the reaction with a molecular velocity $v_{Rb2} = \sqrt{2E_b/(3m_{Rb2})}$ where m_{Rb2} is the molecular mass. The molecular resonance frequency ν_0 will then be Doppler-broadened with a half-width $\Delta\nu_D = \sqrt{3}\nu_0 v_{Rb2}/2c$. Here, c is the speed of light. By comparing

$\Delta\nu_D$ to the observed values of $\Delta\nu_r$ we estimate a maximal binding energy on the order of $E_{b,max} \approx h \times 2.5$ THz. This simple analysis overestimates the value $E_{b,max}$ since it neglects the natural linewidth of the transition and possible saturation broadening. Still, it already strongly constrains the possibly populated molecular levels that are observed in our experiment.

7.3.3 Laser intensity dependence

Next, we investigate the dependence of the ion production rate on laser intensity I_L. In our experimental setup, this measurement is rather involved because the laser driving the REMPI process also confines the atomic cloud. Thus, simply changing only the laser intensity would undesirably also change the density n_0 of the atoms. To prevent this from happening we keep n_0 constant ($n_0 \approx 5 \times 10^{13}$ cm^{-3}) by adjusting the atom number and temperature appropriately. Owing to these experimental complications we can only vary I_L roughly by a factor of 2 (Fig. 7.4a). We set the laser frequency to the value of $\nu_L = \nu_L^0 \equiv 281610$ GHz, on the tail of a large resonance (see Fig. 3). The atomic temperatures in this measurement range between 500 nK and 1.1 μK, well above the critical temperatures for Bose-Einstein condensation. The atomic densities can therefore be described using a Maxwell-Boltzmann distribution. Assuming a simple power-law dependence of the form $\bar{\Gamma}_{ion} \propto I_L^\alpha$ we obtain the best fit using an exponent $\alpha = 1.5(1)$ (solid green line in Fig. 7.4a). This fit is between a linear and a quadratic intensity dependence (dashed red and blue lines, respectively). Thus, at least two of the three transitions composing the ionization process are partially saturated at the typical intensities used.

To better circumvent possible density variations of the atomic cloud induced by changes in laser intensity, we employ a further method which enables us to vary the intensity with negligible effects on the atomic sample. We achieve this by keeping the time-averaged intensity $\langle I_L \rangle$ constant and comparing the ion production rates within a continuous dipole trap and a chopped dipole trap in which the intensity is rapidly switched between 0 and $2I_L$. In both cases the trap is operated at an intensity $\langle I_L \rangle \approx 15$ kW/cm^2. In the chopped configuration the intensity is switched at a frequency of 100 kHz so that the atoms are exposed to the light for 5 μs followed by 5 μs without light. It should be noted that molecules formed in the dark period with sufficiently high kinetic energies may leave the central trapping region before the laser light is switched back on. They are then lost for our REMPI detection. Taking into account the molecular velocity and the transverse extensions of the laser beams we can estimate that this potential loss mechanism leads to errors of less
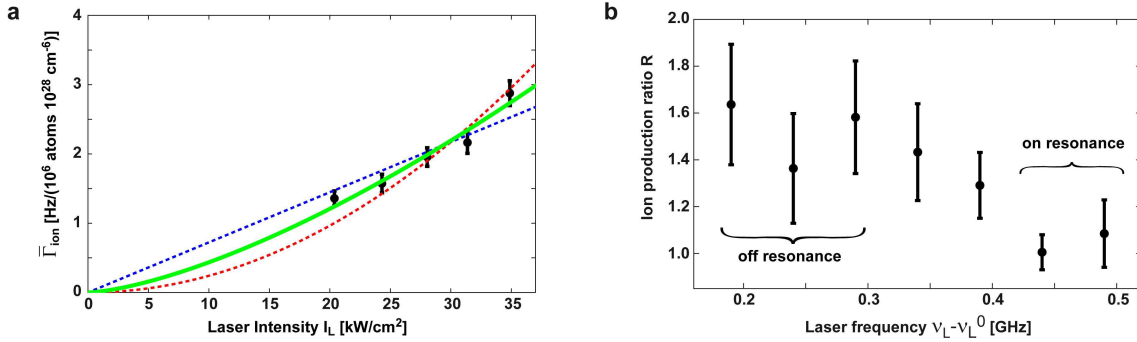
Figure 7.4: Dependence of the ion production rate on the intensity of the dipole trap laser. **a**, Assuming a power-law dependence $\bar{\Gamma}_{\text{ion}} \propto I_{\text{L}}^{\alpha}$, the best fit to the data is achieved for $\alpha \approx 1.5$ (solid green line). Linear and quadratic fits are also given (blue and red dashed lines, respectively). **b**, Measurement of the intensity dependence using a "chopped" dipole trap. The ratio $R \approx 1$ on resonance indicates saturation of both transitions I and II. The error bars indicate statistical uncertainties and represent one standard deviation from the mean.

than 30%, even at the highest binding energies relevant to this work ($E_{\text{b}} \approx h \times 750\,\text{GHz}$, see below). We did not observe evidence of such losses experimentally. Investigations were made by changing the chopping frequency. We define R as ratio of the ion production rates in the chopped and the continuous trap configuration. Figure 7.4b shows the results of these measurements for various laser frequencies ν_{L}. We find a value $R \approx 1.5$ for off-resonant frequency settings $\nu_{\text{L}} - \nu_{\text{L}}^{0} < 0.4\,\text{GHz}$, in good agreement with the result presented in Fig. 7.4a. When scanning the laser onto resonance at $\nu_{\text{L}} - \nu_{\text{L}}^{0} \approx 0.45\,\text{GHz}$ (see also Fig. 7.3b) we obtain $R \approx 1$. This result indicates a linear intensity dependence of the REMPI process in the resonant case, which is explained by the saturation of two of the three molecular transitions involved. It is known that transitions into the ionization continuum (photon III, see Fig. 1e) will not saturate under the present experimental conditions. This means that the excitation pathway through photon I and II must be saturated and therefore both close to resonance.

7.4 Assignment of observed resonances to molecular transitions

However, given the wavelength range of about $1064.5\pm0.15\,\text{nm}$, an inspection of the level structure shows that photon I can only resonantly drive three different transitions which connect vibrational levels in states X and a to vibrational levels in states A, b and c

(see Fig. 1e). Spectroscopic details for these transitions and the corresponding vibrational levels are given in the Methods and in Fig. 5. From recent spectroscopic studies[Str10, Tak11, Dro12] and additional measurements in our laboratory the level structure of all relevant levels of the X, a, A, b, and c states is well known. The absolute precision of most of the level energies is far better than 1 GHz for low rotational quantum numbers J.

In the experimental data (Fig. 7.3a) the central region from $\nu_L - \nu_L^0 = -6$ to 7 GHz is marked by several prominent resonances that are significantly stronger than those observed throughout the rest of the spectrum. These resonance peaks can be assigned to transitions from the X ground state to A and b states. The prominence of these singlet transitions is explained by the near degeneracy of levels due to small hyperfine splittings. Indeed, by analyzing these strong resonances with regard to line splittings and intensities it was possible to consistently assign rotational ladders for total nuclear spin quantum numbers $I = 1, 2, 3$ for the transition $X(v = 115) \rightarrow A(v' = 66)$. The starting point of the rotational ladder for $I = 2$ was fixed by previous spectroscopic measurements in our laboratory. At frequencies $\nu_L - \nu_L^0 \gtrsim 2$ GHz additional strong lines appear that we attribute to the $X (v = 109) \rightarrow b (v' = 73)$ transition. The fact that we observe X state molecules with $I = 1, 2, 3$ is interesting because for $I = 1, 3$ the total parity of the molecule is negative, while for $I = 0, 2$ it is positive. However, a two-body collision state of our spin polarized Rb atoms necessarily has positive total parity due to symmetry arguments and a photoassociation pathway would lead to ground state levels with positive parity. The observed production of molecules with negative total parity must then be a three-body collision effect.

We now consider the role of secondary atom-molecule collisions which would change the product distribution due to molecular relaxation. Two aspects are of importance: depopulation of detected molecular levels, and population of detected molecular levels through relaxation from more weakly bound states. In our experiments reported here we detect molecules that are formed in states with binding energies on the order of hundreds of GHz$\times h$. These molecules leave the reaction with kinetic energies of several Kk_{B}. At these energies the rate coefficients for depopulating atom-molecule collisions are small (see e.g. ref.[Sim06]) and the collision probability before the molecule is either ionized or has left the trap is below 1 %.

For the population processes, we can estimate an upper bound for rate coefficients by assuming recombination to occur only into the most weakly bound state with a binding energy of 24 MHz$\times h$. In this case subsequent atom-molecule collision rates will be roughly comparable to those expected in the ultracold limit. At typical rate coefficients of 10^{-10} cm^3/s (see refs. [Muk04, Sta06, Zah06, Qué07]) and the atomic densities
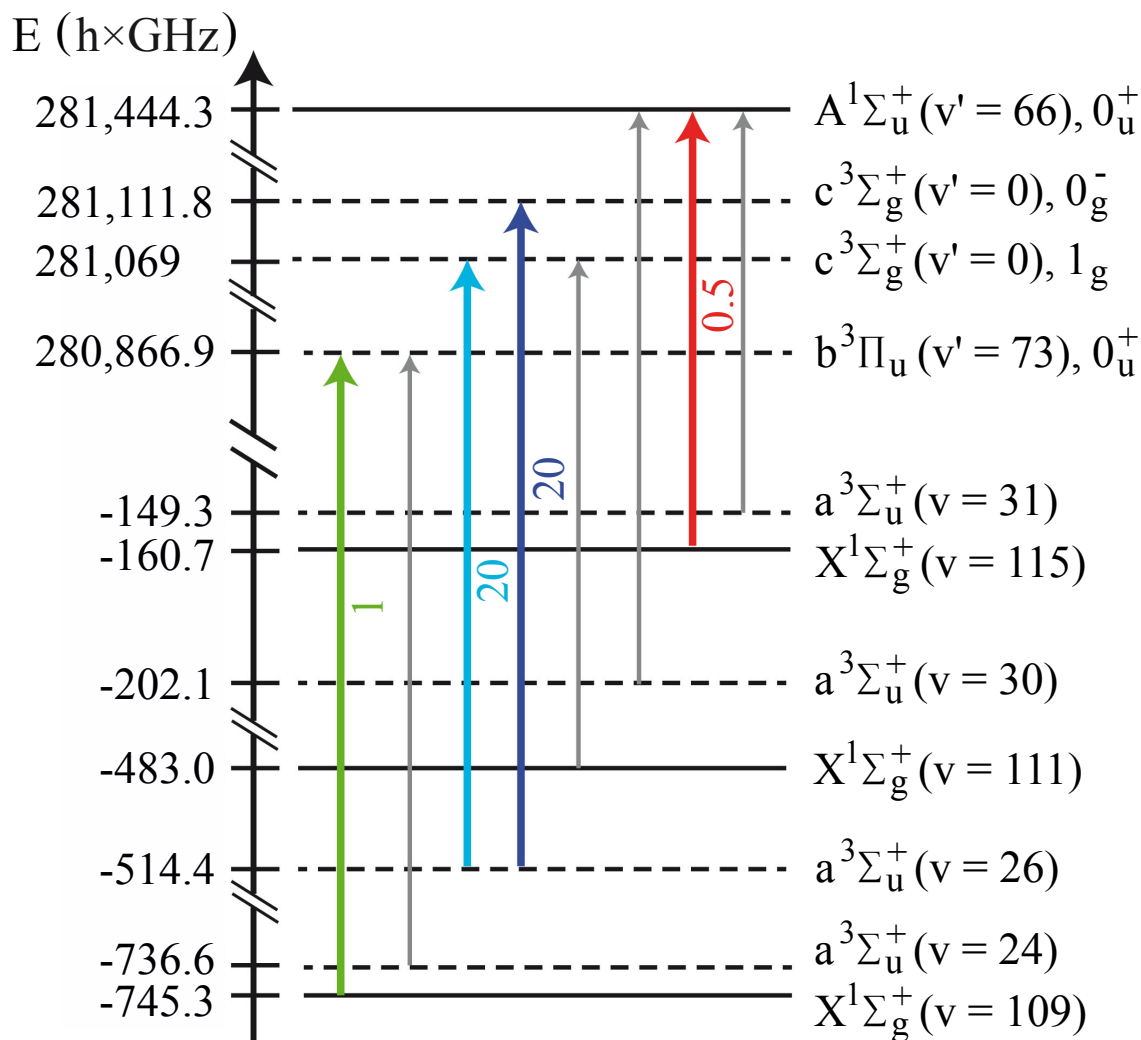
Figure 7.5: Overview over relevant molecular levels and transitions. The vertical axis denotes the energy E_b of the energetically lowest levels of each vibrational manifold with respect to the 5s 5s asymptote. Colored thick arrows represent molecular transitions relevant to the spectrum of Fig. 7.3. The expected relative strengths of these transitions are also given. Grey arrows mark transitions that occur in the relevant spectral region but are so weak that they can be neglected (for further spectroscopic details see Methods). We identify three main molecular transitions for the initial step of the REMPI process. The blue arrows indicate molecules in the $v = 26$ vibrational level of the $a^3\Sigma_u^+$ potential that are excited to the $v' = 0$ level of the $c^3\Sigma_g^+$ potential. This level is split into a 1_g and a 0_g^- component. The red arrow is an excitation from $X^1\Sigma_g^+(v = 115)$ to $A^1\Sigma_u^+(v' = 66)$. The green arrow is an excitation from $X^1\Sigma_g^+(v = 109)$ to $b^3\Pi_u(v' = 73)$. This transition becomes possible through the strong spin-orbit coupling of the A and b states.

$n_0 \sim 1 \times 10^{13}$ cm^{-3} used in the measurement shown in Fig. 7.2, the collision probability before the molecule leaves the atom cloud is around 5%. This small probability grows linearly with density so that the density dependence of the ion production rate should show a significant cubic contribution if secondary collisions were involved (as expected for this effective four-body process). This is inconsistent with the data and thus indicates that the population that we detect is not significantly altered by secondary collisions.

We can roughly estimate the range of molecular rotation J of the populated levels in the ground state. The strong, isolated lines that we have assigned to the $X(v = 115) \rightarrow A(v' = 68)$ transition are all contained within a relatively small spectral region ($|\nu_L - \nu_L^0| < 6\,\text{GHz}$) and are explained by rotational quantum numbers $J \leq 7$. Population of higher rotational quantum numbers would result in a continuation of the strong resonance lines stretching to transition frequencies beyond $\nu_L - \nu_L^0 = 10\,\text{GHz}$, which we do not observe. Similarly, if only rotational quantum numbers $J \leq 5$ were populated, a spectrum would result which does not have enough lines to explain the data. Thus, we can roughly set the limits on the molecular rotation to $J \leq 7$, a value that is also consistent with our observations of the spread of the transitions $X \rightarrow b$ and $a \rightarrow c$ (see Fig. 7.5). Finding quantum numbers as high as $J = 7$ is remarkable because the three-body collisions at μK temperatures clearly take place in an s-wave regime, that is, at vanishing rotational angular momentum. Hence, one could expect to produce X state molecules dominantly at $J = 0$, which, however, we do not observe.

Despite the limited spectral range covered by our measurements, we can already estimate the number of molecular vibrational levels populated in the recombination events. From the three states $X(v = 109)$, $a(v = 26)$ and $X(v = 115)$ that we can observe within our wavelength range, all deliver comparable signals in the spectrum of Fig. 7.3. This suggests that at least all vibrational states more weakly bound than $X(v = 109)$ should be populated, a total of 38 vibrational levels (counting both singlet and triplet states). This is a significant fraction of the 169 existing levels of the X and a states, although restricted to a comparatively small range of binding energies.

7.5   Conclusion

In conclusion, our work represents a first experimental step towards a detailed understanding on how the reaction channels in three-body recombination are populated. A full understanding will clearly require further experimental and theoretical efforts. On the

experimental side the scanning range has to be increased and it could be advantageous to switch to a two-color REMPI scheme in the future. Such studies may finally pave the way to a comprehensive understanding of three-body recombination, which includes the details of the final products.

Reaching beyond the scope of three-body recombination, the great sensitivity of our detection scheme has enabled us to state-selectively probe single molecules that are produced at rates of only a few hertz. We thereby demonstrate a novel scheme for precision molecular spectroscopy in extremely dilute ensembles.

7.6 Methods

7.6.1 Dipole trap and REMPI configuration.

The crossed dipole trap is composed of a horizontal and a vertical beam focused to beam waists of $\sim 90\,\mu$m and $\sim 150\,\mu$m, respectively. It is positioned onto the nodal line of the radiofrequency field of the linear Paul trap with μm precision. The two trap centers are separated by about $300\,\mu$m along the axis of the Paul trap (Fig. 1d). In a typical configuration, the trap frequencies of the dipole trap are $(175, 230, 80)\,$Hz resulting in atom cloud radii of about $(6, 7, 16)\,\mu$m. The short-term frequency stability of the dipole trap laser source is on the order of $1\,$kHz and it is stabilized against thermal drifts to achieve long-term stability of a few MHz. The two beams of the dipole trap are mutually detuned by $160\,$MHz to avoid interference effects in the optical trap. Consequently, two frequencies are in principle available to drive the REMPI process. However, the intensity of the horizontal beam is 4 times larger than the one of the vertical beam and we have not directly observed a corresponding doubling of lines. Further details on the atom-ion apparatus are given in ref [Sch12].

7.6.2 Paul trap configuration.

The linear Paul trap is driven at a radiofrequency of $4.17\,$MHz and an amplitude of about $500\,$V resulting in radial confinement with trap frequencies of $(\omega_{x,Ba}, \omega_{y,Ba}) = 2\pi \times (220, 230)\,$kHz for a ^{138}Ba$^+$ ion. Axial confinement is achieved by applying static voltages to two endcap electrodes yielding $\omega_{z,Ba} = 2\pi \times 40.2$kHz. The trap frequencies for dark Rb$_2^+$ and Rb$^+$ ions produced in the REMPI processes are $(m_{Ba}/m_{dark} \times \omega_{x,Ba}, m_{Ba}/m_{dark} \times \omega_{y,Ba}, \sqrt{m_{Ba}/m_{dark}} \times \omega_{z,Ba})$ where m_{Ba} and m_{dark} denote the mass of the Ba$^+$ ion and the

dark ion, respectively. The depth of the Paul trap depends on the ionic mass and exceeds
2 eV for all ionic species relevant to this work.

7.6.3 Ion detection methods.

We employ two methods to detect Rb_2^+ and Rb^+ ions both of which are not amenable to
fluorescence detection. In the first of these methods we use a single trapped and laser-
cooled $^{138}Ba^+$ ion as a probe. By recording its position and trapping frequencies in small
ion strings with up to 4 ions we detect both the number and the masses of the ions following
each REMPI process (see also[Sch10a]). The second method is based on measuring the
number of ions in the Paul trap by immersing them into an atom cloud and recording
the ion-induced atom loss after a hold time of 2 s (see also[Här12]). During this detection
scheme, we take care to suppress further generation of ions by working with small and
dilute atomic clouds and by detuning the REMPI laser from resonance. Both methods
are background-free in the sense that no ions are captured on timescales of days in the
absence of the atom cloud. Further information on both detection methods is given in the
Supplementary Information.

7.6.4 Spectroscopic details.

Spin-orbit and effective spin-spin coupling in the A, b, and c states lead to Hund's case c
coupling where the relevant levels of states A and b have 0_u^+ symmetry while the levels of
state $c^3\Sigma_g^+$ are grouped into 0_g^- and 1_g components. The level structure of the 0_u^+ states
is quite simple as it is dominated by rotational splittings. Typical rotational constants for
the electronically excited states are on the order of 400 MHz, for the weakly bound X and
a states they are around 100-150 MHz.

Figure 5 shows the relevant optical transitions between the X, a states and the A, b, c
states in our experiment. For the given expected relative strengths of these transitions,
we only consider Franck-Condon factors and the mixing of singlet and triplet states, while
electronic transition moments are ignored. The colored arrows correspond to transitions
with large enough Franck-Condon factors (typ. $10^{-2}...10^{-3}$) so that at laser powers of
$\approx 10^4$ W/cm^2 resonant transitions can be well saturated. Transitions marked with grey
arrows can be neglected due to weak transition strengths, being forbidden in first order
by dipole selection rules.

7.7   Supplemental Material

In this Supplementary Information we describe two methods that we employ to detect small numbers of Rb_2^+ and Rb^+ ions in our linear Paul trap.

7.7.1   Method 1

To implement our first ion detection method allowing mass-sensitive detection of "dark" ions we rely on the presence of a single "bright" ion in the trap. Information on additional ions can be extracted from its fluorescence position. When using this method, our experimental procedure begins with the loading of a single ^{138}Ba$^+$-ion into our linear Paul trap. We laser-cool the ion and image its fluorescence light onto an electron-multiplying charge-coupled device camera. This enables us to determine the position of the trap center to better than $100\,\mathrm{nm}$. The ion is confined at radial and axial trapping frequencies $\omega_{\mathrm{r,Ba}} \approx 2\pi \times 220\,\mathrm{kHz}$ and $\omega_{\mathrm{ax,Ba}} \approx 2\pi \times 40.2\,\mathrm{kHz}$ and typically remains trapped on timescales of days. Next, we prepare an ultracold atomic sample in the crossed dipole trap. At typical atomic temperatures of about $700\,\mathrm{nK}$ the atom cloud has radial and axial extensions of about $7\,\mu\mathrm{m}$ and $15\,\mu\mathrm{m}$ and is thus much smaller than the trapping volume of our Paul trap. To avoid atom-ion collisions we shift the Ba$^+$-ion by about $300\,\mu\mathrm{m}$ with respect to the atom cloud before the atomic sample arrives in the Paul trap. The shifting is performed along the axis of the trap by lowering the voltage on one of the end-cap electrodes. Additionally, we completely extinguish all resonant laser light so that the atoms are only subjected to the light of the dipole trap. The atomic sample is moved into
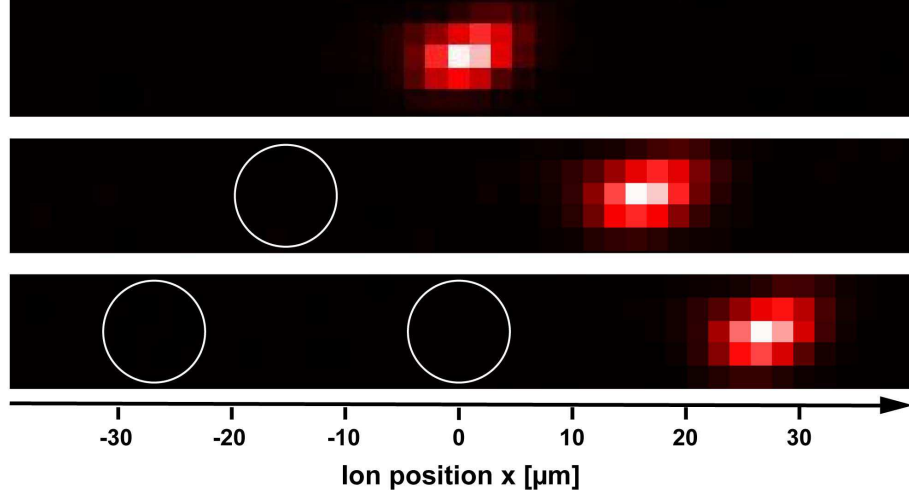
Figure 7.6: Ion detection using a $^{138}\text{Ba}^+$-ion. Positional shifts of the fluorescence of the Ba^+-ion and measurements of the trap oscillation frequencies allow us to perform mass-sensitive detection of up to three "dark" ions in the trap.

Table 7.1: Trap oscillation frequencies of two-ion crystals

Ion species	$\omega_{\text{ax,2ion}}/2\pi$ [kHz]	$\omega_{\text{r}}/2\pi$ [kHz]
$^{138}\text{Ba}^+$ and $^{138}\text{Ba}^+$	40.2	220.0
$^{138}\text{Ba}^+$ and $^{87}\text{Rb}^+$	44.0	345.3
$^{138}\text{Ba}^+$ and $^{87}\text{Rb}_2^+$	37.7	170.7

the center of the radial trapping potential of the Paul trap and is typically held at this position for a time $\tau_{\text{hold}} \approx 10\,\text{s}$. Despite the axial offset from the center of the Paul trap, the atom cloud at this position is fully localized within the trapping volume of the Paul trap. After the hold time the sample is detected using absorption imaging. Subsequently, the ion cooling beams are switched back on for fluorescence detection of the Ba^+-ion.

The presence of a second ion in the trap leads to positional shifts of the $^{138}\text{Ba}^+$-ion by distances on the order of $10\,\mu\text{m}$ (see Fig. 7.6). We make use of the mass-dependent trap frequencies of the Paul trap to gain information on the ion species trapped. In a two-ion Coulomb crystal composed of a Ba^+-ion and a dark ion, the axial center-of-mass frequency $\omega_{\text{ax,2ion}}$ shifts with respect to $\omega_{\text{ax,Ba}}$ depending on the mass of the dark ion m_{dark} [Mor01]. We measure $\omega_{\text{ax,2ion}}$ by modulating the trap drive at frequencies ω_{mod} and by monitoring the induced axial oscillation of the Ba^+-ion, visible as a blurring of the fluorescence signal. In this way, after each ion trapping event, we identify a resonance either at $\omega_{\text{mod}} \approx 2\pi \times 44\,\text{kHz}$ or $\omega_{\text{mod}} \approx 2\pi \times 38\,\text{kHz}$ corresponding to $m_{\text{dark}} = 87\,\text{u}$ and $m_{\text{dark}} = 174\,\text{u}$, respectively (see table 7.1).

We have expanded this method for ion strings with up to four ions including the Ba^+-ion. For this purpose, we perform the following step-by-step analysis.

1. The position x of the Ba^+-ion with respect to the trap center is detected. If $x \neq 0$, the value of x allows us to directly determine the total number of ions in the string.

2. If $x = 0$ we need to distinguish between a single Ba^+ ion and a three-ion string with Ba^+ at its center. This is done by modulating the trap drive at $\omega_{ax,Ba}$, thereby only exciting the Ba^+ ion if no further ions are present.

3. We destructively detect the Rb^+ ions by modulating the trap drive on a $5\,kHz$ wide band around $2 \times \omega_{r,Rb}/(2\pi) = 691\,kHz$. This selectively removes only Rb^+ ions from the string making use of the relatively weak inter-ionic coupling when exciting the ions radially.

4. Steps 1. and 2. are repeated to detect the number of remaining ions.

5. The Rb_2^+ ions are destructively detected via modulation around $2 \times \omega_{r,Rb2}/(2\pi) = 341\,kHz$.

7.7.2 Method 2

We have also developed a second ion detection method that does not require an ion fluorescence signal. Instead, the trapped ions are detected via their interaction with an atomic sample. For this purpose, we produce a comparatively small atom cloud containing about 1×10^5 atoms at a density of a few $10^{12}\,cm^{-3}$. In addition, we set the frequency of the dipole trap laser to an off-resonant value so that the production of additional ions during the ion probing procedure becomes extremely unlikely. We now fully overlap the ion and atom traps for an interaction time $\tau_{int} = 2\,s$. By applying an external electric field of several V/m we set the ion excess micromotion energy to values on the order of tens of $k_B \times mK$ [Ber98, Här12]. Consequently, if ions are present in the trap, strong atom losses occur due to elastic atom-ion collisions. Fig.7.7 shows a histogram of the atom numbers of the probe atom samples consisting of the outcome of about 1,000 experimental runs. The histogram displays several peaks which can be assigned to the discrete number of ions in the trap. Up to five ions were trapped simultaneously and detected with high fidelity.
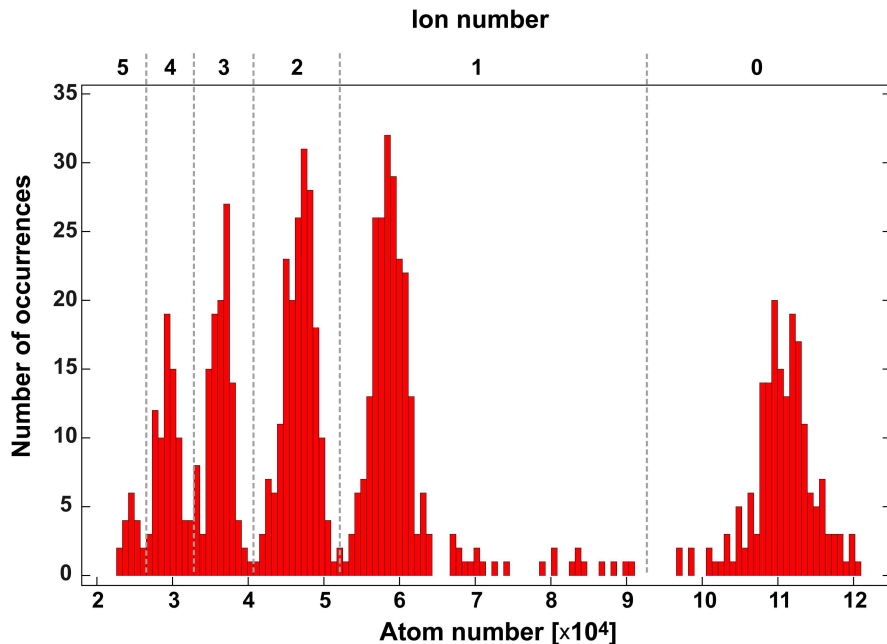
Figure 7.7: Ion detection method based on ion-induced atom loss. We overlap an ultracold atom
cloud containing approximately 110,000 atoms with the center of the Paul trap.
After an interaction time $\tau = 2\,\mathrm{s}$ we detect the ion-induced atom loss via absorption
imaging of the atom cloud. The discrete number of trapped ions is clearly reflected
in the displayed histogram of atom numbers.

The atom loss rate increases nonlinearly with ion number mainly because the inter-ionic
repulsion prevents the ions from all occupying the trap center where the atomic density is
maximal. While ion detection method 2 does not distinguish ionic masses, it has advan-
tages in terms of experimental stability and does not require the trapping of ions amenable
to laser cooling or other fluorescence based detection techniques.

Notes

- In the original publication [Här13c] the relevant excitation energies with respect to $A^1\Sigma_u^+$ and $b^3\Pi_u$ were assigned to the vibrational levels $v'_A = 68$ and $v'_b = 72$. Later it turned out that actually these energies correspond to $v'_A = 66$ and $v'_b = 73$, respectively. Therefore, the numbering was changed accordingly in the present reprint.

Chapter 8

Outlook

During my time with this project one of the main goals was lowering the collision energy in order to reach the s-wave regime. Diving in a completely new area of research made it also possible to observe new and unexpected things while working towards this goal. At the already available collision energies one can investigate many aspects of cold chemistry. The main topic of the present thesis, atom-ion three-body recombination, is but one example of this field. In the following I will point towards several additional experiments that are of interest going further in this direction. Reaching ultracold atom-ion collisions however is still the priority and there are several ideas that I will sketch about how one might actually get there in the near future.

8.1   Cold chemistry

Cold chemistry is already a hot topic when it comes to experimental atom-ion physics. Charge transfer has been investigated in great detail but could be described mostly with classical mechanics so far. However questions regarding more complex topics like three-body recombination or chemistry involving molecular ions are still open.

Shape resonances
Even though the current collision energies are too high to reach the quantum s-wave regime one could in principle already see quantum effects in atom-ion collisions due to shape resonances. A particular partial wave, if in resonance with a bound state behind the centrifugal barrier, can enhance the cross section even if many partial waves contribute

to a collision. Calculations of these resonances for the atom-ion systems in questions are available [Hal13, Idz09], showing a multitude of resonances at currently accessible collision energies. Experimentally, the preparation of defined atom-ion collision energies can be done by either moving the atoms in respect to the ions or vice versa. A precicely defined collision energy is however not possible in the experiment, only collision energy distributions can be prepared. The distribution width is given by the initial conditions, i.e. temperature, while the mean or center collision energy can be tuned by the relative velocity between the atom and the ion systems. Measuring the resonances will require the energy distribution width to be on the order of the resonance width, otherwise the resonances features will be lost in thermal averaging. While it seems to be likely that narrow enough collision energy distributions in the desired relative velocity range can be achieved, experimental demonstration of atom-ion shape resonances does not exist yet.

Molecular ions

Most cold atom-ion experiments so far have been undertaken with atomic ions, mostly because they are simpler to prepare compared to molecular ions. The already rich chemistry observed in atomic atom-ion collisions can be expected to become even more complex and hence more interesting if molecular ions come into play. Chemical processes like particle exchange reactions which go beyond the so far observed binary charge transfer, radiative association and ternary recombination could be investigated in a controlled environment at low collision energies. A promising approach to prepare few or single molecular ions would be to use the reaction products of atomic atom-ion reactions. Making experiments with molecular ions a natural evolution for current generation atom-ion setups.

Three-body recombination spectroscopy

In a similar fashion to the method presented in chapter 7 one could spectroscopically investigate the state distribution after charged three-body recombination. Working with charged instead of a neutral molecule directly, $BaRb^+$ in our case, guarantees that the reaction product is trapped, without an additional ionization step. This would allow a more simple one photon dissociation spectroscopy instead of a multi-photon process required in neutral three-body recombination. In addition one would probe the recombination into a different long-range potential, which is varying as r^{-4} compared to the neutral r^{-6} case. Accessing this similar, but yet complimentary information, would pave the way for a thorough understanding of three-body recombination process itself.

Many-body inelastic processes
Envisioned atom-ion experiments investigating many-body phenomena like polaron physics
are based on the strong and long-range atom-ion interaction, allowing many atoms to in-
teract with a single ion at the same time. But the desired many-body interaction will also
give rise to inelastic processes, which have to be accounted for as they will set bounds on
experimentally accessible regimes. Three-body recombination can be regarded as one of
the simplest many-body reactions which could be extended by adding more interaction
partners. Increasing the amount of atoms interacting with a single ion at the same time
is experimentally feasible, by simply increasing the atomic density or reducing the ion's
kinetic energy further. Disentangling the involved many-body reaction channels however
will be the challenging task.

Controlling cold reactions
Obtaining control over reaction channels will become relevant once these processes set
limits on experimentally accessible regimes. A few control options have already been
demonstrated and several more have been proposed. Also, additional directions will emerge
with the ongoing experimental and theoretical investigation of the reaction dynamics.

- Internal state preparation has been shown to affect and/or suppress reaction channels
  [Hal11, Rat12, Tom15]. This approach depends solely on the species combination
  and experimental tools available for state initialization of the chosen species.

- Feshbach resonances can be used to directly tune the interaction analogous to neutral
  atoms [Idz09]. This idea has proven itself time and time again in ultracold neutrals
  but it requires s-wave collision energies.

- With an increasing three-body cross section towards lower collision energies (see
  chapter 3) schemes to suppress this process could become desirable when approaching
  the s-wave regime. A viable option would be reducing the dimensionality of the
  atom-ion system to directly influence the collision dynamics. Confining atom-ion
  collisions to 1D has been investigated theoretically [Goo10] promising suppression of
  three-body collisions.

- Direct manipulation and suppression of inelastic collisions by light can be extended
  with the concept of blue shielding. A blue detuned laser is being used in order
  to excite a colliding particle pair into a repulsive state, which does not allow a
  close encounter collision anymore and hence no inelastic process. The concept itself

is known ultracold atoms (see e.g. [Wei99]) and could be extended to atom-ion collisions if suitable transitions can be found.

8.2   Towards atom-ion *s*-wave collisions

All current generation atom-ion experiments have a lower bound on their achievable collision energies due to the Paul trap's micromotion. It is possible to reduce the micromotion energy by compensating the responsible electric fields but there are limits to this. One approach is to choose a favorable reduced mass in form of a heavy ion and light atom. An increase of the characteristic energy E^* and at the same time a reduction of micromotion heating then ideally leads to sufficiently low energies for *s*-wave collisions. This approach is covered in the references [Cet12] and [Kry15] which both focus on a fundamental limit of atom-ion collision energies in a Paul trap. I will however look at a complementary approach that aims to circumvent micromotion all together.

Optical ion trapping

An optical dipole trap for a single ion has been demonstrated by now [Sch10b, Hub14, Lam16], making it a possibly viable option for atom-ion experiments. It is however still challenging as a relatively strong confinement is needed to compensate electrical forces due to residual stray electric fields. A good compensation of said electrical fields is therefore a prerequisite. Our currently routinely available compensation of radial stray electric fields, on the level of $E_{\mathrm{DC}} \leq 10\frac{\mathrm{mV}}{\mathrm{m}}$, should be more than sufficient. Also, the required laser sources at the desired wavelengths are readily available by now even with sufficient output powers. I have in detail covered the prerequisites for ion trapping in our setup as well as possible viable trap geometries in my diploma thesis [Krü11].

Dipole trapping of Ba^+ ions has been demonstrated with lifetimes of up to several seconds depending on the chosen wavelength [Lam16]. The remaining challenge lies in co-trapping ultracold neutral Rb atoms in the vicinity of the ion. Ideally the same light field should facilitate a trap to Rb as well and possibly provide much stronger dipole forces for the ion. With the Ba^+ and Rb wavelengths of 493nm and 780nm a reasonable choice is being blue detuned to both, near resonant to 493nm and far off resonance to 780nm. This trap geometry would require on a beam with an intensity minimum which is simple to generate, for example with a single phase plate. Blue detuning also has the advantage of having minimal light at the trap center as the trap photons could affect the collision process of Ba^+-Rb itself.

Ground state cooled ion

Having a ground state cooled ion, with very well compensated micromotion, the ion kinetic energies can be very low. Elastic atom-ion collisions will then redistribute the available micromotion energy, known as micromotion heating, until an equilibrium temperature is reached. But instead of working with a the steady state collision energy one could design experiments where only the initial few collisions are of interest, before the equilibrium temperature is reached. The low collision energies during this initial time will then have a chance to be within the *s*-wave regime. The success of this approach will depend on how well remaining excess micromotion can be compensated because it defines the collision energy of the first collision. But with the already attainable compensation of the excess micromotion energy below the μK level (see e.g. chapter 5 or Ref. [Pou12]) it should be feasible.

Atom-ion physics with Rydberg atoms

A completely different approach to access the ultracold regime in atom-ion collisions emerged in the group of Tilman Pfau recently [Sch16]. Here huge Rydberg atoms which contain an atom within its volume can be seen as the Rydberg core (an ion) interacting with a single atom if the Rydberg electron is on a high enough orbit. This idea has two major advantages. First, the collision energies can be sufficiently low for *s*-wave collisions as the Rydberg atoms have the same kinetic energy as the ultracold atomic gas they are created from. Second, unwanted effects on the ionic core due to residual electrical fields are completely shielded by the Rydberg electron. Second, residual stray electric fields do not introduce unwanted effects on the ionic core as it is completely shielded by the Rydberg electron. However, this clever approach also has the drawback that the electron cannot be completely ignored for the atom-ion interaction. How far this idea can be utilized for ultracold atom-ion physics will depend heavily on whether a regime can be found where the electron presence is of no consequence for the atom-ion interactions of interest.

Threshold ionization

This idea aims to create ultracold ions directly from an ultracold atomic gas. Given enough knowledge about the Rydberg level structure one can excite an atom directly to the ionization threshold and create an ultracold ion in free space. Having no ion trap in place makes electrical stray field compensation crucial as electric forces will accelerate the ion out of the atom cloud and limit experiment times. Already almost two decades ago E-field compensation in Rydberg experiments achieved levels down $E \approx 2 \, \frac{m\text{V}}{\text{m}}$ [Ost99].

Improving this by two more orders of magnitude would equal an acceleration of $\sim 1\,\mathrm{g}$ for Rb^+ which in turn corresponds to overlap times on the order of $\sim 1\,\mathrm{ms}$ providing ample time to investigate ultracold atom-ion collisions.

Switching off the Paul trap

Another approach to work with an ion in free space is switching off the Paul trap which contains an initially laser cooled ion. The heating during the switch off phase is negligible, as the procedure is in principle the same as when loading into an optical trap, just without the optical trap being present. Initial experiments in this direction have already been performed in our laboratory, showing a $50\,\mu\mathrm{s}$ lifetime of the ion after turning off the Paul trap. We found this lifetime to depend heavily on how well residual electrical stray field are compensated. But the lifetime limit was set solely by the presence of the static quadrupole created by the endcaps which are responsible for axial ion confinement. This remaining quadrupole will accelerate the ion into a radial direction which finally results in ion loss. One can in principle also ramp down the axial confinement similar to the radial RF confinement and therefore relax the limits on the ion lifetime.

Bibliography

[Ake12]   N. Akerman, *Trapped ions and free photons*, Ph.D. thesis, Weizmann Institute of Science Rehovot (2012)

[All11]   D. Allcock, L. Guidoni, T. Harty, C. Ballance, M. Blain, A. Steane and D. Lucas, *Reduction of heating rate in a microfabricated ion trap by pulsed-laser cleaning*, New Journal of Physics **13**, 123023 (2011), URL http://stacks.iop.org/1367-2630/13/i=12/a=123023

[All12]   D. Allcock, T. Harty, H. Janacek, N. Linke, C. Ballance, A. Steane, D. Lucas, J. Jarecki, R.L., S. Habermehl, M. Blain, D. Stick and D. Moehring, *Heating rate and electrode charging measurements in a scalable, microfabricated, surface-electrode ion trap*, Applied Physics B **107**, 913–919 (2012), URL http://dx.doi.org/10.1007/s00340-011-4788-5

[And95]   M. H. Anderson, J. R. Ensher, M. R. Matthews, C. E. Wieman and E. A. Cornell, *Observation of Bose-Einstein Condensation in a Dilute Atomic Vapor*, Science **269**, 198–201 (1995), URL http://science.sciencemag.org/content/269/5221/198

[Aud09]   C. Audet, S. Le Digabel and C. Tribes, *NOMAD user guide*, Technical Report G-2009-37, Les cahiers du GERAD (2009), URL https://www.gerad.ca/nomad/Downloads/user_guide.pdf

[Aym03]   M. Aymar, S. Azizi and O. Dulieu, *Model-potential calculations for ground and excited Σ states of Rb_2^+, Cs_2^+ and $RbCs^+$ ions*, J. Phys. B: At. Mol. Opt. Phys. **36**, 4799–4812 (2003), URL http://stacks.iop.org/0953-4075/36/i=24/a=004

[Bat62]   D. R. Bates, A. E. Kingston and R. W. P. McWhirter, *Recombination between electrons and atomic ions. I. Optically thin plasmas*, Proceedings of the Royal

Society of London. Series A. Mathematical and Physical Sciences **267**, 297–312 (1962)

[Bed00]   P. F. Bedaque, E. Braaten and H.-W. Hammer, *Three-body recombination in Bose gases with large scattering length*, Phys. Rev. Lett. **85**, 908–911 (2000), URL http://link.aps.org/doi/10.1103/PhysRevLett.85.908

[Ber98]   D. J. Berkeland, J. D. Miller, J. C. Bergquist, W. M. Itano and D. J. Wineland, *Minimization of ion micromotion in a Paul trap*, Journal of Applied Physics **83**, 5025–5033 (1998), URL http://dx.doi.org/10.1063/1.367318

[Bis13]   U. Bissbort, D. Cocks, A. Negretti, Z. Idziaszek, T. Calarco, F. Schmidt-Kaler, W. Hofstetter and R. Gerritsma, *Emulating Solid-State Physics with a Hybrid System of Ultracold Ions and Atoms*, Phys. Rev. Lett. **111**, 080501 (2013), URL http://link.aps.org/doi/10.1103/PhysRevLett.111.080501

[Bla08]   R. Blatt and D. Wineland, *Entangled states of trapped atomic ions*, Nature **453**, 1008–1015 (2008), URL http://dx.doi.org/10.1038/nature07125

[Bla12]   R. Blatt and C. F. Roos, *Quantum simulations with trapped ions*, Nature Physics **8**, 277–284 (2012), URL http://dx.doi.org/10.1038/nphys2252

[Bra01]   E. Braaten and H.-W. Hammer, *Three-body recombination into deep bound states in a Bose gas with large scattering length*, Phys. Rev. Lett. **87**, 160407 (2001), URL http://link.aps.org/doi/10.1103/PhysRevLett.87.160407

[Bur97]   E. A. Burt, R. W. Ghrist, C. J. Myatt, M. J. Holland, E. A. Cornell and C. E. Wieman, *Coherence, Correlations, and Collisions: What One Learns about Bose-Einstein Condensates from Their Decay*, Phys. Rev. Lett. **79**, 337–340 (1997), URL http://link.aps.org/doi/10.1103/PhysRevLett.79.337

[Cam92]   J. Camp, T. Darling and R. Brown, *Effect of crystallites on surface potential variations of Au and graphite*, New Journal of Physics **71**, 783 (1992), URL http://stacks.iop.org/1367-2630/12/i=9/a=093035

[Cas11]   W. Casteels, J. Tempere and J. Devreese, *Polaronic Properties of an Ion in a Bose-Einstein Condensate in the Strong-Coupling Limit*, Journal of Low Temperature Physics **162**, 266–273 (2011), URL http://dx.doi.org/10.1007/s10909-010-0286-0

[Cet12]   M. Cetina, A. T. Grier and V. Vuletić, *Micromotion-Induced Limit to Atom-Ion Sympathetic Cooling in Paul Traps*, Phys. Rev. Lett. **109**, 253201 (2012), URL http://link.aps.org/doi/10.1103/PhysRevLett.109.253201

[Che14]   K. Chen, S. T. Sullivan and E. R. Hudson, *Neutral Gas Sympathetic Cooling of an Ion in a Paul Trap*, Phys. Rev. Lett. **112**, 143009 (2014), URL http://link.aps.org/doi/10.1103/PhysRevLett.112.143009

[Cho10]   C. W. Chou, D. B. Hume, J. C. J. Koelemeij, D. J. Wineland and T. Rosenband, *Frequency Comparison of Two High-Accuracy Al^+ Optical Clocks*, Phys. Rev. Lett. **104**, 070802 (2010), URL http://link.aps.org/doi/10.1103/PhysRevLett.104.070802

[Chu86]   S. Chu, J. E. Bjorkholm, A. Ashkin and A. Cable, *Experimental Observation of Optically Trapped Atoms*, Phys. Rev. Lett. **57**, 314–317 (1986), URL http://link.aps.org/doi/10.1103/PhysRevLett.57.314

[Chu13]   B. L. Chuah, N. C. Lewty, R. Cazan and M. D. Barrett, *Detection of ion micromotion in a linear Paul trap with a high finesse cavity*, Opt. Express **21**, 10632–10641 (2013), URL http://www.opticsexpress.org/abstract.cfm?URI=oe-21-9-10632

[Chw09]   M. Chwalla, *Precision spectroscopy with $^{40}Ca^+$ ions in a Paul trap*, Ph.D. thesis, Universität Innsbruck (2009)

[Côt00a]   R. Côté, *From Classical Mobility to Hopping Conductivity: Charge Hopping in an Ultracold Gas*, Phys. Rev. Lett. **85**, 5316–5319 (2000), URL http://link.aps.org/doi/10.1103/PhysRevLett.85.5316

[Côt00b]   R. Côté and A. Dalgarno, *Ultracold atom-ion collisions*, Phys. Rev. A **62**, 012709 (2000), URL http://link.aps.org/doi/10.1103/PhysRevA.62.012709

[Côt02]   R. Côté, V. Kharchenko and M. D. Lukin, *Mesoscopic Molecular Ions in Bose-Einstein Condensates*, Phys. Rev. Lett. **89**, 093001 (2002), URL http://link.aps.org/doi/10.1103/PhysRevLett.89.093001

[Dan11]   N. Daniilidis, S. Narayanan, S. A. Möller, R. Clark, T. E. Lee, P. J. Leek, A. Wallraff, S. Schulz, F. Schmidt-Kaler and H. Häffner, *Fabrication and heating rate study of microscopic surface electrode ion traps*, New Journal of Physics **13**, 013032 (2011), URL http://stacks.iop.org/1367-2630/13/i=1/a=013032

[Dav95]   K. B. Davis, M. O. Mewes, M. R. Andrews, N. J. van Druten, D. S. Durfee, D. M. Kurn and W. Ketterle, *Bose-Einstein Condensation in a Gas of Sodium Atoms*, Phys. Rev. Lett. **75**, 3969–3973 (1995), URL http://link.aps.org/doi/10.1103/PhysRevLett.75.3969

[Deb08]   M. Debatin, M. Kröner, J. Mikosch, S. Trippel, N. Morrison, M. Reetz-Lamour, P. Woias, R. Wester and M. Weidemüller, *Planar multipole ion trap*, Phys. Rev. A **77**, 033422 (2008), URL http://link.aps.org/doi/10.1103/PhysRevA.77.033422

[Des06]   L. Deslauriers, S. Olmschenk, D. Stick, W. K. Hensinger, J. Sterk and C. Monroe, *Scaling and Suppression of Anomalous Heating in Ion Traps*, Phys. Rev. Lett. **97**, 103007 (2006), URL http://link.aps.org/doi/10.1103/PhysRevLett.97.103007

[DeV02]   R. G. DeVoe and C. Kurtsiefer, *Experimental study of anomalous heating and trap instabilities in a microscopic ^{137}Ba ion trap*, Phys. Rev. A **65**, 063407 (2002), URL http://link.aps.org/doi/10.1103/PhysRevA.65.063407

[DeV09]   R. G. DeVoe, *Power-Law Distributions for a Trapped Ion Interacting with a Classical Buffer Gas*, Phys. Rev. Lett. **102**, 063001 (2009), URL http://link.aps.org/doi/10.1103/PhysRevLett.102.063001

[D'I05]   J. P. D'Incao and B. D. Esry, *Scattering Length Scaling Laws for Ultracold Three-Body Collisions*, Phys. Rev. Lett. **94**, 213201 (2005), URL http://link.aps.org/doi/10.1103/PhysRevLett.94.213201

[d'I13]   J. d'Incao, *private communication* (2013)

[Doe10]   H. Doerk, Z. Idziaszek and T. Calarco, *Atom-ion quantum gate*, Phys. Rev. A **81**, 012708 (2010), URL http://link.aps.org/doi/10.1103/PhysRevA.81.012708

[Dro12]   A. Drozdova, *Study of Spin-Orbit Coupled Electronic States of Rb_2 , NaCs and NaK Molecules. Laser Spectroscopy and Accurate Coupled-channel Deperturbation Analysis*, Ph.D. thesis, Université de Lyon and Lomonosov State University (2012)

[Efi70]   V. Efimov, *Energy levels arising from resonant two-body forces in a three-body system*, Physics Letters B **33**, 563 – 564 (1970), URL http://dx.doi.org/10.1016/0370-2693(70)90349-7

[Esr99]   B. D. Esry, C. H. Greene and J. P. Burke, *Recombination of Three Atoms in the Ultracold Limit*, Phys. Rev. Lett. **83**, 1751–1754 (1999), URL http://link.aps.org/doi/10.1103/PhysRevLett.83.1751

[Ess98]   T. Esslinger, I. Bloch and T. W. Hänsch, *Bose-Einstein condensation in a quadrupole-Ioffe-configuration trap*, Phys. Rev. A **58**, R2664–R2667 (1998), URL http://link.aps.org/doi/10.1103/PhysRevA.58.R2664

[Fed96]   P. O. Fedichev, M. W. Reynolds and G. V. Shlyapnikov, *Three-body recombination of ultracold atoms to a weakly bound s level*, Phys. Rev. Lett. **77**, 2921–2924 (1996), URL http://link.aps.org/doi/10.1103/PhysRevLett.77.2921

[Fio98]   A. Fioretti, D. Comparat, A. Crubellier, O. Dulieu, F. Masnou-Seeuws and P. Pillet, *Formation of Cold Cs_2 Molecules through Photoassociation*, Phys. Rev. Lett. **80**, 4402–4405 (1998), URL http://link.aps.org/doi/10.1103/PhysRevLett.80.4402

[Flo07]   D. R. Flower and G. J. Harris, *Three-body recombination of hydrogen during primordial star formation*, Monthly Notices of the Royal Astronomical Society **377**, 705–710 (2007), URL http://mnras.oxfordjournals.org/content/377/2/705.abstract

[Gab00]   C. Gabbanini, A. Fioretti, A. Lucchesini, S. Gozzini and M. Mazzoni, *Cold Rubidium Molecules Formed in a Magneto-Optical Trap*, Phys. Rev. Lett. **84**, 2814–2817 (2000), URL http://link.aps.org/doi/10.1103/PhysRevLett.84.2814

[Gao10]   B. Gao, *Universal Properties in Ultracold Ion-Atom Interactions*, Phys. Rev. Lett. **104**, 213201 (2010), URL http://link.aps.org/doi/10.1103/PhysRevLett.104.213201

[Goo10]   J. Goold, H. Doerk, Z. Idziaszek, T. Calarco and T. Busch, *Ion-induced density bubble in a strongly correlated one-dimensional gas*, Phys. Rev. A **81**, 041601 (2010), URL http://link.aps.org/doi/10.1103/PhysRevA.81.041601

[Gri00]   R. Grimm, M. Weidemüller and Y. B. Ovchinnikov, *Optical Dipole Traps for Neutral Atoms*, volume 42 of *Advances In Atomic, Molecular, and Optical Physics*, pages 95 – 170 (Academic Press) (2000), URL http://www.sciencedirect.com/science/article/pii/S1049250X0860186X

[Gri09]   A. T. Grier, M. Cetina, F. Oručević and V. Vuletić, *Observation of Cold Colli-sions between Trapped Ions and Trapped Atoms*, Phys. Rev. Lett. **102**, 223201 (2009), URL http://link.aps.org/doi/10.1103/PhysRevLett.102.223201

[Gue12]   N. L. Guevara, Y. Wang and B. D. Esry, *New Class of Three-Body States*, Phys. Rev. Lett. **108**, 213202 (2012), URL http://link.aps.org/doi/10.1103/PhysRevLett.108.213202

[Hal11]   F. H. J. Hall, M. Aymar, N. Bouloufa-Maafa, O. Dulieu and S. Willitsch, *Light-Assisted Ion-Neutral Reactive Processes in the Cold Regime: Radiative Molecule Formation versus Charge Exchange*, Phys. Rev. Lett. **107**, 243202 (2011), URL http://link.aps.org/doi/10.1103/PhysRevLett.107.243202

[Hal12]   F. H. J. Hall and S. Willitsch, *Millikelvin Reactive Collisions between Sym-pathetically Cooled Molecular Ions and Laser-Cooled Atoms in an Ion-Atom Hybrid Trap*, Phys. Rev. Lett. **109**, 233202 (2012), URL http://link.aps.org/doi/10.1103/PhysRevLett.109.233202

[Hal13]   F. H. Hall, M. Aymar, M. Raoult, O. Dulieu and S. Willitsch, *Light-assisted cold chemical reactions of barium ions with rubidium atoms*, Molecular Physics **111**, 1683–1690 (2013), URL http://dx.doi.org/10.1080/00268976.2013.770930

[Har10]   M. Harlander, M. Brownnutt, W. Hänsel and R. Blatt, *Trapped-ion probing of light-induced charging effects on dielectrics*, New Journal of Physics **12**, 093035 (2010), URL http://stacks.iop.org/1367-2630/12/i=9/a=093035

[Haz13]   S. Haze, S. Hata, M. Fujinaga and T. Mukaiyama, *Observation of elastic colli-sions between lithium atoms and calcium ions*, Phys. Rev. A **87**, 052715 (2013), URL http://link.aps.org/doi/10.1103/PhysRevA.87.052715

[Haz15]   S. Haze, R. Saito, M. Fujinaga and T. Mukaiyama, *Charge-exchange colli-sions between ultracold fermionic lithium atoms and calcium ions*, Phys. Rev. A **91**, 032709 (2015), URL http://link.aps.org/doi/10.1103/PhysRevA.91.032709

[Hem11]   B. Hemmerling, *Towards Direct Frequency Comb Spectroscopy Using Quantum Logic*, Ph.D. thesis, Gottfried Wilhelm Leibniz Universität Hannover (2011)

[Hes83]   H. F. Hess, D. A. Bell, G. P. Kochanski, R. W. Cline, D. Kleppner and T. J. Greytak, *Observation of Three-Body Recombination in Spin-Polarized Hydro-*

gen, Phys. Rev. Lett. **51**, 483–486 (1983), URL http://link.aps.org/doi/10.1103/PhysRevLett.51.483

[Häf08]   H. Häffner, C. Roos and R. Blatt, *Quantum computing with trapped ions*, Physics Reports **469**, 155 – 203 (2008), URL http://www.sciencedirect.com/science/article/pii/S0370157308003463

[Hit12]   D. A. Hite, Y. Colombe, A. C. Wilson, K. R. Brown, U. Warring, R. Jördens, J. D. Jost, K. S. McKay, D. P. Pappas, D. Leibfried and D. J. Wineland, *100-Fold Reduction of Electric-Field Noise in an Ion Trap Cleaned with In-Situ Argon-Ion-Beam Bombardment*, Phys. Rev. Lett. **109**, 103001 (2012), URL http://link.aps.org/doi/10.1103/PhysRevLett.109.103001

[Höl16]   B. Höltkemeier, P. Weckesser, H. López-Carrera and M. Weidemüller, *Buffer-Gas Cooling of a Single Ion in a Multipole Radio Frequency Trap Beyond the Critical Mass Ratio*, Phys. Rev. Lett. **116**, 233003 (2016), URL http://link.aps.org/doi/10.1103/PhysRevLett.116.233003

[Här12]   A. Härter, A. Krükow, A. Brunner, W. Schnitzler, S. Schmid and J. Hecker Denschlag, *Single Ion as a Three-Body Reaction Center in an Ultracold Atomic Gas*, Phys. Rev. Lett. **109**, 123201 (2012), URL http://link.aps.org/doi/10.1103/PhysRevLett.109.123201

[Här13a]   A. Härter, *Two-Body and Three-Body Dynamics in Atom-Ion Experiments*, Ph.D. thesis, Universität Ulm (2013)

[Här13b]   A. Härter, A. Krükow, A. Brunner and J. Hecker Denschlag, *Minimization of ion micromotion using ultracold atomic probes*, Applied Physics Letters **102**, 221115 (2013), URL http://scitation.aip.org/content/aip/journal/apl/102/22/10.1063/1.4809578

[Här13c]   A. Härter, A. Krükow, M. Deiß, B. Drews, E. Tiemann and J. Hecker Denschlag, *Population distribution of product states following three-body recombination in an ultracold atomic gas*, Nature Physics **9**, 512–517 (2013), URL http://www.nature.com/nphys/journal/v9/n8/abs/nphys2661.html

[Här14a]   A. Härter and J. Hecker Denschlag, *Cold atom-ion experiments in hybrid traps*, Contemporary Physics **55**, 33–45 (2014), URL http://dx.doi.org/10.1080/00107514.2013.854618

[Här14b]   A. Härter, A. Krükow, A. Brunner and J. Hecker Denschlag, *Long-term drifts of stray electric fields in a Paul trap*, Applied Physics B **114**, 275–281 (2014), URL http://dx.doi.org/10.1007/s00340-013-5688-7

[Hua06]   Y. Huang, J. Qi, H. K. Pechkis, D. Wang, E. E. Eyler, P. L. Gould and W. C. Stwalley, *Formation, detection and spectroscopy of ultracold Rb_2 in the ground $X^1\Sigma_g^+$ state*, Journal of Physics B: Atomic, Molecular and Optical Physics **39**, S857–S869 (2006), URL http://stacks.iop.org/0953-4075/39/i=19/a=S04

[Hub14]   T. Huber, A. Lambrecht, J. Schmidt, L. Karpa and T. Schaetz, *A far-off-resonance optical trap for a Ba^+ ion*, Nature Commun. **5**, 5587 (2014), URL http://link.aps.org/doi/10.1038/ncomms6587

[Idz07]   Z. Idziaszek, T. Calarco and P. Zoller, *Controlled collisions of a single atom and an ion guided by movable trapping potentials*, Phys. Rev. A **76**, 033409 (2007), URL http://link.aps.org/doi/10.1103/PhysRevA.76.033409

[Idz09]   Z. Idziaszek, T. Calarco, P. S. Julienne and A. Simoni, *Quantum theory of ultracold atom-ion collisions*, Phys. Rev. A **79**, 010702 (2009), URL http://link.aps.org/doi/10.1103/PhysRevA.79.010702

[Idz11]   Z. Idziaszek, A. Simoni, T. Calarco and P. S. Julienne, *Multichannel quantum-defect theory for ultracold atom-ion collisions*, New Journal of Physics **13**, 083005 (2011), URL http://stacks.iop.org/1367-2630/13/i=8/a=083005

[Ino98]   S. Inouye, M. R. Andrews, J. Stenger, H.-J. Miesner, D. M. Stamper-Kurn and W. Ketterle, *Observation of Feshbach resonances in a Bose-Einstein condensate*, Nature **392**, 151–154 (1998), URL http://dx.doi.org/10.1038/32354

[Joc03]   S. Jochim, M. Bartenstein, A. Altmeyer, G. Hendl, S. Riedl, C. Chin, J. Hecker Denschlag and R. Grimm, *Bose-Einstein Condensation of Molecules*, Science **302**, 2101–2103 (2003), URL http://science.sciencemag.org/content/302/5653/2101

[Ket99]   W. Ketterle, D. Durfee and D. Stamper-Kurn, *Making, probing and understanding Bose-Einstein condensates*, in *Bose-Einstein condensation in atomic gases*, edited by M. Inguscio, S. Stringari and C. Wieman, volume 140 of *Proceedings of the International School of Physics "Enrico Fermi"*, pages 67–176 (IOS Press, Amsterdam) (1999)

[Krü11]   A. Krükow, *Verbesserte und neuartige Fallenkonfigurationen im BaRbI-Experiment*, Master's thesis, Universität Ulm (2011)

[Krü16a]   A. Krükow, A. Mohammadi, A. Härter and J. Hecker Denschlag, *Reactive two-body and three-body collisions of* Ba^+ *in an ultracold Rb gas*, Phys. Rev. A **94**, 030701 (2016), URL http://link.aps.org/doi/10.1103/PhysRevA.94.030701

[Krü16b]   A. Krükow, J. Pérez-Ríos, A. Mohammadi, A. Härter, J. Hecker Denschlag and C. H. Greene, *Energy Scaling of Cold Atom-atom-ion Three-body Recombination*, Phys. Rev. Lett. **116**, 193201 (2016), URL http://journals.aps.org/prl/abstract/10.1103/PhysRevLett.116.193201

[Kra06]   T. Kraemer, M. Mark, P. Waldburger, J. G. Danzl, C. Chin, B. Engeser, A. D. Lange, K. Pilch, A. Jaakkola, H. C. Nägerl and R. Grimm, *Evidence for Efimov quantum states in an ultracold gas of caesium atoms*, Nature **440**, 315–318 (2006), URL http://dx.doi.org/10.1038/nature04626

[Krs03]   P. S. Krstić, R. K. Janev and D. R. Schultz, *Three-body, diatomic association in cold hydrogen plasmas*, Journal of Physics B: Atomic, Molecular and Optical Physics **36**, L249 (2003), URL http://stacks.iop.org/0953-4075/36/i=16/a=103

[Kry11]   M. Krych, W. Skomorowski, F. Pawłowski, R. Moszynski and Z. Idziaszek, *Sympathetic cooling of the* Ba^+ *ion by collisions with ultracold Rb atoms: Theoretical prospects*, Phys. Rev. A **83**, 032723 (2011), URL http://link.aps.org/doi/10.1103/PhysRevA.83.032723

[Kry15]   M. Krych and Z. Idziaszek, *Description of ion motion in a Paul trap immersed in a cold atomic gas*, Phys. Rev. A **91**, 023430 (2015), URL http://link.aps.org/doi/10.1103/PhysRevA.91.023430

[Lab08]   J. Labaziewicz, Y. Ge, D. Leibrandt, S. Wang, R. Shewmon and I. Chuang, *Temperature Dependence of Electric Field Noise above Gold Surfaces*, Phys. Rev. Lett. **101**, 180602 (2008), URL http://link.aps.org/doi/10.1103/PhysRevLett.101.180602

[Lam16]   A. Lambrecht, J. Schmidt, P. Weckesser, M. Debatin, L. Karpa and T. Schaetz, *Long lifetimes in optical ion traps*, arXiv:1609.06429 (2016), URL https://arxiv.org/abs/1609.06429

[Le 11]   S. Le Digabel, *Algorithm 909: NOMAD: Nonlinear Optimization with the MADS algorithm*, ACM Transactions on Mathematical Software **37**, 1–15 (2011), URL http://doi.acm.org/10.1145/1916461.1916468

[Lei03]   D. Leibfried, R. Blatt, C. Monroe and D. Wineland, *Quantum dynamics of single trapped ions*, Rev. Mod. Phys. **75**, 281–324 (2003), URL http://link.aps.org/doi/10.1103/RevModPhys.75.281

[Lin09]   Y.-J. Lin, A. R. Perry, R. L. Compton, I. B. Spielman and J. V. Porto, *Rapid production of ^{87}Rb Bose-Einstein condensates in a combined magnetic and optical potential*, Phys. Rev. A **79**, 063631 (2009), URL http://link.aps.org/doi/10.1103/PhysRevA.79.063631

[Loz06]   J. Lozeille, A. Fioretti, C. Gabbanini, Y. Huang, H. K. Pechkis, D. Wang, P. L. Gould, E. E. Eyler, W. C. Stwalley, M. Aymar and O. Dulieu, *Detection by two-photon ionization and magnetic trapping of cold Rb_2 triplet state molecules*, Eur. Phys. J. D **39**, 261–269 (2006), URL http://dx.doi.org/10.1140/epjd/e2006-00084-4

[Maj68]   F. G. Major and H. G. Dehmelt, *Exchange-Collision Technique for the rf Spectroscopy of Stored Ions*, Phys. Rev. **170**, 91 (1968), URL http://link.aps.org/doi/10.1103/PhysRev.170.91

[Mak03]   O. P. Makarov, R. Côté, H. Michels and W. W. Smith, *Radiative charge-transfer lifetime of the excited state of* $(NaCa)^+$, Phys. Rev. A **67**, 042705 (2003), URL http://link.aps.org/doi/10.1103/PhysRevA.67.042705

[Mas05]   P. Massignan, C. J. Pethick and H. Smith, *Static properties of positive ions in atomic Bose-Einstein condensates*, Phys. Rev. A **71**, 023606 (2005), URL http://link.aps.org/doi/10.1103/PhysRevA.71.023606

[Mig85]   A. L. Migdall, J. V. Prodan, W. D. Phillips, T. H. Bergeman and H. J. Metcalf, *First Observation of Magnetically Trapped Neutral Atoms*, Phys. Rev. Lett. **54**, 2596–2599 (1985), URL http://link.aps.org/doi/10.1103/PhysRevLett.54.2596

[Mon95]   C. Monroe, D. M. Meekhof, B. E. King, S. R. Jefferts, W. M. Itano, D. J. Wineland and P. Gould, *Resolved-Sideband Raman Cooling of a Bound Atom to the 3D Zero-Point Energy*, Phys. Rev. Lett. **75**, 4011–4014 (1995), URL http://link.aps.org/doi/10.1103/PhysRevLett.75.4011

[Mon16]   T. Monz, D. Nigg, E. A. Martinez, M. F. Brandl, P. Schindler, R. Rines, S. X. Wang, I. L. Chuang and R. Blatt, *Realization of a scalable Shor algorithm*, Science **351**, 1068–1070 (2016), URL http://science.sciencemag.org/content/351/6277/1068

[Mor01]   G. Morigi and H. Walther, *Two-species Coulomb chains for quantum information*, Eur. Phys. J. D **13**, 261–269 (2001), URL http://dx.doi.org/10.1007/s100530170275

[Mud09]   M. Mudrich, P. Heister, T. Hippler, C. Giese, O. Dulieu and F. Stienkemeier, *Spectroscopy of triplet states of Rb_2 by femtosecond pump-probe photoionization of doped helium nanodroplets*, Phys. Rev. A **80**, 042512 (2009), URL http://link.aps.org/doi/10.1103/PhysRevA.80.042512

[Muk04]   T. Mukaiyama, J. R. Abo-Shaeer, K. Xu, J. K. Chin and W. Ketterle, *Dissociation and Decay of Ultracold Sodium Molecules*, Phys. Rev. Lett. **92**, 180402 (2004), URL http://link.aps.org/doi/10.1103/PhysRevLett.92.180402

[Nar11]   S. Narayanan, N. Daniilidis, S. A. Möller, R. Clark, F. Ziesel, K. Singer, F. Schmidt-Kaler and H. Häffner, *Electric field compensation and sensing with a single ion in a planar trap*, Journal of Applied Physics **110**, 114909 (2011), URL http://link.aip.org/link/?JAP/110/114909/1

[Neu80]   W. Neuhauser, M. Hohenstatt, P. E. Toschek and H. Dehmelt, *Localized visible Ba^+ mono-ion oscillator*, Phys. Rev. A **22**, 1137–1140 (1980), URL http://link.aps.org/doi/10.1103/PhysRevA.22.1137

[Ost99]   A. Osterwalder and F. Merkt, *Using High Rydberg States as Electric Field Sensors*, Phys. Rev. Lett. **82**, 1831–1834 (1999), URL http://link.aps.org/doi/10.1103/PhysRevLett.82.1831

[Pla12]   R. Plašil, I. Zymak, P. Jusko, D. Mulin, D. Gerlich and J. Glosík, *Stabilization of H+–H2 collision complexes between 11 and 28K*, Philosophical Transactions of the Royal Society of London A: Mathematical, Physical and Engineering Sciences **370**, 5066–5073 (2012), URL http://dx.doi.org/10.1098/rsta.2012.0098

[Pou12]   G. Poulsen, Y. Miroshnychenko and M. Drewsen, *Efficient ground-state cooling of an ion in a large room-temperature linear Paul trap with a sub-Hertz heating rate*, Phys. Rev. A **86**, 051402 (2012), URL http://link.aps.org/doi/10.1103/PhysRevA.86.051402

[PR14]   J. Pérez-Ríos, S. Ragole, J. Wang and C. H. Greene, *Comparison of classical and quantal calculations of helium three-body recombination*, J. Chem. Phys. **140**, 044307 (2014), URL http://scitation.aip.org/content/aip/journal/jcp/140/4/10.1063/1.4861851

[PR15]   J. Pérez-Ríos and C. H. Greene, *Communication: Classical threshold law for ion-neutral-neutral three-body recombination*, The Journal of Chemical Physics **143**, 041105 (2015), URL http://scitation.aip.org/content/aip/journal/jcp/143/4/10.1063/1.4927702

[Pyk13]   K. Pyka, N. Herschbach, J. Keller and T. E. Mehlstäubler, *A high-precision segmented Paul trap with minimized micromotion for an optical multiple-ion clock*, Applied Physics B **114**, 231–241 (2013), URL http://dx.doi.org/10.1007/s00340-013-5580-5

[Qué07]   G. Quéméner, J.-M. Launay and P. Honvault, *Ultracold collisions between Li atoms and* Li_2 *diatoms in high vibrational states*, Phys. Rev. A **75**, 050701 (2007), URL http://link.aps.org/doi/10.1103/PhysRevA.75.050701

[Raa87]   E. L. Raab, M. Prentiss, A. Cable, S. Chu and D. E. Pritchard, *Trapping of Neutral Sodium Atoms with Radiation Pressure*, Phys. Rev. Lett. **59**, 2631–2634 (1987), URL http://link.aps.org/doi/10.1103/PhysRevLett.59.2631

[Raa00]   C. Raab, J. Eschner, J. Bolle, H. Oberst, F. Schmidt-Kaler and R. Blatt, *Motional Sidebands and Direct Measurement of the Cooling Rate in the Resonance Fluorescence of a Single Trapped Ion*, Phys. Rev. Lett. **85**, 538–541 (2000), URL http://link.aps.org/doi/10.1103/PhysRevLett.85.538

[Rat12]   L. Ratschbacher, C. Zipkes and M. Sias, C.AND Köhl, *Controlling chemical reactions of a single particle*, Nature Physics **8**, 649 (2012), URL http://www.nature.com/doifinder/10.1038/nphys2373

[Rat13]   L. Ratschbacher, C. Sias, L. Carcagni, J. M. Silver, C. Zipkes and M. Köhl, *Decoherence of a Single-Ion Qubit Immersed in a Spin-Polarized Atomic Bath*, Phys. Rev. Lett. **110**, 160402 (2013), URL http://link.aps.org/doi/10.1103/PhysRevLett.110.160402

[Rav12]   K. Ravi, S. Lee, A. Sharma, G. Werth and S. A. Rangwala, *Cooling and stabilization by collisions in a mixed ion-atom system*, Nature Commun. **3**, 1126 (2012), URL http://www.nature.com/doifinder/10.1038/ncomms2131

[Rel11]   W. G. Rellergert, S. T. Sullivan, S. Kotochigova, A. Petrov, K. Chen, S. J. Schowalter and E. R. Hudson, *Measurement of a Large Chemical Reaction Rate between Ultracold Closed-Shell ^{40}Ca Atoms and Open-Shell ^{174}Yb$^+$Ions Held in a Hybrid Atom-Ion Trap*, Phys. Rev. Lett. **107**, 243201 (2011), URL http://link.aps.org/doi/10.1103/PhysRevLett.107.243201

[Rel13]   W. G. Rellergert, S. T. Sullivan, S. J. Schowalter, S. Kotochigova and E. R. Chen, Kuang andHudson, *Evidence for sympathetic vibrational cooling of translationally cold molecules*, Nature **495**, 490–494 (2013), URL http://www.nature.com/doifinder/10.1038/nature11937

[Ros92]   F. Rossi and G. Opat, *Observations of the effects of adsorbates on patch potentials*, J. Phys. D: Appl. Phys. **25**, 1349 (1992), URL http://stacks.iop.org/1367-2630/12/i=9/a=093035

[Ros08]   T. Rosenband, D. B. Hume, P. O. Schmidt, C. W. Chou, A. Brusch, L. Lorini, W. H. Oskay, R. E. Drullinger, T. M. Fortier, J. E. Stalnaker, S. A. Diddams, W. C. Swann, N. R. Newbury, W. M. Itano, D. J. Wineland and J. C. Bergquist, *Frequency Ratio of Al$^+$ and Hg$^+$ Single-Ion Optical Clocks; Metrology at the 17th Decimal Place*, Science **319**, 1808–1812 (2008), URL http://dx.doi.org/10.1126/science.1154622

[Sal08]   W. Salzmann, T. Mullins, J. Eng, M. Albert, R. Wester, M. Weidemüller, A. Merli, S. M. Weber, F. Sauer, M. Plewicki, F. Weise, L. Wöste and A. Lindinger, *Coherent transients in the femtosecond photoassociation of ultracold molecules*, Phys. Rev. Lett. **100**, 233003 (2008)

[Sch10a]   S. Schmid, A. Härter and J. Hecker Denschlag, *Dynamics of a Cold Trapped Ion in a Bose-Einstein Condensate*, Phys. Rev. Lett. **105**, 133202 (2010), URL http://link.aps.org/doi/10.1103/PhysRevLett.105.133202

[Sch10b]   C. Schneider, M. Enderlein, T. Huber and T. Schaetz, *Optical trapping of an ion*, Nat. Photonics **4**, 772 (2010), URL http://www.nature.com/doifinder/10.1038/nphoton.2010.236

[Sch11]   S. Schmid, *Dynamics of a cold trapped ion in a Bose-Einstein condensate*, Ph.D. thesis, Universität Ulm (2011)

[Sch12]   S. Schmid, A. Härter, A. Frisch, S. Hoinka and J. Hecker Denschlag, *An apparatus for immersing trapped ions into an ultracold gas of neutral atoms*, Review of

Scientific Instruments **83**, 053108 (2012), URL http://scitation.aip.org/content/aip/journal/rsi/83/5/10.1063/1.4718356

[Sch16]   M. Schlagmüller, T. C. Liebisch, F. Engel, K. S. Kleinbach, F. Böttcher, U. Hermann, K. M. Westphal, A. Gaj, R. Löw, S. Hofferberth, T. Pfau, J. Pérez-Ríos and C. H. Greene, *Ultracold Chemical Reactions of a Single Rydberg Atom in a Dense Gas*, Phys. Rev. X **6**, 031020 (2016), URL http://link.aps.org/doi/10.1103/PhysRevX.6.031020

[Söd99]   J. Söding, D. Guéry-Odelin, P. Desbiolles, F. Chevy, H. Inamori and J. Dalibard, *Three-body decay of a Rubidium Bose-Einstein condensate*, Applied Physics B **69**, 257–261 (1999), URL http://dx.doi.org/10.1007/s003400050805

[Sia14]   C. Sias and M. Köhl, *Hybrid Quantum Systems of Atoms and Ions*, in *Quantum Gas Experiments*, edited by P. Törmä and K. Sengstock, page 267 (Wold Scientific, Singapore) (2014)

[Sil92]   I. F. Silvera, *Prospects for Bose-Einstein condensation in atomic hydrogen and other gases*, Journal of Low Temperature Physics **89**, 287–296 (1992), URL http://dx.doi.org/10.1007/BF00692601

[Sim06]   A. Simoni and J.-M. Launay, *Ultracold atom-molecule collisions with hyperfine coupling*, Laser Physics **16**, 707–712 (2006), URL http://dx.doi.org/10.1134/S1054660X0604027X

[Sin10]   K. Singer, U. Poschinger, M. Murphy, P. Ivanov, F. Ziesel, T. Calarco and F. Schmidt-Kaler, *Colloquium : Trapped ions as quantum bits: Essential numerical tools*, Rev. Mod. Phys. **82**, 2609–2632 (2010), URL http://link.aps.org/doi/10.1103/RevModPhys.82.2609

[Siv12]   I. Sivarajah, D. S. Goodman, J. E. Wells, F. A. Narducci and W. W. Smith, *Evidence of sympathetic cooling of Na^+ ions by a Na magneto-optical trap in a hybrid trap*, Phys. Rev. A **86**, 063419 (2012), URL http://link.aps.org/doi/10.1103/PhysRevA.86.063419

[SJ15]   H. da Silva Jr, M. Raoult, M. Aymar and O. Dulieu, *Formation of molecular ions by radiative association of cold trapped atoms and ions*, New Journal of Physics **17**, 045015 (2015), URL http://stacks.iop.org/1367-2630/17/i=4/a=045015

[Smi03]   W. W. Smith, E. Babenko, R. Côté and H. H. Michels, *On the collisional cooling of co-trapped atomic and molecular ions by ultracold atoms: Ca^+ + Na and $Na_2^+(v^*,J^*)$ + Na*, in *Coherence and Quantum Optics VIII*, edited by N. Bigelow, J. Eberly, C. R. Stroud and I. Walmsley, Proceedings of the Eighth Rochester Conference on Coherence and Quantum Optics, held at the University of Rochester, June 13-16, 2001, pages 623–624 (Kluwer Academic / Plenum Publishers, New York) (2003)

[Smi13]   W. W. Smith, D. S. Goodman, I. Sivarajah, J. E. Wells, S. Banerjee, R. Côté, H. H. Michels, J. A. Mongtomery and F. A. Narducci, *Experiments with an ion-neutral hybrid trap: cold charge-exchange collisions*, Applied Physics B **114**, 75–80 (2013), URL http://dx.doi.org/10.1007/s00340-013-5672-2

[Spe12]   N. Spethmann, F. Kindermann, S. John, C. Weber, D. Meschede and A. Widera, *Dynamics of Single Neutral Impurity Atoms Immersed in an Ultracold Gas*, Phys. Rev. Lett. **109**, 235301 (2012), URL http://link.aps.org/doi/10.1103/PhysRevLett.109.235301

[Sta06]   P. Staanum, S. D. Kraft, J. Lange, R. Wester and M. Weidemüller, *Experimental Investigation of Ultracold Atom-Molecule Collisions*, Phys. Rev. Lett. **96**, 023201 (2006), URL http://link.aps.org/doi/10.1103/PhysRevLett.96.023201

[Str10]   C. Strauss, T. Takekoshi, F. Lang, K. Winkler, R. Grimm, J. Hecker Denschlag and E. Tiemann, *Hyperfine, rotational, and vibrational structure of the $a^3\Sigma_u^+$ state of $^{87}Rb_2$*, Phys. Rev. A **82**, 052514 (2010), URL http://link.aps.org/doi/10.1103/PhysRevA.82.052514

[Sul11]   S. T. Sullivan, W. G. Rellergert, S. Kotochigova, K. Chen, S. J. Schowalter and E. R. Hudson, *Trapping molecular ions formed via photo-associative ionization of ultracold atoms*, Phys. Chem. Chem. Phys. **13**, 18859–18863 (2011), URL http://dx.doi.org/10.1039/C1CP21205B

[Sul12]   S. T. Sullivan, W. G. Rellergert, S. Kotochigova and E. R. Hudson, *Role of Electronic Excitations in Ground-State-Forbidden Inelastic Collisions Between Ultracold Atoms and Ions*, Phys. Rev. Lett. **109**, 223002 (2012), URL http://link.aps.org/doi/10.1103/PhysRevLett.109.223002

[Sun09]   H. Suno and B. D. Esry, *Three-body recombination in cold helium-helium-alkali-metal-atom collisions*, Phys. Rev. A **80**, 062702 (2009), URL http://link.aps.org/doi/10.1103/PhysRevA.80.062702

[Tak11]   T. Takekoshi, C. Strauss, F. Lang, J. H. Denschlag, M. Lysebo and L. Veseth, *Hyperfine, rotational, and Zeeman structure of the lowest vibrational levels of the $^{87}Rb_2$ (1) $^3\Sigma_{\mathrm{g}}^+$ state*, Phys. Rev. A **83**, 062504 (2011), URL http://link.aps.org/doi/10.1103/PhysRevA.83.062504

[Tan12]   U. Tanaka, K. Masuda, Y. Akimoto, K. Koda, Y. Ibaraki and S. Urabe, *Micromotion compensation in a surface electrode trap by parametric excitation of trapped ions*, Applied Physics B **107**, 907–912 (2012), URL http://dx.doi.org/10.1007/s00340-011-4762-2

[Tho00]   R. C. Thompson and J. Papadimitriou, *Simple model for the laser cooling of an ion in a Penning trap*, Journal of Physics B: Atomic, Molecular and Optical Physics **33**, 3393 (2000), URL http://stacks.iop.org/0953-4075/33/i=17/a=317

[Tom15]   M. Tomza, *Ultracold magnetically tunable interactions without radiative-charge-transfer losses between* $Ca^+, Sr^+, Ba^+,$ *and* Yb^+ *ions and Cr atoms*, Phys. Rev. A **92**, 062701 (2015), URL http://link.aps.org/doi/10.1103/PhysRevA.92.062701

[Tur00]   Q. A. Turchette, D. Kielpinski, B. E. King, D. Leibfried, D. M. Meekhof, C. J. Myatt, M. A. Rowe, C. A. Sackett, C. S. Wood, W. M. Itano, C. Monroe and D. J. Wineland, *Heating of trapped ions from the quantum ground state*, Phys. Rev. A **61**, 063418 (2000), URL http://link.aps.org/doi/10.1103/PhysRevA.61.063418

[Wan11a] S. X. Wang, G. H. Low, N. S. Lachenmyer, Y. Ge, P. F. Herskind and I. L. Chuang, *Laser-induced charging of microfabricated ion traps*, Journal of Applied Physics **110**, 104901 (2011), URL http://link.aip.org/link/?JAP/110/104901/1

[Wan11b] Y. Wang, J. P. D'Incao and B. D. Esry, *Cold three-body collisions in hydrogen-hydrogen-alkali-metal atomic systems*, Phys. Rev. A **83**, 032703 (2011), URL http://link.aps.org/doi/10.1103/PhysRevA.83.032703

[Web03]   T. Weber, J. Herbig, M. Mark, H.-C. Nägerl and R. Grimm, *Three-Body Recombination at Large Scattering Lengths in an Ultracold Atomic Gas*, Phys.

Rev. Lett. **91**, 123201 (2003), URL http://link.aps.org/doi/10.1103/PhysRevLett.91.123201

[Wei99]   J. Weiner, V. S. Bagnato, S. Zilio and P. S. Julienne, *Experiments and theory in cold and ultracold collisions*, Rev. Mod. Phys. **71**, 1–85 (1999), URL http://link.aps.org/doi/10.1103/RevModPhys.71.1

[Wei10]   C. Weitenberg, M. Endres, J. F. Sherson, M. Cheneau, P. Schauß, T. Fukuhara, I. Bloch and S. Kuhr, *Single-spin addressing in an atomic Mott insulator*, Nature **471**, 319–324 (2010), URL http://dx.doi.org/10.1038/32354

[Wil15]   S. Willitsch, *Ion-atom hybrid systems*, in *Ion Traps for Tomorrow's Applications*, edited by M. Knoop, I. Marzoli and G. Morigi, volume 189 of *Proceedings of the International School of Physics "Enrico Fermi"*, page 255 (IOS, Amsterdam) (2015)

[Win81]   D. Wineland and W. M. Itano, *Spectroscopy of a single Mg+ ion*, Physics Letters A **82**, 75 – 78 (1981), URL http://www.sciencedirect.com/science/article/pii/0375960181909427

[Yu91]   N. Yu, W. Nagourney and H. Dehmelt, *Demonstration of new Paul–Straubel trap for trapping single ions*, Journal of Applied Physics **69**, 3779–3781 (1991), URL http://link.aip.org/link/?JAP/69/3779/1

[Zah06]   N. Zahzam, T. Vogt, M. Mudrich, D. Comparat and P. Pillet, *Atom-Molecule Collisions in an Optically Trapped Gas*, Phys. Rev. Lett. **96**, 023202 (2006), URL http://link.aps.org/doi/10.1103/PhysRevLett.96.023202

[Zip10a]   C. Zipkes, S. Palzer, L. Ratschbacher, C. Sias and M. Köhl, *Cold Heteronuclear Atom-Ion Collisions*, Phys. Rev. Lett. **105**, 133201 (2010), URL http://link.aps.org/doi/10.1103/PhysRevLett.105.133201

[Zip10b]   C. Zipkes, S. Palzer, C. Sias and M. Köhl, *A trapped single ion inside a Bose-Einstein condensate*, Nature **464**, 388–391 (2010), URL http://dx.doi.org/10.1038/nature08865

[Zip11a]   C. Zipkes, *A Trapped Single Ion Inside a Bose-Einstein Condensate*, Ph.D. thesis, University of Cambridge (2011)

[Zip11b]   C. Zipkes, L. Ratschbacher, C. Sias and M. Köhl, *Kinetics of a single trapped ion in an ultracold buffer gas*, New Journal of Physics **13**, 053020 (2011), URL http://stacks.iop.org/1367-2630/13/i=5/a=053020

Erklärung

Ich versichere hiermit, dass ich die Arbeit selbständig angefertigt habe und keine anderen als die angegebenen Quellen und Hilfsmittel benutzt sowie die wörtlich oder inhaltlich übernommenen Stellen als solche kenntlich gemacht habe.

Ulm, den 22.12.2016

....

Artjom Krükow

Danksagung

An dieser Stelle möchte ich all denjenigen danken die mir dabei geholfen haben es bis zu diesen Zeilen zu schaffen.

Mein Dank geht natürlich zu aller erst an meinen Betreuer Johannes. Als Initiator und Hauptverantwortlicher des Barbie-Projekts hat er mir diese Arbeit erst ermöglicht. Er hat mir bei der Umsetzung von Projekten aller Art den nötigen Freiraum gelassen, stand einem aber jederzeit bei auftretenden Problemen mit Rat und Tat zur Seite.

Danke auch an das komplette Barbie-Team von damals und heute: Arne, Stefan, Wolfgang, Andi, Amir, Tobi, Joschi und nochmals Amir. Arne hat mir das Arbeiten im Labor von null auf beigebracht, da er mich schon in der Diplomarbeit betreut hat. Die notwendige effiziente Arbeitsweise für ein Projekt dieser Größe hat er mir dann am Anfang der Doktorandenzeit auch noch eingebläut. Gratis dazu gab es die abfärbende Sucht nach koffeinhaltigen Dosengetränken, die aber bei uns beiden gegen Ende wieder kontrollierbar wurde. Stefan für den soliden Grundstein des Labors. Es gibt tatsächlich Stellschrauben, die seit dem Umzug 2010 nicht mehr angefasst wurden! Dank Wolfgangs mitgebrachter Ionenkompetenz fragen heute immer noch Besucher wofür denn die Autobatterien sind. Andi für das neue Verständnis unserer Paulfalle, dein Trafo läuft und läuft und läuft. Amir for arriving at the right time. Managing a lab like ours completely on your own is not fun. Tobi für den DPG Trip nach Berlin. Joschi für die Einsicht das Fahrrad stehen zu lassen und endlich mit vernünftigen sechs Zylindern (wenn auch ohne Turbo) zur Uni zu fahren. Again Amir for always being positive no matter what happens.

Danke auch an das Rubidium-Team Markus, Björn und Lena sowie das Lila-Team Tommy, Daniel und Wolfgang für das angenehme Klima in der Gruppe. Diskussionsbedarf gab es immer, egal ob wissenschaftlich oder nicht, im Labor, auf Konferenz, im Biergarten oder auf dem Weihnachtsmarkt.

Merci an unser Sekretariat mit Martina und Astrid, für das Übernehmen von bürokratischen Problemen jeder Art. Großes Lob gilt auch Moritz, allzeit bereit seine Werkstatt für das Wohl der Wissenschaft einzusetzen. Auch an alle anderen im Institut, Wladimir, Holger und natürlich die komplette Halbleitergruppe um Klaus. Ihr tragt massiv zur Abwechslung im Institut bei.

Zu guter Letzt danke ich meiner Familie. Anatoli und Olga, ihr habt mich immer unterstützt und mir damit diesen Weg erst möglich gemacht. Gemma, du hast mir die Augen für das Wesentliche geöffnet. Danke!

Original publication reprints

This appendix contains original reprints of the publications presented in this thesis:

- A. Krükow, A. Mohammadi, A. Härter and J. Hecker Denschlag,
  "Reactive Two-body and Three-body Collisions of Ba$^+$ in an Ultracold Rb Gas",
  Physical Review A **94**, 030701 (R) (2016)
  ©2016 American Physical Society

- A. Krükow, A. Mohammadi, A. Härter and J. Hecker Denschlag,
  "Energy Scaling of Cold Atom-atom-ion Three-body Recombination",
  Physical Review Letters **116**, 193201 (2016)
  ©2016 American Physical Society

- A. Härter, A. Krükow, A. Brunner, W. Schnitzler, S. Schmid, and J. Hecker Denschlag,
  "Single Ion as a Three-Body Reaction Center in an Ultracold Atomic Gas",
  Physical Review Letters **109**, 123201 (2012)
  ©2012 American Physical Society

- A. Härter, A. Krükow, A. Brunner and J. Hecker Denschlag,
  "Minimization of ion micromotion using ultracold atomic probes",
  Applied Physics Letters **102**, 221115 (2013)

- A. Härter, A. Krükow, A. Brunner and J. Hecker Denschlag,
  "Long-term drifts of stray electric fields in a Paul trap",
  Applied Physics B **114**, 275-281 (2014)
  ©Springer-Verlag Berlin Heidelberg 2013, with permission of Springer

- A. Härter, A. Krükow, M. Deiß, B. Drews, E. Tiemann and J. Hecker Denschlag,
  "Shedding Light on Three-Body Recombination in an Ultracold Atomic Gas",
  Nature Physics **9**, 512-517 (2013)

Reactive two-body and three-body collisions of Ba$^+$ in an ultracold Rb gas

Artjom Krükow, Amir Mohammadi, Arne Härter, and Johannes Hecker Denschlag

Institut für Quantenmaterie and Center for Integrated Quantum Science and Technology IQST, Universität Ulm, 89069 Ulm, Germany
(Received 3 February 2016; published 6 September 2016)

We analyze reactive collisions of a single Ba$^+$ ion in contact with an ultracold gas of Rb atoms at low three-body collision energies of 2.2(9) mK $\times k_B$. Mapping out the Ba$^+$ loss rate dependence on the Rb atom density we can discern two-body reactive collisions from three-body ones and determine both rate coefficients, which are $k_2 = 3.1(6)(6) \times 10^{-13}$ cm^3 s^{-1} and $k_3 = 1.04(4)(45) \times 10^{-24}$ cm^6 s^{-1}, respectively (statistical and systematic errors in parentheses). Thus, the measured ternary recombination dominates over binary reactions even at moderate atom densities of $n \approx 10^{12}$ cm^{-3}. The results for Ba$^+$ and Rb are representative for a wide range of cold ion-atom systems and can serve as guidance for the future development of the field of hybrid atom-ion research.

Cold atom-ion physics in hybrid traps is a young, developing field [1–3], which builds on the relatively long-range r^{-4} polarization potential between an atom and an ion. In general, this potential promises large cross sections and therefore strong interactions between particles. As a consequence, a number of interesting research proposals have been brought forward ranging from sympathetic cooling down to ultracold temperatures [4], to studying the physics of strongly correlated many-body systems, e.g., ultracold charge transport [5], novel many-body bound states [6] and strong-coupling polarons [7], quantum information processing [8], and quantum simulation [9]. Most of these ideas rely on interactions mediated by elastic atom-ion collisions, while inelastic collisions and chemical reactions are undesired as they represent a time limit for the suggested experiments. Therefore it is important to identify and investigate possible reactions and to eventually gain control over them. Inelastic processes can be divided up into classes such as two-body or three-body collisions. In general, binary collisions are dominant at low enough atomic densities, while ternary collisions will eventually take over with increasing density. This knowledge has been extensively applied in the field of ultracold neutral atoms by typically working with low enough atomic densities (e.g., smaller than about 10^{14} cm^{-3} for ^{87}Rb) in order to keep three-body losses negligible [10]. Considering the low-density limit, theoretical predictions for cold hybrid atom-ion systems have been focusing on binary inelastic/reactive atom-ion collisions (e.g., Refs. [11,12]) which were discussed as the limiting factors for proposed atom-ion experiments [4,13–15]. Along the same lines, measurements on atom-ion reactions in the low mK regime were, until recently, unanimously interpreted in terms of pure two-body decay [16–21].

In this Rapid Communication we show, however, that in general the decay analysis requires the simultaneous consideration of both two- and three-body reactions. Our measurements reveal that at mK temperatures inelastic three-body collisions of the ion can dominate over its two-body reactions, even at moderate atomic densities down to 3×10^{11} cm^{-3}. Indeed, the main focus of this work lies on how to clearly distinguish two-body from three-body processes and extract the corresponding rate coefficients. One could in principle argue that in order to study only two-body reactions the atomic density simply needs to be lowered sufficiently. This is, however, not practical

in standard setups with magnetic or dipole traps because the resulting reaction rate can be so small that the ion lifetime exceeds the atomic cloud lifetime. Alternatively, one could consider working with a magneto-optical trap (MOT) which allows for both low densities and long lifetimes due to continuous loading. However, in a MOT the reaction-rate measurements of the ground-state atoms are swamped beneath a background of reactions of electronically excited atoms occurring at much higher rates.

For our investigations we use a heteronuclear combination of Ba$^+$ + Rb, where both two-body and three-body collisions lead to reactions and hence to ion loss in the experiment. This complements a recent experiment of ours with homonuclear Rb$^+$ + Rb + Rb [22] for which reactive and inelastic two-body collisions are either forbidden or irrelevant. Furthermore, we note that in parallel to the work discussed here, we have studied the energy scaling of atom-ion three-body recombination [23].

We measure the density dependence of the reaction rate $\Gamma = k_2 n + k_3 n^2$ and extract the binary and ternary loss rate coefficients k_2 and k_3. Here, n is the peak atom density at the cloud center where the ion is located. For the analysis the evolution of $n(t)$ needs to be included, as the atom cloud is decaying during the time t due to elastic atom-ion collisions. We experimentally determine $n(t)$ by excluding experimental runs where the ion has undergone a reaction during the interaction time t in order to avoid systematic errors introduced by reactive collisions.

The experiments are performed in a hybrid apparatus that has already been described in detail elsewhere [24]. We prepare a single ^{138}Ba$^+$ in a linear Paul trap and bring it into contact with an ultracold cloud of spin-polarized ^{87}Rb ($F = 1$, $m_F = -1$). The atoms are prepared at a separate location from which they are transported to the Paul trap and loaded into a far off-resonant crossed optical dipole trap. During the final preparation stage for the atoms, the cloud and the ion are separated by about 100 μm along the Paul trap axis to avoid unwanted atom-ion interactions. By ramping one endcap voltage of the linear Paul trap to its final value, we shift the ion into the center of the atom cloud within 10 ms and start the atom-ion interaction. We use thermal atom clouds consisting of typically $N \approx 40$–135×10^3 atoms at temperatures of $T \approx 330$ nK with peak densities between $n \approx 6$ and 84×10^{11} cm^{-3}. The Ba$^+$ ion is confined in a

linear Paul trap which is operated at a frequency of 4.21 MHz with radial and axial trapping frequencies of $(\omega_r; \omega_a) = 2\pi \times (59.5; 38.4)$ kHz. Single ^{138}Ba$^+$ ions are loaded by isotope-selective, resonant two-photon ionization. Using standard laser cooling techniques these are cooled to Doppler temperatures of ≈ 0.5 mK. Before immersing the Ba$^+$ into the atomic bath we switch off the laser cooling, which guarantees that the ion is in the electronic ground state during the atom-ion interaction. The average kinetic energy $\overline{E}_{kin}$ of the ion is determined by the interplay of elastic collisions and the driven micromotion [17,25–28]. $\overline{E}_{kin}$ is adjusted by tuning the excess micromotion of the ion and sets the average three-body collision energy $\overline{E}_{col}$, through the relation $\overline{E}_{col} \approx 0.55\overline{E}_{kin}$ [23]. For the experiments discussed in the following, we work either at an energy of $\overline{E}_{kin} \approx 4$ or of 70 mK $\times k_B$.

We start our investigations by measuring the lifetime of a single Ba$^+$ in contact with a thermal cloud of Rb atoms. For this, we immerse the ion ($\overline{E}_{kin} \approx 67$ mK $\times k_B$) into the atom cloud (density $n \approx 16 \times 10^{11}$ cm^{-3}) for various periods of time t. After the interaction, we check if the Ba$^+$ is still present by switching on the laser cooling for 100 ms and collecting its fluorescence on a electron multiplying CCD (EMCCD) camera. If no Ba$^+$ is detected, we conclude that a reaction must have taken place. If we apply additional laser cooling with a red detuning of 2 GHz for several seconds, typically 50% of the initially undetected Ba$^+$ ions can be recovered. These ions have gained high kinetic energies in a chemical reaction, which will be discussed later. Figure 1 shows the measured probability p to detect the Ba$^+$ ion as a function of the interaction time t (please note the time-scale change after 0.8 s). We model the decay using the rate equation $\dot{p} = -\Gamma(t)p$, with the loss rate $\Gamma(t) = k_2 n(t) + k_3 n(t)^2$, where $n(t)$ is the time-dependent
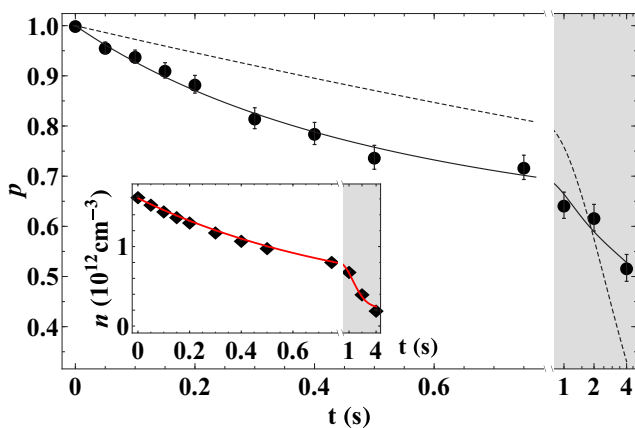
atom density at the location of the ion. Integrating the equation yields

$$p(t) = \exp\left(-\int_0^t \Gamma(t')dt'\right). \quad (1)$$

A constant density $n(t)$ would lead to an exponential decay, $p(t) = \exp(-\Gamma t)$, which does not describe the observed loss very well (Fig. 1, dashed line). As the inset of Fig. 1 shows, the density decreases during the interaction time. This is because elastic atom-ion collisions either remove atoms from the shallow atom trap or heat up the atomic ensemble. If we take into account the decay of $n(t)$, a fit of Eq. (1) (solid line) describes the data very well. In other words, for a proper description of the ion loss Γ and to determine the rate constants k_2 and k_3, the evolution of the density $n(t)$ has to be accurately determined. This, however, is somewhat involved and will be discussed in the following.

To determine $n(t)$, we measure the remaining atom number N and temperature T of the cloud via absorption imaging after 15 ms time of flight. Figure 2(a) shows histograms of the atom number distributions for various interaction times t. Initially the distribution is Gaussian. As time goes on, elastic atom-ion collisions shift this distribution towards lower atom numbers. In addition, a broad tail develops. This tail can be
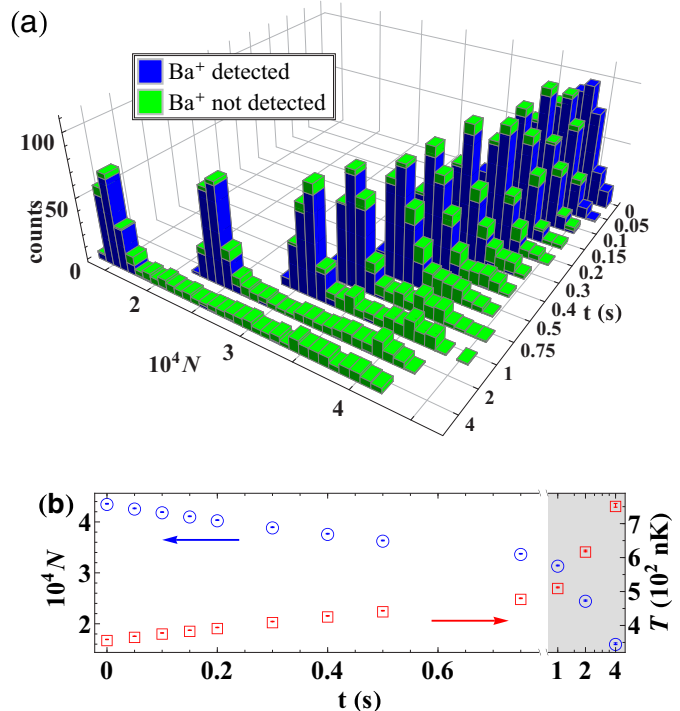

(a)

FIG. 1. Probability p to detect the Ba$^+$ ion after the interaction time t with a Rb atom cloud at an average ion kinetic energy of $\overline{E}_{kin} \approx 67$ mK $\times k_B$. One data point is the average of the binary result over roughly 330 single-ion experiments. A fit (solid line) taking into account the decay of the atom density during the interaction reproduces this behavior while a simple exponential fit (dashed line) does not. The inset shows the corresponding atom density evolution, which is well described by an exponential decay with an offset (solid line). Note the time-scale change at 0.8 s, as indicated by the shaded background. All error bars represent the 1σ statistical uncertainty of the measurements.

FIG. 2. (a) Histogram of the atom numbers N belonging to the measurement in Fig. 1. A Gaussian atom number distribution develops a broad tail with increasing interaction times. Experimental runs where the Ba$^+$ ion was detected (not detected) after the interaction are marked in blue (green), respectively. Atom numbers within the tail (Gaussian peak) of the distribution correspond to runs with (without) a reactive collision, respectively. (b) Average atom number N (circles) and temperature T (squares) over all runs without reactions, corresponding to the blue colored counts in (a).

explained as a consequence of reactive atom-ion collisions that release substantial amounts of energy which eject the product ion out of the atom cloud onto a large orbit trajectory in the Paul trap. This is consistent with the recovery of hot Ba^+ ions when additional far red-detuned laser cooling is applied, as mentioned above. Although two-body and three-body reactions at mK temperatures are predicted to dominantly produce translationally cold molecular $BaRb^+$ ions [29,30], additional kinetic energy can be released in fast secondary processes such as photodissociation or collisional relaxation. Once the ion is on the large orbit, the atom-ion collision rate is significantly reduced, essentially stopping the continuous atom loss [22]. From Fig. 2(a) we find that the counts in the tail almost exclusively correspond to experimental runs where a reaction with Ba^+ occurred (green color), whereas the counts in the Gaussian dominantly correspond to runs without reactions (blue color).

For our analysis we only consider system trajectories without reactions, making sure that the ion has been constantly exposed to the central density $n(t)$. The average atom number N and temperature T of these postselected trajectories are plotted in Fig. 2(b). We then calculate the peak atom density (shown in Fig. 1 inset) $n = (\frac{m}{2\pi k_B})^{3/2} \frac{\omega_x \omega_y \omega_z N}{T^{3/2}}$, with the mass m, using separately measured trap frequencies ($\omega_x, \omega_y, \omega_z$) of the atom dipole trap. From these sampling points we extract the time-dependent density $n(t)$.

We are now ready to quantitatively analyze the reaction rate and to extract binary and ternary reaction-rate constants. In order to obtain a high accuracy (and as a check for consistency) we perform Ba^+ lifetime measurements at ten different initial peak densities [Fig. 3(a)]. Atom clouds with different densities are prepared by varying the trap frequencies and the atom number but keeping the atom temperature T at a constant value of $T \approx 330$ nK. This temperature was chosen in order to be sufficiently above the critical temperature T_c for Bose-Einstein condensation and to have negligible losses due to evaporative cooling. The trap depths are between 5 and 10 $\mu K \times k_B$, resulting in trap frequencies of ($\omega_x, \omega_y, \omega_z$) $\approx$ $2\pi \times$ (16 to 27; 97 to 151; 107 to 161) Hz. The mean ion kinetic energy is 4.0(1.6) mK $\times k_B$, as determined in Ref. [23]. The densities between $n \approx 6$ and 22×10^{11} cm^{-3} are prepared with $N \approx 40 \times 10^3$ atoms, while densities between $n \approx 24$ and 84×10^{11} cm^{-3} are prepared with $N \approx 135 \times 10^3$ atoms.

In a first simple analysis we do not include the density evolution and fit exponential decays (dashed lines) to each data set in Fig. 3(a). The resulting loss rates Γ are then plotted as a function of their respective initial atom densities $n(t=0)$ in Fig. 3(b). By fitting $\Gamma = k_2 n + k_3 n^2$ (blue dashed line) we obtain a quasipure quadratic density dependence, where $k_3 = 1.03(2)(45) \times 10^{-24}$ cm^6 s^{-1} and k_2 is consistent with zero. For comparison, if we try to describe the data only by two-body reactions, $\Gamma \propto n$, no agreement is found (red dashed line).

Now, we perform a more rigorous analysis, where we account for the density decay during the interaction time, which can be as much as 20 % for the experimental runs in Fig. 3. This will enable us to also extract a reliable k_2 rate constant from the data. With the previously described method we determine $n(t)$ for each Ba^+ lifetime curve. We then fit Eq. (1) to all of the ten measured decays in
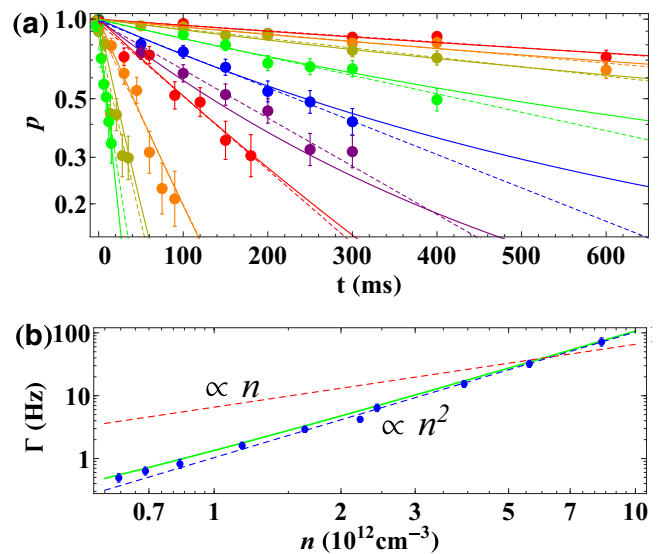

FIG. 3. (a) Logarithmic plot of p as a function of the interaction time t for ten different initial atom peak densities. Each data point corresponds to an average of roughly 100 single-ion experiments. The dashed curves are simple exponential fits, while the solid curves originate from a simultaneous fit of Eq. (1) to the full data set with two free parameters, the two-body rate coefficient k_2 and the three-body rate coefficient k_3 (see text for details). (b) Double-logarithmic plot of the Ba^+ loss rates Γ extracted from an exponential fit to each individual data set in (a) over the respective initial peak densities (solid circles). A fit of the form $\Gamma = k_2 n + k_3 n^2$ to the loss rates yields a pure quadratic density dependence (blue dashed curve). For comparison, this function was also plotted using k_2 and k_3 from (a) (green curve). A pure linear dependence ($\Gamma \propto n$) does not describe the data (red dashed curve).

Fig. 3(a) (solid lines) simultaneously, with only two free fit parameters, the binary and ternary rate coefficients k_2 and k_3, which amount to $k_2 = 3.1(6)(6) \times 10^{-13}$ cm^3 s^{-1} and $k_3 = 1.04(4)(45) \times 10^{-24}$ cm^6 s^{-1}. The first parentheses denote the 1σ statistical uncertainty of the fitted values. The second ones give the 1σ systematic error due to the atom density uncertainty of 20%, which translates linearly into k_2 and quadratically to k_3.

Notably, both approaches yield the same k_3 within their uncertainties, but only the latter provides a nonzero k_2, which emphasizes the necessity to include the atom cloud decay. We plot $\Gamma = k_2 n + k_3 n^2$, using the extracted k_2 and k_3 coefficients in Fig. 3(b) (green curve). Even at low densities $n < 10^{12}$ cm^{-3}, the green curve deviates only slightly from the pure three-body loss (blue dashed line), highlighting the small contribution of binary reactions to the total ion loss.

We now compare the obtained rate coefficients to the results of other groups in the field. Our extracted two-body charge-transfer rate coefficient k_2 for the Ba^+ + Rb system is compatible with a MOT measurement from Ref. [29] where an upper bound of $k_2 < 5 \times 10^{-13}$ cm^3 s^{-1} is given for ground-state charge transfer. An *ab initio* calculation within Ref. [29] predicts $k_2 \approx 1 \times 10^{-14}$ cm^3 s^{-1}, which is

a factor of 30 smaller compared to our present k_2. A possible explanation for this large discrepancy is an additional two-body loss channel that might appear in our experiment. Indeed, calculated Ba$^+$ + Rb molecular potential energy curves (see, e.g., Ref. [29]) indicate that the 1064 nm dipole laser can near-resonantly photoexcite a colliding atom-ion pair to a repulsive molecular potential energy curve. For the potential curves that correlate with ionized Rb$^+$ and electronically excited neutral Ba, this process is experimentally indistinguishable from charge transfer.

We note that the three-body rate coefficient k_3, determined in this work for Ba$^+$ + Rb + Rb is of similar magnitude as the one for Rb$^+$ + Rb + Rb [22], which is only by a factor of 3 smaller. This can be understood as a consequence of the same long-range atom-ion interaction potential of both systems, as it only depends on the polarizability of the Rb atom. Indeed, a theoretical classical trajectory study predicted very similar three-body cross sections for Ba$^+$ and Rb$^+$ [30]. Furthermore, since in cold reactive ternary collisions typically large, weakly bound molecules should be formed [23], the short-range details of the molecular interaction potential do not contribute. This suggests a universal behavior of cold atom-atom-ion three-body recombination, leading to similar reaction-rate coefficients for a variety of hybrid atom-ion systems.

In conclusion, we have studied reactive collisions of a cold, single Ba$^+$ ion in contact with an ultracold cloud of Rb atoms. Mapping out the Ba$^+$ loss dependence on the Rb atom density enabled us to extract both the binary (k_2) and ternary (k_3) reaction-rate coefficients at mK × k_B ion energies. The Ba$^+$ + Rb + Rb three-body rate coefficient k_3 is comparatively large, about four orders of magnitude larger than the one for ultracold neutral Rb + Rb + Rb collisions [31]. Moreover, it dominates over the two-body loss down to comparatively low densities of $k_2/k_3 \approx 3 \times 10^{11}$ cm^{-3}. If working with degenerate quantum gases such as Bose-Einstein condensates with typical densities around 10^{14} cm^{-3}, three-body recombination will occur on the sub-ms time scale, limiting the time for atom-ion experiments. As shown in parallel work of ours [23], this time scale gets even shorter when lowering the collision energy E_{col}, as k_3 scales as $k_3 \propto E_{col}^{-3/4}$. In view of the number of proposed experiments where reactive collisions are unwanted, we expect a future demand for schemes to suppress three-body reactions besides the existing ones for two-body reactions [15].

[1] A. Härter and J. Hecker Denschlag, Contemp. Phys. **55**, 33 (2014).
[2] C. Sias and M. Köhl, in *Quantum Gas Experiments* (World Scientific, Singapore, 2014), p. 267.
[3] S. Willitsch, in *Ion Traps for Tomorrow's Applications*, Proceedings of the International School of Physics "Enrico Fermi," Course 189, Varenna, 2013, edited by M. Knoop, I. Marzoli, and G. Morigi (IOS, Amsterdam, 2015), p. 255.
[4] M. Krych, W. Skomorowski, F. Pawłowski, R. Moszynski, and Z. Idziaszek, Phys. Rev. A **83**, 032723 (2011).
[5] R. Côté, Phys. Rev. Lett. **85**, 5316 (2000).
[6] R. Côté, V. Kharchenko, and M. D. Lukin, Phys. Rev. Lett. **89**, 093001 (2002).
[7] W. Casteels, J. Tempere, and J. Devreese, J. Low Temp. Phys. **162**, 266 (2011).
[8] H. Doerk, Z. Idziaszek, and T. Calarco, Phys. Rev. A **81**, 012708 (2010).
[9] U. Bissbort, D. Cocks, A. Negretti, Z. Idziaszek, T. Calarco, F. Schmidt-Kaler, W. Hofstetter, and R. Gerritsma, Phys. Rev. Lett. **111**, 080501 (2013).
[10] W. Ketterle, D. Durfee, and D. Stamper-Kurn, in *Bose-Einstein Condensation in Atomic Gases*, Proceedings of the International School of Physics Enrico Fermi, Course CXL, Varenna, 1998, edited by M. Inguscio, S. Stringari, and C. Wieman (IOS, Amsterdam, 1999), p. 67.
[11] R. Côté and A. Dalgarno, Phys. Rev. A **62**, 012709 (2000).
[12] H. da Silva, Jr., M. Raoult, M. Aymar, and O. Dulieu, New J. Phys. **17**, 045015 (2015).
[13] O. P. Makarov, R. Côté, H. Michels, and W. W. Smith, Phys. Rev. A **67**, 042705 (2003).
[14] S. T. Sullivan, W. G. Rellergert, S. Kotochigova, and E. R. Hudson, Phys. Rev. Lett. **109**, 223002 (2012).
[15] M. Tomza, Phys. Rev. A **92**, 062701 (2015).
[16] A. T. Grier, M. Cetina, F. Oručević, and V. Vuletić, Phys. Rev. Lett. **102**, 223201 (2009).
[17] C. Zipkes, S. Palzer, L. Ratschbacher, C. Sias, and M. Köhl, Phys. Rev. Lett. **105**, 133201 (2010).
[18] S. Schmid, A. Härter, and J. Hecker Denschlag, Phys. Rev. Lett. **105**, 133202 (2010).
[19] F. H. J. Hall, M. Aymar, N. Bouloufa-Maafa, O. Dulieu, and S. Willitsch, Phys. Rev. Lett. **107**, 243202 (2011).
[20] W. W. Smith, D. S. Goodman, I. Sivarajah, J. E. Wells, S. Banerjee, R. Côté, H. H. Michels, J. A. Montgomery, and F. A. Narducci, Appl. Phys. B **114**, 75 (2013).
[21] S. Haze, R. Saito, M. Fujinaga, and T. Mukaiyama, Phys. Rev. A **91**, 032709 (2015).
[22] A. Härter, A. Krükow, A. Brunner, W. Schnitzler, S. Schmid, and J. Hecker Denschlag, Phys. Rev. Lett. **109**, 123201 (2012).
[23] A. Krükow, A. Mohammadi, A. Härter, J. Hecker Denschlag, J. Pérez-Ríos, and C. H. Greene, Phys. Rev. Lett. **116**, 193201 (2016).
[24] S. Schmid, A. Härter, A. Frisch, S. Hoinka, and J. Hecker Denschlag, Rev. Sci. Instrum. **83**, 053108 (2012).
[25] D. J. Berkeland, J. D. Miller, J. C. Bergquist, W. M. Itano, and D. J. Wineland, J. Appl. Phys. **83**, 5025 (1998).

[26] R. G. DeVoe, Phys. Rev. Lett. **102**, 063001 (2009).

[27] M. Cetina, A. T. Grier, and V. Vuletić, Phys. Rev. Lett. **109**, 253201 (2012).

[28] M. Krych and Z. Idziaszek, Phys. Rev. A **91**, 023430 (2015).

[29] F. H. Hall, M. Aymar, M. Raoult, O. Dulieu, and S. Willitsch, Mol. Phys. **111**, 1683 (2013).

[30] J. Pérez-Ríos and C. H. Greene, J. Chem. Phys. **143**, 041105 (2015).

[31] B. D. Esry, C. H. Greene, and J. P. Burke, Phys. Rev. Lett. **83**, 1751 (1999).

Energy Scaling of Cold Atom-Atom-Ion Three-Body Recombination

Artjom Krükow, Amir Mohammadi, Arne Härter, and Johannes Hecker Denschlag
*Institut für Quantenmaterie and Center for Integrated Quantum Science and Technology (IQST),
Universität Ulm, 89069 Ulm, Germany*

Jesús Pérez-Ríos and Chris H. Greene
Department of Physics and Astronomy, Purdue University, West Lafayette, Indiana 47907, USA

We study three-body recombination of $Ba^+ + Rb + Rb$ in the mK regime where a single $^{138}Ba^+$ ion in a Paul trap is immersed into a cloud of ultracold ^{87}Rb atoms. We measure the energy dependence of the three-body rate coefficient k_3 and compare the results to the theoretical prediction, $k_3 \propto E_{col}^{-3/4}$, where E_{col} is the collision energy. We find agreement if we assume that the nonthermal ion energy distribution is determined by at least two different micromotion induced energy scales. Furthermore, using classical trajectory calculations we predict how the median binding energy of the formed molecules scales with the collision energy. Our studies give new insights into the kinetics of an ion immersed in an ultracold atom cloud and yield important prospects for atom-ion experiments targeting the s-wave regime.

When three atoms collide, a diatomic molecule can form in a three-body recombination (TBR) process. In cold neutral atomic gases, TBR was investigated for spin-polarized hydrogen as well as alkalis (see, e.g., [1–3]). In the context of Bose-Einstein condensation, TBR plays a crucial role as a main loss mechanism. By now, the scaling of TBR as a function of collision energy and scattering lengths in neutral ultracold gases has been investigated in detail [4]. When considering TBR in atom-ion systems, one can expect three-body interactions to be more pronounced due to the underlying longer-range r^{-4} polarization potential. Energy scaling of TBR in charged gases was studied at temperatures down to a few K, especially for hydrogen and helium due to their relevance in plasmas and astrophysics (see, e.g., [5,6]). Depending on the studied temperature range a variety of power laws was found but not a common threshold law. The recent development of novel hybrid traps for both laser cooled atoms and ions has opened the possibility to investigate cold atom-ion interactions and chemical reactions in the mK regime and below. First experiments in such setups studied elastic and reactive two-body collisions (see, e.g., [7–14]). In accordance with the well-known Langevin theory, the corresponding reactive rates were measured to be independent of the collision energy [8,10]. Very recently we predicted a theoretical threshold law on the scaling properties for cold atom-atom-ion three-body collisions [15]. Understanding the scaling of reaction rates with quantities such as the collision energy is crucial for fundamentally understanding TBR and for the prospects of the experimental realization of ultracold s-wave atom-ion collisions. Furthermore, as we show here, studying TBR allows for insights into the kinetics of an ion immersed in a cloud of atoms. Experimentally, TBR in the

mK regime was recently observed for $Rb^+ + Rb + Rb$ [16] and $Ba^+ + Rb + Rb$ [17]. In the Ba^+ experiments TBR was already dominating over two-body reactions even for moderate atomic densities of 10^{12} cm^{-3}.

This Letter reports on the combined theoretical and experimental investigation of the energy scaling of three-body atom-atom-ion collisions in the mK regime. We measure the TBR rate coefficient $\bar{k}_3$ of Ba^+ in an ultracold Rb cloud as a function of the mean collision energy of the ion, $\bar{E}_{col}$, which we control via the excess micromotion (eMM) of the Paul trap. $\bar{k}_3$ is formally distinguished from k_3, which is the TBR rate coefficient for a precise collision energy E_{col} in the center-of-mass frame. By averaging k_3 over the ion energy distribution $\bar{k}_3$ is obtained. We calculate k_3 using classical trajectory calculations (CTC) [15,18] and derive its energy scaling, $k_3 \propto E_{col}^{-3/4}$. Agreement is found between theory and experiment if we assume that the energy distribution of the ion depends on multiple energy scales due to various sources of excess micromotion. Besides the prediction of k_3, the CTC calculations also provide the binding energy distribution of the formed molecules and the scaling properties of these distributions when the collision energy is varied.

The experiments are performed in a hybrid apparatus that has already been described in detail elsewhere [19]. After loading a single $^{138}Ba^+$ ion by isotope selective, resonant two-photon ionization, it is stored in a linear Paul trap driven at a frequency of 4.21 MHz with radial and axial trapping frequencies of $(\omega_r; \omega_a) = 2\pi \times (59.5; 38.4)$ kHz, respectively. There, it is laser cooled to Doppler temperatures of ≈0.5 mK. In order to perform our experiments in the electronic ground state, we switch off the cooling and

repumper light, before immersing the ion into the ultracold atomic cloud.

Once in the cloud, there is a complicated interplay of elastic two-body atom-ion collisions and the driven micromotion of the Paul trap. This interplay leads to a non-Maxwell-Boltzmann distribution of the ion's kinetic energy E_{kin} [8,20–22] with an equilibration time on the ms time scale [23]. The average kinetic energy $\bar{E}_{kin}$ of the ion in the atom cloud is then determined by the available energy sources for the ion, such as the eMM energy [8]. In our experiment we can adjust $\bar{E}_{kin}$ by controlling one part of the eMM energy, E_{fMM}, which is set via static electric fields. Concretely, we can write $\bar{E}_{kin} = c_{dyn}(E_{fMM} + E_{min})$, where the offset energy E_{min} contains all other energy contributions, e.g., phase micromotion (ϕMM) [24] or residual collisional effects [21,22]. The proportionality factor $c_{dyn} \approx 5.0$, which depends on the atom-ion mass ratio and the trap parameters, is extracted from a MC calculation similar to [25]. We can tune E_{fMM} accurately between $5 \mu K \times k_B$ and 100 mK $\times k_B$. E_{min}, on the other hand, is not known precisely. From independent measurements and MC calculations based on the scaling of elastic atom-ion collisions, we estimate E_{min} to be in the range between 200 and $800 \mu K \times k_B$.

The cloud consists of $N \approx 1.2 \times 10^5$ ^{87}Rb atoms at a temperature of $T \approx 700$ nK with a peak density of $n \approx 19 \times 10^{11}$ cm^{-3}. It is cigar shaped with a radial and axial size of roughly 10 and 50 μm, respectively. The atoms are spin polarized ($F = 1$, $m_F = -1$) and confined in a far off-resonant crossed optical dipole trap at a wavelength of 1064 nm with a trap depth of $\approx 10 \mu K \times k_B$. We shift the ion into the cloud over a distance of 120 μm within 2 ms by changing the end cap voltage of the linear ion trap. After an interaction time of $\tau = 300$ ms, during which the Ba$^+$ ion is typically lost with a probability of up to 65%, we separate the two traps again and detect whether the Ba$^+$ ion is still present. For this, we shine a laser cooling beam focused to a waist of 20 μm through the Paul trap center and collect the possible fluorescence on a EMCCD camera for 100 ms. If no Ba$^+$ is detected, we conclude that a reaction must have taken place during τ [26].

Repeating the single ion experiment roughly 170 times we extract the probability p that Ba$^+$ is still present. For the given experimental settings the ion loss is well described by an exponential decay of the form $p = \exp(-\Gamma\tau)$. This can be seen in the inset of Fig. 1, where we plot p as a function of interaction time τ measured at $E_{fMM} \approx 8 \mu K$. Figure 1 plots the loss rate Γ as a function of E_{fMM}. A Ba$^+$ ion in our experiment is lost either by a two-body charge transfer or by a three-body event [17]. The corresponding loss rate Γ of the ion is $\Gamma = -nk_2 - n^2\bar{k}_3$. The charge transfer rate coefficient k_2 has been previously measured for Ba$^+$ + Rb, $k_2 = 3.1(6)(6) \times 10^{-13}$ cm^3/s (statistical and systematic errors in parentheses) [17] (see also [9,27]), and contributes less than 1 s^{-1} to the loss rate Γ for the given atomic
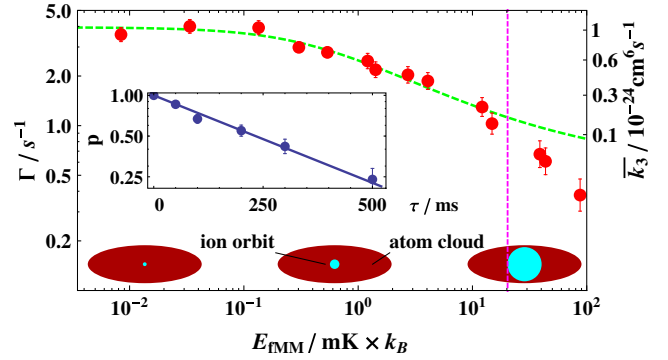

FIG. 1.   Double-logarithmic plot of the measured loss rate Γ for Ba$^+$ as a function of the tuned eMM energy E_{fMM}. Red circles are the experimental data; the curve represents a fit of Eq. (1) (see text for details). The corresponding values of $\bar{k}_3$ are indicated on the right-hand side. The inset is the Logarithmic plot of the decay curve of the Ba$^+$ ion. p is the probability to recover Ba$^+$ after interacting with Rb. The straight line is an exponential fit to the data. The sketch shows the ion orbit in the atom cloud. With increasing ion energy its orbit becomes comparable to the atom cloud size.

density. Also, it has been verified that k_2 is energy independent [7,8,10], consistent with Langevin theory. By subtracting this constant k_2 loss from Γ and dividing by the (constant) density n^2 we obtain $\bar{k}_3$ [see Figs. 1 and 3(b)]. Clearly, $\bar{k}_3$ is energy dependent. As we discuss later, we expect a scaling of k_3 with a power law, $k_3 \propto E_{col}^{\alpha}$. Neglecting the atom motion due to ultracold temperatures we can express E_{col} in terms of the ion kinetic energy E_{kin}, $E_{col} = \{1 - [m_{Ba}/(m_{Ba} + 2m_{Rb})]\}E_{kin}$. We attempt to describe the scaling of the measured $\bar{k}_3$ with a power law $\bar{k}_3 \propto \bar{E}_{kin}^{\alpha}$ by fitting the expression

$$\bar{k}_3 = \bar{k}_{3,min}[(E_{fMM} + E_{min})/E_{min}]^{\alpha} \qquad (1)$$

to the data. Here, E_{min} and α are free parameters. The constant $\bar{k}_{3,min} = 1.04(4)(45) \times 10^{-24}$ cm^6/s is $\bar{k}_3$ at $E_{fMM} = 0$ and was determined in a parallel study [17]. For the fit we discard data points above $E_{fMM} > 20$ mK $\times k_B$, as for such energies, the ion is not localized well enough in the center of the cloud. It probes areas of the atomic cloud at lower densities, hence decreasing the observed loss rate (see the sketch in Fig. 1). The fit yields $\alpha = -0.46(9)$ and $E_{min} = 410(180) \mu K \times k_B$ (green dashed line in Fig. 1), with the errors denoting a 1σ statistical uncertainty of the fitted values. Interestingly, in our previous study of TBR of Rb$^+$ + Rb + Rb [16] we observed a similar scaling exponent of $\alpha = -0.43$.

We now turn to investigate the scaling of TBR theoretically with a CTC formalism. A classical treatment of the collision dynamics is appropriate, since the experiments described here in general involve much higher energies than the threshold energy of ~ 50 nK $\times k_B$ for entering the s-wave regime of Ba$^+$ − Rb. We have adapted a recently

developed method for the calculation of three-body recombination cross sections based on classical trajectories [15,18] for the study of atom-atom-ion recombination. The method employed relies on mapping the three-body problem into a six-dimensional configuration space, described in hyperspherical coordinates, after separating out the center-of-mass motion [18]. Since the kinetic energy of the ion is typically several orders of magnitude higher than the temperature of the ultracold neutral atoms we fix one of the hyperangles associated to the ratio of the atom-ion versus the atom-atom initial momentum, guaranteeing that in the center-of-mass coordinate system 95% of the collision energy E_{col} is along the direction of the ion. In the classical trajectory calculations only Rb-Rb collisions in triplet states are considered and spin flip transitions are neglected. For the Rb-Rb pair interaction we employ the $a^3\Sigma_u^+$ potential of Strauss *et al.* [28]. On the other hand, the $Ba^+ - Rb$ interaction potential is taken to be $-C_4(1 - (r_m/r)^4/2)/r^4$, where $C_4 = 160$ a.u. denotes the experimental long-range value of the interaction and r_m represents the position of the minimum of the potential, taken from Ref. [29].

The TBR rate for $Ba^+ + Rb + Rb$ has been computed by running 10^5 trajectories per collision energy. We checked that during the simulation the total energy and angular momentum are conserved up to the fifth decimal place. Details about the numerical method employed to solve Hamilton's equations of motion, in conjunction with the sampling of the initial conditions, can be found in [18]. Figure 2(a) shows a three-body trajectory that results in a recombination event with a collision energy of $100\ \mu K \times k_B$. This particular trajectory leads to a large size ($\sim$800 a_0), very weakly bound molecular ion. Counting the fraction of trajectories that lead to molecule formation we can extract the TBR rate coefficient k_3 for $Ba^+ + Rb + Rb$. Figure 2(b) plots k_3 as a function of collision energy E_{col}. We compare these CTC calculations (diamonds) with an analytically derived scaling law [15] where $k_3 \propto E_{col}^{-3/4}$ [dashed line in Fig. 2(b)] and find very good agreement.

Strikingly, the theory prediction of $\alpha = -0.75$ does not seem to agree well with the experimentally observed value of $\alpha = -0.46(9)$ from the fit of Eq. (1) to our data. We explain this discrepancy as follows. In contrast to the theoretical approach where k_3 is determined for a precisely defined collision energy E_{col}, in the experiments we observe $\bar{k}_3$, an average over a distribution $P(E_{col}, \{E_i^S\})$ of collision energies, calculated as

$$\bar{k}_3(\{E_i^S\}) = \int k_3(E_{col})P(E_{col}, \{E_i^S\})dE_{col}. \quad (2)$$

Here, $\{E_i^S\}$ is a list of the relevant energy scales that determine the distribution, such as the experimentally tuned E_{fMM} or $E_{\phi MM}$. We extract these distributions with a MC calculation based on [25]. If only a single scale E_1^S is
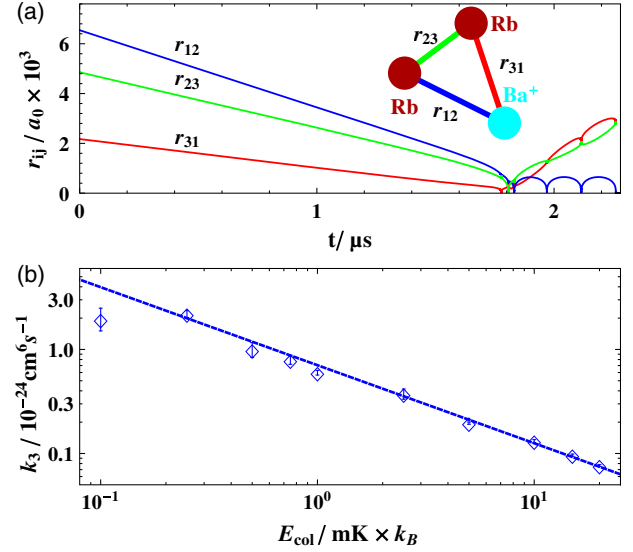

FIG. 2. (a) A typical trajectory at a collision energy of $100\ \mu K \times k_B$ associated with the three-body collision $Ba^+ + Rb + Rb$ that leads to the formation of $BaRb^+$. We show the distances r_{ij} between the particles as indicated in the sketch. (b) Double log plot of k_3 obtained with CTC for $Ba^+ + Rb + Rb$ as a function of the collision energy E_{col} (circles). The straight line shows the analytically predicted power-law dependence $k_3 \propto E_{col}^{-3/4}$.

present, the energy distributions can be expressed as functions of the ratio E_{col}/E_1^S,

$$P(E_{col}, E_1^S)dE_{col} = \tilde{P}(E_{col}/E_1^S)dE_{col}/E_1^S. \quad (3)$$

Figure 3(a) shows three calculated distributions, each with its own scale E_1^S. The distributions $P(E_{col}, E_{fMM})$ for $E_{fMM} = 1$ mK (green) and 20 mK (red) have the exact same shape, a consequence of Eq. (3). The third distribution $P(E_{col}, E_{\phi MM} = 1$ mK) (blue), generated with a phase micromotion, has a somewhat different shape. Using Eq. (2) one can show that distributions that satisfy Eq. (3) translate the power law $k_3 \propto E_{col}^{-3/4}$ into $\bar{k}_3 \propto (E_1^S)^{-3/4}$. In our experiment, however, where at least two energy scales, E_{fMM} and E_{min}, occur, this translation of the scaling breaks down and Eq. (1) cannot be used in the data analysis anymore. Instead, we calculate $\bar{k}_3$ with Eq. (2) to directly compare theory and experiment. The choice and magnitude of E_{min} is the only free model parameter. Here, we assume that E_{min} is entirely determined by phase micromotion, $E_{min} = E_{\phi MM}$. The phase micromotion is chosen to be shared equally between both pairs of opposing radio frequency (rf) driven electrodes [24]. Figure 3(b) shows the experimental $\bar{k}_3$ (full circles), together with the calculation (blue solid line) with $E_{\phi MM} = 790\ \mu K$ [30]. The shape of the theory curve describes the experimental data quite well, apart from an overall factor of about 1.1
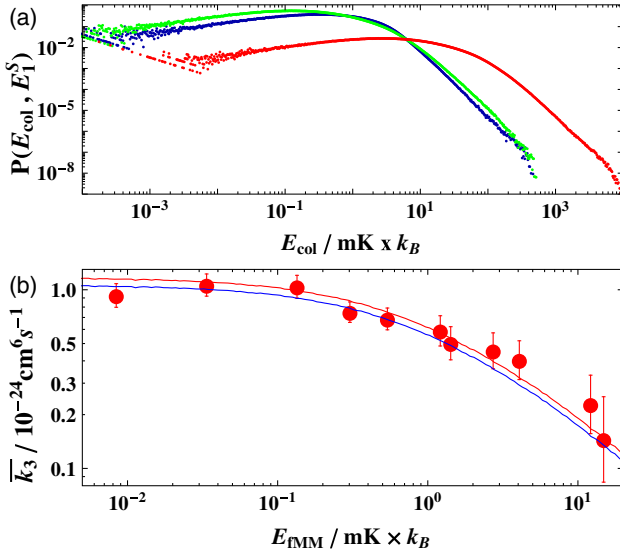
FIG. 3.   (a) Calculated ion energy distributions $P(E_{col}, E_1^S)$, each with a single energy scale E_1^S. An energy of $E_1^S = E_{fMM} = 1$ mK (20 mK) was used for the green (red) distribution. Choosing $E_1^S = E_{\phi MM} = 1$ mK produces the blue distribution, which has a different shape compared to both previous distributions. (b) Comparison of the experimental (full circles) $\bar{k}_3$ data as a function of E_{fMM} with the full calculation (blue line). The red line is the same calculation but multiplied by 1.1.

(see blue and red solid lines). In general, the overall magnitude and energy dependence of $\bar{k}_3$ is reproduced by the presented *ab initio* CTC treatment down to the mK regime, which is remarkable as E_{min} is the only free parameter.

We now turn to briefly discuss the molecular products after TBR. In a previous study of TBR for He, it was suggested that the binding energy of the products is correlated with the collision energy [18]. We find again the same behavior for TBR of an ion with two atoms. Figure 4(a) shows two logarithmically binned histograms of molecular binding energies after TBR. The maximum of each histogram can be considered the typical binding energy and is shown in Fig. 4(b) as a function of the collision energy E_{col}. A fit to a power-law dependence gives $E_{binding} \sim E_{col}^{0.88\pm0.02}$ for the energy range investigated here. Thus, our calculations suggest that the formation of deeply bound molecules after TBR should be highly improbable at low collision energies.

The present CTC results also suggest that BaRb$^+$ should be the dominant product state of the three-body recombination in the collision energy range considered here. Indeed, we have observed the formation of BaRb$^+$ ions in our experiment. However, collisional or light induced secondary processes lead to short lifetimes. A detailed study of the initial TBR products and involved secondary reactions is currently in progress and needs to be discussed elsewhere.
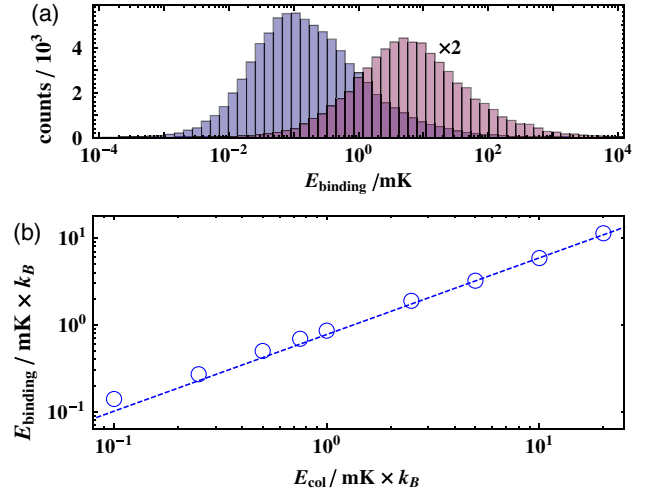

FIG. 4.   (a) Logarithmically binned histogram of the binding energies at collision energies of 100 μK $\times k_B$ (blue) and 10 mK $\times k_B$ (red). The second histogram is magnified by a factor of 2. (b) Double-logarithmic plot of the typical binding energy of the formed molecule as a function of the collision energy. The dashed line represents a power law fit.

In conclusion, we have investigated the energy scaling of three-body recombination in an atom-ion system down to mK energies. Single Ba$^+$ ions in contact with ultracold Rb atoms have been used to measure the TBR rate coefficient $\bar{k}_3$. Utilizing classical trajectory calculations, we numerically accessed the TBR rate coefficient k_3 for the Ba$^+$ + Rb + Rb system for various collision energies. We find a power law scaling of the form $k_3(E_{col}) \propto E_{col}^\alpha$ with an exponent $\alpha = -3/4$. Our experimental and theoretical studies indicate that the presence of several energy scales gives rise to energy distributions of the immersed ion that impede a direct application of scaling laws to the measured data. The obtained energy scaling provides an important insight for prospects of atom-ion experiments in the ultracold regime, as the already strong TBR rate observed here will increase by another three orders of magnitude once the *s*-wave regime at 50 nK is reached.

[1] H. F. Hess, D. A. Bell, G. P. Kochanski, R. W. Cline, D. Kleppner, and T. J. Greytak, Phys. Rev. Lett. **51**, 483 (1983).
[2] E. A. Burt, R. W. Ghrist, C. J. Myatt, M. J. Holland, E. A. Cornell, and C. E. Wieman, Phys. Rev. Lett. **79**, 337 (1997).

[3] B. D. Esry, C. H. Greene, and J. P. Burke, Phys. Rev. Lett. **83**, 1751 (1999).

[4] J. P. D'Incao and B. D. Esry, Phys. Rev. Lett. **94**, 213201 (2005).

[5] P. S. Krstić, R. K. Janev, and D. R. Schultz, J. Phys. B **36**, L249 (2003).

[6] R. Plašil, I. Zymak, P. Jusko, D. Mulin, D. Gerlich, and J. Glosík, Phil. Trans. R. Soc. A **370**, 5066 (2012).

[7] A. T. Grier, M. Cetina, F. Oručević, and V. Vuletić, Phys. Rev. Lett. **102**, 223201 (2009).

[8] C. Zipkes, S. Palzer, L. Ratschbacher, C. Sias, and M. Köhl, Phys. Rev. Lett. **105**, 133201 (2010).

[9] S. Schmid, A. Härter, and J. Hecker Denschlag, Phys. Rev. Lett. **105**, 133202 (2010).

[10] F. H. J. Hall, M. Aymar, N. Bouloufa-Maafa, O. Dulieu, and S. Willitsch, Phys. Rev. Lett. **107**, 243202 (2011).

[11] S. T. Sullivan, W. G. Rellergert, S. Kotochigova, and E. R. Hudson, Phys. Rev. Lett. **109**, 223002 (2012).

[12] K. Ravi, S. Lee, A. Sharma, G. Werth, and S. A. Rangwala, Nat. Commun. **3**, 1126 (2012).

[13] I. Sivarajah, D. S. Goodman, J. E. Wells, F. A. Narducci, and W. W. Smith, Phys. Rev. A **86**, 063419 (2012).

[14] S. Haze, S. Hata, M. Fujinaga, and T. Mukaiyama, Phys. Rev. A **87**, 052715 (2013).

[15] J. Pérez-Ríos and C. H. Greene, J. Chem. Phys. **143**, 041105 (2015).

[16] A. Härter, A. Krükow, A. Brunner, W. Schnitzler, S. Schmid, and J. Hecker Denschlag, Phys. Rev. Lett. **109**, 123201 (2012).

[17] A. Krükow, A. Mohammadi, A. Härter, and J. Hecker Denschlag, arXiv:1602.01381.

[18] J. Pérez-Ríos, S. Ragole, J. Wang, and C. H. Greene, J. Chem. Phys. **140**, 044307 (2014).

[19] S. Schmid, A. Härter, A. Frisch, S. Hoinka, and J. Hecker Denschlag, Rev. Sci. Instrum. **83**, 053108 (2012).

[20] R. G. DeVoe, Phys. Rev. Lett. **102**, 063001 (2009).

[21] M. Cetina, A. T. Grier, and V. Vuletić, Phys. Rev. Lett. **109**, 253201 (2012).

[22] M. Krych and Z. Idziaszek, Phys. Rev. A **91**, 023430 (2015).

[23] The equilibration time can be estimated from the Langevin collision rate, which at our given density is about 4 ms^{-1}.

[24] D. J. Berkeland, J. D. Miller, J. C. Bergquist, W. M. Itano, and D. J. Wineland, J. Appl. Phys. **83**, 5025 (1998).

[25] C. Zipkes, L. Ratschbacher, C. Sias, and M. Köhl, New J. Phys. **13**, 053020 (2011).

[26] We note that our detection scheme cannot detect a reaction if the final product (e.g., after a secondary process) is again a cold Ba^+ ion. From parallel experiments where we investigate the reaction products, however, we have no evidence for such a reaction outcome. In fact, our present work shows good agreement between theory and experiment if we assume that a reaction channel producing cold Ba^+ ions is negligible.

[27] F. H. Hall, M. Aymar, M. Raoult, O. Dulieu, and S. Willitsch, Mol. Phys. **111**, 1683 (2013).

[28] C. Strauss, T. Takekoshi, F. Lang, K. Winkler, R. Grimm, J. Hecker Denschlag, and E. Tiemann, Phys. Rev. A **82**, 052514 (2010).

[29] M. Krych, W. Skomorowski, F. Pawłowski, R. Moszynski, and Z. Idziaszek, Phys. Rev. A **83**, 032723 (2011).

[30] Such a phase micromotion can be caused by a relative length difference of $\Delta l / l \approx 10^{-3}$ between the cables supplying opposing rf electrodes, which is well within the tolerances of our setup.

PHYSICAL REVIEW LETTERS

Single Ion as a Three-Body Reaction Center in an Ultracold Atomic Gas

Arne Härter, Artjom Krükow, Andreas Brunner, Wolfgang Schnitzler, Stefan Schmid, and Johannes Hecker Denschlag
Institut für Quantenmaterie and Center for Integrated Quantum Science and Technology IQST, Universität Ulm, 89069 Ulm, Germany

We report on three-body recombination of a single trapped Rb^+ ion and two neutral Rb atoms in an ultracold atom cloud. We observe that the corresponding rate coefficient K_3 depends on collision energy and is about a factor of 1000 larger than for three colliding neutral Rb atoms. In the three-body recombination process large energies up to several 0.1 eV are released leading to an ejection of the ion from the atom cloud. It is sympathetically recooled back into the cloud via elastic binary collisions with cold atoms. Further, we find that the final ionic product of the three-body processes is again an atomic Rb^+ ion suggesting that the ion merely acts as a catalyzer, possibly in the formation of deeply bound Rb_2 molecules.

Early on in the quest for ultracold quantum gases, three-body recombination played a crucial role as a limiting factor for Bose-Einstein condensation. It was first investigated in spin-polarized hydrogen [1] and somewhat later for alkali atoms [2,3]. Recently, three-body recombination was investigated with single atom resolution [4]. Combining ultracold atoms with cold trapped ions is an emerging field where large scattering cross sections naturally come into play due to the comparatively long range $1/r^4$ polarization interaction potential. Two-body collisions between atoms and ions in the low energy regime have been recently studied [5–11]. In this Letter, we report on three-body collisions involving two ultracold ^{87}Rb atoms and a ^{87}Rb$^+$ ion at mK temperatures. The ion in our experiment can be regarded as a reaction center, facilitating molecule formation through its large interaction radius.

For the work presented here, it is essential that we work with ions and atoms of the same species. This renders charge transfer reactions irrelevant, which otherwise would strongly constrain our measurements. As Rb$^+$ is not amenable to laser cooling and cannot be imaged, we detect the ion and investigate its dynamics in an indirect way, i.e., through its action on the atom cloud. In our experiments, we place a single ion into the center of an atomic sample resulting in a continuous loss of atoms due to elastic atom-ion collisions. This behavior is interrupted when a highly energetic three-body process ejects the ion from the atom cloud. By examining the statistics of ion-induced atom loss in hundreds of repetitions of the experiment, we can investigate a number of important details of the three-body process, such as its quadratic density dependence, the energy that it releases, its rate coefficient K_3, the dependence of K_3 on collisional energy, and its reaction products. Furthermore, our measurements also demonstrate sympathetic cooling of an ion from eV energies down to about 1 mK using an ultracold buffer gas.

The atom-ion collision experiments are conducted in a hybrid apparatus (for details see Ref. [12]) where a single ^{87}Rb$^+$ ion, trapped in a linear Paul trap, is brought in contact with an ultracold cloud of spin polarized ^{87}Rb atoms ($F = 1$, $m_F = -1$). The atom cloud is previously prepared at a separate location from where it is transported to the Paul trap and loaded into a far off-resonant crossed optical dipole trap. The dipole trap is at first spatially separated from the trapped ion by about 50 μm. To start the atom-ion collision experiments, it is then centered on the ion with μm precision within a few 100 ms. At this point the atom cloud consists of $N_{at} \approx 4.0 \times 10^4$ atoms at a temperature of $T_{at} \approx 1.2$ μK and a peak density $n_{at} \approx 1.1 \times 10^{12}$ cm^{-3}. At trapping frequencies of (190, 198, 55) Hz this results in a cigar shaped cloud with radial and axial extensions of about 10 and 35 μm, respectively.

The single Rb$^+$ ion is confined in a Paul trap driven at a frequency of 4.17 MHz resulting in radial and axial trapping frequencies of 350 and 72 kHz, respectively. As the trap is about 4 eV deep, the ion typically remains trapped for thousands of experimental cycles. It is initially produced by photoionization of an atom from a cold Rb cloud in the Paul trap [13]. Typical kinetic energies E_{ion} of the ion after sympathetic cooling in the atom cloud are about a few mK · k_B. This energy scale is mainly set by two quantities: (1) The excess micromotion [14] in the Paul trap whose main part we can control by compensating stray electric fields [13]. (2) Heating effects induced by the interplay of micromotion and elastic collisions [15–17].

As described in Ref. [8], an ion immersed in an ultracold atom cloud leads to atom loss by expelling atoms from the shallow optical trap (≈ 10 μK · k_B trap depth) via elastic collisions. The radio frequency (rf) driven micromotion is a constant source of energy which drives these loss-afflicting collisions. Figure 1(a) shows such a decay of an atom cloud at relatively low densities ($\approx 10^{11}$ cm^{-3}) and
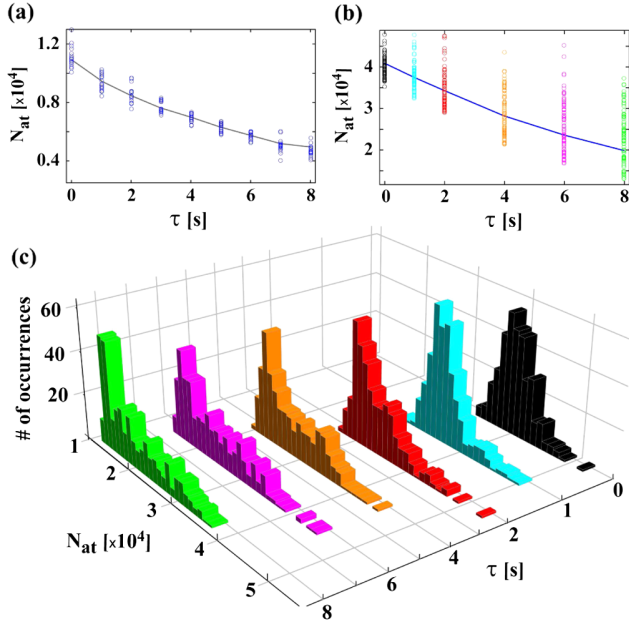
FIG. 1 (color online). Decay of the atom cloud under influence of a single trapped ion. (a) Remaining atom numbers after interaction time τ for an ion with $E_{ion} \approx 35$ mK $\cdot$ k_B [18] and $n_{at} \approx 10^{11}$ cm^{-3}. The solid line indicates the decay of the mean atom number. (b) Same as (a) but $E_{ion} \approx 0.5$ mK $\cdot$ k_B [18] and $n_{at} \approx 1.1 \times 10^{12}$ cm^{-3}. (c) Histograms containing the data shown in (b).

relatively high ion energies (≈ 35 mK $\cdot$ k_B [18]). Plotted is the number of remaining atoms after an atom-ion interaction time τ. Each data point corresponds to a single measurement. Overall, the plot shows a relatively smooth decay of the atom cloud with a relative scatter of the atom number of less than 10%. This changes drastically when we carry out the experiments at low ion energies (≈ 0.5 mK $\cdot$ k_B [18]) and larger densities ($\approx 10^{12}$ cm^{-3}) [Fig. 1(b)]. Here, the scatter dramatically increases with τ and is on the order of the number of lost atoms. In Fig. 1(c) histograms are shown which contain the data of Fig. 1(b). With increasing time τ, the initial Gaussian distribution develops a striking tail towards large atom numbers. At the tips of the tails we find cases where even after interaction times of several seconds barely any atoms have been lost, a signature of missing atom-ion interaction. Apparently, sporadically the ion is ejected from the atom cloud and promoted onto a large orbit for a period of time during which atom-ion collisions are negligible [Fig. 2(a)]. In principle, this is reminiscent of the energy distributions with high energy tails that have recently been predicted for trapped ions immersed in a buffer gas [15,16]. However, it turns out that such an explanation is inconsistent with our observations on the grounds of energetics and scaling. Rather, we find that it is a three-body recombination process involving the ion and two neutrals that ejects the ion from the cloud. Due to the large trap depth the ion is not
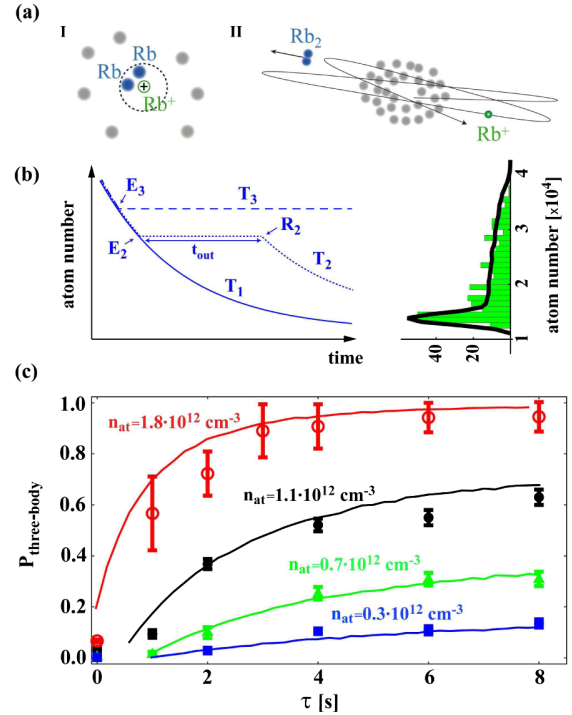

FIG. 2 (color online). (a) Illustration of an atom-atom-ion collision. (I) Two atoms simultaneously enter the interaction radius of the ion and a three-body process takes place. (II) The three-body reaction ejects the ion onto a trajectory much larger than the atom cloud. (b) Illustration of our simple model. *Left:* Various possible time traces for the atom number. If only binary atom-ion collisions occur the atomic sample decays exponentially (Trace T_1). Three-body events (E_2, E_3) interrupt the atom loss until the atom is recooled and reenters the sample at point R_2 (Traces T_2 and T_3). *Right:* Atom number histogram from Fig. 1(c) ($\tau = 8$ s) and the corresponding simulation result (solid black line). (c) Plot of the probability $P_{three-body}$ for initial atomic densities $(1.8, 1.1, 0.7, 0.3) \times 10^{12}$ cm^{-3} and atom numbers $(6.5, 4.0, 2.8, 1.6) \times 10^4$, respectively. The solid lines are results of the numerical simulation.

lost in such an event, but it is recooled back into the cloud through binary collisions after some time.

Figure 2(b) illustrates in a simple picture how the decay of the atom number over time can follow different paths. The solid trace T_1 shows the case when only binary atom-ion collisions occur. Such traces result in the narrow Gaussian peak of the atom number distribution shown on the right of Fig. 2(b). Traces T_2 and T_3 exhibit three-body collisions at points E_2 and E_3. At point R_2 the ion reenters the atom cloud after an interruption time t_{out}. Rare three-body events and long times t_{out} result in a long tail of the distribution. We can reproduce the histograms in Fig. 1 with a simple Monte Carlo type simulation (for details see Supplemental Material [19]). We assume an initial Gaussian distribution of the atom number which then decays exponentially with the binary atom-ion collision rate $K_2 n_{at}$. Here, K_2 is a rate constant given by the product

of the elastic cross section and the ion velocity. A three-body event, occurring at a rate $K_3 n_{at}^2$, interrupts this decay for a period t_{out}. As the ion can only be recooled by the atomic sample, we assume the rate for reentry of the ion into the atom cloud to be proportional to the number of atoms $1/\langle t_{out} \rangle = N_{at}/c_{out}$ with c_{out} being a constant that depends on the trap parameters. Figure 2(b) (right) shows exemplarily that the model can describe well the histograms in Fig. 1. In the following, we continue the analysis by studying $P_{three-body}$ which is the probability that at least one three-body process takes place within time τ. For each τ we determine $P_{three-body}$ from our histograms. $P_{three-body}$ is the count number of the tail of a histogram divided by the histogram's total count number (for details see Supplemental Material [19]). Figure 2(c) shows these data for four atomic densities, including the data in Fig. 1(c). All four data sets have in common that the number of three-body events first rapidly increases and subsequently levels off. The levelling off is mainly due to the fact that the probability for a three-body reaction is strongly density-dependent. Surprisingly, in the beginning of the interaction ($\tau \lesssim 1$ s) only very few three-body events are detected for the lower density samples. We explain this delay by an initial phase of sympathetic cooling of the Rb$^+$ ion which experiences significant heating during the preparation (e.g., rf evaporative cooling) of the atom cloud. From numerical calculations similar to Ref. [16] we estimate that recooling times of about 1 s in atom clouds with $n_{at} \approx 10^{12}$ cm^{-3} correspond roughly to ion kinetic energies of a few 100 K $\cdot$ k_B. The ion will typically undergo several thousand binary collisions with cold atoms until it is sympathetically recooled to mK $\cdot$ k_B energies. We are able to describe all four data sets in Fig. 2(c) consistently with our simple Monte Carlo model (continuous lines) [20]. From a fit to the data sets we obtain rate coefficients $K_2 = 5.0(5) \times 10^{-9}$ cm^3/s and $K_3 = 3.3(3) \times 10^{-25}$ cm^6/s and the reentry parameter $c_{out} \approx 1.7 \times 10^5$ s. The errors given exclude systematic uncertainties in the atomic density. We note that the value for our atom-atom-ion K_3 rate coefficient is more than three orders of magnitude larger than the three-body coefficient for three colliding neutral ^{87}Rb atoms [2]. The value of K_2 roughly agrees with previously obtained results [7,8]. For the typical atom numbers used here the obtained value of c_{out} results in several seconds of negligible atom-ion interaction following each ejection of the ion.

In order to challenge our analysis we have attempted to model the events that send the ion into orbit as two-body processes. The corresponding linear density dependence of the event rate yields inconsistent fit results such that we can exclude two-body interactions as an explanation for our data (for details see Supplemental Material [19]). As a cautionary note, we point out that three-body recombination processes to weakly bound molecular states with binding energies $\lesssim 10$ meV are not detected in our experiments

as the ion will not leave the atom cloud. Thus, the true three-body coefficient may even be significantly larger.

In a further experiment, we quantify the kinetic energy gained by the ion in a three-body event. The idea is to lower the depth of the ion trap such that an ion with an energy of a few 0.1 eV escapes while a cold ion remains trapped. The experiment is performed as follows. We prepare a first atom cloud which we bring to interaction with an ion for 4 s. Similar to the previously described experiments, we measure the ion-induced atom loss from which we judge whether or not the ion has participated in a three-body event. Directly afterwards, the ion trap depth is reduced to one of 5 values U_{red} by lowering one of the end cap voltages of the Paul trap within 300 ms. The voltage is held at this value for 200 ms and ramped back up within 200 ms. Subsequently, we probe the ion's presence in the trap via the loss it inflicts on a second atom cloud. This cloud is prepared within 40 s and contains about 5×10^4 atoms. Figure 3(a) shows the remaining atom number of the atom cloud after 6 s of interaction time [21]. An atom number $\lesssim 1 \times 10^4$ indicates the presence of an ion while a number around 4.5×10^4 shows its absence. The clear splitting of the two groups of data allows for ion detection with an efficiency close to unity. Figure 3(a) contains two different plot symbols, distinguishing two classes of ions. Black squares correspond to ions that have participated in a three-body event within the first atom cloud while grey circles correspond to ions where only binary collisions were detected. We now analyze the data points of
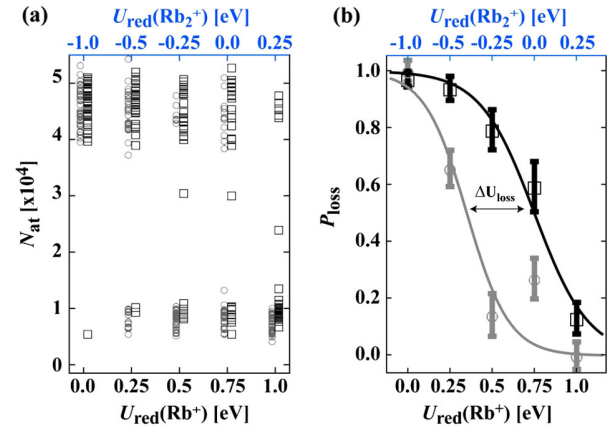

FIG. 3 (color online). (a) Probing the ion's presence using an atom cloud. A low (high) remaining atom number N_{at} signals the presence (absence) of an ion. For better visibility, we have slightly offset in energy the black squares corresponding to ions that have participated in a three-body process from the grey circles corresponding to ions where purely binary collisions were detected. (b) Ion loss probability P_{loss} calculated from the data in (a). The continuous lines are fits to the data using a broadened step function. The trap depths U_{red} are determined for our Paul trap geometry using methods detailed in Ref. [22] for both Rb$^+$ (bottom abscissa scale) and Rb$_2^+$ (top). A trap with negative trap depth value is nontrapping.
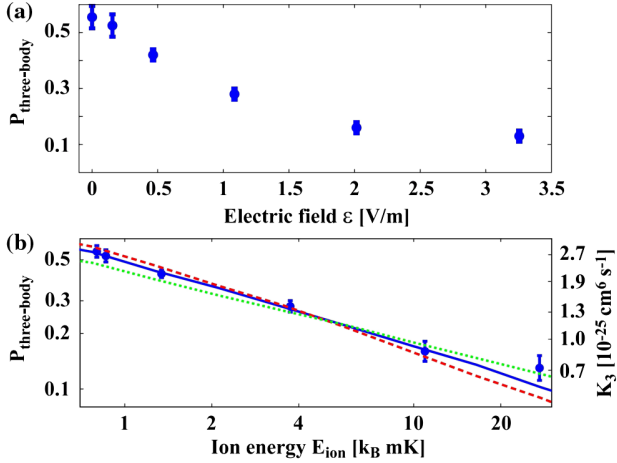
FIG. 4 (color online). (a) $P_{\text{three-body}}$ as a function of the external electric field. (b) Double-logarithmic plot of $P_{\text{three-body}}$ as a function of the ion energy E_{ion} [18]. A scale for the three-body coefficients K_3 as derived from the simulation is also given (see text for details).

Fig. 3(a) by calculating the probability for ion loss P_{loss} for each trap depth (P_{loss} = Number of lost ions/Number of trials). The result is shown in Fig. 3(b). As expected, ions that were previously involved in a three-body recombination process can in general escape from deeper traps than ions only involved in binary interactions. To obtain a more quantitative measure of the ion energy we fit broadened step functions of the form $1/[1 + \exp\{(U_{\text{red}} - U_{\text{loss}})/d\}]$ to the data. The width of the steps d is on the order of 0.15 eV. From the energy offset between the two fit curves we estimate the gained energy $\Delta U_{\text{loss}} \approx 0.4$ eV. We note that for trap depths $U_{\text{red}} \lesssim 0.25$ eV the probability of loss is high in general. This suggests that the stability of our trap is compromised at shallow trap settings. In fact, lowering the voltage of only one of the two end caps renders the trap quite asymmetric. This degrades the ideal quadrupole field configuration and thus the stability of the ion trap. As a consequence, the accuracy with which we can determine the energy released in the three-body process is limited. Still, we find a clear splitting between the step functions of 0.4 eV in Fig. 3(b). Thus, a resolution of the measurement on the order of 0.1 eV seems plausible.

Mainly two recombination processes come into consideration. In a reaction of the type $\text{Rb} + \text{Rb} + \text{Rb}^+ \rightarrow \text{Rb}_2 + \text{Rb}^+$ the formation of a neutral molecule is catalyzed by the ion which carries away 2/3 of the energy released. If deeply bound Rb_2 molecules are produced, binding energies of up to ~ 0.5 eV are released, in agreement with the measurement. A second possible recombination process, $\text{Rb} + \text{Rb} + \text{Rb}^+ \rightarrow \text{Rb}_2^+ + \text{Rb}$, produces a molecular ion and a neutral atom. However, as indicated in Fig. 3, the molecular ion, due to its higher mass, experiences a significantly shallower trap than the atomic ion and would immediately be lost for our parameter range. We

thus infer that the ion at hand is Rb^+. However, we cannot completely exclude the formation of an intermediate molecular ionic state which may subsequently dissociate.

In a third type of measurement, we study the dependence of the three-body coefficient on the ion kinetic energy which we can tune by controlling the ion micromotion. For this we apply a static electric field ε perpendicular to the axis of the Paul trap and let the ion interact for $\tau = 8$ s with an atom cloud with $n_{\text{at}} \approx 1.0 \times 10^{12}$ cm^{-3}. We find $P_{\text{three-body}}$ to increase roughly by a factor of 5 when reducing ϵ from 3.25 V/m to 0 V/m [Fig. 4(a)].

In order to express the electric field values in terms of kinetic energy, we make use of the relation $E_{\text{EMM}} = c_{\text{trap}}\epsilon^2 + E_{\text{res}}$ with c_{trap} being a constant that depends on the trap configuration and the ion mass [14]. E_{res} stands for residual uncompensated micromotion energy. The ion energy can be expressed as $E_{\text{ion}} = c_{\text{dyn}}E_{\text{EMM}}$ [18]. c_{dyn} is a constant which depends on the atom-ion mass ratio and the spatial extension of the atom cloud and for our experiments can be estimated to be about 2 [16]. We attempt to describe our data with a power-law dependence of the form $K_3 \propto E_{\text{ion}}^\alpha$ within our simulation. Good agreement with the data is achieved for $\alpha = -0.43$, $E_{\text{res}} = 370$ μK $\cdot k_B$ and a maximal value for K_3 of 2.75×10^{-25} cm^6/s [solid trace in Fig. 4(b)]. For comparison, curves for exponents $\alpha = -0.5$ and $\alpha = -0.33$ (dashed and dotted traces, respectively) are shown as well. A residual energy $E_{\text{res}} = 370$ μK $\cdot k_B$ is a reasonable value for our current setup and in agreement with other measurements of ours [13].

In conclusion, we have studied three-body recombination involving a single trapped ion and two of its parent atoms at collision energies approaching the sub-mK regime. With a relatively simple model we can understand the two- and three-body collision dynamics and extract corresponding rate coefficients. We observe an increase of the three-body rate coefficient with decreasing collision energy, a behavior that can be expected to become crucial for future experiments targeting even lower temperatures. After a three-body event, ion energies on the order of 0.4 eV were measured, indicating that deeply bound molecules have been created. Since we have not observed Rb_2^+ ions, the formation of Rb_2 seems probable. The ion would then act as an atomic size catalyzer at mK temperatures.

[1] H. F. Hess, D. A. Bell, G. P. Kochanski, R. W. Cline, D. Kleppner, and T. J. Greytak, Phys. Rev. Lett. **51**, 483 (1983).
[2] B. D. Esry, C. H. Greene, and J. P. Burke, Phys. Rev. Lett. **83**, 1751 (1999).

[3]   E. A. Burt, R. W. Ghrist, C. J. Myatt, M. J. Holland, E. A. Cornell, and C. E. Wieman, Phys. Rev. Lett. **79**, 337 (1997).

[4]   N. Spethmann *et al.*, arXiv:1204.6051v1.

[5]   R. Côté and A. Dalgarno, Phys. Rev. A **62**, 012709 (2000).

[6]   A. T. Grier, M. Cetina, F. Oručević, and V. Vuletić, Phys. Rev. Lett. **102**, 223201 (2009).

[7]   C. Zipkes, S. Palzer, C. Sias, and M. Köhl, Nature (London) **464**, 388 (2010).

[8]   S. Schmid, A. Härter, and J. Hecker Denschlag, Phys. Rev. Lett. **105**, 133202 (2010).

[9]   K. Ravi *et al.*, arXiv:1112.5825v1.

[10]   F. H. J. Hall, M. Aymar, N. Bouloufa-Maafa, O. Dulieu, and S. Willitsch, Phys. Rev. Lett. **107**, 243202 (2011).

[11]   W. G. Rellergert, S. T. Sullivan, S. Kotochigova, A. Petrov, K. Chen, S. J. Schowalter, and E. R. Hudson, Phys. Rev. Lett. **107**, 243201 (2011).

[12]   S. Schmid, A. Härter, A. Frisch, S. Hoinka, and J. Hecker Denschlag, Rev. Sci. Instrum. **83**, 053108 (2012).

[13]   A. Härter *et al.* (to be published).

[14]   D. J. Berkeland, J. D. Miller, J. C. Bergquist, W. M. Itano, and D. J. Wineland, J. Appl. Phys. **83**, 5025 (1998).

[15]   R. G. DeVoe, Phys. Rev. Lett. **102**, 063001 (2009).

[16]   C. Zipkes, L. Ratschbacher, C. Sias, and M. Köhl, New J. Phys. **13**, 053020 (2011).

[17]   M. Cetina, A. Grier, and V. Vuletić, arXiv:1205.2806v1.

[18]   Due to the nonthermal energy distribution of the immersed ion, [15,16] we use the median as an energy measure.

[19]   See Supplemental Material at http://link.aps.org/supplemental/10.1103/PhysRevLett.109.123201 for (1) description of the fitting routine to acquire $P_{\text{three-body}}$, (2) description of the Monte Carlo simulation, and (3) simulation results assuming purely two-body interactions.

[20]   The initial cooldown time is accounted for by adjusting the starting time for each data set.

[21]   We deliberately apply an offset electric field of about 6 V/m to increase the excess micromotion energy. In this way, we make three-body reactions unlikely and induce a rapid loss of atoms through binary atom-ion collisions.

[22]   K. Singer, U. Poschinger, M. Murphy, P. Ivanov, F. Ziesel, T. Calarco, and F. Schmidt-Kaler, Rev. Mod. Phys. **82**, 2609 (2010).

Supplemental Material

Arne Härter,[1] Artjom Krükow,[1] Andreas Brunner,[1] Wolfgang Schnitzler,[1] Stefan Schmid,[1] and Johannes Hecker Denschlag[1]

[1]*Institut für Quantenmaterie, Universität Ulm, 89069 Ulm, Germany*
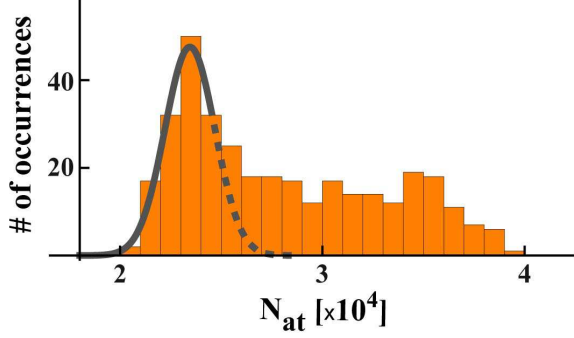
(Dated: July 17, 2012)

FIG. 1. Illustration of the fit method used to determine $P_{\text{threebody}}$. The histogram shown is taken from Fig. 1 of the main text ($\tau = 4\,\text{s}$).

1. Method to determine $P_{\text{threebody}}$

$P_{\text{threebody}}$ is the probability for at least one three-body process to happen within time τ. We describe here in more detail how we extract $P_{\text{threebody}}$ from an atom number histogram. Fig. 1 shows such a histogram which consists of two components: a Gaussian distribution on the left hand side and a tail on the right hand side. We assume that only counts outside the Gaussian (i.e. within the tail) correspond to experimental runs with atom-atom-ion three-body events. Then,

$$P_{\text{threebody}} = \frac{\text{Sum of all counts in the tail}}{\text{Total number of counts of histogram}}.$$

A Gaussian fit to the peak on the left hand side of the histogram separates the tail from the Gaussian distribution. For the fit we use the data points roughly up to the top of the peak of the distribution (solid line in the figure). In addition, we estimate the uncertainty of $P_{\text{threebody}}$. For this, we vary the number of columns used for the fit and record the corresponding fluctuations of the fit results.

2. Description of the numerical simulation

Based on Monte Carlo techniques, we have implemented a simple numerical simulation of the atom-ion interactions. The simulation takes into account the binary atom-ion collisions leading to atom loss, recooling of the ion and the three-body events which eject the ion from the atom cloud.

Initially the ion is positioned at the center of the atom cloud.

Time advances in small steps Δt. The evolution of atom number N_{at} and density n_{at} (for the time being) follows

$$N_{\text{at}}(t + \Delta t) = N_{\text{at}}(t) - K_2 n_{\text{at}}(t)\Delta t$$

and

$$n_{\text{at}}(t + \Delta t) = n_{\text{at}}(t)\frac{N_{\text{at}}(t + \Delta t)}{N_{\text{at}}(t)}.$$

Thus, in our simple model two-body collisions lead to an exponential decay of the atom number, which is a sufficiently good approximation of the observed behavior. We neglect ion-induced temperature changes of the atom cloud which would lead to corrections of the density evolution.

The possibility of a three-body event is included in the simulation in a probabilistic way. We compute

$$\wp_{\text{threebody}} = K_3 n_{\text{at}}(t)^2 \Delta t$$

which is the probability that within the time step Δt a three-body event will take place. If the three-body event does happen, the simulation stops the evolution of N_{at} and n_{at} until a reentry of the ion into the atom cloud takes place. The probability for the reentry within a time step Δt is

$$\wp_{\text{reentry}} = \frac{N_{\text{at}}(t)}{c_{\text{out}}}\Delta t.$$

The simulation runs until the total interaction time τ is reached. By performing many runs of the simulation we arrive at the atom number distribution in figure 2b and the averaged values for $P_{\text{threebody}}$ in figures 2c and 4 of the main text.

3. Modelling of the ion ejections as two-body events

An important test of our interpretation of the experimental data is the comparison with a model that does not contain three-body collisions. Instead, events sending the ion onto large orbits are also modelled as two-body processes. We can adapt our simulation of the previous section by simply replacing the probability density $\wp_{\text{threebody}}$ by $\wp_{\text{twobody}}^*$ where

$$\wp_{\text{twobody}}^* = K_2^* n_{\text{at}}(t)\Delta t. \tag{1}$$

Fig. 2 shows the simulation results using a best fit value of $K_2^* = 2.0 \times 10^{-13}\,\text{cm}^3/\text{s}$. While a data set for a single density can still be described reasonably well, this clearly does not work for all four sets with a single K_2^* rate constant. Thus we exclude two-body interactions as the cause of the ion-ejection.
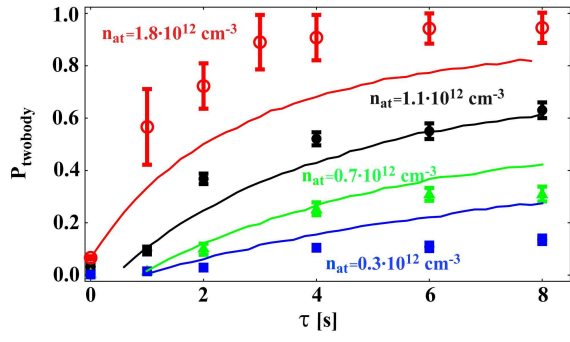
FIG. 2. Data points from Fig. 2c of the main text and results of simulations of the ion ejection as two-body events.

Minimization of ion micromotion using ultracold atomic probes

A. Härter, A. Krükow, A. Brunner,[a)] and J. Hecker Denschlag
Institut für Quantenmaterie and Center for Integrated Quantum Science and Technology IQST,
Universität Ulm, 89069 Ulm, Germany

We report on a sensitive method to minimize excess micromotion of an ion in a Paul trap. The ion is placed in an ultracold cloud of neutral Rb atoms in which ionic micromotion induces atomic losses and heating. Micromotion is minimized by applying static electric offset fields such that both loss and heating are minimized. We achieve a compensation on the level of the most precise compensation methods to date. In contrast to these methods, our scheme is applicable even for ions that cannot be optically probed. Furthermore, it avoids the formation of temporary patch charges which are a main issue for the long-term stability of micromotion minimization. © 2013 AIP Publishing LLC. [http://dx.doi.org/10.1063/1.4809578]

In the last decades, there has been tremendous progress in experiments with ions confined in Paul traps. Single or well-defined numbers of ions have been prepared and manipulated on the quantum level.[1–4] Laser cooling and manipulation of these strongly isolated quantum objects can then be used for precision spectroscopy, quantum simulation, and quantum computation. For such experiments, control over the ionic excess micromotion is a pre-condition. Furthermore, a young line of research investigates cold collisions between trapped ions and ultracold neutral atomic gases.[5–10] Here, excess micromotion sets the dominant energy scale and it needs to be compensated with high precision to reduce the atom-ion collision energies to the mK regime and beyond.

Micromotion is a driven oscillatory motion of the ions in the radio frequency (rf) field of the Paul trap. Ideally, the ion is trapped at a node of the rf field, where micromotion is minimal. However, possible stray electric fields displace the ion from this location and into trap regions with increased rf fields. These in turn increase the micromotion amplitudes by inducing the so-called excess micromotion. This micromotion contribution thus needs to be minimized by compensating the stray electric fields. To date, a number of methods have been devised to accurately compensate excess micromotion, all of which employ resonant scattering of light off the ion. Such methods employ, e.g., motional side-band spectroscopy,[11–13] photon correlation measurements,[11,14] precise position detection of the ion while changing the rf confinement,[11] or detection of ionic motional excitation when resonantly modulating the ion trap potential.[15,16] For the ionic species typically used in these experiments, resonant light at wavelengths below 500 nm is needed. This is known to produce unstable patch charges on dielectric surfaces making frequent readjustments of the compensation voltages necessary. Also, the laser-based compensation methods fail when working with "dark" ions, such as Rb$^+$, where optical transitions are not accessible.

Here, we present a compensation method where ion micromotion is probed by immersing a single ion into an ultracold ^{87}Rb atom cloud. The ion collides with the atoms at typical rates of several kHz. Since the atomic temperatures

T_{at} in our experiments are on the order of 1 μK, the dominant energy scale for these collisions is set by the ion micromotion which typically is orders of magnitude larger. Through the collisions, energy is transferred from the ion to the atoms.[6,7,17] If the transferred energy is larger than the atom trap depth, the colliding atom will be lost. Otherwise, the atom remains trapped and eventually rethermalizes with the rest of the cloud leading to an increase of the atomic temperature. After several seconds of immersion and typically many thousand collisions, we detect both the number of remaining atoms and the final atomic temperature by standard absorption imaging techniques. In an iterative process, we minimize the loss and heating of the atom cloud by applying electric compensation fields, thus minimizing excess micromotion.

The experiments are performed with ^{87}Rb$^+$ ions confined in a linear Paul trap of which the design is discussed in detail in Ref. 18. The effective radial distance from the trap center to the four rf electrodes is $R' = 2.6$ mm and the trap is driven at a frequency of $\Omega = 2\pi \times 4.17$ MHz and an amplitude of $V_0 = 500$ V. The endcap electrodes are supplied with static voltages of about 8 V. This configuration results in trapping frequencies of $(\omega_r, \omega_z) = 2\pi \times (350, 51)$ kHz. To compensate radial ion micromotion, we apply electric offset fields perpendicular to the trap axis by using two pairs of compensation electrodes.

We begin our investigations by immersing the ion into the center of a comparatively dilute atom cloud which is held in a far-detuned optical dipole trap.[7] At atomic trap frequencies of $(136, 141, 40)$ Hz, initial atom number $N_{at} = 1.1 \times 10^4$, and temperature $T_{at} = 1.1\ \mu$K, the initial atomic peak density is $n_{at} = 1 \times 10^{11}$ cm^{-3}. The atom clouds are reproduced within an experimental cycle time of about 30 s with fluctuations in atom number of less than 5%, even for thousands of experimental cycles.

Figure 1(a) shows both decay and heating of the atom cloud as a function of the interaction time τ when exposed to a single ion. This measurement was performed for two micromotion settings as determined by the radial electric offset field ε_r. For a small offset field ($\varepsilon_r < 0.1$ V/m, blue data points), atom loss and heating are suppressed as compared to a field of $\varepsilon_r = 4$ V/m (black data points). In addition to the electric fields, also the number of trapped ions obviously strongly

a)Current address: 3. Physikalisches Institut, Universität Stuttgart, 70569 Stuttgart, Germany

affects the losses and heating of the atom cloud. As we want to carry out all our minimization experiments with a single ion, we have developed a way to determine the ion number in the cloud by simply looking at atomic losses. Fig. 1(b) shows a histogram of about 1000 atom loss experiments where atomic clouds ($N_{at} = 1.1 \times 10^5$, $n_{at} = 3 \times 10^{12}$ cm^{-3}) were exposed to a variable number of trapped Rb$^+$ ions for 2 s at electric fields of several V/m. The well separated peaks of the distribution of the histogram reflect the number of trapped ions, as indicated in the graph. As an example, an atom number around 6×10^4 indicates the presence of a single trapped ion. We then use such a single ion for the investigations of ion micromotion.

We now perform a first micromotion compensation measurement for which we immerse the single ion for a fixed interaction time $\tau = 8$ s into the dilute atom cloud ($N_{at} = 1.1 \times 10^4$, $n_{at} = 1 \times 10^{11}$ cm^{-3}). We vary the radial electric fields between $\varepsilon_r = \pm 5$ V/m and measure the final atom numbers and temperatures (Fig. 2). At each electric field setting, we perform about 15 individual measurements which are shown as the scattered grey points in the figure.

Each data point was measured with a freshly prepared atom cloud. While most of these points lie within a relatively small range of scatter, there are some extreme outliers with almost no atom loss or heating effect (best seen in Fig. 2(a)). These extreme events occur predominantly when ion micromotion is well compensated and are explained by three-body recombination processes between the ion and two neutral atoms, as described in detail in Ref. 19. Briefly, the energy released upon recombination ejects the ion from the atom cloud so that atom-ion collisions temporarily stop and no more losses occur. In the measurement shown in Fig. 2, the atomic density is low enough that three-body recombination processes are quite rare.

At this point of our investigations, we want to suppress their influence on the data. To do this, we first determine the mean atom number and temperature at each interaction time from all data points at this field setting. Then, we ignore those data points which lie outside a 2σ environment around these mean values and average over the remaining measurement outcomes. In this way, the influence of the extreme events is filtered out to a large part and the mean values given in Fig. 2 contain almost exclusively two-body atom-ion collisions.

Figure 2 shows a monotonic dependence on the electric field strength $|\varepsilon_r|$, both in the atom numbers and the atomic temperatures. Atom losses and heating are minimal for a vanishing offset field. Furthermore, as one might expect, the data are symmetric with respect to the sign of the electric field. Scans of this type can be used to minimize electric fields with a sensitivity given by how precisely we can determine the center of the peak (dip). Fitting a parabola to the data (see insets in Fig. 2) allows us to extract the optimal
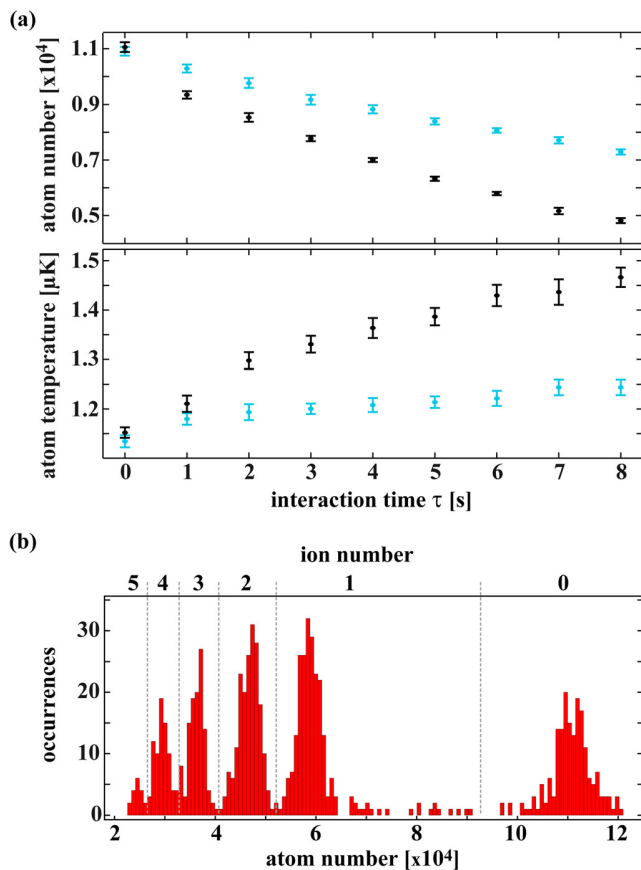

FIG. 1. Atomic signals after atom-ion interaction. (a) Evolution of atom numbers (upper panel) and atomic temperatures (lower panel) during interaction with a single ion. The measurement was performed both for $\varepsilon_r < 0.1$ V/m (blue data points) and for $\varepsilon_r = 4$ V/m (black data points). (b) Histogram of remaining atom numbers after exposing about 1000 atom clouds for 2 s to a variable number of trapped ions. The peak structure of the histogram indicates that the atom number decreases in nearly discrete steps with an increasing number of ions in the trap (indicated on the top axis). This result is used to determine an unknown number of ions in the trap by measuring the losses that the ions inflict on a cold atom cloud.
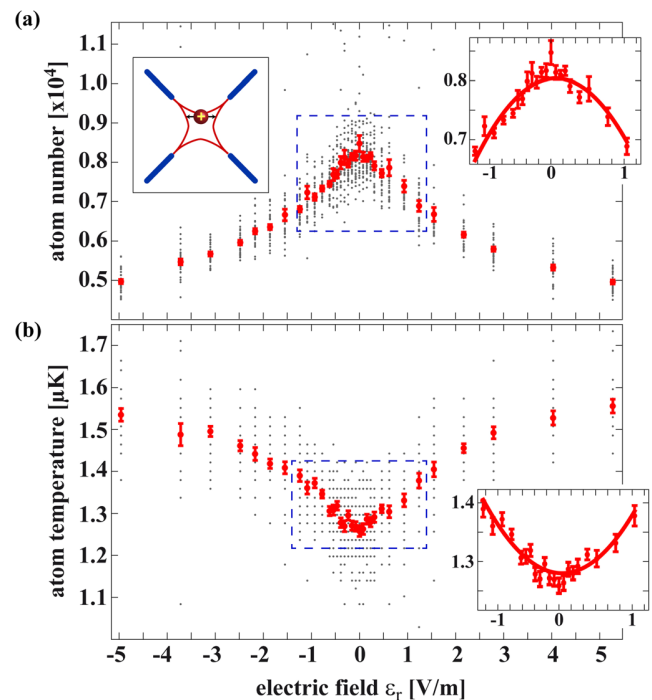

FIG. 2. Micromotion compensation using a dilute atom cloud. Insets: Parabolas are fitted locally to the atom number maximum and the temperature minimum. This allows for electric field compensation down to $\Delta\varepsilon_r < 0.05$ V/m.

electric field setting to within $\Delta\varepsilon_r < 0.05$ V/m. A corresponding parameter of crucial importance in cold atom-ion interactions is the average micromotion energy[11]

$$E_r = \frac{m_{ion}}{16}(q_r r \, \Omega)^2 \,, \tag{1}$$

where m_{ion} is the ionic mass, $q_r = 2eV_0/(m_{ion}R'^2\Omega^2) \approx 0.24$ and $r = e\varepsilon_r/(m_{ion}\omega_r^2)$ is the displacement of the ion from the rf node. Using Eq. (1), we derive a residual radial micromotion energy of $E_r = k_B \times 3.2\,\mu$K from our uncertainty in the electric offset field ε_r.

It turns out that we can increase the sensitivity by carrying out the measurement using a larger and denser atom cloud ($N_{at} = 9 \times 10^4$, $n_{at} = 1.5 \times 10^{12}$ cm^{-3}). The increase in density by more than an order of magnitude compared to the previous measurement strongly increases the three-body atom-ion recombination rate. This can be seen when comparing the data scatter in Figs. 3 and 2(a). Especially for small electric fields ε_r the scatter in Fig. 3 is large, indicating that nearly every atom-ion interaction period includes at least one three-body event. Thus, it does not make sense to sort out data with three-body events. We simply take the mean of all data points. Oddly, this changes the form of the data curve (as compared to Fig. 2(a)) which is now cusp-shaped. The cusp can be explained by two facts: (1) Three body-recombination events in general lead to an increase in the final atom number, as an ejected ion does not kick out atoms. (2) The probability for three-body events increases strongly with decreasing micromotion. As seen in the inset of Fig. 3(a), a parabola is not the ideal fit to the cusp. A cusp function such as $c_1|\varepsilon_r - c_2| + c_3$, where $c_{1,2,3}$ are fit parameters, does much better. We obtain an uncertainty of $\Delta\varepsilon_r < 0.02$ V/m which corresponds to a micromotion energy $E_r = k_B \times 0.6\,\mu$K.

The data shown in Figs. 1–3 are obtained by varying electric offset fields in the vertical direction, perpendicular to the trap axis. Measurements in the horizontal direction are performed in a similar way with similar results. In a symmetrically driven linear Paul trap, ideally, there is no micromotion along the trap axis. We drive our trap in an asymmetric way where two of the four rf electrodes are grounded. This
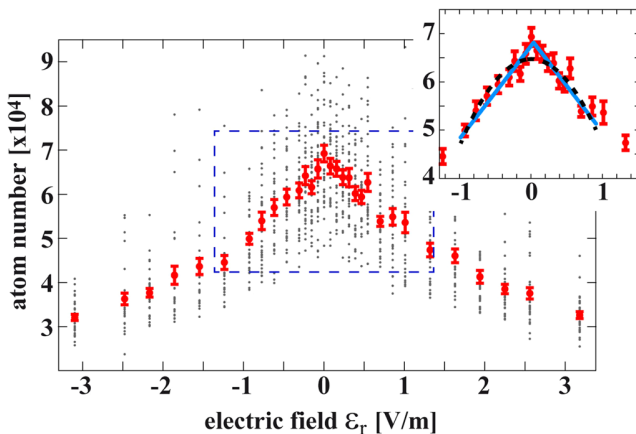

FIG. 4. Influence of axial ion micromotion on atom number and atom temperature. By scanning the electric field ε_z, the ion is moved across the atom cloud. Losses and heating are a convolution of both micromotion and atomic density. The parabolic fits allow us to determine the electric field uncertainty to $\Delta\varepsilon_z < 0.06$ V/m and the position of the rf frequency node to within $\Delta z \approx 0.7\,\mu$m.

leads to non-vanishing rf fields (and micromotion) everywhere along the trap axis except in the central point (see schematic in Fig. 4), analogous to the radial directions. Although these axial rf fields are significantly weaker than the corresponding radial ones, they still result in large micromotion energies if the ion is strongly shifted from the trap center. Due to the small axial trapping frequency of about 50 kHz, ions in our trap are highly susceptible to electric stray fields in axial direction. We adjust the axial offset electric fields by changing the voltage on one of the endcap electrodes. Figure 4 shows a scan over several V/m which moves the ion through the entire atom cloud. The inner parabolically shaped parts of the data around $\varepsilon_r = 0$ are similar to the curves in Figs. 2 and 3. The outer wings, however, mainly reflect the decrease of the density at the edge of the atom cloud. Here, the ion probes the Gaussian density distribution of the atoms (as discussed in Ref. 7). Again, fitting a parabola to the central region of Fig. 4 we obtain an electric field uncertainty of $\Delta\varepsilon_z < 0.06$ V/m which corresponds to a positional accuracy of $\Delta z < 0.7\,\mu$m and a residual axial micromotion energy $E_z = k_B \cdot 21\,\mu$K.[20] Thus, the micromotion energy is significantly larger than for the radial directions. Stronger axial confinement of the ion would increase the achievable positional accuracy of this measurement and thereby reduce the corresponding micromotion energy.

The micromotion minimization scheme using atomic probes works in all three spatial dimensions. This is a great advantage as it relaxes the experimental complexity, e.g., in terms of optical access to the trap center. Practically, however, a good compensation in one direction requires an iterative process of compensating all three dimensions. Only then can the micromotion energy of the ion be significantly reduced. Indeed, the data shown in this work were acquired after micromotion in the remaining two dimensions had already been minimized.

FIG. 3. Same as Fig. 2 but using an atomic sample at a density of $n_{at} \approx 1.5 \times 10^{12}$ cm^{-3}. The additional effects of three-body atom-ion recombination increase the electric field sensitivity and allow for field compensation down to $\Delta\varepsilon_r < 0.02$ V/m.
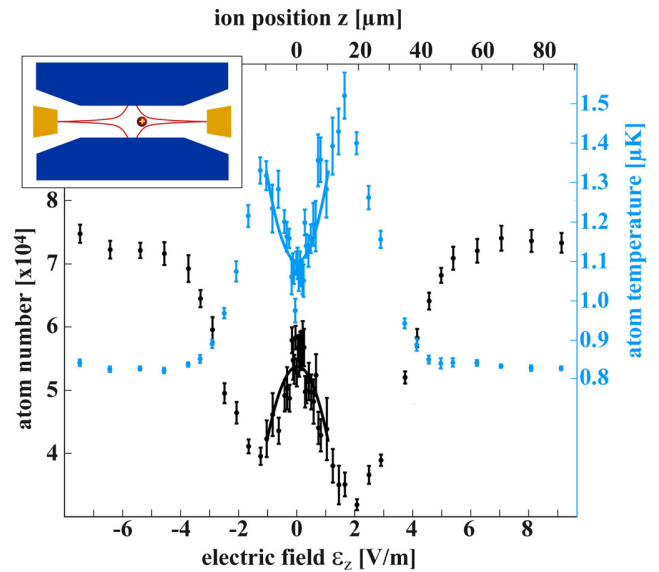
TABLE I. Comparison of commonly used figures of merit to quantify ion micromotion. Residual electric field uncertainties $\Delta\varepsilon_{r,z}$ and corresponding micromotion amplitudes $u_{r,z}$ and energies $E_{r,z}$ are given along with the trap drive frequency and the secular frequencies. The first seven rows show values extracted from information of the given references. The last row gives the values obtained in this work.

Ion species	Ref.	$\Delta\varepsilon_r$ [V/m]	u_r [nm]	E_r [μK k_B]	$\Delta\varepsilon_z$ [V/m]	u_z [nm]	E_z [μK k_B]	$\Omega/2\pi$ [MHz]	$\omega_r/2\pi$ [MHz]	$\omega_z/2\pi$ [MHz]
^{138}Ba$^+$	13	1.8	7	230	…	…	…	5.3	1.2	0.4
^{172}Yb$^+$	14	0.9	1.1	175	0.3	0.2	5.4	25.7	0.48	0.12
^{40}Ca$^+$	15	0.4/2.5	6/40	380/17000	…	…	…	15	1.2/1.4	0.4
^{27}Al$^+$	21	7	2.5	710	…	…	…	59	6	3
^{88}Sr$^+$	22	1	0.8	33	…	…	…	22	3.6	3.1
^{40}Ca$^+$	23	0.4	0.4	4.8	…	…	…	23.5	3.4	1.2
^{25}Mg$^+$	24	…	…	…	…	0.2	0.75	25	4.5	2
^{87}Rb$^+$		0.02	0.5	0.5	0.06	3.4	21	4.17	0.35	0.05

To verify that the atom-based micromotion compensation yields the same optimal electric field settings as established optical methods, we perform measurements on a single ^{138}Ba$^+$ ion with no atom cloud being present. We laser cool the ion and detect its fluorescence on a charge-coupled device camera. We use two micromotion minimization methods: (1) minimizing position changes of the ion when changing the trap frequency of the Paul trap[11] and (2) minimizing motional excitation of the ion while modulating the rf with the trap frequency.[15,16] With these methods we are able to compensate radial electric fields to about 0.1 V/m and to position the ion axially to better than 1 μm (corresponding to $\Delta\varepsilon_z \approx 0.09$ V/m).

In order to benchmark our minimization method, we compare its accuracy to the ones of various optical methods, as reported in the literature. Table I lists the field uncertainties $\Delta\varepsilon_{r,z}$, the motional micromotion amplitudes $u_{r,z}$, and the micromotion kinetic energies $E_{r,z}$ for a variety of species and ion traps. Care has to be taken when directly comparing the results, as the set-ups, trap frequencies, and rf-drive frequencies differ substantially. Nevertheless, the table shows that atom-based micromotion compensation is as precise as the reported values achieved with optical methods.

In conclusion, we have presented a method to compensate ion excess micromotion in a Paul trap. The trapped ion is immersed into an atomic cloud. Micromotion is detected in terms of atomic loss and heating of the cloud as induced by two-body and three-body collisions between ion and atoms. Our minimization results are as precise as reported values for fluorescence-based detection methods. While our minimization method is certainly somewhat slower than most optical ones, it works in all three dimensions while requiring optical access from only a single direction. Besides compensation of excess micromotion due to stray electric fields, as demonstrated here, it should also work to reduce excess micromotion due to phase differences of opposing rf electrodes of the Paul trap. The method can be used for all ionic species, including "dark" ions without accessible optical transitions, as long as collisions with the atomic gas are mainly elastic. Finally, as it does not involve optical ion detection, creation of patch charges is avoided. Hence, long-term stability of the compensation settings is achieved, which is a prerequisite for precision compensation of micromotion.

[1] D. Leibfried, R. Blatt, C. Monroe, and D. J. Wineland, Rev. Mod. Phys. **75**, 281 (2003).
[2] R. Blatt and D. Wineland, Nature **453**, 1008 (2008).
[3] H. Häffner, C. Roos, and R. Blatt, Phys. Rep. **469**, 155–203 (2008).
[4] R. Blatt and C. F. Roos, Nature Phys. **8**, 277–284 (2012).
[5] A. Grier, M. Cetina, F. Orucevic, and V. Vuletic, Phys. Rev. Lett. **102**, 223201 (2009).
[6] C. Zipkes, S. Palzer, C. Sias, and M. Köhl, Nature **464**, 388 (2010).
[7] S. Schmid, A. Härter, and J. Hecker Denschlag, Phys. Rev. Lett. **105**, 133202 (2010).
[8] F. H. J. Hall, M. Aymar, N. Bouloufa-Maafa, O. Dulieu, and S. Willitsch, Phys. Rev. Lett. **107**, 243202 (2011).
[9] W. Rellergert, S. Sullivan, S. Kotochigova, A. Petrov, K. Chen, S. Schowalter, and E. Hudson, Phys. Rev. Lett. **107**, 243201 (2011).
[10] K. Ravi, S. Lee, A. Sharma, G. Werth, and S. A. Rangwala, Nat. Commun. **3**, 1126 (2012).
[11] D. J. Berkeland, J. D. Miller, J. C. Bergquist, W. M. Itano, and D. J. Wineland, J. Appl. Phys. **83**, 5025 (1998).
[12] C. Raab, J. Eschner, J. Bolle, H. Oberst, F. Schmidt-Kaler, and R. Blatt, Phys. Rev. Lett. **85**, 538 (2000).
[13] B. L. Chuah, N. C. Lewty, R. Cazan, and M. D. Barrett, Opt. Express **21**, 10632 (2013).
[14] K. Pyka, N. Herschbach, J. Keller, and T. Mehlstäubler, e-print arXiv:1206.5111.
[15] S. Narayanan, N. Daniilidis, S. A. Möller, R. Clark, F. Ziesel, K. Singer, F. Schmidt-Kaler, and H. Häffner, J. Appl. Phys. **110**, 114909 (2011).
[16] U. Tanaka, K. Masuda, Y. Akimoto, K. Koda, Y. Ibaraki, and S. Urabe, Appl. Phys. B **107**, 907 (2012).
[17] C. Zipkes, L. Ratschbacher, C. Sias, and M. Köhl, New J. Phys. **13**, 053020 (2011).
[18] S. Schmid, A. Härter, A. Frisch, S. Hoinka, and J. Hecker Denschlag, Rev. Sci. Instrum. **83**, 053108 (2012).
[19] A. Härter, A. Krükow, A. Brunner, W. Schnitzler, S. Schmid, and J. Hecker Denschlag, Phys. Rev. Lett. **109**, 123201 (2012).
[20] To calculate E_z we use Eq. (1) and replace q_r and r by q_z and z. In our trap $q_z \approx 0.04 \cdot q_r \approx 0.01$.
[21] C. W. Chou, D. B. Hume, J. C. J. Koelemeij, D. J. Wineland, and T. Rosenband, Phys. Rev. Lett. **104**, 070802 (2010).
[22] N. Akerman, "Trapped ions and free photons," Ph.D. dissertation (Weizmann Institute of Science, Rehovot, 2012).
[23] M. Chwalla, "Precision spectroscopy with ^{40}Ca$^+$ ions in a Paul trap," Ph.D. dissertation (Universität Innsbruck, 2009).
[24] B. Hemmerling, "Towards direct frequency comb spectroscopy using quantum logic," Ph.D. dissertation (Gottfried Wilhelm Leibniz Universität Hannover, 2011).

Long-term drifts of stray electric fields in a Paul trap

A. Härter · A. Krükow · A. Brunner ·
J. Hecker Denschlag

Abstract We investigate the evolution of quasi-static stray electric fields in a linear Paul trap over a period of several months. Depending on how these electric fields are initially induced, we observe very different timescales for the field drifts. Photo-induced electric fields decay on timescales of days. We interpret this as photo-electrically generated charges on insulating materials which decay via discharge currents. In contrast, stray fields due to the exposure of the ion trap to a beam of Ba atoms mainly exhibit slow dynamics on the order of months. We explain this observation as a consequence of a coating of the trap electrodes by the atomic beam. This may lead to contact potentials which can slowly drift over time due to atomic diffusion and chemical processes on the surface. In order not to perturb the field evolutions, we suppress the generation of additional charges and atomic coatings in the Paul trap during the measurements. For this, we shield the ion trap from ambient light and only allow the use of near-infrared lasers. Furthermore, we minimize the flux of atoms into the ion trap chamber. Long-term operation of our shielded trap led us to a regime of very low residual electric field drifts of less than 0.03 V/m per day.

A. Härter · A. Krükow · A. Brunner · J. Hecker Denschlag (✉)
Institut für Quantenmaterie and Center for Integrated Quantum Science and Technology (IQST), Universität Ulm, 89069 Ulm, Germany
e-mail: johannes.denschlag@uni-ulm.de

Present Address:
A. Brunner
Universität Stuttgart, 3. Physikalisches Institut, 70569 Stuttgart, Germany

1 Introduction

Paul traps have become essential tools in widely different fields of research ranging from quantum information [1–3] and quantum simulation [4] to precision metrology [5] and cold collisions between ions and neutrals [6–11]. The further development of all these lines of research hinges on continuing improvements of the Paul trap architectures and on a better understanding of the current experimental issues.

Ideally, a single ion in a Paul trap is only subjected to the electric fields generated by the voltages applied to the trap electrodes. However, even small spatial variations of the electrode surface potential (i.e. patch potentials) in the vicinity of the trap center create stray electric fields that significantly perturb this ideal configuration. This leads to undesired experimental complications. Quasi-static stray fields lead to positional shifts of the trapped ion [12–19] and thus to excess micromotion [20]. Rapidly fluctuating stray fields lead to ion heating [15–18, 21–25].

For the following discussion, we will formally group patch potentials into two categories.

Patch potentials of category 1 can decay via electronic discharge currents, similar to a capacitor that is shorted with a resistor. Thus, their evolution is in general governed by the motion of electrons. For example, the photoelectric effect can generate charges on the dielectric surfaces of the Paul trap. These surfaces could be the trap mounts but also insulating oxide layers on the trap electrodes. The photo-electric effect typically appears with light at wavelengths below about 500 nm. As most of the trapped ion species require light at such "blue" wavelengths for laser cooling and interrogation, light-induced patch charges will continuously be created while the experiments are carried out. In addition, patch potentials of category 1 can also be

generated in other ways such as the direct deposition of electrons and ions on dielectric surfaces (see e.g. [14]).

Patch potentials of category 2 are stable as long as the surface atoms do not move. They are due to a spatial variation of the material's work function which depends on its composition, its crystal orientation, and its surface adsorbates [26, 27]. Surface adsorbates can be elements or compounds which are physically or chemically bound onto the surface. Crystal orientation comes into play for neighboring grains in a polycrystalline structure. A change in composition comes about, e.g. when two different metals are brought into contact. This gives rise to the contact potential, i.e. the difference of the work functions of the two metals. Ion traps are often loaded from atomic beams that are directed toward the trap center. If the atomic beam hits the Paul trap electrodes, atoms are deposited on the electrode surface, potentially forming contact potentials. Furthermore, as previously mentioned, the formation and deposition of chemical compounds on the trap surface can also create electric stray fields.

Patch potentials of both categories have been observed to cause deteriorations of Paul traps leading to strong ion heating effects [15–17, 21–25]. However, the influence and evolution of the patch potentials of category 2 was often masked by the presence of photo-induced patch potentials.

Here, we study the long-term dynamics of quasi-static electric fields in a Paul trap in an environment where we systematically suppress both continuous surface contamination and continuous photo-induced patch charge buildup. We observe smooth drifts of the quasi-static electric stray fields on various timescales from days to months. We interpret these different timescales as indications of different physical and chemical processes that take place. For example, electric fields induced by the exposure of the trap to laser light typically decay within a few days. Fields induced by creating an atomic beam using a barium oven show slower dynamics on the order of months. After longer time periods without surface contamination and photo-induced charging, the stray electric fields settle smoothly toward a stable value with very small residual drifts as low as 0.03 V/m per day.

In our setup, we achieve the suppression of surface contamination and photo-induced patch charges as follows. We create and probe ions (Rb$^+$) in a linear Paul trap by using only near-infrared light sources (λ = 780 and 1,064 nm) and small clouds of $\approx 10^5$ ultracold Rb atoms, which have previously been optically transported into the chamber [28]. Thus, the net flux of atoms into the chamber is negligible. We measure the electric stray fields by applying compensating electric fields until the excess micromotion of the ion is minimized [29].

2 Experimental setup and methods

The design of our linear Paul trap is shown in Fig. 1. The effective distance from the trap center to each of the four radiofrequency (rf) electrodes is 2.6 mm, while the distance to the endcap electrodes measures 7 mm. To create radial confinement, a voltage driven at a frequency of 4.17 MHz with an amplitude of 500 V is applied to two of the rf electrodes while the other two are held at ground potential. Axial confinement is generated by applying static voltages of about 8 V to the two endcap electrodes. Under these experimental conditions, an ^{87}Rb$^+$ ion is confined at radial trapping frequencies of about 350 kHz and an axial trapping frequency of about 50 kHz. The total depth of the trap is on the order of 4 eV and allows for ion storage times of many days, even without any type of cooling. The Paul trap is part of a hybrid atom-ion trap setup that brings the trapped ion into contact with an ultracold cloud of atoms [30]. Ensembles of ^{87}Rb atoms are prepared in a separate vacuum chamber and transported into the Paul trap using a long-distance optical transport line. They are then loaded into a crossed dipole trap where further evaporative cooling down to typical temperatures of 700 nK is performed. The atom numbers typically range between 10^5 and 10^6 atoms. Both the optical transport and the crossed dipole trap are implemented using several W of laser power at a wavelength of 1,064 nm. To perform absorption imaging of the atoms, resonant laser light at 780 nm is used. After this destructive imaging process, a new atom cloud is prepared within 30 s for the next measurement. To load an ion, a Rb atom cloud with a density of several 10^{13} cm^{-3} is prepared and positioned at the center of the Paul trap. Three-body
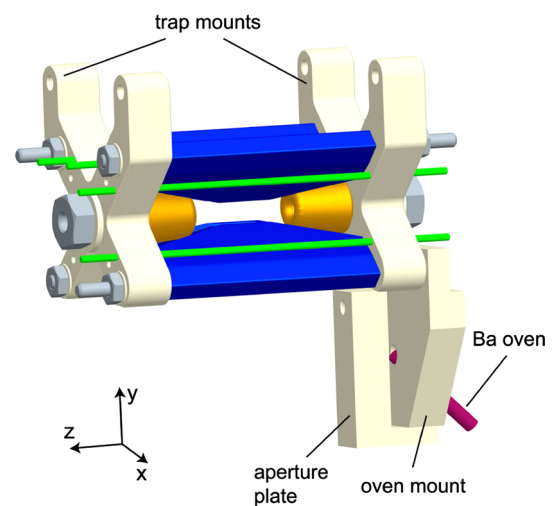

Fig. 1 Paul trap with mounts. The trap consists of four rf electrodes (*blue*), two endcap electrodes (*yellow*), and two pairs of compensation electrodes (*green*). The mounts for the trap and the barium oven are made of MACOR. The aperture plate was installed to reduce the amount of barium deposited on the trap electrodes

recombination processes in the atom cloud produce Rb_2 molecules that are subsequently ionized by a REMPI process using photons from the dipole trap laser [28]. Subsequently, the molecular Rb_2^+ ions quickly dissociate via collisions with neutral atoms and finally yield Rb^+ ions.

To detect the number of trapped Rb^+ ions and measure their micromotion, we employ a sensitive probing scheme using ultracold atomic clouds [29]. For this, we immerse the ions into clouds consisting of about 10^5 atoms at densities around 10^{12} cm^{-3}. After a few seconds of interaction time, we detect the final atom number and atom temperature which depend on the number of ions and their micromotion. This enables us to reliably work with a single ion and, by minimizing its excess micromotion with the help of electric compensation fields, to measure the stray electric fields acting on the ion [20, 29]. Due to the production time required for the atom clouds, an electric field measurement requires about an hour of measurement time, resulting in a limited temporal resolution. The measurement precision is high and typically ranges around 0.1 V/m for the results presented here.

3 Results

As a first step, we investigate the susceptibility of our trap setup with respect to laser light at various wavelengths that are available in our laboratory (Fig. 2). For these and the following measurements, each laser beam propagates through the center of the ion trap in horizontal direction at an angle of 45° with respect to the trap axis. In particular, the laser beam and its specular reflection from the vacuum windows do not directly impinge on any trap electrode or trap mount. Only some stray scattered light from the windows illuminates the trap parts diffusely and quite evenly. Both the trap electrodes and the trap mounts can be "charged up" via the photoelectric effect. The trap mounts and the mounts for the barium oven are made of machinable glass-ceramic (MACOR), which is very susceptible for accumulating charges. Charges can also accumulate on the trap electrode surfaces as these often feature undesired insulating coatings such as oxide layers. As expected, for wavelengths below 500 nm, we find a sharp increase in light-induced buildup of electric fields (see Fig. 2). For 780 nm or the even longer wavelength of 1,064 nm, we did not detect any measurable light-induced electric fields.

In general, we find the photo-induced stray electric fields to be pointing mostly in vertical ($+y$-axis) and axial ($+z$-axis) direction. There might be a number of reasons how this asymmetry in the direction of the electric stray field comes about. One reason could be that the laser light illuminates the trap setup asymmetrically. However, we can exclude this possibility as the field direction is quite
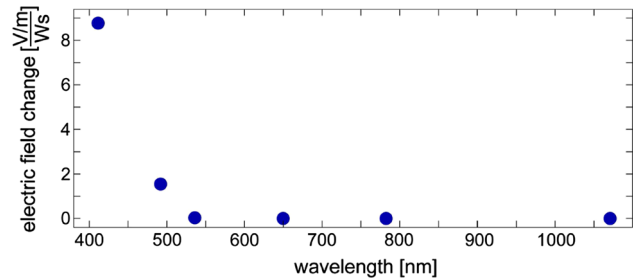

Fig. 2 Changes of the *vertical* stray electric field normalized to laser power and exposure time. The field changes were observed to be linear in both laser power and exposure time. At wavelengths below 500 nm, light-induced electric fields sharply increase

insensitive to changes in the propagation direction of the laser light, in particular when it is flipped by 90° in the horizontal plane. Another possible explanation for the asymmetry could be the presence, e.g. of a single dust particle on the trap electrodes, which is something we cannot rule out. An obvious asymmetry, however, is already inherent in our Paul trap setup due to the location of the mount and aperture plate of the barium oven (see Fig. 1, lower right). Indeed, we estimate that these two parts (which are made of MACOR) can lead to significant electric stray fields at the location of the ion. For one, they can potentially be charged to voltages of up to 500 V, as determined by the amplitude of the rf trap drive. (The rf fields prevent the patch potentials from saturating at a low voltage, the value of which would be normally set by the difference of the work function and the photon energy.) Secondly, our trap geometry is relatively open such that external electric fields can penetrate quite well to the position of the ion. We cannot deterministically charge the aperture plate or the oven mount to a certain voltage in order to test their effect on the electric field at the position of the ion. However, we can apply voltages to the Ba oven itself which should create electric fields of similar magnitude and orientation. We find that a voltage of 1 V on the oven indeed results in a dominant electric field contribution of +0.1 V/m in y-direction. The other two field components are each about a factor of 6 smaller (-0.016 V/m in x-direction and $+0.016$ V/m in z-direction). These values set a lower bound to the expected fields originating from a charged aperture plate which is located closer to the ion than the oven.

Next, we start a long-term experiment where we monitor the evolution of all three spatial components of the stray electric field over a time span of about 4 months (Fig. 3). Before the start of these measurements, the ion trap was operated with Ba^+ ions so that both the barium oven and the necessary lasers were frequently used. Consequently, there is a substantial stray electric field to begin with. During the measurements (except for two short occasions),
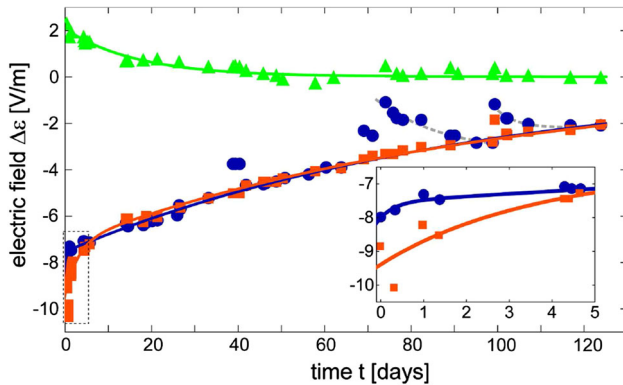
Fig. 3 Long-term drift of the *horizontal* (*x*-direction, *orange squares*), *vertical* (*y*-direction, *blue circles*), and axial (*z*-direction, *green triangles*) electric fields. Except for two occasions ($t \approx 70$ and $t \approx 100$ days), the trap was isolated from any light below a wavelength of 780 nm. *Solid lines* are double-exponential fits with long-term time constants on the order of 3 months. Offsets of the electric fields are chosen such that $\Delta \varepsilon$ converges toward 0 in the long-term limit. *Inset* zoom into the initial field evolution with time constants of 0.3 and 2.7 days (cf. Table 1)

the whole experimental setup is almost entirely shielded from ambient light by means of light-tight protective covers to avoid any patch charge buildup. All three electric field components (in *x*-, *y*-, *z*-direction) show a more or less monotonic decay and converge toward long-term limits which are each set to $\Delta \varepsilon = 0$ in the plot. The solid lines in Fig. 3 are double-exponential fits of the form

$$\varepsilon(t) = \Delta \varepsilon_1 \exp(-t/\tau_1) + \Delta \varepsilon_2 \exp(-t/\tau_2),$$

where $\Delta \varepsilon_{1,2}$ are the electric field shifts and $\tau_{1,2}$ are the time constants of the exponential decay curves. For the two radial directions (*x*- and *y*-directions), we find relatively rapid initial decays with time constants $\tau_1 = 0.3$–2.7 days (see inset of Fig. 3) and subsequent slow decays with $\tau_2 \approx 90$ days. In axial direction, the time constants are 0.6 and 18 days. For all three directions, the slow decays are dominant as they account for roughly 80–95 % of the electric field shifts (see Table 1).

On two occasions ($t \approx 70$ and $t \approx 100$ days), the light-tight protective covers around the experimental setup had to be removed for several hours so that the Paul trap was subjected (quite uniformly) to ambient white light from the fluorescent ceiling lights. As a consequence, the electric field in vertical (*y*) direction shows a sharp increase and then decays back toward its long-term behavior within several days. We investigate this effect in detail below.

After about 100 days, the daily drift of the vertical field was below 0.03 V/m yielding extremely stable experimental conditions. In addition, this slow drift allows for a precise prediction of the expected electric fields at a given time so that the field compensation can be adjusted without requiring additional measurements.

After the time period shown in Fig. 3, we make use of the low stray field drift to selectively test the dynamics of photo-induced patch charges. For this measurement, we shine through the chamber about 2.5 mW of laser power at a wavelength of 413 nm (3 eV) for 4 min. The direction of the laser beam and the conditions with respect to trap illumination are the same as for the measurements in Fig. 2, as discussed in the beginning of Sect. 3. The strongest effect is again observed in the vertical electric field component which increases by about 6 V/m. The axial field component increases by 1.5 V/m, and the horizontal component increases by 0.6 V/m. The laser was then switched off and the decay of the vertical field component was monitored over 5 days (Fig. 4). The data are fit by a double-exponential curve with an initial decay on a timescale $\tau_1 = 1.2$ days and a slow decay with $\tau_2 = 11$ days. This slow decay accounts for about 80 % of the field shift. The observed initial increase and subsequent decay of the electric field are in rough agreement with the behavior seen in Fig. 3 after the Paul trap had been subjected to ambient light. Thus, our data in Figs. 3 and 4 clearly indicate that photo-induced electric fields decay on typical timescales of a few days.

We explain the evolution of the photo-induced stray fields as follows: Initially, the photoelectric effect generates charges on electrically isolated surfaces resulting in electric stray potentials. Over time these potentials discharge by the finite resistivity of the material. In case of a charging of the aperture plate or the oven mount, we can estimate a timescale for the discharge. At room temperature, MACOR has a specific volume resistivity of about $10^{17}\ \Omega\,\mathrm{cm}$. The typical resistance of a cm-sized component then is on the order of $10^{17}\ \Omega$. The electric capacitance of a cm^2-sized plate is about $4\varepsilon_0$ cm, with ε_0 denoting the vacuum permittivity. Thus, the decay constant is on the order of 10 h, which roughly agrees with our observed timescales. We note that the resistivity of MACOR is strongly temperature dependent. We do not have a precise knowledge of the temperature of the mount but from our estimate it is clear that timescales for the discharging of the MACOR parts should not be much longer than a few days. The fact that we observe not only a single timescale for the field decay indicates that there is more than one contribution to the stray fields. A charged up MACOR part might exhibit a different discharge behavior than a dust particle or an isolated patch on the electrode surface. In any case, the data in Fig. 4 and especially in Fig. 3 (at $t \approx 70$ and $t \approx 100$ days) clearly indicate that photo-induced fields always decay on a timescale faster than 2 weeks. The question is then how the very slow drift taking place over about 90 days can be explained (see Fig. 3). Our observations suggest that the electric fields linked to this slow decay have a different origin than the photoelectric effect.

Table 1 Overview of the observed drift time constants and the corresponding electric field shifts

Direction	Cause	τ_1 (days)	$\Delta\varepsilon_1$ (V/m)	τ_2 (days)	$\Delta\varepsilon_2$ (V/m)
Vertical (Fig. 3)	Blue light + oven operation	0.3 ± 0.4	-0.4 ± 0.2	90 ± 10	-7.4 ± 0.4
Horizontal (Fig. 3)	Blue light + oven operation	2.7 ± 0.8	-2.1 ± 0.3	94 ± 21	-7.3 ± 0.7
Axial (Fig. 3)	Blue light + oven operation	0.6 ± 0.8	0.4 ± 0.2	18 ± 3	1.9 ± 0.1
Vertical (Fig. 4)	Blue light	1.2 ± 0.1	1.2 ± 0.1	11 ± 0.3	4.9 ± 0.1

Oven-induced and light-induced effects give rise to drifts with opposite signs
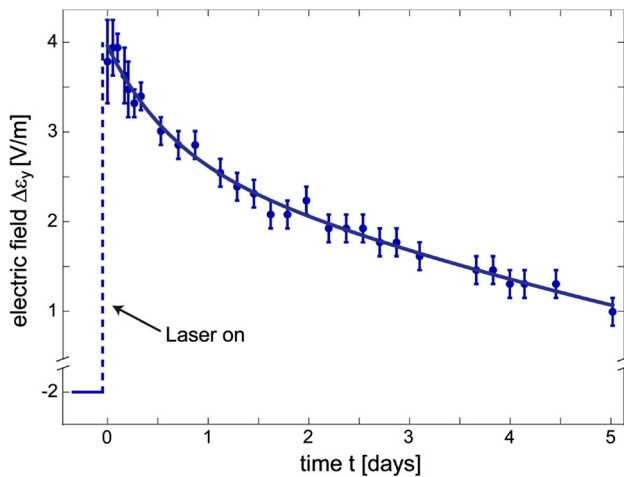

Fig. 4 *Vertical* electric field shift induced by subjecting the Paul trap to light at 413 nm. The subsequent relaxation is fit by a double-exponential function with a dominant slow decay accounting for 80 % of the field shift. The corresponding time constant is $\tau_2 = 11$ days

Fig. 5 *Vertical* electric field shift induced by heating the barium oven for 10 min. During the oven heating time, the field dropped by about 7.5 V/m. After the oven was turned off, the field shows a drift toward higher values. The *straight solid line* is a guide to the eye

We conjecture that the slow drifts originate from the dynamics of potentials of category 2, e.g. contact potentials. These potentials may change due to slow chemical reactions in the ultrahigh vacuum environment or by diffusion and migration processes on the electrode surface. It is known that barium reacts and forms compounds with O_2, N_2, CO_2, and H_2O. It also acts as a getter material, inclosing non-reactive gases. Thus, the mobility of Ba on a surface is sizeable. (Interestingly, the work function of barium is known to remain quite constant (≈ 2.5 eV) even when contaminated with other substances.) Diffusion or migration of barium on the electrode surface can coat certain compound layers and set other ones free—thus giving rise to slowly changing contact potentials. At room temperature, the vapor pressure of barium is very low. Even at 200 °C, it only reaches 10^{-12} mbar. This suggests that barium coatings have a long lifetime at ambient temperatures. Previous studies have investigated the influence of barium contaminations on Paul trap electrodes made of Be–Cu [16]. Long timescales for the quasi-static electric stray field drifts on the order of months were found, similar to our time constant for the slow drift
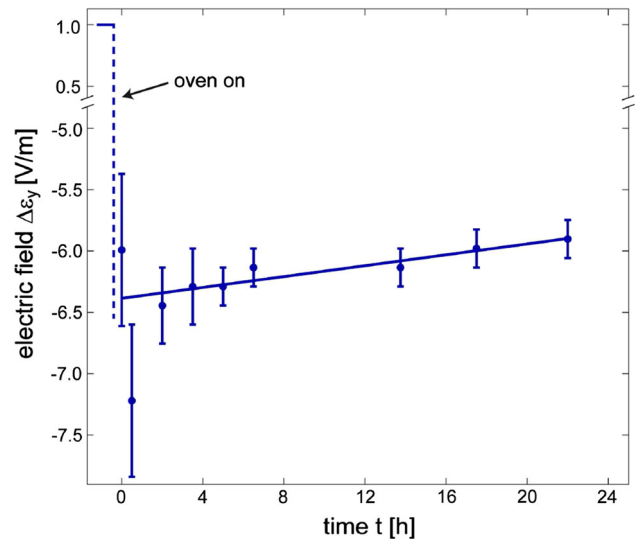
($\tau_2 = 90$ days) in Fig. 3. Furthermore, it was found in [15] that baking out a Paul trap with tungsten electrodes that had been coated with Ba significantly changed electric stray fields.

In order to test our conjecture, we now investigate the influence of the barium oven (while keeping any light below a wavelength of 780 nm blocked off). Immediately after the measurements of Fig. 4 are completed, the oven is heated to a temperature of more than 600 °C for 10 min inducing a drop of the vertical electric field component by about 7.5 V/m (Fig. 5). The horizontal and axial fields each drop by about 2 V/m (not shown). This electric field drop may be partially explained by a rapid discharging of leftover light-induced charges on the oven mount caused by the heat dissipated by the oven. The conductivity of MACOR increases by more than ten orders of magnitude when heated from room temperature to several 100 °C. It can thus be expected that any leftover charges in the vicinity of the oven will be efficiently removed at such high temperatures. However, the electric field $\Delta\varepsilon$ drops much further than the initial value of -2 V/m in Fig. 4, namely down to -6.5 V/m. This additional negative electric field

drop cannot be explained by the discharge of the charges that were previously produced photoelectrically.

One possible explanation for this field contribution is the effect of contact potentials on the trap electrodes. Despite the collimation of the atomic beam through the aperture plate, a fraction of the atoms emerging from the barium oven reaches the rf electrodes close to the trap center. Such a coating of the electrodes might immediately change the distribution of the contact potentials in close vicinity to the ion. These potentials can be up to about a couple of Volts (V), as determined by the difference in work function of the metals involved. In our setup, there is a clear asymmetry on how the Ba oven may coat the trap electrodes with Ba atoms. The two lower rf electrodes will each be coated only on one side, whereas the two upper electrodes will probably be coated over the full tip. It is then to be expected that contact potentials of the upper electrodes dominate over the potentials of the lower ones. As the work function of Ba is lower than that of stainless steel, an electric field component should build up which points toward the negative y-axis. This is indeed what we observe. Furthermore, there is also an asymmetry in z-direction, as the atomic beam from the oven passes at an angle of about 45° through the blades (see Fig. 1). This may give rise to an electric stray field component in z-direction.

Figure 5 shows that after the oven is turned off, the vertical electric field component increases by about 0.5 V/m per day. Such a behavior agrees with the observations at the beginning of the long-term measurements shown in the inset of Fig. 3. This again supports our interpretation that the 90-day long drift behavior of the electric field in Fig. 3 is a result of initially coating the trap electrodes and mounts with Ba which afterward migrates and undergoes chemical reactions on the surface.

4 Conclusion

In conclusion, we have investigated the long-term drifts of quasi-static electric stray fields in a linear Paul trap. We find drifts on timescales ranging from about half a day to 3 months. We suggest that these different timescales reflect different physical or chemical processes. Light-induced electric fields decay on relatively short timescales on the order of a few days. This is most probably due to charges located on insulating material which slowly discharge via the high electric resistance. In contrast, electric fields which are induced by turning on the Ba oven exhibit long-term drifts on timescales of up to 90 days. Guided by analysis, our interpretation is that the oven coats the trap electrodes or mounts. As a consequence, contact potentials appear which give rise to the electric fields. These fields

show long-term drifts possibly due to slow migration or reaction processes taking place on the electrode surface.

Patch potentials have been identified as the common source of both quasi-static and fluctuating electric fields. The timescales for the drifts and fluctuations of these fields is reflected by the dynamics taking place on different length scales of the patches. It has been found that atomic contamination of Paul traps lead to both quasi-static and rapidly fluctuating patch fields [14, 17, 16]. Our findings on the evolution and the origins of quasi-static charges may thus provide new insights into mechanisms connected to rapidly fluctuating charges such as anomalous heating effects. The results presented here are a first investigation with our setup in the direction of surface dynamics of patch potentials. In the future, the experiments can easily be refined to obtain more detailed information and to test hypotheses. For example, by locally applying laser fields on trap mounts and electrodes (either to heat them up or to produce photo-induced patch charges in a controlled way), we should be able to spatially probe surface properties. Another result of our work is that by systematically avoiding the creation of electric patch potentials, we are able to get into a regime of very small and predictable electric stray field drifts as low as 0.03 V/m per day. Such stability of the trap conditions may prove valuable for the future development of precision ion trap experiments.

References

1. D. Leibfried, R. Blatt, C. Monroe, D.J. Wineland, Rev. Mod. Phys. **75**, 281 (2003)
2. R. Blatt, D. Wineland, Nature **453**, 1008–1015 (2008)
3. H. Häffner, C. Roos, R. Blatt, Phys. Rep. **469**, 155–203 (2008)
4. R. Blatt, C.F. Roos, Nat. Phys. **8**, 277–284 (2012)
5. T. Rosenband, D.B. Hume, P.O. Schmidt, C.W. Chou, A. Brusch, L. Lorini, W.H. Oskay, R.E. Drullinger, T.M. Fortier, J.E. Stalnaker, S.A. Diddams, W.C. Swann, N.R. Newbury, W.M. Itano, D.J. Wineland, J.C. Bergquist, Science **319**(5871), 1808–1812 (2008)
6. S. Schmid, A. Härter, J. Hecker Denschlag, Phys. Rev. Lett. **105**, 133202 (2010)
7. C. Zipkes, S. Palzer, C. Sias, M. Köhl, Nature **464**, 388 (2010)
8. A. Grier, M. Cetina, F. Orucevic, V. Vuletic, Phys. Rev. Lett. **102**, 223201 (2009)
9. W.G. Rellergert, S.T. Sullivan, S. Kotochigova, A. Petrov, K. Chen, S.J. Schowalter, E.R. Hudson, Phys. Rev. Lett. **107**, 243201 (2011)
10. K. Ravi, S. Lee, A. Sharma, G. Werth, S.A. Rangwala, Nat. Commun. **3**, 1126 (2012)
11. F.H.J. Hall, M. Aymar, N. Bouloufa-Maafa, O. Dulieu, S. Willitsch, Phys. Rev. Lett. **107**, 243202 (2011)

12. M. Harlander, M. Brownnutt, W. Hänsel, R. Blatt, New J. Phys. **12**, 093035 (2010)

13. S.X. Wang, G. Hao Low, N.S. Lachenmyer, Y. Ge, P.F. Herskind, I.L. Chuang, J. Appl. Phys. **110**, 104901 (2011)

14. N. Daniilidis, S. Narayanan, S.A. Möller, R. Clark, T.E. Lee, P.J. Leek, A. Wallraff, F. St. Schulz, F. Schmidt-Kaler, H. Häffner, New J. Phys. **13**(1), 013032 (2011)

15. N. Yu, W. Nagourney, H. Dehmelt, J. Appl. Phys. **69**(6), 3779–3781 (1991)

16. R.G. DeVoe, C. Kurtsiefer, Phys. Rev. A **65**, 063407 (2002)

17. S. Narayanan, N. Daniilidis, S.A. Möller, R. Clark, F. Ziesel, K. Singer, F. Schmidt-Kaler, H. Häffner, J. Appl. Phys. **110**(11), 114909 (2011)

18. D.T.C. Allcock, T.P. Harty, H.A. Janacek, N.M. Linke, C.J. Ballance, A.M. Steane, D.M. Lucas, R.L. Jarecki Jr., S.D. Habermehl, M.G. Blain, D. Stick, D.L. Moehring, Appl. Phys. B **107**(4), 913–919 (2012)

19. M. Debatin, M. Kröner, J. Mikosch, S. Trippel, N. Morrison, M. Reetz-Lamour, P. Woias, R. Wester, M. Weidemüller, Phys. Rev. A **77**, 033422 (2008)

20. D.J. Berkeland, J.D. Miller, J.C. Bergquist, W.M. Itano, D.J. Wineland, J. Appl. Phys. **83**(10), 5025–5033 (1998)

21. Q.A. Turchette, D. Kielpinski, B.E. King, D. Leibfried, D.M. Meekhof, C.J. Myatt, M.A. Rowe, C.A. Sackett, C.S. Wood, W.M. Itano, C. Monroe, D.J. Wineland, Phys. Rev. A **61**, 063418 (2000)

22. L. Deslauriers, S. Olmschenk, D. Stick, W.K. Hensinger, J. Sterk, C. Monroe, Phys. Rev. Lett. **97**, 103007 (2006)

23. J. Labaziewicz, Y. Ge, D.R. Leibrandt, S.X. Wang, R. Shewmon, I.L. Chuang, Phys. Rev. Lett. **101**, 180602 (2008)

24. D.T.C. Allcock, L. Guidoni, T.P. Harty, C.J. Ballance, M.G. Blain, A.M. Steane, D.M. Lucas, New J. Phys. **13**(12), 123023 (2011)

25. D.A. Hite, Y. Colombe, A.C. Wilson, K.R. Brown, U. Warring, R. Jördens, J.D. Jost, K.S. McKay, D.P. Pappas, D. Leibfried, D.J. Wineland, Phys. Rev. Lett. **109**, 103001 (2012)

26. F. Rossi, G.I. Opat, J. Phys. D Appl. Phys. **25**, 1349 (1992)

27. J.B. Camp, T.W. Darling, R.E. Brown, New J. Phys. **71**, 783 (1992)

28. A. Härter, A. Krükow, M. Dei B. Drews, E. Tiemann, J. Hecker Denschlag, Nat. Phys. **9**, 512–517 (2013)

29. A. Härter, A. Krükow, A. Brunner, J. Hecker Denschlag, Appl. Phys. Lett. **102**, 221115 (2013)

30. S. Schmid, A. Härter, A. Frisch, S. Hoinka, J. Hecker Denschlag, Rev. Sci. Instrum. **83**, 053108 (2012)

Population distribution of product states following three-body recombination in an ultracold atomic gas

A. Härter[1], A. Krükow[1], M. Deiß[1], B. Drews[1], E. Tiemann[2] and J. Hecker Denschlag[1]*

Three-body recombination is a collision process where two atoms combine to form a molecule and a third atom carries away part of the released reaction energy. Here, we experimentally determine for the first time the population distribution of the molecular reaction products after a three-body recombination for non-resonant particle interactions. The key to our measurements is a sensitive detection scheme that combines the photoionization of the molecules with subsequent ion trapping. Using an ultracold ^{87}Rb gas at very low kinetic energy below $h \times 20$ kHz, we find a broad population of final states with binding energies of up to $h \times 750$ GHz. This is in contrast with previous experiments, performed in the resonant interaction regime, that found a dominant population of only the most weakly bound molecular state or the occurrence of Efimov resonances. This work may contribute to the development of an in-depth model that can qualitatively and quantitatively predict the reaction products of three-body recombination.

Whereas cold collisions of two atoms are well understood, the addition of a third collision partner markedly complicates the interaction dynamics. In the context of Bose–Einstein condensation in atomic gases, three-body recombination plays a crucial role[1–4] and it constitutes a present frontier of few-body physics[5–7]. Until now, recombination events were mainly investigated by measuring atom loss rates. Discussions of the final states populated in the recombination process were restricted to the special case of resonant interactions[8,9] and culminated in the observations of Efimov resonances[10–12] and of molecules in the most weakly bound states[13,14]. However, in the more general case of non-resonant interaction, that is, a modulus of the scattering length smaller than or comparable to the van der Waals radius, the recombination products might depend on details of the interaction potential. In fact, ongoing theoretical studies using simplified models indicate that recombination does not necessarily always favour the most weakly bound state (J. d'Incao, private communication; see also ref. 15). In general, recombination processes are of fundamental interest in various physical systems[1,16,17]. The control and tunability of ultracold atomic systems provide an experimental testbed for a detailed understanding of the nature of these processes.

Here, we demonstrate the probing of molecules with binding energies up to $h \times 750$ GHz (where h is Planck's constant) generated through three-body recombination of ultracold thermal ^{87}Rb atoms. We produce the atomic sample in an optical dipole trap located within a linear Paul trap. The recombination and detection process is illustrated in Fig. 1a–d. Following a recombination event, the created Rb_2 molecule can undergo resonance-enhanced multi-photon ionization (REMPI) by absorbing photons from the dipole trap laser at a wavelength of around 1,064.5 nm. The ion is then captured in the Paul trap and detected essentially background-free with very high sensitivity on the single-particle level. Figure 1e shows a simplified scheme of the Rb_2 and Rb_2^+ potential energy curves. From weakly bound molecular states, three photons suffice

to reach the molecular ionization threshold. An additional photon may dissociate the molecular ion. By scanning the frequency of the dipole trap laser by more than 60 GHz we obtained a high-resolution spectrum featuring more than 100 resonance peaks. This dense and complex spectrum contains information concerning which vibrational, rotational and hyperfine levels of the Rb_2 molecule are populated. We present an analysis of these data and make a first assignment of the most prominent resonances. This assignment indicates that in the recombination events a broad range of levels is populated in terms of vibrational, rotational, electronic and nuclear spin quantum numbers.

Our experimental scheme to detect cold molecules makes use of the generally excellent detection efficiencies attainable for trapped ions. It is related to proven techniques where cold molecules in magneto-optical traps were photoionized from the singlet and triplet ground states[18–23] (see also ref. 24). Our method is unique as it introduces the use of a hybrid atom–ion trap that significantly improves the detection sensitivity. We perform the following experimental sequence. A thermal atomic sample typically containing $N_{at} \approx 5 \times 10^5$ spin-polarized ^{87}Rb atoms in the $|F = 1, m_F = -1\rangle$ hyperfine state is prepared in a crossed optical dipole trap at a magnetic field of about 5 G. The trap is positioned onto the nodal line of the radiofrequency field of a linear Paul trap. Along the axis of the Paul trap the centres of the atom and ion trap are separated by about $300\,\mu m$ to avoid unwanted atom–ion collisions (Fig. 1d). At atomic temperatures of about 700 nK and peak densities $n_0 \approx 5 \times 10^{13}$ cm^{-3} the total three-body recombination rate in the gas is $\Gamma_{rec} = L_3 n_0^2 N_{at} / 3^{5/2} \approx 10$ kHz. Here, the three-body loss rate coefficient L_3 was taken from ref. 3. At the rate Γ_{rec}, pairs of Rb_2 molecules and Rb atoms are formed as final products of the reactions. Both the atom and molecule would generally be lost from the shallow neutral particle trap owing to the comparatively large kinetic energy they gain in the recombination event (in our case typically of the order of a few $K \times k_B$, where

---

^{1}Institut für Quantenmaterie and Center for Integrated Quantum Science and Technology IQST, Universität Ulm, 89069 Ulm, Germany, ^{2}Institut für Quantenoptik, Leibniz Universität Hannover, 30167 Hannover, Germany. *e-mail: johannes.denschlag@uni-ulm.de
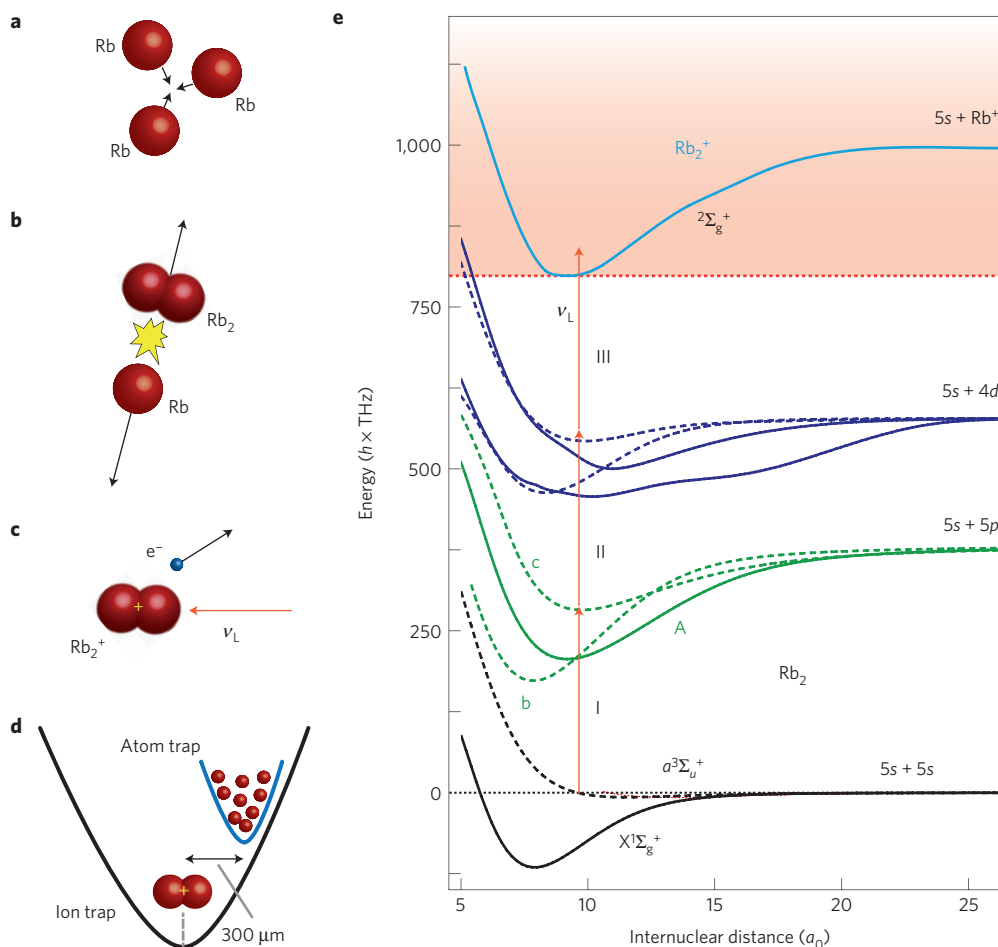
Figure 1 | Illustration of recombination and ionization in the atom–ion trap. a,b, A three-body collision in the ultracold gas of ^{87}Rb atoms (**a**) leads to a recombination event in which a Rb$_2$ molecule is formed with high kinetic energy (**b**). **c,** While the atom is lost from the trap, the molecule can be photoionized in a REMPI process and trapped in the Paul trap. **d,** The relative positions of the atom and ion trap centres are shifted by about 300 µm to avoid atom–ion collisions. **e,** Potential energy curves of the Rb$_2$ and Rb$_2^+$ molecule adapted from refs 18,35. The curves A, b, c are $A^1\Sigma_u^+$, $b^3\Pi_u$, $c^3\Sigma_u^+$. The internuclear distance is given in units of Bohr radii a_0. A REMPI path with three photons is shown. It can create Rb$_2^+$ ions in vibrational states up to $v \approx 17$.

k_B is the Boltzmann constant). The molecule, however, can be state-selectively ionized in a REMPI process driven by the dipole trap laser. All of these molecular ions remain trapped in the deep Paul trap and are detected with single-particle sensitivity (Methods). In each experimental run, we hold the atomic sample for a time $\tau \approx 10$ s. After this time we measure the number of produced ions in the trap from which we derive (after averaging over tens of runs) the ion production rate Γ_{ion} normalized to a cloud atom number of 10^6 atoms.

As a consistency check of our assumption that Rb$_2$ molecules are ionized in the REMPI process, we verify the production of Rb$_2^+$ molecules. For this, we perform ion mass spectrometry in the Paul trap (Methods). We detect primarily molecular Rb$_2^+$ ions, a good fraction of atomic Rb$^+$ ions but no Rb$_3^+$ ions. Our experiments show that Rb$^+$ ions are produced in light-assisted collisions of Rb$_2^+$ ions with Rb atoms on timescales below a few milliseconds. Details of this dissociation mechanism are under investigation and will be discussed elsewhere.

Two pathways for the production of our neutral Rb$_2$ molecules come immediately to mind. One pathway is far-off-resonant photoassociation of two colliding Rb atoms (here with a detuning of about 500 GHz × h). This pathway can be ruled out using several arguments, the background of which will be discussed in more depth later. For one, we observe molecules with a parity that is incompatible with photoassociation of totally

spin-polarized ensembles. Furthermore, we observe a dependence of the ion production rate on light intensity that is too weak to explain photoassociation.

The second pathway is three-body recombination of Rb atoms. Indeed, by investigating the dependence of the ion production rate Γ_{ion} (which is normalized to a cloud atom number of 10^6 atoms) on atomic density, we find the expected quadratic dependence (Fig. 2). For this measurement the density was adjusted by varying the cloud atom number while keeping the light intensity of the dipole trap constant.

Next, we investigate the dependence of the ion production rate on the wavelength of the narrow-linewidth dipole trap laser (Methods). We scan the wavelength over a range of about 0.3 nm around 1,064.5 nm, corresponding to a frequency range of about 60 GHz. Typical frequency step sizes are 50 or 100 MHz. We obtain a rich spectrum of resonance lines that is shown in Fig. 3a. The quantity $\bar{\Gamma}_{\mathrm{ion}}$ denotes the ion production rate normalized to the atom number of the cloud and to the square of the atomic peak density. We find strongly varying resonance strengths and at first sight fairly irregular frequency spacings. In the following we will argue that most resonance lines can be attributed to respective well-defined molecular levels (resolving vibrational, rotational and often even hyperfine structure) that have been populated in the recombination process. These levels are located in the triplet or singlet ground state, $a^3\Sigma_u^+$ and $X^1\Sigma_g^+$, respectively. The relatively
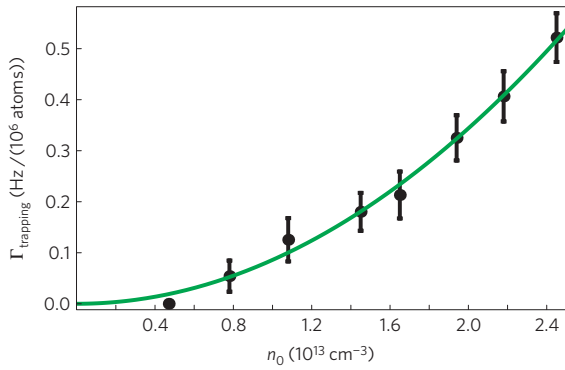
Figure 2 | Dependence of the ion production rate Γ_{ion} on atomic density. Γ_{ion} is normalized to a cloud atom number of 10^6 atoms. The data are well described by a quadratic fit (solid green line). They were taken at a constant dipole trap laser intensity $I_L = 36\,kW\,cm^{-2}$ and a laser frequency of $\nu_L = 281,630\,GHz$. The error bars indicate statistical uncertainties and represent one standard deviation from the mean.

dense distribution of these lines reflects that a fairly broad range of states is populated. A direct assignment of the observed resonances is challenging, as it hinges on the precise knowledge of the level structure of all the relevant ground and excited states. In the following we will access and understand the data step by step.

One feature of the spectrum that stands out is the narrow linewidth of many lines. For example, Fig. 3b shows a resonance of which the substructures have typical half-widths $\Delta\nu_r \approx 50\,MHz$.

This allows us to roughly estimate the maximal binding energy of the molecules involved. As the velocity of the colliding ultracold atoms is extremely low, the kinetics of the recombination products is dominated by the released molecular binding energy E_b. Owing to energy and momentum conservation the molecules will be expelled from the reaction with a molecular velocity $v_{Rb2} = \sqrt{2E_b/(3m_{Rb2})}$, where m_{Rb2} is the molecular mass. The molecular resonance frequency ν_0 will then be Doppler-broadened with a half-width $\Delta\nu_D = \sqrt{3}\nu_0 v_{Rb2}/2c$. Here, c is the speed of light. By comparing $\Delta\nu_D$ to the observed values of $\Delta\nu_r$ we estimate a maximal binding energy of the order of $E_{b,max} \approx h \times 2.5\,THz$. This simple analysis overestimates the value $E_{b,max}$ because it neglects the natural linewidth of the transition and possible saturation broadening. Still, it already strongly constrains the possibly populated molecular levels that are observed in our experiment.

Next, we investigate the dependence of the ion production rate on laser intensity I_L. In our experimental set-up, this measurement is rather involved because the laser driving the REMPI process also confines the atomic cloud. Thus, simply changing only the laser intensity would undesirably also change the density n_0 of the atoms. To prevent this from happening we keep n_0 constant ($n_0 \approx 5 \times 10^{13}\,cm^{-3}$) by adjusting the atom number and temperature appropriately. Owing to these experimental complications we can vary I_L only roughly by a factor of 2 (Fig. 4a). We set the laser frequency to the value of $\nu_L = \nu_L^0 \equiv 281,610\,GHz$, on the tail of a large resonance (Fig. 3). The atomic temperatures in this measurement range between 500 nK and 1.1 µK, well above the critical temperatures for Bose–Einstein condensation. The atomic densities can therefore be described using a Maxwell–Boltzmann
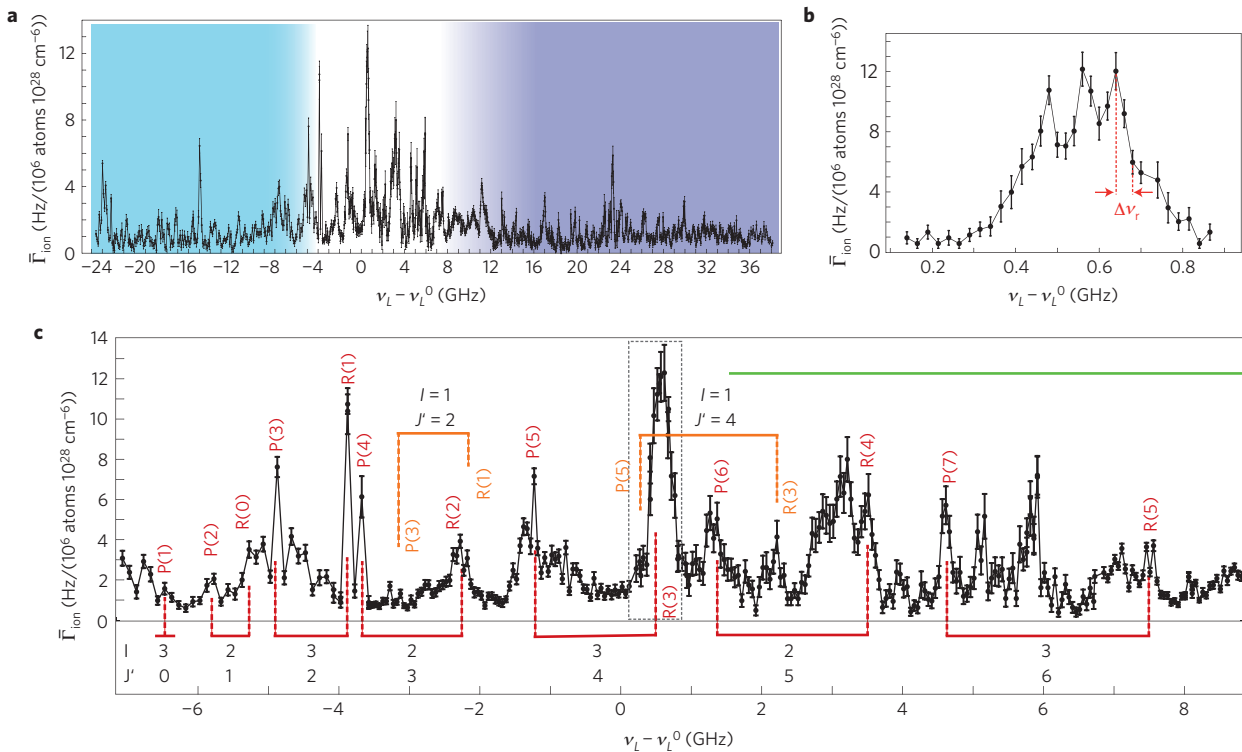

Figure 3 | REMPI spectrum. a, A scan of the dipole trap laser frequency ν_L over more than 60 GHz around an offset frequency $\nu_L^0 = 281.610\,THz$ shows a multitude of resonance lines. Each data point is the result of 30–60 repetitions of the experiment with ion detection on the single-particle level. The total spectrum was obtained over a time span of 2 months. Checks of the long-term consistency of resonance positions and strengths were performed. Spectral regions dominated by transitions to $c^3\Sigma_g^+$ are indicated by the shaded areas in dark and light blue (0_g^- and 1_g component, respectively). **b,** High-resolution scan of the strong resonance at $\nu_L - \nu_L^0 \approx 0.5\,GHz$. **c,** Central spectral region with assigned P/R branches of the transition $X^1\Sigma_g^+ (v = 115) \rightarrow A^1\Sigma_u^+ (v' = 68)$. The corresponding quantum numbers I and J' are given. P(J) marks the transition $J \rightarrow J+1$; R(J) marks the transition $J \rightarrow J-1$. These lines can be grouped into pairs sharing the same J' of the excited state and I quantum number. The region where also transitions to $b^3\Pi_u$ appear is marked by a green horizontal bar. The error bars indicate statistical uncertainties and represent one standard deviation from the mean.
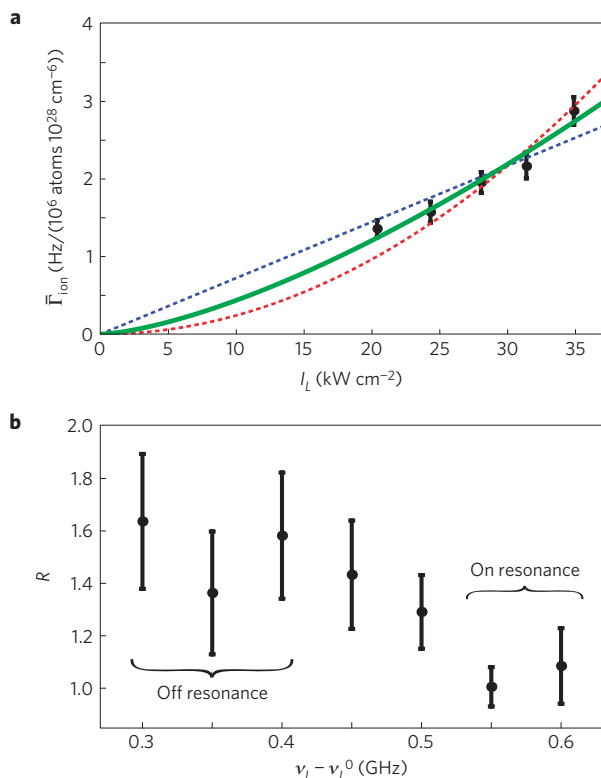
a

b

Figure 4 | Dependence of the ion production rate on the intensity of the dipole trap laser. a, Assuming a power-law dependence $\bar{\Gamma}_{ion} \propto I_L^\alpha$, the best fit to the data is achieved for $\alpha \approx 1.5$ (solid green line). Linear and quadratic fits are also given (blue and red dashed lines, respectively).
b, Measurement of the intensity dependence using a chopped dipole trap. The ratio $R \approx 1$ on resonance indicates saturation of both transitions I and II. The error bars indicate statistical uncertainties and represent one standard deviation from the mean.

distribution. Assuming a simple power-law dependence of the form $\bar{\Gamma}_{ion} \propto I_L^\alpha$ we obtain the best fit using an exponent $\alpha = 1.5(1)$ (solid green line in Fig. 4a). This fit is between a linear and a quadratic intensity dependence (dashed red and blue lines, respectively). Thus, at least two of the three transitions composing the ionization process are partially saturated at the typical intensities used.

To better circumvent possible density variations of the atomic cloud induced by changes in laser intensity, we employ a further method that enables us to vary the intensity with negligible effects on the atomic sample. We achieve this by keeping the time-averaged intensity $\langle I_L \rangle$ constant and comparing the ion production rates within a continuous dipole trap and a chopped dipole trap in which the intensity is rapidly switched between 0 and $2I_L$. In both cases the trap is operated at an intensity $\langle I_L \rangle \approx 15 \, \text{kW cm}^{-2}$. In the chopped configuration the intensity is switched at a frequency of 100 kHz so that the atoms are exposed to the light for 5 μs followed by 5 μs without light. It should be noted that molecules formed in the dark period with sufficiently high kinetic energies may leave the central trapping region before the laser light is switched back on. They are then lost for our REMPI detection. Taking into account the molecular velocity and the transverse extensions of the laser beams we can estimate that this potential loss mechanism leads to errors of less than 30%, even at the highest binding energies relevant to this work ($E_b \approx h \times 750 \, \text{GHz}$, see below). We did not observe evidence of such losses experimentally. Investigations were made by changing the chopping frequency. We define R as the ratio of the ion production rates in the chopped and the continuous trap configuration. Figure 4b shows the results of these
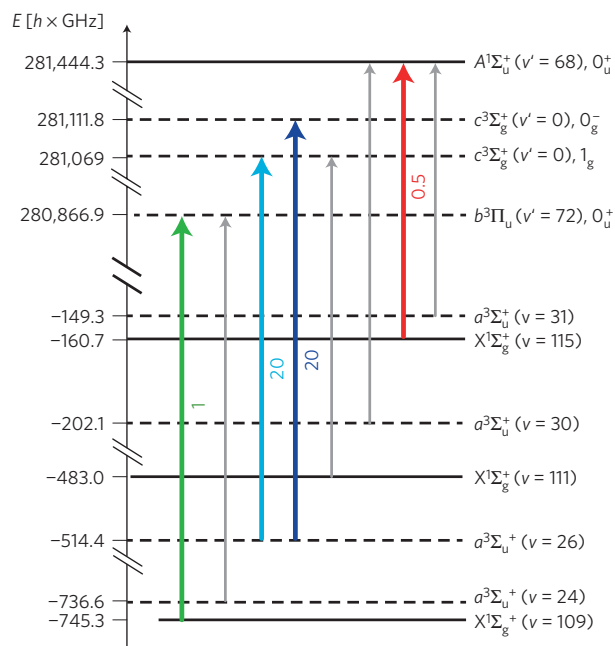
Figure 5 | Overview over relevant molecular levels and transitions. The vertical axis denotes the energy E_b of the energetically lowest levels of each vibrational manifold with respect to the 5s 5s asymptote. Coloured thick arrows represent molecular transitions relevant to the spectrum of Fig. 3. The expected relative strengths of these transitions are also given. Grey arrows mark transitions that occur in the relevant spectral region but are so weak that they can be neglected (for further spectroscopic details, see Methods). We identify three main molecular transitions for the initial step of the REMPI process. The blue arrows indicate molecules in the $v = 26$ vibrational level of the $a^3\Sigma_u^+$ potential that are excited to the $v' = 0$ level of the $c^3\Sigma_g^+$ potential. This level is split into a 1_g and a 0_g^- component. The red arrow is an excitation from $X^1\Sigma_g^+(v = 115)$ to $A^1\Sigma_u^+(v' = 68)$. The green arrow is an excitation from $X^1\Sigma_g^+(v = 109)$ to $b^3\Pi_u(v' = 72)$. This transition becomes possible through the strong spin–orbit coupling of the A and b states.

measurements for various laser frequencies ν_L. We find a value $R \approx 1.5$ for off-resonant frequency settings $\nu_L - \nu_L^0 < 0.4 \, \text{GHz}$, in good agreement with the result presented in Fig. 4a. When scanning the laser onto resonance at $\nu_L - \nu_L^0 \approx 0.45 \, \text{GHz}$ (Fig. 3b) we obtain $R \approx 1$. This result indicates a linear intensity dependence of the REMPI process in the resonant case, which is explained by the saturation of two of the three molecular transitions involved. It is known that transitions into the ionization continuum (photon III, Fig. 1e) will not saturate under the present experimental conditions. This means that the excitation pathway through photon I and II must be saturated and therefore both are close to resonance.

However, given the wavelength range of about $1,064.5 \pm 0.15 \, \text{nm}$, an inspection of the level structure shows that photon I can only resonantly drive three different transitions that connect vibrational levels in states X and a to vibrational levels in states A, b and c (Fig. 1e). Spectroscopic details for these transitions and the corresponding vibrational levels are given in the Methods and in Fig. 5. From recent spectroscopic studies[25–27] and further measurements in our laboratory the level structure of all relevant levels of the X, a, A, b, and c states is well known. The absolute precision of most of the level energies is far better than 1 GHz for low rotational quantum numbers J.

In the experimental data (Fig. 3a) the central region from $\nu_L - \nu_L^0 = -6$ to 7 GHz is marked by several prominent resonances that are significantly stronger than those observed throughout the rest of the spectrum. These resonance peaks can be assigned

to transitions from the X ground state to A and b states. The prominence of these singlet transitions is explained by the near degeneracy of levels due to small hyperfine splittings. Indeed, by analysing these strong resonances with regard to line splittings and intensities it was possible to consistently assign rotational ladders for total nuclear spin quantum numbers $I = 1, 2, 3$ for the transition $X(v = 115) \rightarrow A(v' = 68)$. The starting point of the rotational ladder for $I = 2$ was fixed by spectroscopic measurements in our laboratory. At frequencies $v_L - v_L^0 \gtrsim 2$ GHz additional strong lines appear that we attribute to the $X(v = 109) \rightarrow b(v' = 72)$ transition. The fact that we observe X state molecules with $I = 1, 2, 3$ is interesting because for $I = 1, 3$ the total parity of the molecule is negative, whereas for $I = 0, 2$ it is positive. However, a two-body collision state of our spin-polarized Rb atoms necessarily has positive total parity due to symmetry arguments and a photoassociation pathway would lead to ground-state levels with positive parity. The observed production of molecules with negative total parity must then be a three-body collision effect.

We now consider the role of secondary atom–molecule collisions that would change the product distribution owing to molecular relaxation. Two aspects are of importance: depopulation of detected molecular levels, and population of detected molecular levels through relaxation from more weakly bound states. In our experiments reported here we detect molecules that are formed in states with binding energies of the order of hundreds of GHz × h. These molecules leave the reaction with kinetic energies of several $K \times k_B$. At these energies the rate coefficients for depopulating atom–molecule collisions are small (see for example ref. 15) and the collision probability before the molecule is either ionized or has left the trap is below 1%.

For the population processes, we can estimate an upper bound for rate coefficients by assuming recombination to occur only into the most weakly bound state with a binding energy of 24 MHz × h. In this case subsequent atom–molecule collision rates will be roughly comparable to those expected in the ultracold limit. At typical rate coefficients of 10^{-10} cm³ s⁻¹ (refs 28–31) and the atomic densities $n_0 \sim 1 \times 10^{13}$ cm⁻³ used in the measurement shown in Fig. 2, the collision probability before the molecule leaves the atom cloud is around 5%. This small probability grows linearly with density so that the density dependence of the ion production rate should show a significant cubic contribution if secondary collisions were involved (as expected for this effective four-body process). This is inconsistent with the data and thus indicates that the population that we detect is not significantly altered by secondary collisions.

We can roughly estimate the range of molecular rotation J of the populated levels in the ground state. The strong, isolated lines that we have assigned to the $X(v = 115) \rightarrow A(v' = 68)$ transition are all contained within a relatively small spectral region ($|v_L - v_L^0| < 6$ GHz) and are explained by rotational quantum numbers $J \leq 7$. Population of higher rotational quantum numbers would result in a continuation of the strong resonance lines stretching to transition frequencies beyond $v_L - v_L^0 = 10$ GHz, which we do not observe. Similarly, if only rotational quantum numbers $J \leq 5$ were populated, a spectrum would result that does not have enough lines to explain the data. Thus, we can roughly set the limits on the molecular rotation to $J \leq 7$, a value that is also consistent with our observations of the spread of the transitions $X \rightarrow b$ and $a \rightarrow c$ (Fig. 5). Finding quantum numbers as high as $J = 7$ is remarkable because the three-body collisions at microkelvin temperatures clearly take place in an s-wave regime, that is, at vanishing rotational angular momentum. Hence, one could expect to produce X state molecules dominantly at $J = 0$, which, however, we do not observe.

Despite the limited spectral range covered by our measurements, we can already estimate the number of molecular vibrational levels populated in the recombination events. From the three

states $X(v = 109)$, $a(v = 26)$ and $X(v = 115)$ that we can observe within our wavelength range, all deliver comparable signals in the spectrum of Fig. 3. This suggests that at least all vibrational states more weakly bound than $X(v = 109)$ should be populated, a total of 38 vibrational levels (counting both singlet and triplet states). This is a significant fraction of the 169 existing levels of the X and a states, although restricted to a comparatively small range of binding energies.

In conclusion, our work represents a first experimental step towards a detailed understanding on how the reaction channels in three-body recombination are populated. A full understanding will clearly require further experimental and theoretical efforts. On the experimental side the scanning range has to be increased and it could be advantageous to switch to a two-colour REMPI scheme in the future. Such studies may finally pave the way to a comprehensive understanding of three-body recombination, which includes the details of the final products.

Reaching beyond the scope of three-body recombination, the great sensitivity of our detection scheme has enabled us to state-selectively probe single molecules that are produced at rates of only a few hertz. We thereby demonstrate a new scheme for precision molecular spectroscopy in extremely dilute ensembles.

Methods

Dipole trap and REMPI configuration. The crossed dipole trap is composed of a horizontal and a vertical beam focused to beam waists of ~90 μm and ~150 μm, respectively. It is positioned onto the nodal line of the radiofrequency field of the linear Paul trap with micrometre precision. The two trap centres are separated by about 300 μm along the axis of the Paul trap (Fig. 1d). In a typical configuration, the trap frequencies of the dipole trap are $(175, 230, 80)$ Hz resulting in atom cloud radii of about $(6, 7, 16)$ μm. The short-term frequency stability of the dipole trap laser source is of the order of 1 kHz and it is stabilized against thermal drifts to achieve long-term stability of a few megahertz. The two beams of the dipole trap are mutually detuned by 160 MHz to avoid interference effects in the optical trap. Consequently, two frequencies are in principle available to drive the REMPI process. However, the intensity of the horizontal beam is 4 times larger than the one of the vertical beam and we have not directly observed a corresponding doubling of lines. Further details on the atom–ion apparatus are given in ref. 32.

Paul trap configuration. The linear Paul trap is driven at a radiofrequency of 4.17 MHz and an amplitude of about 500 V resulting in radial confinement with trap frequencies of $(\omega_{x,\text{Ba}}, \omega_{y,\text{Ba}}) = 2\pi \times (220, 230)$ kHz for a ^{138}Ba$^+$ ion. Axial confinement is achieved by applying static voltages to two endcap electrodes yielding $\omega_{z,\text{Ba}} = 2\pi \times 40.2$ kHz. The trap frequencies for dark Rb$_2^+$ and Rb$^+$ ions produced in the REMPI processes are $(m_{\text{Ba}}/m_{\text{dark}} \times \omega_{x,\text{Ba}}, m_{\text{Ba}}/m_{\text{dark}} \times \omega_{y,\text{Ba}}, \sqrt{m_{\text{Ba}}/m_{\text{dark}}} \times \omega_{z,\text{Ba}})$, where m_{Ba} and m_{dark} denote the mass of the Ba$^+$ ion and the dark ion, respectively. The depth of the Paul trap depends on the ionic mass and exceeds 2 eV for all ionic species relevant to this work.

Ion detection methods. We employ two methods to detect Rb$_2^+$ and Rb$^+$ ions, both of which are not amenable to fluorescence detection. In the first of these methods we use a single trapped and laser-cooled ^{138}Ba$^+$ ion as a probe. By recording its position and trapping frequencies in small ion strings with up to 4 ions we detect both the number and the masses of the ions following each REMPI process (see also ref. 33). The second method is based on measuring the number of ions in the Paul trap by immersing them into an atom cloud and recording the ion-induced atom loss after a hold time of 2 s (see also ref. 34). During this detection scheme, we take care to suppress further generation of ions by working with small and dilute atomic clouds and by detuning the REMPI laser from resonance. Both methods are background-free in the sense that no ions are captured on timescales of days in the absence of the atom cloud. Further information on both detection methods is given in the Supplementary Information.

Spectroscopic details. Spin–orbit and effective spin–spin coupling in the A, b, and c states lead to Hund's case c coupling where the relevant levels of states A and b have 0_u^+ symmetry whereas the levels of state $c^3\Sigma_g^+$ are grouped into 0_g^- and 1_g components. The level structure of the 0_u^+ states is quite simple as it is dominated by rotational splittings. Typical rotational constants for the electronically excited states are of the order of 400 MHz; for the weakly bound X and a states they are around 100–150 MHz.

Figure 5 shows the relevant optical transitions between the X, a states and the A, b, c states in our experiment. For the given expected relative strengths of these transitions, we consider only Franck–Condon factors and the mixing of singlet and triplet states, and electronic transition moments are ignored. The coloured arrows

correspond to transitions with large enough Franck–Condon factors (typically 10^{-2}–10^{-3}) so that at laser powers of $\approx 10^4$ W cm^{-2} resonant transitions can be well saturated. Transitions marked with grey arrows can be neglected owing to weak transition strengths, being forbidden in first order by dipole selection rules.

References

1. Hess, H. F. *et al*. Observation of three-body recombination in spin-polarized hydrogen. *Phys. Rev. Lett.* **51**, 483–486 (1983).
2. Burt, E. A. *et al*. Coherence, correlations, and collisions: What one learns about Bose–Einstein condensates from their decay. *Phys. Rev. Lett.* **79**, 337–340 (1997).
3. Söding, J. *et al*. Three-body decay of a rubidium Bose–Einstein condensate. *Appl. Phys. B* **69**, 257–261 (1999).
4. Esry, B. D., Greene, C. H. & Burke, J. P. Recombination of three atoms in the ultracold limit. *Phys. Rev. Lett.* **83**, 1751–1754 (1999).
5. Suno, H. & Esry, B. D. Three-body recombination in cold helium–helium-alkali-metal-atom collisions. *Phys. Rev. A* **80**, 062702 (2009).
6. Wang, Y., D'Incao, J. P. & Esry, B. D. Cold three-body collisions in hydrogen–hydrogen-alkali-metal atomic systems. *Phys. Rev. A* **83**, 032703 (2011).
7. Guevara, N. L., Wang, Y. & Esry, B. D. New class of three-body states. *Phys. Rev. Lett.* **108**, 213202 (2012).
8. Fedichev, P. O., Reynolds, M. W. & Shlyapnikov, G. V. Three-body recombination of ultracold atoms to a weakly bound *s* level. *Phys. Rev. Lett.* **77**, 2921–2924 (1996).
9. Bedaque, P. F., Braaten, E. & Hammer, H-W. Three-body recombination in Bose gases with large scattering length. *Phys. Rev. Lett.* **85**, 908–911 (2000).
10. Efimov, V. Energy levels arising from resonant two-body forces in a three-body system. *Phys. Lett. B* **33**, 563–564 (1970).
11. Braaten, E. & Hammer, H-W. Three-body recombination into deep bound states in a Bose gas with large scattering length. *Phys. Rev. Lett.* **87**, 160407 (2001).
12. Kraemer, T. *et al*. Evidence for Efimov quantum states in an ultracold gas of caesium atoms. *Nature* **440**, 315–318 (2006).
13. Weber, T., Herbig, J., Mark, M., Nägerl, H-C. & Grimm, R. Three-body recombination at large scattering lengths in an ultracold atomic gas. *Phys. Rev. Lett.* **91**, 123201 (2003).
14. Jochim, S. *et al*. Pure gas of optically trapped molecules created from Fermionic atoms. *Phys. Rev. Lett.* **91**, 240402 (2003).
15. Simoni, A. & Launay, J-M. Ultracold atom-molecule collisions with hyperfine coupling. *Laser Phys.* **16**, 707–712 (2006).
16. Bates, D. R., Kingston, A. E. & McWhirter, R. W. P. Recombination between electrons and atomic ions. I. Optically thin plasmas. *Proc. R. Soc. Lond. Ser A.* **267**, 297–312 (1962).
17. Flower, D. R. & Harris, G. J. Three-body recombination of hydrogen during primordial star formation. *Mon. Not. R. Astronom. Soc.* **377**, 705–710 (2007).
18. Lozeille, J. *et al*. Detection by two-photon ionization and magnetic trapping of cold Rb$_2$ triplet state molecules. *Eur. Phys. J. D* **39**, 261–269 (2006).
19. Fioretti, A. *et al*. Formation of cold Cs$_2$ molecules through photoassociation. *Phys. Rev. Lett.* **80**, 4402–4405 (1998).
20. Gabbanini, C., Fioretti, A., Lucchesini, A., Gozzini, S. & Mazzoni, M. Cold rubidium molecules formed in a magneto-optical trap. *Phys. Rev. Lett.* **84**, 2814–2817 (2000).
21. Huang, Y. *et al*. Formation, detection and spectroscopy of ultracold Rb$_2$ in the ground $X\,^1\Sigma_g^+$ state. *J. Phys. B* **39**, S857–S869 (2006).
22. Salzmann, W. *et al*. Coherent transients in the femtosecond photoassociation of ultracold molecules. *Phys. Rev. Lett.* **100**, 233003 (2008).
23. Sullivan, S. T. *et al*. Trapping molecular ions formed via photo-associative ionization of ultracold atoms. *Phys. Chem. Chem. Phys.* **13**, 18859–18863 (2011).
24. Mudrich, M. *et al*. Spectroscopy of triplet states of Rb$_2$ by femtosecond pump–probe photoionization of doped helium nanodroplets. *Phys. Rev. A* **80**, 042512 (2009).
25. Strauss, C. *et al*. Hyperfine, rotational, and vibrational structure of the $a^3\Sigma_u^+$ state of ^{87}Rb$_2$. *Phys. Rev. A* **82**, 052514 (2010).
26. Takekoshi, T. *et al*. Hyperfine, rotational, and Zeeman structure of the lowest vibrational levels of the ^{87}Rb$_2$ (1) $^3\Sigma_g^+$ state. *Phys. Rev. A* **83**, 062504 (2011).
27. Drozdova, A. *Study of Spin-Orbit Coupled Electronic States of* Rb$_2$, *NaCs and NaK Molecules. Laser Spectroscopy and Accurate Coupled-channel Deperturbation Analysis* PhD thesis, Univ. de Lyon and Lomonosov State Univ. (2012).
28. Mukaiyama, T., Abo-Shaeer, J. R., Xu, K., Chin, J. K. & Ketterle, W. Dissociation and decay of ultracold sodium molecules. *Phys. Rev. Lett.* **92**, 180402 (2004).
29. Staanum, P., Kraft, S. D., Lange, J., Wester, R. & Weidemüller, M. Experimental investigation of ultracold atom-molecule collisions. *Phys. Rev. Lett.* **96**, 023201 (2006).
30. Zahzam, N., Vogt, T., Mudrich, M., Comparat, D. & Pillet, P. Atom-molecule collisions in an optically trapped gas. *Phys. Rev. Lett.* **96**, 023202 (2006).
31. Quéméner, G., Launay, J-M. & Honvault, P. Ultracold collisions between Li atoms and Li$_2$ diatoms in high vibrational states. *Phys. Rev. A* **75**, 050701 (2007).
32. Schmid, S., Härter, A., Frisch, A., Hoinka, S. & Hecker Denschlag, J. An apparatus for immersing trapped ions into an ultracold gas of neutral atoms. *Rev. Sci. Instrum.* **83**, 053108 (2012).
33. Schmid, S., Härter, A. & Hecker Denschlag, J. Dynamics of a cold trapped ion in a Bose–Einstein condensate. *Phys. Rev. Lett.* **105**, 133202 (2010).
34. Härter, A. *et al*. Single ion as a three-body reaction center in an ultracold atomic gas. *Phys. Rev. Lett.* **109**, 123201 (2012).
35. Aymar, M., Azizi, S. & Dulieu, O. Model-potential calculations for ground and excited Σ states of Rb$_2^+$, Cs$_2^+$ and RbCs$^+$ ions. *J. Phys. B* **36**, 4799–4812 (2003).

Acknowledgements

Author contributions

A.H. and A.K. performed the experiments in the atom–ion trap set-up; M.D. and B.D. performed spectroscopic measurements on Rb$_2$ molecules; A.H., A.K., E.T. and J.H.D. analysed data; A.H., E.T. and J.H.D. wrote the paper.

Additional information

Supplementary information is available in the online version of the paper. Reprints and permissions information is available online at www.nature.com/reprints. Correspondence and requests for materials should be addressed to J.H.D.

Competing financial interests

The authors declare no competing financial interests.

Population distribution of product states following three-body recombination in an ultracold atomic gas

A. Härter[1], A. Krükow[1], M. Deiß[1], B. Drews[1], E. Tiemann[2], & J. Hecker Denschlag[1]

[1] *Institut für Quantenmaterie and Center for Integrated Quantum Science and Technology IQST, Universität Ulm, 89069 Ulm, Germany*
[2] *Institut für Quantenoptik, Leibniz Universität Hannover, 30167 Hannover, Germany*

In this Supplementary Information we describe two methods that we employ to detect small numbers of Rb_2^+ and Rb^+ ions in our linear Paul trap.

Method 1

To implement our first ion detection method allowing mass-sensitive detection of "dark" ions we rely on the presence of a single "bright" ion in the trap. Information on additional ions can be extracted from its fluorescence position. When using this method, our experimental procedure begins with the loading of a single $^{138}Ba^+$-ion into our linear Paul trap. We laser-cool the ion and image its fluorescence light onto an electron-multiplying charge-coupled device camera. This enables us to determine the position of the trap center to better than 100 nm. The ion is confined at radial and axial trapping frequencies $\omega_{r,Ba} \approx 2\pi \times 220$kHz and $\omega_{ax,Ba} \approx 2\pi \times 40.2$kHz and typically remains trapped on timescales of days. Next, we prepare an ultracold atomic sample in the crossed dipole trap. At typical atomic temperatures of about 700 nK the atom cloud has radial and axial extensions of about 7 μm and 15 μm and is thus much smaller than the trapping volume of our Paul trap. To avoid atom-ion collisions we shift the Ba^+-ion by about 300 μm with respect to the atom cloud before the atomic sample arrives in the Paul trap. The shifting is performed along the axis of the trap by lowering the voltage on one of the endcap electrodes. Additionally, we completely extinguish all resonant laser light so that the atoms are only subjected to the light of the dipole trap. The atomic sample is moved into the center of the radial trapping potential of the Paul trap and is typically held at this position for a time $\tau_{hold} \approx 10$ s. Despite the axial offset from the center of the Paul trap, the atom cloud at this position is fully localized within the trapping volume of the Paul trap. After the hold time the sample is detected using absorption imaging. Subsequently, the ion cooling beams are switched back on for fluorescence detection of the Ba^+-ion.

The presence of a second ion in the trap leads to positional shifts of the $^{138}Ba^+$-ion by distances on the order of 10 μm (see Fig. 1). We make use of the mass-dependent trap frequencies of the Paul trap to gain information on the ion species trapped. In a two-ion Coulomb crystal composed of a Ba^+-ion and a dark ion, the axial center-of-mass frequency $\omega_{ax,2ion}$ shifts with respect to $\omega_{ax,Ba}$ depending on the mass of the dark ion m_{dark} [?]. We measure $\omega_{ax,2ion}$ by modulating the trap drive at frequencies ω_{mod} and by monitoring the induced axial oscillation of the Ba^+-ion, visible as a blurring of the fluorescence signal. In this way, after each ion trapping event, we identify a resonance either
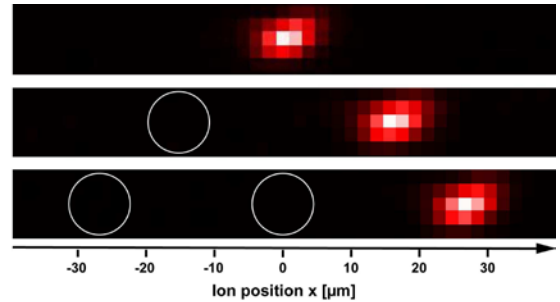

Figure 1 | Ion detection using a $^{138}Ba^+$-ion. Positional shifts of the fluorescence of the Ba^+-ion and measurements of the trap oscillation frequencies allow us to perform mass-sensitive detection of up to three "dark" ions in the trap.

Table 1 | Trap oscillation frequencies of two-ion crystals

Ion species	$\omega_{ax,2ion}/2\pi$ [kHz]	$\omega_r/2\pi$ [kHz]
$^{138}Ba^+$ and $^{138}Ba^+$	40.2	220.0
$^{138}Ba^+$ and $^{87}Rb^+$	44.0	345.3
$^{138}Ba^+$ and $^{87}Rb_2^+$	37.7	170.7

at $\omega_{mod} \approx 2\pi \times 44$ kHz or $\omega_{mod} \approx 2\pi \times 38$ kHz corresponding to $m_{dark} = 87$ u and $m_{dark} = 174$ u, respectively (see table 1).

We have expanded this method for ion strings with up to four ions including the Ba^+-ion. For this purpose, we perform the following step-by-step analysis.

1. The position x of the Ba^+-ion with respect to the trap center is detected. If $x \neq 0$, the value of x allows us to directly determine the total number of ions in the string.

2. If $x = 0$ we need to distinguish between a single Ba^+ ion and a three-ion string with Ba^+ at its center. This is done by modulating the trap drive at $\omega_{ax,Ba}$, thereby only exciting the Ba^+ ion if no further ions are present.

3. We destructively detect the Rb^+ ions by modulating the trap drive on a 5 kHz wide band around $2 \times \omega_{r,Rb}/(2\pi) = 691$ kHz. This selectively removes only Rb^+ ions from the string making use of the relatively weak inter-ionic coupling when exciting the ions radially.

4. Steps 1. and 2. are repeated to detect the number of remaining ions.
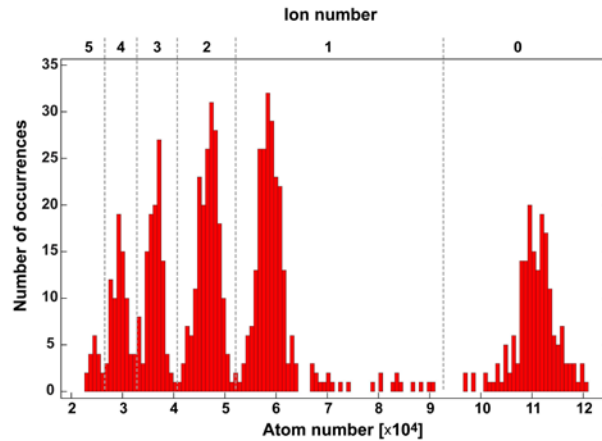
Figure 2 | Ion detection method based on ion-induced atom loss.
We overlap an ultracold atom cloud containing approximately 110,000 atoms with the center of the Paul trap. After an interaction time $\tau = 2\,\mathrm{s}$ we detect the ion-induced atom loss via absorption imaging of the atom cloud. The discrete number of trapped ions is clearly reflected in the displayed histogram of atom numbers.

5. The Rb_2^+ ions are destructively detected via modulation around $2 \times \omega_{\mathrm{r,Rb2}}/(2\pi) = 341\,\mathrm{kHz}$.

Method 2

We have also developed a second ion detection method that does not require an ion fluorescence signal. Instead, the trapped ions are detected via their interaction with an atomic sample. For this purpose, we produce a comparatively small atom cloud containing about 1×10^5 atoms at a density of a few $10^{12}\,\mathrm{cm}^{-3}$. In addition, we set the frequency of the dipole trap laser to an off-resonant value so that the production of additional ions during the ion probing procedure becomes extremely unlikely. We now fully overlap the ion and atom traps for an interaction time $\tau_{\mathrm{int}} = 2\,\mathrm{s}$. By applying an external electric field of several V/m we set the ion excess micromotion energy to values on the order of tens of $k_{\mathrm{B}} \times \mathrm{mK}$ [?,?]. Consequently, if ions are present in the trap, strong atom losses occur due to elastic atom-ion collisions. Fig.2 shows a histogram of the atom numbers of the probe atom samples consisting of the outcome of about 1,000 experimental runs. The histogram displays several peaks which can be assigned to the discrete number of ions in the trap. Up to five ions were trapped simultaneously and detected with high fidelity. The atom loss rate increases nonlinearly with ion number mainly because the interionic repulsion prevents the ions from all occupying the trap center where the atomic density is maximal. While ion detection method 2 does not distinguish ionic masses, it has advantages in terms of experimental stability and does not require the trapping of ions amenable to laser cooling or other fluorescence based detection techniques.